Numerical modeling of meteorite impact-induced shock and elastic wave propagation and crater formation in heterogeneous material

by

M. Sc. Nicole Güldemeister

DISSERTATION

submitted to obtain the academic degree
Doctor rerum naturalium (Dr. rer. nat.)
presented at the Department of Earth Sciences,
Freie Universität Berlin

Institut für Geologische Wissenschaften, Fachrichtung Geophysik
der Freien Universität zu Berlin
2017

Betreuer:	**Prof. Dr. Kai Wünnemann**
Erster Gutachter:	**Prof. Dr. Georg Kaufmann**
Zweiter Gutachter:	**Prof. Dr. Kai Wünnemann**
Tag der Disputation:	**19. Januar 2018**

Abstract

Impact processes have shaped the development and evolution of the planetary bodies in our solar system. Despite the importance of this fundamental geological process, the consequences of impact events for targets with varying properties have not been sufficiently quantified. Thus, this thesis investigates the effect of target properties on impact-induced shock and elastic wave propagation and the crater formation using numerical simulations. This approach aims to offer a better understanding of impact processes on heterogeneous targets, which is key for quantitatively assessing of the role of impact and collision processes in the formation of the solar system and the evolution of planetary surfaces. For this study, the iSALE shock physics code has been used to conduct numerical simulations of impact processes within the Multidisciplinary Experimental and Modeling Impact Research Network (MEMIN). The usage of numerical models first requires rigorous validation and calibration of numerical parametrizations of the thermodynamic and mechanical response of material upon impact (so-called material models) against experimental observations. Then, the study focuses on the simulation of laboratory impact experiments in quartzite and in dry and water-saturated sandstone. Finally, the numerical data are applied to impact cratering in nature.

To investigate the entire cratering process in detail, the first thing needed is an understanding of the propagation of the shock wave and how the target material responds to shock loading as a function of petrophysical properties is needed. To provide detailed quantitative insights, mesoscale models, where single pores and grains are resolved, have been developed and analyzed in this thesis to gain a detailed understanding of shock wave-induced pore collapse. Pore collapse results in localized pressure amplifications, which can be up to four times greater than the average shock pressure in a porous sample. Mesoscale simulations, therefore, can explain the observed localized high shock pressure phases that appear next to more or less unshocked grains in impactites and meteorites; they can also explain the occurrence of shock effects such as the formation of diaplectic quartz glass in experiments in the low-pressure range.

In addition to the investigation of the shock wave, the elastic wave, which eventually evolves from the initial shock wave, has been recorded and analyzed using numerical sensors in iSALE. A systematic modeling study of impacts into targets with varying properties and the analysis of recorded seismic signals resulted in the determination of the so-called

seismic efficiency k, which relates the seismic energy to the impact energy. According to our results, k decreases slightly with porosity and is approximately two orders of magnitude lower for water-saturated materials than for dry nonporous material. The seismic quality factor Q, which quantifies how fast the wave attenuates, ranges between 35 and 80 for "dry" materials and is much lower (<10) for "wet" materials. The seismic magnitude of an impact event is about one order of magnitude larger for a solid or porous target than for a water-saturated target, showing that the seismic consequences are significantly dependent on target properties, and less seismic energy is induced if targets contain water.

Finally, the numerical results obtained at the laboratory scale were then extrapolated to natural crater dimensions. Therefore, numerical models were used to investigate crater formation beyond the scale of laboratory impact experiments, where crater size is controlled by the yield strength of the target material. It is well known that on the scale of natural impact craters, crater size is primarily controlled by gravity. In the current study, scaling parameters have been determined for cohesive materials, whereby the dynamic strength of the materials was accounted for.

Zusammenfassung

Impaktprozesse haben wesentlich zur Entwicklung und Evolution von planetaren Körpern in unserem Sonnensystem beigetragen. Auch wenn die Bedeutung dieses fundamentalen Prozesses allgemein bekannt ist, wurden die Konsequenzen von Impaktereignissen unter der Berücksichtigung von Targeteigenschaften bisher nicht ausreichend quantifiziert. Diese Arbeit beschäftigt sich mit der Untersuchung des Einflusses von Targeteigenschaften auf die impaktinduzierte Stoßwellenausbreitung, die elastische Wellenausbreitung und auf die Kraterbildung unter Verwendung von numerischen Simulationen. Dieser Ansatz hat das Ziel, ein besseres Verständnis von Kraterprozessen in heterogenen Targetmaterialien zu erlangen. Dies ist Voraussetzung für eine quantitative Bewertung, welche Rolle Impakt- und Kollisionsprozesse in der Entwicklung unseres Sonnensystems und der Evolution von planetaren Oberflächen spielen. Der *iSALE shock physics code* wird benutzt um numerische Simulationen von Kraterprozessen im Rahmen des "Multidisciplinary Experimental and Modelling Impact research Network" (MEMIN) auszuführen. Die Verwendung von numerischen Modellen setzt eine komplexe Validierung und Kalibrierung von numerischen Parametrizierungen des thermodynamischen und mechanischen Verhaltens des Materials (sogenannter Materialmodelle), basierend auf experimentelle Beobachtungen, während eines Impaktes voraus. Die Studie konzentriert sich vorwiegend auf die Modellierung von Impaktexperimenten in Quarzit und in trockenen und wassergesättigten Sandstein. Letztendlich werden die numerischen Daten auf Impaktkrater in der Natur angewendet.
Um den gesamten Kraterprozess im Detail zu untersuchen, ist es zunächst nötig ein gutes Verständnis über die Ausbreitung der Stoßwelle und wie das Targetmaterial als Funktion seiner petrophysikalischen Eigenschaften auf die Stoßwelle reagiert, zu erlangen. Mesoskalige Modelle, in denen einzelne Poren und Kornstrukturen aufgelöst werden, wurden entwickelt und analysiert um einem detaillierten Verständnis über stoßwelleninduzierten Porenkollaps gerecht zu werden. Porenkollaps führt zu lokalen Druckerhöhungen, die das Vierfache der gemittelten Stoßwellendrücke in einem porösen Material erreichen können. Mesoskalige Modelle können so das Auftreten von beobachteten lokalen Stoßwelleneffekten direkt neben ungeschockten Körnern in Impaktiten und Meteoriten sowie die Bildung von diaplaktischem Quarzglas in Experimenten im Niedrigdruckbereich erklären.
Zusätzlich zu der Untersuchung der Stoßwellen, wurden elastische Wellen mit Hilfe von numerischen Sensoren aufgezeichnet und ausgewertet. Eine systematische Modellierungs-

studie von Impakten in Zielgesteinen unterschiedlicher Eigenschaften und die Analyse aufgenommener seismischer Signale führt zur Bestimmung der sogenannten seismischen Effizienz k, welche die seismische Energie mit der Impaktenergie in Relation setzt. Laut der ausgeführten Studie nimmt k mit Zunahme der Porosität leicht ab und ist ungefähr zwei Größenordnungen kleiner für wassergesättigte Materialien als für Festgesteine ohne Wasseranteil. Der sogenannte seismische Qualitätsfaktor Q quantifiziert das Abklingverhalten der elastischen Welle in einem bestimmten Material, und liegt zwischen Werten von 35 und 80 für trockenes Material und ist signifikant kleiner ($<$10) für nasse Materialien. Die seismische Magnitude eines Impaktereignisses ist ungefähr eine Magnitude größer in einem Festgestein ohne Wasser als in einem Gestein welches Wasser enthält. Dies führt zu dem Schluss, dass seismische Konsequenzen signifikant von den Eigenschaften des Zielgesteins abhängig sind und weniger seismische Energie in wassergesättigte Gesteine induziert wird. Die numerischen Ergebnisse auf der Skala von Laborexperimenten konnten letztendlich auf natürliche Kraterdimensionen hochskaliert werden. Dafür wurden numerische Modelle verwendet um den Kraterbildungsprozess nicht nur auf der Skala von Laborexperimenten, wo die Kratergröße durch die Festigkeit des Zielgesteins dominiert wird, zu untersuchen. Auf der Skala von natürlichen Impaktkratern wird die Kratergröße hauptsächlich durch die Schwerkraft kontrolliert. Beim Hochskalieren der numerischen Ergebnisse wurde die dynamische Festigkeit des Materials berücksichtigt und Skalierungsparameter für Festgesteine bestimmt.

Statement of Contributions

This work was carried out within my time as a research student at the Museum of Natural History in Berlin as part of the DFG Multidisciplinary Experimental and Modeling Impact Crater Research Network (MEMIN). My work focuses on the numerical modeling of impact processes (Project 5 within MEMIN I). The financial support was given by Deutsche Forschungsgemeinschaft (DFG Project 355/6-1/2). The PhD thesis represents a cumulative dissertation as most of the chapters have been completely or partly published in peer reviewed journals. The thesis consists of four individual manuscripts (Chapters 4, 5, 6 and 7). The Chapters 4 to 5 represent published peer-reviewed papers where Chapter 5 represents only parts of the published paper. The PhD candidate N. Güldemeister is the first author of the articles presented in chapter 4, 6 and 7 and the second author of the article presented in chapter 5. Chapter 1 (introduction), chapter 2 (background), chapter 3 (methodology) and chapter 8 (conclusions) have been written as part of this thesis to explain the links between the different aspects of impact cratering I address in the published papers and to provide additional background information and details not provided in the papers. The citations of all articles are combined and stated in the reference section. The published and submitted articles presented in **Chapter 4 to 7** are as follows:

Chapter 4: *Propagation of impact-induced shock waves in porous sandstone using mesoscale modeling. Güldemeister N., Durr N., Wünnemann K. and Hiermaier S. Meteoritics and Planetary Science 48, 115-133 (2013).*

Chapter 5: *Diaplectic quartz glass and SiO_2 melt experimentally generated at only 5 GPa shock pressure in porous sandstone: Laboratory observations and meso-scale numerical modeling. A. Kowitz, N. Güldemeister, W. U. Reimold, R. T. Schmitt and K. Wünnemann. Earth and Planetary Science Letters 384, 17-26 (2013).*

Chapter 6: *Quantitative analysis of impact-induced seismic signals by numerical modeling. N. Güldemeister and K. Wünnemann. ICARUS 296, 15-27 (2017).*

Chapter 7: *Scaling impact crater dimensions in cohesive rock by numerical modeling and*

laboratory experiments N. Güldemeister, K. Wünnemann and M.H. Poelchau. Geological Society of America Special Papers 518 (2015): SPE518-02.

All numerical simulations using the shock physics code iSALE have been carried out by the PhD candidate under the supervision and assistance of her supervisor Kai Wünnemann. The experiments described in Kowitz *et al.* (2013b) have exclusively been analyzed by the first author of the article A. Kowitz. The contribution to the article of N. Güldemeister was about 10 %.

Additional to the manuscripts that are covered in this thesis, N. Güldemeister has participated as a co-author in following published works:

Mesoscale investigation of shock wave effects in dry and water-saturated sandstone. N. Durr, M. Sauer, N. Güldemeister, K. Wünnemann and S. Hiermaier. Proceedings of the 12th Hypervelocity Impact Symposium, Procedia Engineering 58 289-298 (2013).

Acoustic Emission Analysis of Experimental Impact Processes in Comparison to Ultrasound Measurements and Numerical Modeling. D. Moser, N. Güldemeister, K. Wünnemann and C. Grosse. Journal of Acoustic Emission (JAE) Online Volumes 31, 50-66 (2013).

Revision and recalibration of existing shock classifications for quartzose rocks using low-shock pressure ($2.5 - 20\,GPa$) recovery experiments and meso-scale numerical modeling. A. Kowitz, N. Güldemeister, R. T. Schmitt, W. U. Reimold, K. Wünnemann and A. Holzwarth. Meteoritics and Planetary Science 10, 1741-1761 (2016).

List of Abbreviations

Abbreviation	Explanation
ANEOS	Analytical equation of state
BSE	Backscattered electron
CPPR	Cells per projectile radius
CPL	Cells per pore length
EOS	Equation of state
HEL	Hugionot elastic limit
iSALE	impact-SALE (Simplified Arbitrary Lagrangian Eulerian)
MEMIN	Multidisciplinary Experimental and Modeling
	Impact Crater Research Network
MfN	Museum für Naturkunde Berlin
EMI	Fraunhofer Ernst-Mach-Institute Freiburg
PDF	Planar deformation features
Qu	Quartzite
Ss	Sandstone

List of Symbols and Units

Physical values		
P	Pressure	P
T	Temperature	$°C$
E	Specific internal energy	Pa
V	Specific volume	$m^3 \cdot kg^{-1}$
S	Entropy	$J \cdot K^{-1}$
σ	Stress	P
ε	Strain	
u_p	Particle velocity	$m \cdot s^{-1}$
Δt	Pulse duration	μs
λ	Wave length	mm
E_{kin}	Kinetic energy	J
E_{seis}	Seismic energy	J
E_{imp}	Impact energy	J

Material parameter		
c	Speed of sound	$m \cdot s^{-1}$
ρ	Density	$kg \cdot cm^{-3}$
α	Distension	
ϕ	Porosity	%
κ	Controls rate of compaction	
χ	Sound speed ratio	
ε_e	Elastic threshold strain	
ε_V	Compressive volumetric strain	
E	Young's modulus	Pa
D	Damage	
Y	Yield strength	Pa
Y_{eff}	Effective strength	Pa
UCS	Uniaxial compressive strength	Pa

Seismic parameter

v_P	P wave velocity	$m \cdot s^{-1}$
v_S	S wave velocity	$m \cdot s^{-1}$
k	Seismic efficiency	
Q	Seismic quality factor	
M	Seismic magnitude	

Projectile and target characteristics

L	Impactor diameter	m
a	Impactor radius	m
δ	Impactor density	$kg{\cdot}cm^{-3}$
m	Imapctor mass	kg
U	Impact velocity	$m \cdot s^{-1}$
g	Gravity	$m \cdot s^{-2}$

Crater dimensions

D	Crater diameter	m
d	Crater depth	m
V	Crater volume	m^3

Scaling parameters

π_D	Scaled crater diameter
π_V	Scaled crater volume
π_2	Gravity scaled imapct size
π_3	Strength scaled imapct size
π_4	Dimensionless ratio of projectile and target density
π_d	Dimensionless ratio for crater depth
C_v	Scaling parameter for crater volume
γ	Scaling exponent for crater volume
ζ	Coupling parameter
μ	Scaling exponent for velocity
ν	Scaling exponent of coupling parameter

Contents

List of Figures

List of Tables

1 Introduction

1.1 Impact cratering

Impacts, or the collisions of solid bodies, are fundamental geological processes, and their dominance is ubiquitous in the entire solar system (Shoemaker, 1977). Impacts occur over a large range in scale, from collisions of small dust particles to the collisions of cosmic bodies such as comets or small asteroids, to collisions of planetesimals and giant impacts on planets. The Moon was most likely formed by such a giant impact after the formation of the Earth, as shown in an artistic illustration in Figure 1.1A. After the formation of other planetary bodies, the remains of planetary accretion processes can be found in the asteroid belt between the terrestrial and outer planets. The asteroid belt is the main source region of cosmic objects whose orbits bring them in close proximity to the terrestrial planets and, therefore pose a hazard. The more or less cratered landscapes of planets and asteroids testify to the frequency of impact events in the past. The craters of different sizes and the various environmental consequences depend not only on the size, but also on velocity and mass of the impactor (Collins *et al.*, 2005); resulting craters also depend on the properties of the target rocks.

Recent events document that impacts of cosmic bodies on planetary surfaces is an ongoing process – e.g. the impact of Comet Shoemaker-Levy 9 into Jupiter (Weaver *et al.*, 1995; Zahnle and MacLow, 1994), the 15-m-sized meteorite impact crater, formed on September 15, 2007 in Carancas, Peru, (Kenkmann *et al.*, 2009, Figure 1.1B), or the recently observed air burst of the Chelyabinsk meteorite in Russia in February 2013 (Figure 1.1C) - and such impacts will occur again in the future. These recent events provide evidence that impacts indeed pose a threat to mankind and the environment. The largest known event that elucidates the significance of impact events is the Chicxulub event that caused a large mass extinction of species in the evolution of Earth's biosphere at the Cretaceous-Tertiary (K/T) boundary 65 Ma ago (e.g. Alvarez *et al.*, 1980). This event clearly shows that at least once in Earth's history the impact of a large asteroid changed the environment dramatically.

Figure 1.1: (A) Formation of the Moon as a result of the collision of a large body with our Earth (artist's representation). (B) Carancas crater, Peru (Kenkmann *et al.*, 2009). (C) Chelyabinsk, Russia, impact flash recorded with a dashboard camera.

The frequency of these events has changed significantly since the early evolution of planets. The flux of impactors was much more intense in the past, as planetary surfaces are peppered with craters. In contrast to the heavily cratered landscape of e.g. the Moon, Mercury, Mars and asteroids, the crater record on Earth only includes 190 impact structures (as of September 2016, http://www.passc.net/EarthImpactDatabase/; Figure 1.2). The relatively small number of impact structures on Earth is due to high erosion rates, tectonic activity and vegetation cover which remove or conceal the evidence of

impact structures. However, the known crater record is still incomplete, and it is most likely that a large number of impact craters have not been detected yet.

Figure 1.2: Map with the location of impact structures on Earth. Map shows 190 confirmed impact structures (http://www.passc.net/EarthImpactDatabase/).

Additionally to the fact that impacts have a strong effect on the evolution of Earth, the heavily cratered landscapes of planetary bodies provide some important insight into the evolution of our solar system. Based on the assumption that an old planetary surface, which has longer exposure to cosmic bombardment, exhibits more crater structures, the age of a planetary surface can be determined by using crater size-frequency distribution (e.g. Baldwin, 1971; McGill, 1977; Grieve and Dence, 1979; Hartmann, 1965, 1977; Michael and Neukum, 2010). The impact structure also provides information about the characteristics of the impacted material, as the morphology of the crater depends to some extent on the properties of the target material (e.g. Holsapple and Housen, 2007; Kenkmann *et al.*, 2011; Schäfer *et al.*, 2006; Elbeshausen *et al.*, 2009; Wünnemann *et al.*, 2006, 2011). Additionally, the size of the impacts can give insights about the released energy during the impact event (e.g. Schmidt and Housen, 1987; Holsapple, 1987, 1993), which then can be used to predict possible consequences for the environment (Collins *et al.*, 2005).
However, in contrast to other natural catastrophes like volcanic eruptions or earthquakes, impact events can not be directly observed, as they occur very infrequently and the location and time of an event are not precisely predictable. Thus, the study of impact cratering requires an interdisciplinary approach. Field observations, laboratory experiments and numerical simulations have to be combined to study impact cratering processes

holistically. Impact experiments in the laboratory provide a better understanding of the behavior of materials under extreme temperature, pressure, and stress conditions typical for hypervelocity impact processes. As laboratory experiments are often limited to certain conditions, another essential tool to investigate impact structures are numerical simulations of impact processes. They significantly contribute to a better understanding of impact processes and their dynamics. Simulations are able to cover the entire cratering process while it is difficult to record crater growth, fracturing, shock wave propagation, ejection of material in real-time experiments. Furthermore, field observations at natural terrestrial craters or by remote sensing of extraterrestrial craters are limited to the final state of the crater. Numerical simulations further allow for a much more systematic investigation of the effect of material properties of the projectile and the target on impact processes.
The effect of the projectile material on the cratering processes has been studied previously in some detail (e.g. Collins *et al.*, 2005). By contrast, the effect of target properties and the consequences on the impact cratering process is not well understood, yet. However, it is well known that porosity, in particular, is one of the key parameters that has an influence on shock wave propagation and, thus, on the cratering process (Zel'dovich and Raizer, 2002; Wünnemann *et al.*, 2008; Housen and Holsapple, 2003; Kieffer *et al.*, 1976; O'Keefe *et al.*, 2001).
In this work numerical modeling will be the main method to study the significant effect of target properties, in particular porosity, on shock and elastic wave propagation and on the crater formation process in detail. The central questions that are addressed in this study are as follows:

How do petrophysical properties of rocks affect hypervelocity impact processes, and what are the consequences for the environment?

How does shock wave propagation depend on porosity?

How is impact-induced seismicity affected by porosity?

How does the crater size depend on the porosity and strength of the target rocks?

1.2 Impact cratering, shock and elastic wave propagation in porous and water-saturated rocks

Porosity is a typical property of rocks of the upper crust on Earth and other planetary bodies. Regolith, a loose dust-like material, covers the surface of most bodies in the solar system such as Moon, Mars, Mercury, and asteroids. It is characterized by a significant amount of porosity. The presence of subsurface water is very common on Earth, and its existence on Mars is widely accepted. In addition, due to their very low densities, comets are thought to be very porous (Richardson *et al.*, 2007). This may also be true for a number of asteroids whose bulk density is much lower than their rocky composition suggests (Britt *et al.*, 2002).

Thus, the presence of porosity and water is common on planetary surfaces and in crustal rocks, and it seems that porosity has a significant effect on the formation of impact craters and wave propagation.

In a number of studies of terrestrial and extraterrestrial craters that have employed impact experiments, and numerical modeling (e.g. Kieffer *et al.*, 1976; Love *et al.*, 1993; O'Keefe *et al.*, 2001; Holsapple *et al.*, 2002; Goldin *et al.*, 2006; Britt *et al.*, 2002), the effect of porosity has been addressed previously, but a systematic, quantitative study is lacking so far.

Figure 1.3 compares shock wave propagation in a nonporous and a porous target material. The snapshots were generated from a numerical simulation of an iron projectile impacting at $5\,km \cdot s^{-1}$ onto either a porous or nonporous quartzite target. The shock wave amplitude is lower and decreases much faster in the porous target relative to the nonporous target. The resulting crater is larger in depth and smaller in diameter for the porous target material.

It is well known that porosity and the presence of water, further, affects the compression of material, how a material is released from pressure, and what maximum pressures and temperatures the material experiences during shock wave propagation. Peak pressure and peak temperature distributions for different target materials (nonporous, porous, and water saturated) have been determined in a preliminary numerical study within this work and are shown in Figure 1.4.

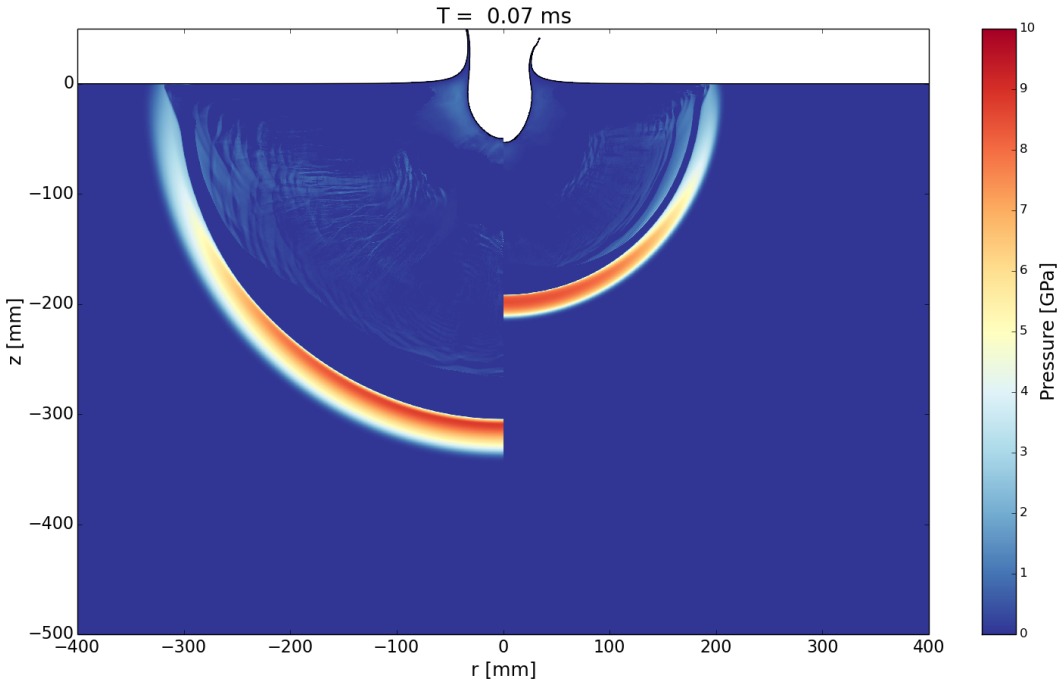

Figure 1.3: Snapshot of the shock wave propagation through a nonporous (left) and porous (right) target material. Simulations are shown for a quartzite target after $0.07\,ms$. An iron projectile was impacting at $5\,km \cdot s^{-1}$ onto the target. The colors indicate pressure contours.

The maximum pressures the material experiences during the passage of a shock wave are much higher and cover a much larger volume in the vicinity of the crater in case of a nonporous material than in the case for a porous material, where only very small amounts of target material undergo shock pressures above $2\,GPa$. The shock wave itself can be responsible for the formation of melt. Regarding temperature distributions, porous material exhibits higher peak temperatures that extend over a larger volume in comparison to the nonporous material. If water is present, temperatures are higher than in case of a nonporous target, but lower than in case of a "dry" porous rock. Pressure distribution behaves in the opposite way. Apparently, shock waves attenuate faster due to the crushing of open pore space. The additional plastic work involved in the compaction of pore space causes higher shock temperatures in porous material than in nonporous materials at the same shock pressures (already shown by Zel'dovich and Raizer, 2002). This may result in an increase in shock-induced melting in porous materials; however, on the other hand, the shock wave attenuates faster in porous material, and low impedance pore contents, i.e., air and/or water, result in lower shock wave velocities and pressures in porous materials so that a smaller volume of material experiences sufficiently high shock pressures. The competing effect is illustrated in Figure 1.4. The net effect, the faster attenuation of shock waves and the lower critical pressure for the production of impact melt has been quantified by numerical models (Wünnemann *et al.*, 2008).

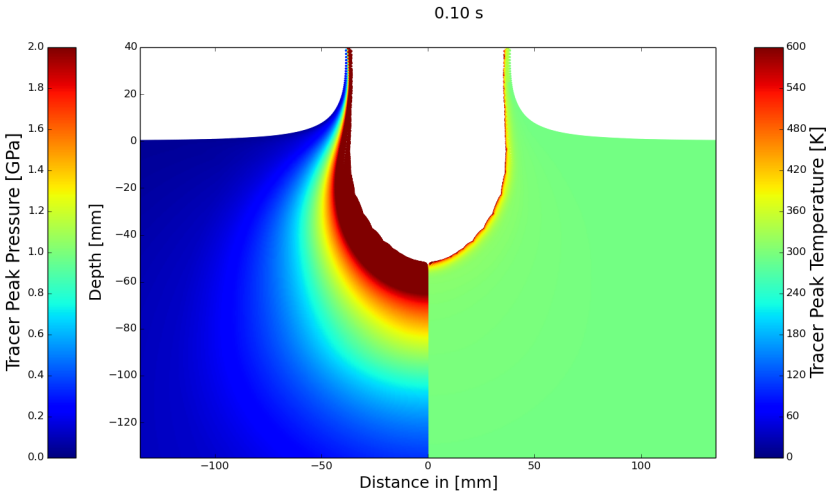

(a) Solid/Nonporous material

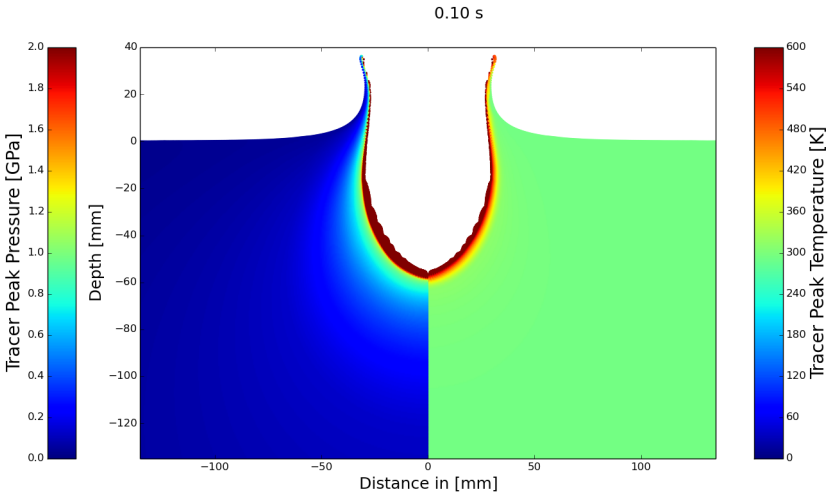

(b) Porous material

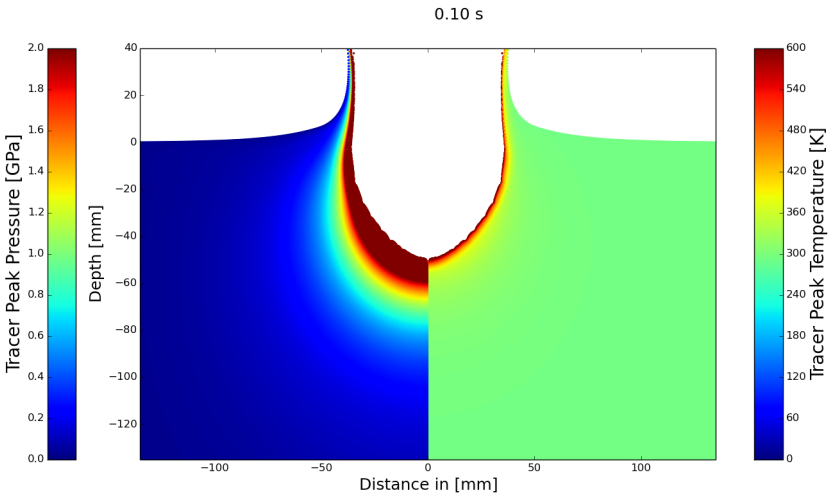

(c) Water-saturated material

Figure 1.4: Peak pressure and peak temperature distribution in a nonporous, a porous, and a completely water-saturated material. Simulations performed for the impact of an iron projectile impacting at $5\,km \cdot s^{-1}$. The porous material has a porosity of 25 % and the water-saturated material a water content of 25 %.

To gain a better understanding about the entire crater formation process, profound knowledge about the propagation of the shock wave and how material responds to shock loading is essential. This can be achieved by making use of so-called "mesoscale simulations" (see Chapter 4 and 5). At the size of single pores and grains, rocks are usually heterogeneous. Mesoscale models can resolve these heterogeneities, such as single pores and grains, and enable researchers to track the propagation of a shock wave through heterogeneities and determine how, e.g. pores are closed by high pressures. The results from mesoscale simulations are directly comparable to observations on samples from impact craters or in laboratory experiments (Wicklein, 2006; Kowitz *et al.*, 2013a; Davison *et al.*, 2011). By using mesoscale models it can be shown that lithological heterogeneities can explain the localized appearance of shock features (e.g. due to shearing along interfaces or closure of open cracks and pores). For instance, on the one hand the crushing of pores causes a localized pressure amplification (which may explain in some cases the localized occurrence of shock-melting), but on the other hand the extra plastic work that is done by pore space collapse results in an overall decrease of the shock amplitude. A quantification of such effects is important for the interpretation of the observations in thin sections of experimental or natural samples and for the development of macroscopic models that describe the crushing of pores in large rock units. The macroscale models, in contrast to the mesoscale models, treat the material as a homogeneous unit of constant properties. They are applicable to investigating the whole impact process, which includes the first contact of the projectile with the target, the crater formation process, as well as the final crater modification.

Specific target properties affect not only the propagation of the shock wave, but also the amplitudes and decay of elastic waves that eventually evolve from the shock front. Figure 1.5 presents a simplified illustration how the shock and elastic wave attenuates as a function of distance to the point of impact. In general, shock waves attenuate much faster than elastic waves. Elastic wave velocities and amplitudes are usually smaller in porous and water-saturated materials than in nonporous materials. The decay behavior of the different waves may also change with increasing material porosity or water saturation. Thus, not only the decay behavior of the shock wave (shock regime in Figure 1.5) is dependent on material properties, but that of the elastic wave (elastic regime in Figure 1.5) is also most likely affected.

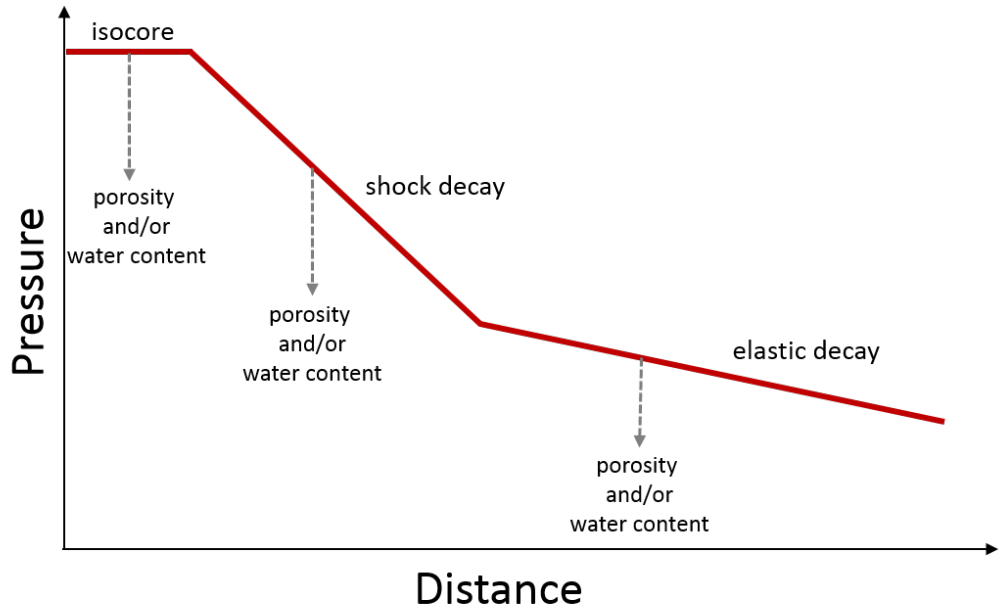

Figure 1.5: Pressure decay of the shock and elastic wave as a function of distance. Pressure amplitudes and the decay of pressures change with increasing porosity and/or water.

An immediate and most obvious consequence for the generation and propagation of shock waves induced by a hypervelocity impact is the formation of a crater. As discussed above, shock waves are significantly affected by heterogeneities such as porosity. Craters resulting from shock compression also strongly depend on the petrophysical properties of the rocks they form in. For a comprehensive understanding of the relationship between crater size and impactor and target properties, material properties such as density, strength, porosity, and water content have to be taken into account. Our present understanding is based on laboratory experiments (e.g. Hiermaier *et al.*, 1997; Riedel, 2000; Hertzsch *et al.*, 2005; Heider and Kenkmann, 2003; Kenkmann *et al.*, 2011) that have some limitations in terms of size scale, target materials, and the influence of strength vs. gravity as an important mechanism controlling crater size (see Chapter 7).

As repeatedly mentioned, **numerical modeling** is a very useful and important tool for overcoming experimental limitations and investigating the effect of porosity and water saturation during crater formation on different scales. Numerical models have previously been used in a wide range of applications in impact research (e.g. Melosh and Ivanov, 1999; Wünnemann and Ivanov, 2003; Wünnemann *et al.*, 2006; Elbeshausen *et al.*, 2009; Davison *et al.*, 2010, 2011). Numerical models provide insights into the dynamic process during an impact event that are difficult or impossible to record in experiments. As Figure 1.6 demonstrates, numerical modeling enables researchers to study impact processes on all scales. These simulations can be performed on the very small scale where grain structures and pore spaces are explicitly resolved using mesoscale models (Figure 1.6A-B).

It further enables the modeling of crater formation on the scale of laboratory experiments, which makes experiments and models directly comparable (Figure 1.6C-D); additionally, it allows for simulating large-scale natural crater formation. Experimental observations serve as important benchmarks to calibrate and validate numerical models. However, laboratory experiments are limited to the small scale, and most previous experiments have been carried out in cohesion-less materials (e.g. sand). They are limited to a small parameter space, as target and projectile properties cannot be varied independently. Many questions regarding the impact formation process have been addressed by experiments, but some questions still remain because of experimental limitations. Thus, numerical modeling provides insights into impact phenomena where experiments are often limited. However, rigorous testing and validation of models is crucial, and this can be done by comparing numerical results with experiments. Numerical modeling can, then, be used to accurately quantify the separate effects of specific target properties such as porosity or water saturation independent of one another, as they can be varied in the models arbitrarily.

It is even possible to create "virtual materials", e.g. liquid water with porosity or a granular material with no porosity. This may only be of academic interest with no actual analog in nature, but the study of such materials is of great value for systematic studies of the effect of, for example, porosity on crater formation or shock wave propagation. Further, natural craters on Earth or on any planetary body can be reproduced by numerical methods (Figure 1.6E-F). Here numerical simulations can provide insights into the entire cratering process whereas natural observations only provide information about the final state of the crater.

In summary, the most important advantage of numerical modeling is that the investigation of processes from the small to the large scale is possible and that impact conditions such as projectile and target properties can be varied independently. They provide insight into the cratering process, which cannot be investigated using neither laboratory experiments nor field observations. Numerical models present an ideal tool to upscale experimental results to dimensions of natural craters.

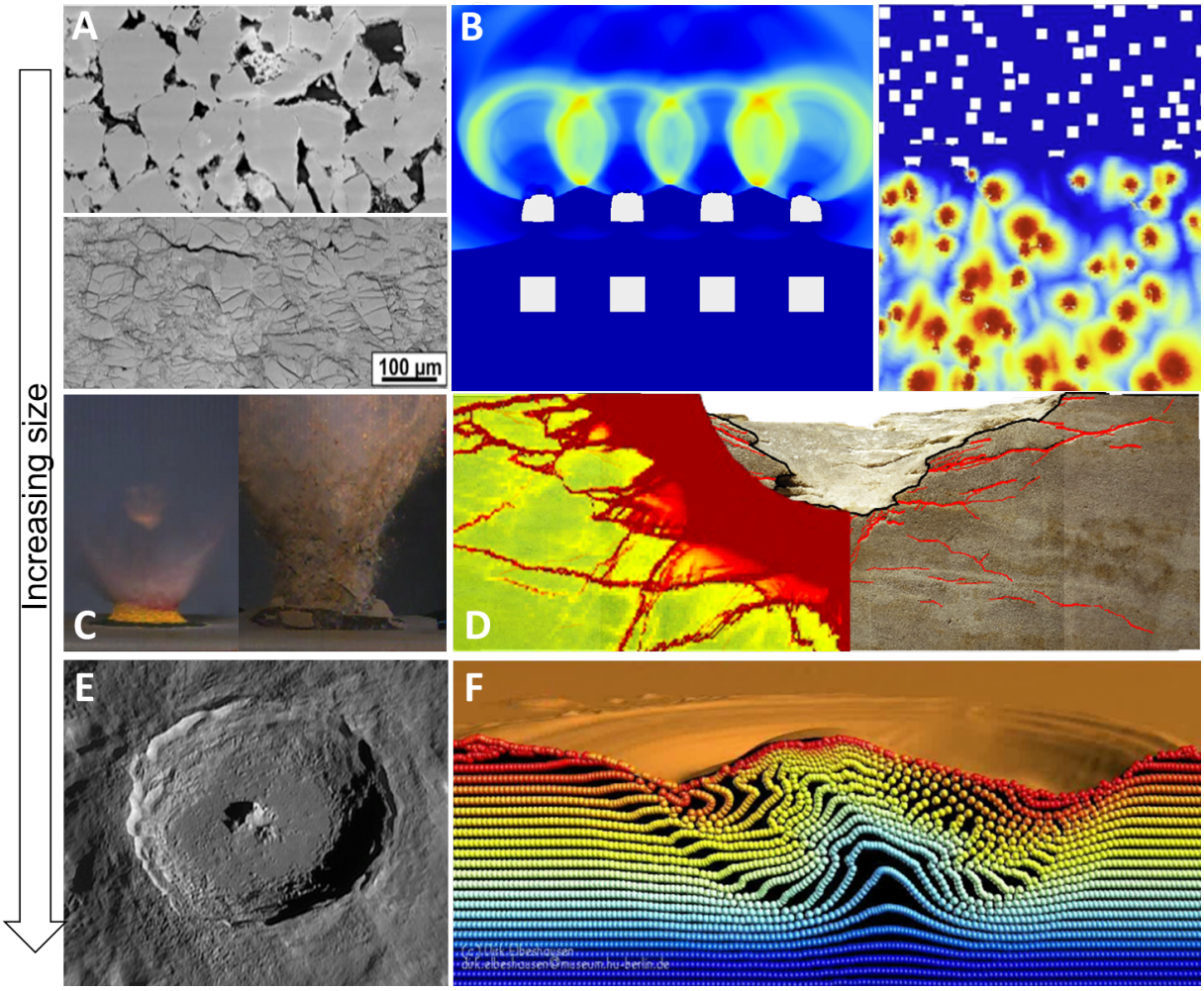

Figure 1.6: Numerical modeling and observations of impact processes on different scale. Scale range from single grains and pores (A and B) to the scale of laboratory experiments (C and D), and to very large craters on Earth and planetary surfaces (E and F). Subfigures A (Kowitz *et al.*, 2013a), C (Image courtesy to EMI Freiburg) and E present the experimental and natural observations. Subfigures B shows the numerical model of the collapse of a set of pores and the evolving pressure distribution (Kowitz *et al.*, 2013a), D (Schäfer *et al.*, 2006) shows the comparison of the crater in the numerical model and experiment, and F shows a three-dimensional (3D) simulation of a complex crater (Elbeshausen, 2012).

1.3 The Multidisciplinary Experimental and Modeling Impact Crater Research Network (MEMIN)

Our present study of the geologic process of impact cratering is based on detailed field studies of natural craters, laboratory experiments, and numerical simulations. This PhD thesis has been carried out within the Multidisciplinary Experimental and Modeling Impact Research Network (MEMIN; www.memin.de), financed by the German Research Foundation (DFG), and established to combine these different approaches and bring the expertise of several disciplines together in order to answer essential questions about the crater formation process. Its main objective is to investigate the dynamics of the impact process and the effect of porosity and water saturation on the cratering process. The program is subdivided into seven projects focusing on different aspects of laboratory impact experiments and making also use of numerical simulations. Each project addresses different objectives that contribute to the overall goal to provide, eventually, a well-determined representation of the entire impact process.

Central to the MEMIN project are two-stage light gas guns (located at the Fraunhofer Ernst-Mach Institute in Freiburg, Germany) that are capable of producing craters in the decimeter range in cohesive rocks, a size that could not be achieved in previous experiments at the laboratory scale. The novelty of the MEMIN project lies in its use of natural materials, which have not been addressed in previous experiments. In the laboratory impact experiment, steel, aluminum, and iron meteorites have been used as projectiles, 2.5 to 12 mm in diameter impacting on target blocks of edge length up to $80 \times 80 \times 50\,cm$ with impact velocities between 2.5 and 7.8 $km\,s^{-1}$. Parametric studies have been carried out to investigate the role of water, porosity, target layering, and impact velocity on cratering mechanics, shock effects, and distribution of the projectile material. The MEMIN project includes the mineralogical and mechanical characterization of the target before and after the impact experiment, the investigation of the impact experiment with respect to fracture propagation, stresses, crater growth and ejecta dynamics. This PhD thesis was conducted within the subproject ***"Numerical modeling of impact cratering processes"***. The modeling project is of particular importance in several respects: (1) the models provide insights into processes beyond observational limitations and, thus, aid the interpretation and analysis of the obtained data; (2) in turn, observational constraints serve as important

benchmarks to calibrate and validate models; and (3) models present the only method to upscale the experimental results and apply the important findings to natural craters. The modeling project, therefore, significantly aids in narrowing the dimensional gap between laboratory impact experiments and planetary impacts.

1.4 Objectives and goals

This thesis is motivated by the fact that our present quantitative understanding of the consequences of impact processes does not sufficiently take into account the effect of varying material properties. This objective is approached by the use of numerical modeling as a tool to simulate shock and elastic wave propagation, the collapse of pore structures, and the crater formation process. The goal is to provide a comprehensive study of different important aspects related to shock waves and cratering going from the very small scale (mesoscale) to the very large scale (upscaling of laboratory-size craters to natural craters). The study aims to predict the consequences of an impact event quantitatively. The consequences depend on projectile properties (mass, size, velocity, composition), which have been studied in detail previously, but they also depend significantly on target properties, which this study is focusing on. Thus, special attention in this study has been given to the **effect of porosity** on the propagation of the shock wave and the elastic wave as well as on the crater size. Additionally, the effect of water saturation and strength have been analyzed. In order to assess the consequences of impact processes, detailed knowledge about impact-induced compressive waves and the response of different materials to compression is required in order to carry out further studies regarding the elastic wave in the far field.
The aim of this thesis can be subdivided into the following questions:

- **How does shock wave propagation depend on material properties?**
- **How does elastic wave propagation depend on material properties, and what are the consequences of impact-induced seismicity?**
- **How does crater formation/size depend on material properties?**

Following steps are necessary in order to assess the main aims of this research project:

(1) Validation and calibration of numerical material models by observations from laboratory experiments carried out within the *MEMIN* project

(2) Development of new material models that take into account complex geologic materials, such as dry and water-saturated sandstone, to treat the behavior of heterogeneous rocks much more realistically, based on the existing equations of state for quartzite and water

(3) Validation of new models by comparing laboratory cratering experiments and numerical models with respect to crater morphology and morphometry, shock wave modification in the target rock, and the properties of the elastic wave

Analyzing the effect of material properties makes the following steps necessary:

(1) Development of mesoscale models in order to

- quantify localized shock amplification as result of pore space crushing
- describe material mixtures
- validate macroscopic models to describe the bulk behavior of porous and water-saturated materials in large-scale models of crater formation
- quantify processes on different scales by bringing meso- and macroscale observations into accordance

(2) Characterization of seismic properties for different materials, which requires

- calibrating the numerical model with regard to real-time measurements
- investigating the elastic wave
- quantifying seismic parameters using experimental and numerical methods

(3) Upscaling of numerical models from laboratory impact experiments to natural crater dimensions taking into account the effect of cohesion, crushing strength, porosity and water saturation, which includes

- conducting suite of numerical experiments from strength-dominated to pure gravity-dominated crater formation
- modifying existing scaling relationships to account for specific target properties

1.5 Structure of the thesis

The thesis is subdivided into eight chapters. Chapter 1 introduces the relevance and importance of impact cratering, the concepts of crater formation, and the used method of numerical modeling and how it presents an essential tool in impact studies. It also presents the umbrella research project and states the main objectives of the thesis. Chapter 2 provides some theoretical background information related to impact cratering in order to establish a better understanding of the basic concepts as part of the different objectives addressed in this thesis. Further, an overview of the numerical method used, the shock physics code iSALE, is given in Chapter 3. The subsequent chapters (Chapters 4 to 7) are self-contained and represent manuscripts that have already been published. The three subjects that are covered herein are mainly pore collapse, seismic shaking, and

crater formation in order to quantify the consequences of impact cratering focusing on the effect of target properties. Each chapter has its own introduction, methods and result sections and ends with a conclusion summarizing the main points of the chapter. Finally, a conclusion chapter completes the thesis.

Following this chapter (Chapter 1), **Chapter 2** consists of some important background information about shock wave physics, crater mechanics, seismic waves and scaling relationships.

Chapter 3 summarizes the numerical method that has been used to address the objectives of this study. It provides information about the iSALE shock physics code and covers some of the main features that have been implemented in the code and that are essential for this thesis.

In **Chapter 4**, a mesoscale model, in which single pores and grains are resolved, has been developed in order to investigate shock wave-induced pore collapse and the behavior of heterogeneous material in detail. Focus is given to the shock wave propagation in porous material by a detailed comparison of mesoscale models, where individual pores are resolved, and macroscale models, where the effect of pore space crushing on shock propagation is parametrized (in the following, also referred to as "homogenized models"). The study allows, for the first time, a quantification of localized amplification of shock pressure as a consequence of the collapse of pores space. This chapter has been published in Güldemeister *et al.* (2013). A similar study has been carried out by Durr *et al.* (2013), in which I appeared as a co-author. The study applies a different numerical approach than the one used in this study and therefore provides a good validation of the numerical method.

Chapter 5 presents laboratory observations and analyses from shock experiments in porous sandstone and compares them with findings from mesoscale modeling. The study confirms the predictions from the analyses carried out in Chapter 4 and also represents a good validation of the numerical model. The quantification of localized shock amplification explains the occurrence of shock effects in experiments in the low-pressure range. This chapter is based on parts of an article published by Kowitz *et al.* (2013a) but presents only those parts of the original publications that represent my contribution to this study. Kowitz *et al.* (2016), in which I also appear as a co-author, additionally carried out a systematic porosity study to investigate the dependency of the diaplectic quartz glass/SiO_2 melt formation on porosity.

Chapter 6 focuses on the investigation of the elastic wave in order to quantify how important seismic parameters depend on material properties. This requires a sophisticated calibration and validation of material models of porous (and also water-saturated) materials. This chapter provides an estimation of the seismic magnitude induced by seismic shaking after impact events on an arbitrary scale - current estimates range over more

than three orders of magnitude. This chapter has been published in Güldemeister and Wünnemann (2017). An essential basis to carry out this study was provided by Moser *et al.* (2013) (a work I contributed to as a co-author). In particular, Moser *et al.* (2013) presents some important information about wave velocities for different target materials that can be used to calibrate the numerical material models.

Chapter 7 deals with the macro-scale effects (crater size) as a function of target properties, in particular porosity and strength. The numerical models and laboratory experiments in cohesive rock, as partly presented in the previous chapters, can be extrapolated to the dimension of natural craters. This chapter was published in a Geological Society of America (GSA) special paper as Güldemeister *et al.* (2015).

Chapter 8 recapitulates the most important results of the preceding chapters. This chapter addresses to what extent the objectives and goals formulated in the introduction have been met. At the end, limitations, conclusions, and an outlook are given.

2 Background

The objective of this chapter is to give the reader an overview of shock wave physics, seismic waves related to impact events, crater mechanics and a simple parametrization of the relationship between crater size and the kinetic energy of the impactor (expressed as so-called scaling laws). Principles of shock wave physics and crater mechanics are the basis for understanding the physical processes that eventually result in a crater structure and the specific modifications of rocks and mineral phases that allow for an unequivocal identification of an impact event.

2.1 Impact-induced waves

Shock waves

An understanding of the physics behind the highly dynamic process of the generation and propagation of shock waves is crucial for the study of hypervelocity impact events. Melosh (1989) and Zel'dovich and Raizer (2002) provide a detailed description of shock waves. Here, some important information is summarized.

During an impact event, a shock wave is generated at the interface between the impacting body (impactor) and the surface (target). It is important to note that the shock wave is a solitary wave that propagates through the impactor in the opposite direction of the impact and through the target in the impact direction. Shock waves are plastic compressive waves which propagate faster than the speed of sound c (Zel'dovich and Raizer, 2002). The shock wave can be approximated by a mathematical discontinuity where the state parameters, density, pressure, particle velocity and internal energy abruptly change from pre-shock conditions to a shock state (Figure 2.1).

These changes in state parameters across a shock front are described by the Rankine-Hugoniot equations.

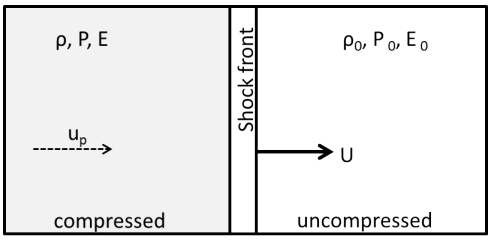

Figure 2.1: Properties describing the state of the medium before (uncompressed) and after (compressed) a shock wave has propagated through the medium. ρ_0 and ρ are the uncompressed and compressed densities, U and u_p are the shock and particle velocities, P_0 and P are the uncompressed and compressed pressures, and E_0 and E are the uncompressed and compressed specific internal energies. The shock front propagates at velocity U (modified after Melosh, 1989).

The equations are based on the conservation of mass, momentum, and energy and relate the pre-shock state with the shock state. Note, that entropy is not conserved in this process.

$$\text{Conservation of mass:} \quad \rho(U - u_p) = \rho_0 U \tag{2.1}$$

$$\text{Conservation of momentum:} \quad P - P_0 = \rho_0 u_p U \tag{2.2}$$

$$\text{Conservation of energy:} \quad E - E_0 = \frac{1}{2}(P + P_0)\left(\frac{1}{\rho_0} - \frac{1}{\rho}\right) \tag{2.3}$$

where ρ_0 and ρ are the uncompressed and compressed densities, U is the propagation velocity of the shock front, u_p is the particle velocity, P_0 and P are the uncompressed and compressed pressures, and E_0 and E are the uncompressed and compressed specific internal energies, respectively. When the shock wave hits the free surface (the interface between rock and atmosphere) of the projectile, it is reflected as a release wave traveling backwards through compressed material unloading the matter from high shock pressure. The velocity of the so-called rarefaction wave is larger than the shock wave velocity because the rarefaction wave propagates through compressed material. During the release of the material, phase transitions (solid, melt, vapor) occur depending on the peak pressure during shock compression.

The response of matter to a shock compression can be illustrated by the so-called Hugoniot curve in the pressure-specific volume ($P-V$) space and particle velocity-shock velocity (u_p-U) space as shown in Figure 2.2. The Hugoniot curve does not represent a thermodynamic state, but connects different possible shock states. Both representations can be converted into one another by the Hugoniot equations (Equations 2.1 - 2.3). Figure 2.2B illustrates the linear relationship between the particle and shock wave velocity in the shock wave regime. Note that in the case of a solid-state phase transition, each phase can still be parametrized by a straight line (not shown here). The Hugoniot curve depends on material properties such as porosity or temperature (Figure 2.2A). The thermodynamic path of

matter from an unshocked state to a shock state on a specific point on the Hugoniot curve is given by the so-called Rayleigh line (dotted lines in Figure 2.2A). The Rayleigh line starts at the initial pressure P_0 and specific volume of the material, which may differ for nonporous (V_0) and porous (V_{00}) material, and ends at the shock state (P_{shock}). The PdV work that is done during shock compression is given by the triangle formed by the initial volume, V_0 or V_{00}, the shocked specific volume V_{shock} and the shock pressure P_{shock}. Eventually, the material is released from shock by the propagation of a rarefaction wave that is generated at the free surface and travels in the wake of the shock front. The gradual unloading of matter is much less abrupt than shock loading at the shock front. The thermodynamic path is given by an adiabate that may be approximated by the Hugoniot curve (solid lines in Figure 2.2A). The PdV gain during release is approximated by the area bounded by the Hugoniot curve and the shocked specific volume of the material. The energy gain after the passage of the shock wave remains as heat in the material defined by the area bounded by the Hugoniot and the Rayleigh line of the material. Besides shock-induced heating, the material also remains in motion as it also retains some rest particle velocity, which drives the opening of the crater resulting from a hypervelocity impact when shock waves are induced. As shown in Figure 2.2 the shock and release paths significantly differ for porous and nonporous materials. To shock a porous material to the same pressure as a nonporous material, more PdV work, is required, as the initial specific volume is larger for porous material and some additional work is required to crush out open pore space. As a consequence of the increased PdV-work porous material also experiences more shock-induced heating than nonporous material.

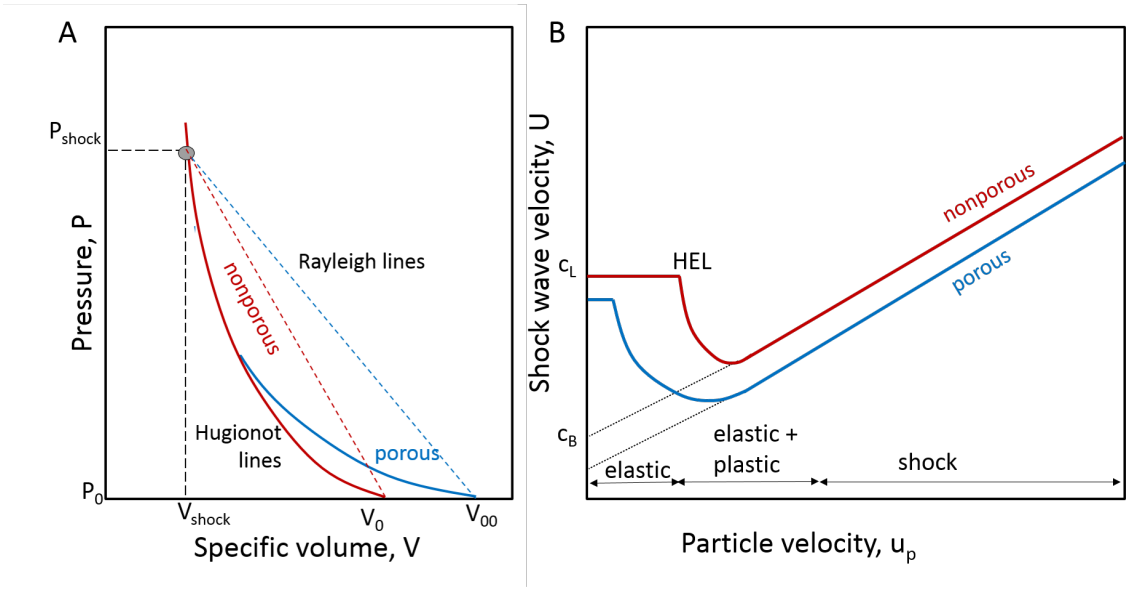

Figure 2.2: Hugoniot curves in (A) the pressure–specific volume space (P–V) and in (B) the particle velocity–shock velocity u_p–U (modified after Melosh, 1989). The P–V plot shows the change in volume and pressure of a nonporous and porous material as they respond to shock. The material is abruptly shocked to its shocked state shown by the corresponding Rayleigh line.

As the shock wave propagates through the target material it attenuates. This is due to geometric spreading in the case of a spherical shock front, the release wave that gradually overtakes the shock front and other dissipative processes. Eventually, at some distance the shock wave weakens first into a plastic wave preceded by an elastic precursor and then at further distances converges into a pure elastic wave. The described concept is presented in Figure 2.3 showing shock pressures as they decrease with depth during a typical impact scenario for different time steps, where the initially developed shock wave with a preceding elastic precursor is shown. During crater formation, the rarefaction wave then has caught up and has weakened the plastic wave and an entirely elastic wave remains. The initial shock wave has turned in a pure elastic wave. This is depicted on the left side of Figure 2.3, which shows two snapshots at different time steps of the propagating wave, the initial shock wave and the resulting elastic wave.
A more detailed description, as well as a description how pressure amplitudes decay for the different wave types, is provided in Chapter 6.

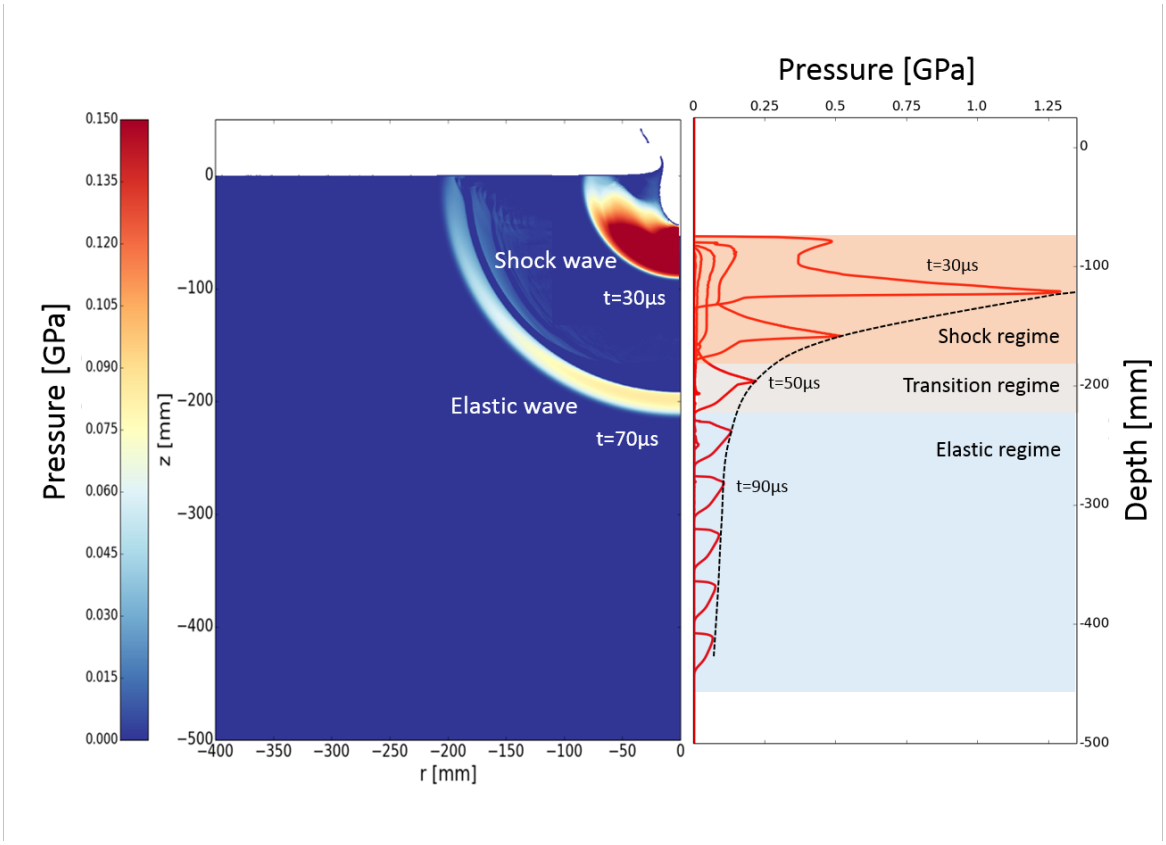

Figure 2.3: Snapshots of the propagation of the shock and elastic wave (left) and pressure profiles as a function of distance for various time steps (right) for a sandstone target. Separate regimes (shock, elastic, and a transition regime) are shown. In the shock regime the wave attenuates much faster than in the elastic regime. The wave in the transition regime consists of a shock part and an elastic part.

Elastic waves

Elastic (or seismic waves), which evolve from the shock front as previously mentioned, behave much differently than shock waves and are often neglected during impact events, as the shock wave is the prominent wave that results in the formation of a crater and the observable shock features. In contrast to shock waves, where the deformation is plastic (permanent), seismic waves cause only an elastic strain, and material remains unchanged after the passage of the wave. According to Melosh (1989), the structure of the elastic wave induced by an impact is very complex. It may have multiple pulses which are related to the elastic precursor, the elastic remnant of the plastic wave, and other reverberations that result from free surfaces and interfaces with different seismic impedance in the target material. Body waves and surface waves are excited by an impact whereby surface waves attenuate less rapidly than body waves and only become important at larger distances. So far, not very much is known about elastic waves that are radiated by an impact; they have mostly only been considered as generated from earthquakes. However, seismic or elastic waves generated during impact events may induce seismic shaking, which may result in different consequences such as the modification of the crater structure (in particular on planetary surfaces) or ground shaking similar to an earthquake event. The destructive effects of impact-induced waves are not as severe as those from waves generated by earthquakes. This is partially due to the smaller seismic energy that is induced during an impact event, as well as the fact that impacts mostly generate P-waves and earthquakes generate more S-waves, which are more destructive. In the numerical approach used within this thesis, only the recording of P-waves has been considered.
Nevertheless, seismicity and, thus, the generation of elastic waves on planetary bodies is very often induced by impact events. The importance of impacts and impact-induced seismicity is elevated by the fact that they are often the main source for seismicity on planetary surfaces due to the absence of tectonic activities. Considering the lunar surface, impacts played a major role in the past, and thus the Moon represents a very good example of where seismic signals from natural and man-made rocket impacts have been detected by seismometers, as was done during the Apollo program (Nakamura, 2005; Nakamura *et al.*, 1982). Figure 2.4 shows an example of seismic signals during the Apollo mission recorded for a normal and a shallow moonquake as well as for an impact event.
Thus, for the analysis of previous mission data (e.g. Apollo) and future mission plans (InSight on Mars) impact-induced seismicity is important. As already mentioned by Richardson *et al.* (2005), it is possible to use meteoritic impacts as a seismic source for the seismic exploration of Mars. The concept of using impacts as seismic sources becomes significantly important as these impacts add a substantial number of seismic sources to an

otherwise seismically quiet planet (Richardson *et al.*, 2005).

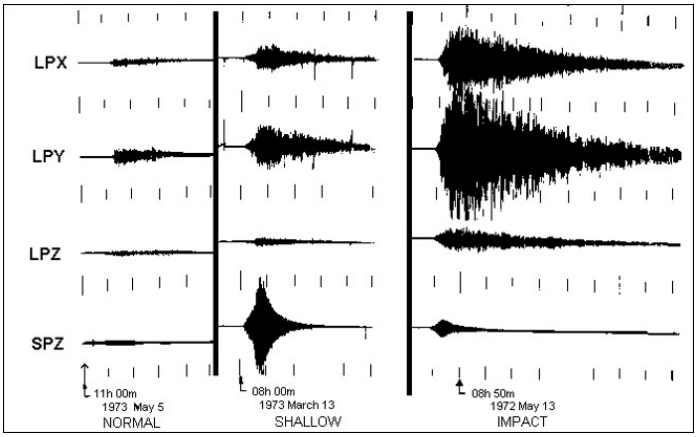

Figure 2.4: Seismic signals recorded by seismometers during different seismic events on the Moon. Seismic events included a normal and shallow moonquake as well as an impact event (Latham *et al.*, 1970).

Generally, recording seismic signals from natural observations is very difficult in case of planetary bodies, and these recordings are often only available for earthquake events on Earth. But, impact-induced seismic waves can also be recorded during laboratory impact experiments and by using numerical simulations as done within the MEMIN project and presented in Figure 2.5, which shows seismic signals that have been recorded during an impact experiment (left) and during the corresponding simulation (right). As already pointed out, numerical models have the advantage of using a much larger parameter space with respect to target and projectile properties and can bridge the gap between laboratory-scale and natural-scale crater sizes.

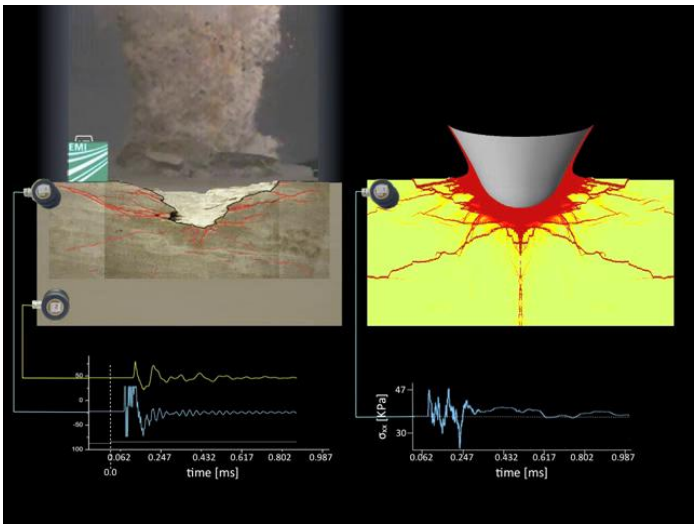

Figure 2.5: Recording of seismic signals during laboratory experiments and numerical simulations. At the top, the result of the experiment and model is shown; at the bottom, the recorded signals are shown as a function of time.

2.2 Cratering mechanics

The process of crater formation is, in general, divided into three stages (first proposed by Gault *et al.*, 1968): the contact and compression stage, the excavation stage, and the modification stage. The different stages are illustrated in Figure 2.6 (after French, 1998). Each of the stages is dominated by different physical phenomena. In this work, focus is given to the compression stage, where the propagation and effect of the shock wave is most evident, and the excavation stage, resulting in the so-called transient crater that represents the best measure of the energy of the impactor.
More detailed information about the development of impact craters and the different stages of cratering mechanisms can be found in e.g. Melosh (1989); Gault *et al.* (1968); O'Keefe and Ahrens (1993).

The contact and compression stage

This stage begins with the first contact of the projectile and the target material. Upon impact, material of the projectile and the target is compressed and a shock wave is generated. The downwards propagating shock front (into the target) accelerates matter almost to the initial impact velocity; the upwards propagating shock front (into the projectile) decelerates the penetration of the projectile. The penetration of the projectile and the compression of matter to approximately twice its initial density (depends on impact velocity and, thus, the pressure of the generated shock wave) results in a strong deformation (pancaking) of the projectile and the opening of a crater in the target comparable in size to the projectile.
At the rear of the projectile, the shock wave is reflected at the free surface, then it experiences a phase transition and travels back as a so-called rarefaction or release wave following the downward directed shock front (see Section 2.1). As a consequence, the material unloads to the initial lithostatic pressure. During the release of the material, vaporization, melting, or material failure may occur depending in the peak shock pressure. During the contact and compression stage, most of the kinetic energy is transferred from the projectile into the target material. This stage approximately ends when the entire projectile is released from high shock pressure. The contact and compression stage is by far the shortest of all three stages. It lasts only a few microseconds in the case of laboratory impact experiments with a typical impactor size of less than $1\,cm$. In the case of a natural impactor 1 km in diameter impacting at $10\,km \cdot s^{-1}$, the duration of the contact and compression stage is about $0.2\,s$.

Excavation stage

During the excavation stage, the shock wave further propagates into the target. The amplitude decreases with distance from the point of impact due to geometric spreading, but mostly because the rarefaction wave travels faster than the shock front, overtakes it, and causes a rapid attenuation of the shock amplitude. As shock wave compression is an unisentropic process, the target material gains entropy and some rest-temperature and rest-particle velocity remains in the material after unloading. In particular, the rest-particle velocity sets material into motion, driving the so-called excavation flow. This material flow is a direct consequence of shock compression and causes the formation of a crater many times larger than the size of the projectile. The excavation flow cannot displace material beyond its own weight (buoyancy forces) or strength (the resistance of matter against deformation), which eventually prevents the crater from growing further. The so-called transient crater describes the state when buoyancy and/or strength are in equilibrium with the excavation flow. As this may not occur everywhere at the same time, the transient crater may be rather understood as a virtual construct. However, for most laboratory and small natural craters, the transient crater may be approximated by the cavity at a specific point in time. The concept of the transient crater is well accepted as the best measure of the energy of the projectile and is of particular importance for the concept of scaling laws that allow for upscaling of laboratory cratering experiments to natural crater sizes.

Modification stage

The modification stage describes all processes that cause the transformation of the transient crater into the final crater morphology. It begins when the crater has been fully excavated, which does not necessarily have to happen everywhere at the same point in time. If strength is the dominating process that stops crater growth, a simple bowl- or cone-shaped crater structure forms that does not experience any modification from the transient to the final crater. These are called strength-dominated craters and mostly occur on the scale of less than a meter. If gravity is the dominating force limiting the size of the transient crater, different types of craters with significantly different morphologies occur. If the transient crater is smaller than some threshold, which depends on the given gravity and is significantly different on e.g. Earth and Moon, material slumps from the oversteepened crater walls into the inner part and forms a lense of brecciated material. If the transient crater is larger than the critical threshold diameter, crater collapse is much more pronounced. First, the deepest point of the transient crater becomes unstable and rises upwards to form a central peak. The crater wall collapses downwards and inwards forming a terraced crater rim. The formation of complex craters are not subject of this

study. The craters on the laboratory scale (which are mainly covered in this thesis) are simple craters where the modification stage plays only a minor role, and the final crater is often comparable to the transient crater. The so-called simple crater formation is shown in Figure 2.6.

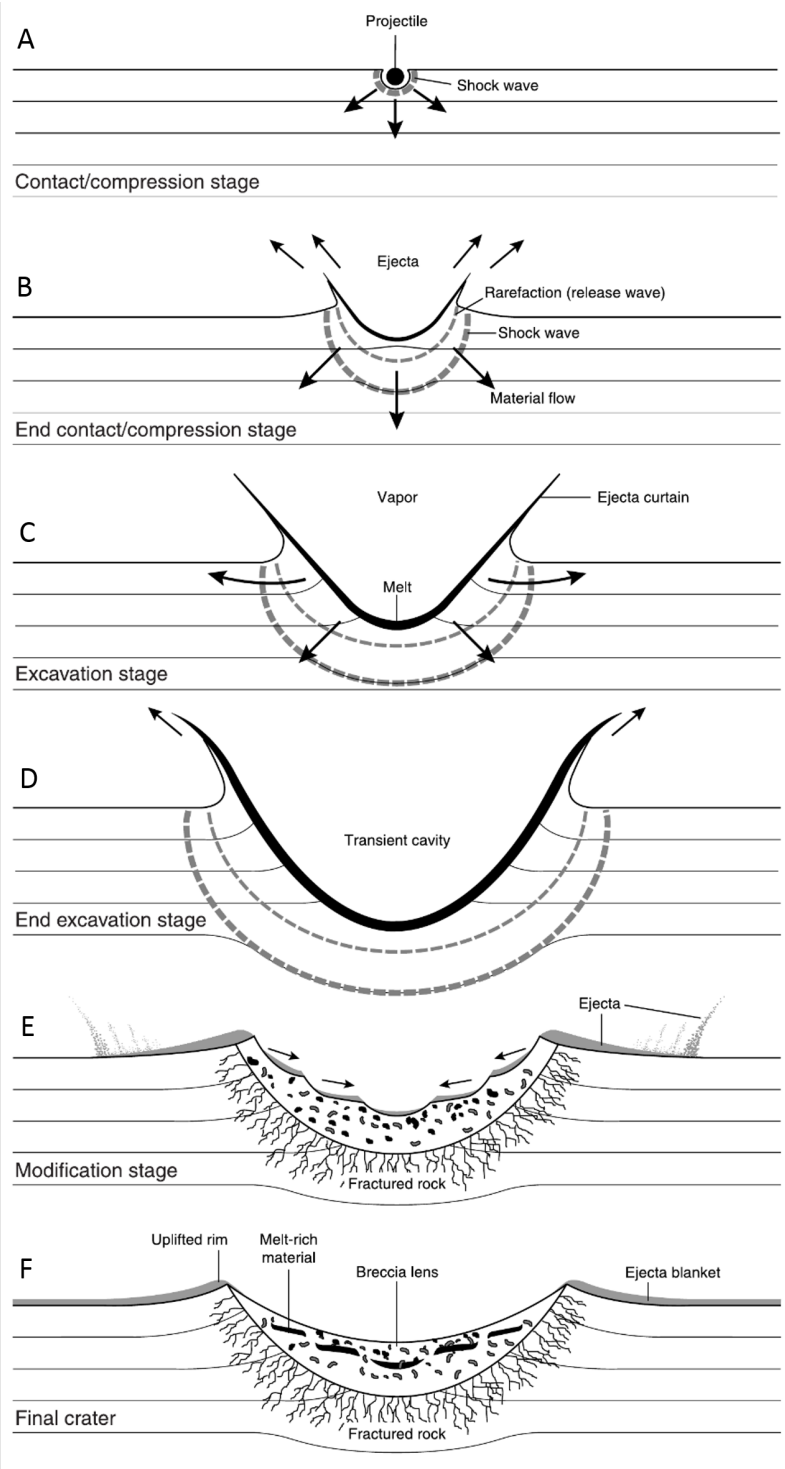

Figure 2.6: Stages of the development of a simple impact structure. The (A) contact and compression stage; (B) start of the excavation stage; (D) end of the excavation stage; and (F) final simple crater. After French (1998).

2.3 Scaling laws

Craters can vary in a large range of sizes, and it is of interest what size of a projectile forms a crater of a given size. To study the relationship between crater size and impact energy, in previous studies laboratory impact experiments have been carried out. However, laboratory experiments can only be conducted on a completely different size scale than impacts that occur in nature. Therefore, scaling laws allow for the extrapolation of small-scale laboratory cratering experiments to the dimensions of natural craters.
These scaling laws are based on the so-called point-source assumption. An impact is very similar to an explosion event and can therefore be approximated as a point-source. During an impact, energy and momentum are displaced in a specific depth similar to an explosive detonation. However, impacts are believed to deposit more momentum into the target than explosions do (Melosh, 1989).
How much of the energy of the impactor is actually available for the point source is determined by a coupling parameter. The coupling parameter leads to the point-source approximation in order to explain the deposition of energy and momentum in the target material by the impactor. It combines the characteristics of the projectile (diameter L, impact velocity U, density δ) in a simple scalar parameter (Holsapple and Schmidt, 1987):

$$\zeta = LU^{\mu}\delta^{\nu} \tag{2.4}$$

Here, μ and ν are constants that have to be determined.
Early numerical and experimental studies of impacts into metals led to the assumption that either the kinetic energy of the impactor or its momentum sufficed as the coupling parameter. For $\nu = 1/3$ and $\mu = 2/3$, the result is energy scaling, since the coupling parameter ζ which is then only a function of the impactor energy. For $\nu = \mu = 2/3$, the momentum of the impactor is the dominant factor, and momentum scaling applies. Using experimental studies, it was shown that μ lies between the energy and momentum limits $(1/3 < \mu < 2/3)$.
The coupling parameter can be utilized as a measure of the impactor diameter and velocity in order to derive the scaling approach in cratering, which is governed by the coupling parameter by a dimensional analysis (Holsapple and Schmidt, 1987). Thus, the usage of the above-introduced coupling parameter leads to pi-parameters and power-law scaling. According to Holsapple and Schmidt (1987), the point-source limit, which is defined by the coupling parameter, gives a special case of the general functional form for any crater-dependent variable. How this is done in detail is described further by Holsapple and Schmidt (1987).
Scaling laws represent simple parametrization that relate the characteristics of the impactor

(diameter L, density δ, impact velocity U, mass m), the target (density ρ, strength Y, gravity g), and the morphometry of the transient crater (diameter D, depth d, volume V). Most commonly, the so-called pi-group scaling is used (e.g. Holsapple, 1993). Pi-group scaling incorporates physical impact parameters into dimensionless parameters. Thus, crater volume or diameter can be expressed as functions of dimensionless ratios. The dimensionless ratios make laboratory craters directly comparable to kilometer-sized craters and, therefore, enable prediction of crater sizes for an impactor of a given size, mass, and velocity. The scaled crater dimensions π_V and π_D can then be related to the gravity-scaled impact size π_2, the strength-scaled impact size π_3, and the ratio of target and projectile density π_4 :

$$\left.\begin{matrix}\pi_V \\ \pi_D\end{matrix}\right\} = f\left(\pi_2, \pi_3, \pi_4\right) \tag{2.5}$$

$$\left.\begin{matrix}\pi_V \\ \pi_D\end{matrix}\right\} = \left.\begin{matrix}\frac{V\cdot\rho}{m} \\ D\cdot\left(\frac{\rho}{m}\right)^{\frac{1}{3}}\end{matrix}\right\} = f\left(\frac{g\cdot L}{U^2}, \frac{Y}{\rho\cdot U^2}, \frac{\rho}{\delta}\right) \tag{2.6}$$

Experimental studies have shown that π_V, π_D, and π_2, π_3, respectively, are related by power laws (e.g. Schmidt and Housen, 1987). Therefore, Equation 2.6 can, for example, be expressed as a simple power law (e.g. Schmidt and Housen, 1987):

$$\pi_V = C_V \pi_2^{-\gamma} \tag{2.7}$$

respectively

$$\pi_D = C_D \pi_2^{-\beta} \tag{2.8}$$

where C_V and C_D are experimentally determined constants; and β and γ are material-dependent scaling parameters (Melosh, 1989). The dimensionless ratio for the crater depth π_d is not considered in this work. The effect of the impact angle, which has been investigated numerically in detail by Elbeshausen *et al.* (2009) and by Davison *et al.* (2011) and experimentally in several studies, e.g. Gault and Wedekind (1978); Burchell and Whitehorn (2003), has been neglected in this work.

Considering the objectives of this thesis, the fact that laboratory impact experiments are mostly carried out in the strength regime when using cohesive materials becomes important. Here, strength is the dominating factor controlling crater size. Experiments where gravity dominates the cratering process (gravity regime) have so far only used granular materials reaching only very small crater sizes, as presented in Figure 2.7. Thus, experiments in the laboratory are limited in the size of the impact, where the impactor is usually only a few *mm* in diameter and the greater effect of gravity over strength is not

covered. On the scale of planetary surfaces, crater growth is, in most cases, limited by gravity. Strength of the material is apparently less important. For small impactors, target strength is much larger than the lithostatic pressure, whereas at larger scales, strength is rather low and gravity dominates. Therefore, depending on the size of the impactor, π_2 or π_3 will dominate over the other. The change in the dominance of one regime over the other (transition regime) is approximated by $Y = \rho\, g\, a$, where a is the radius of the impactor. Taking into account different target properties, in particular target strength, the treatment of the mentioned transition regime between strength and gravity becomes important.

As discussed above, scaling parameters are material dependent which has been of great interest in experimental studies in the past. Differences in the coefficient of friction or porosity have been discussed as a reason for those dependencies. A first approach for considering porosity in scaling laws is given in Housen and Holsapple (2003). Since it is, as mentioned, difficult to vary different parameters independently in experiments, there exist no reliable experimental studies with respect to the influence of the coefficient of friction. Both porosity and friction coefficient have not been considered in scaling laws so far.

Since strength is also a material property, it requires a special treatment when considering scaling laws. Strength is already included in the definition of π_3, which may not suffice for the correct definition of the strength value that has to be used. Therefore, the strength that is considered when using the scaling relationship may needs a certain definition. The posed problem will be addressed in detail in Chapter 7.

Numerical models are used to upscale these experiments to natural dimensions where gravity dominates the cratering process. Further, numerical modeling enables one to accurately quantify the separate effects of specific target properties such as porosity or water saturation that cannot be varied independently in experiments.

However, the use of models is restricted to numerical experiments that strongly rely on the material models that are used in the simulation. An accurate material model is essential for the reliability of a numerical model and its use in upscaling laboratory-sized craters to natural craters. In this thesis, focus is given to an accurate definition of strength, which is usually overestimated in experiments and underestimated in numerical methods.

Here the importance of the calibration and validation of the numerical models to upscale experimental data comes into play. So, the often-mentioned calibration and validation of material models becomes very important; this is mainly carried out in the Chapters 4 and 5. Validating the numerical models against laboratory-scale experiments increases the level of confidence for model results of realistic dimensions for natural craters. Chapter 7 investigates the effect of strength and porosity on crater size and how specific scaling parameters can be obtained for impact scenarios where crater size is controlled by both gravity and strength.

The scaling parameters may be significantly affected by the material model used to describe strength, i.e., the dynamic resistance of material against shear deformation. Strength is a very complex material property that depends on the strain rate, confining pressure, temperature, and the deformation history. In the definition of the dimensionless parameter π_3, it is expressed only by a scalar value, which may oversimplify the conditions, and it is unclear which measurable strength parameter should be used for Y in pi-group scaling.

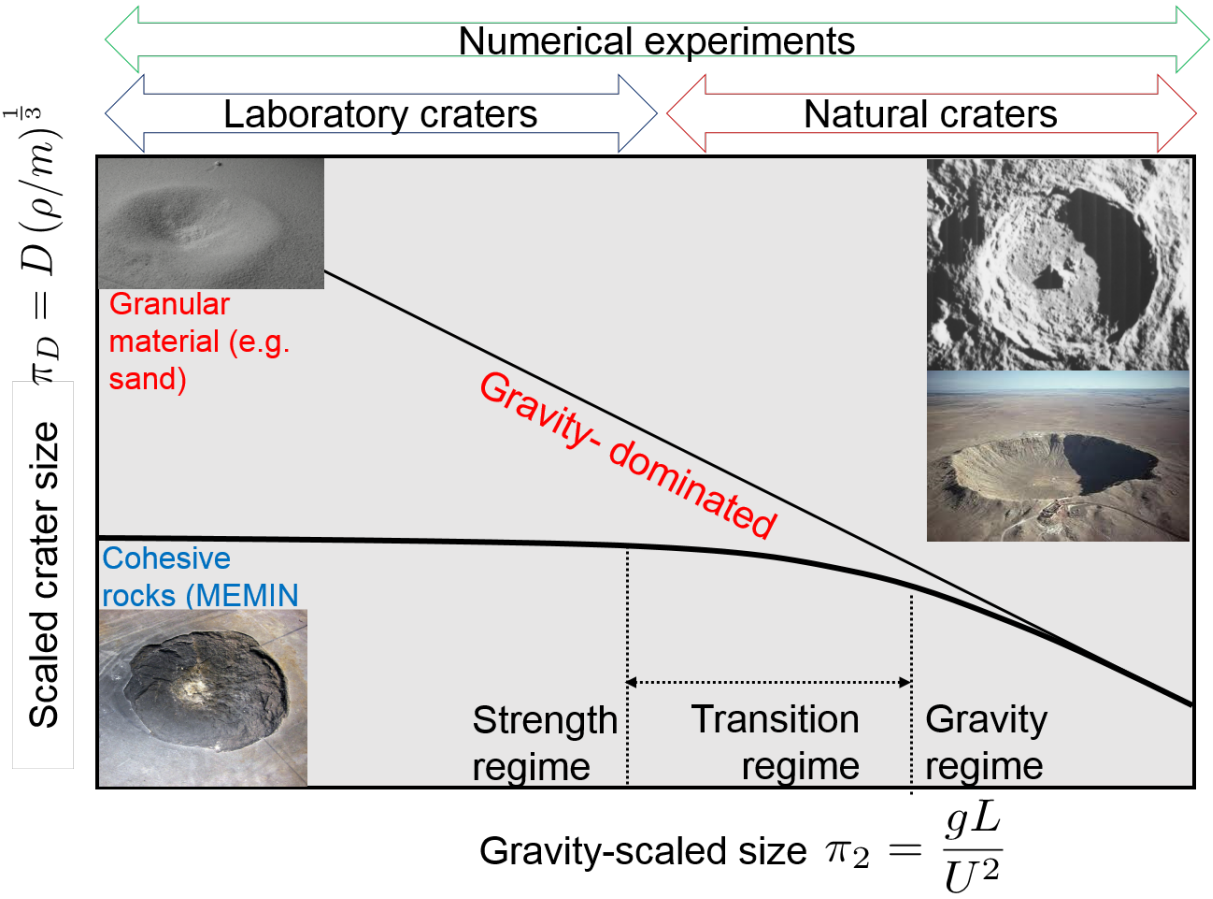

Figure 2.7: Relationship between strength and gravity scaling for impacts (modified after Holsapple, 1993). The transition from strength-dominated to gravity-dominated crater formation is dependent on the strength of the material. In the strength regime, the scaled crater size is independent of the gravity-scaled size π_2. As π_2 increases, the effect of gravity dominates the crater formation process. For similar gravity-scaled sizes π_2, the scaled crater size is larger for weak materials (e.g. granular materials) than for strong materials (e.g. cohesive rocks as used in MEMIN). It is also shown in which regime terrestrial or planetary impact craters and laboratory experimental craters are usually formed. As shown, numerical simulations cover the entire parameter space.

3 Methodology

Computer codes to simulate meteoritic impacts on Earth, on any planetary surface, or the collision of bodies have been developed for many decades and now reach a high level of sophistication. Among various methodological approaches to investigate impact cratering processes, such as laboratory experiments or field observations, numerical modeling represents an important tool providing insights beyond laboratory experiments and static observations. Numerical modeling has become complementary to other approaches, but it is the only method available to study large-scale planetary collisions at their full scale (e.g. O'Keefe and Ahrens, 1993; Melosh and Ivanov, 1999; Pierazzo and Melosh, 1999; Ivanov and Deutsch, 1999, 2002; Ivanov and Artemieva, 2002; Ivanov, 2003; Wünnemann and Ivanov, 2003; Shuvalov and Dypvik, 2004; Ivanov, 2005a).

Numerical models are based on the principles of the conservation of energy, mass, and momentum and of continuum mechanics. In addition, material models are a crucial component that describe the behavior of geo-materials under extreme pressures, temperatures, and shear stresses typically occurring during crater formation and shock wave compression. To model impact processes, a so-called hydrocode is used. These hydrocodes were originally developed to model fluid flow. For an overview of hydrocodes see e.g. Anderson (1987). In these hydrocodes, only simplified material models were implemented that did not account for specific material properties, such as strength, brittle-ductile failure, porosity, and water saturation, that are typical for planetary surfaces (sedimentary rocks on Earth, regolith breccia for example on Mars or Moon, comets). Over the last decades, more sophisticated rheology models and equations of state have been added. The development of these codes, which are called shock physics codes because of all the additional considerations e.g. strength, has resulted in increasingly more realistic models capable of reproducing small-scale laboratory shock and cratering experiments, and the morphology of large crater structures on planetary surfaces. Nevertheless, numerical models are based on the assumption of the relevant physics that govern the processes of interest. Numerical models require some set of discretization of space and time. This discretization may be material-based, such as in Lagrangian meshes or particle codes (so-called smooth particle hydrodynamics, or SPH codes, Monaghan (1992)), where the discrete mesh of particles move with matter, or fixed in space as in Eulerian grids (see Section 3.2) (Collins *et al.*, 2002, 2012; Pierazzo and Collins, 2003). Independent of the numerical discretization

method, all codes consist of three components: (1) the Newtonian laws of motion; (2) an equation of state to quantify the thermodynamic behavior of matter; and (3) a constitutive model that describes the mechanical response of matter to deformation.
Within the MEMIN project, different codes based on varying numerical methods and material models that come with different strengths and weaknesses have been used to study the impact process. Besides the two hydrocodes *SOPHIA* (developed at EMI Freiburg; Hiermaier *et al.* (1997)) and *AUTODYN* (commercial, used by EMI), the shock physics code ***iSALE*** has been used to model crater formation and the propagation of shock and elastic waves. This thesis exclusively makes use of iSALE to address the main objectives and goals pointed out in Section 1.4. Thus, all simulations presented in Chapters 4 to 7 use the iSALE shock physics code, which will be introduced in Section 3.1.

3.1 The iSALE shock physics code

For a general overview of iSALE, installation, and guidelines, refer to the iSALE webpage, http://www.isale-code.de. Recently the fourth stable version of iSALE (*iSALE-Dellen*) has been released and is accessible to academic users. Scientists who intend to use the code have to request access to iSALE. Experienced users can also be granted developer status. While both users and developers have full access to the code, only developers can make modifications available to the user community. The usage of iSALE is restricted to non-commercial activities. In this work, different versions of the code (stable releases) were used, as the code went through several developmental stages during the time of the PhD project this thesis is based on. To carry out mesoscale simulations (Chapter 4 and 5) an earlier version of iSALE (version number 1250) was used. For all other tasks (recording of seismic waves, application of scaling laws) the third stable release, iSALE-Chicxulub, was used.
iSALE is a multi-material, multi-rheology hydrocode. It is based on the SALE hydrocode solution algorithm (Amsden *et al.*, 1980) that was designed to simulate fluid flow at all speeds. SALE stands for Simplified Arbitrary Lagrangian Eulerian. The original SALE code could only consider one material per cell. It was only capable of dealing with gases or non-viscous fluids and only very simple equations of state for gases were implemented. Numerous authors have contributed to the code since then (e.g. Melosh *et al.*, 1992; Ivanov *et al.*, 1997; Wünnemann and Lange, 2002; Wünnemann and Ivanov, 2003; Collins *et al.*, 2004) to adapt it for simulating hypervelocity impact processes in solid materials. SALE was modified to include an elasto-plastic constitutive model, fragmentation models, various equations of state (EOS), and multiple materials (Melosh *et al.*, 1992; Ivanov *et al.*, 1997). More recent improvements include a modified strength model (Collins *et al.*,

2004) and a porosity compaction model (see Section 3.6 for a description of the ε–α model; Wünnemann *et al.* (2006); Collins *et al.* (2011a)) as well as a three-dimensional (3D) version of the code (Elbeshausen *et al.*, 2009; Elbeshausen and Wünnemann, 2011b). The 3D code also includes a fast and accurate adaptive interface reconstruction algorithm, and it is parallelized by using Message Passing Interfaces.
iSALE has been used in many studies for crater formation on planetary surfaces (e.g. Wünnemann *et al.*, 2005; Wünnemann and Ivanov, 2003; Collins *et al.*, 2002; Goldin *et al.*, 2006; Collins and Wünnemann, 2005). To ensure the reliability of the code, iSALE has been tested during several validation studies and benchmarked against other hydrocodes (Pierazzo *et al.*, 2008). It has been further validated against experimental data from laboratory-scale impacts (Pierazzo *et al.*, 2008; Davison *et al.*, 2011).
The numerical code consists of three components: the numerical solver of the equations describing the motion of matter, based on the conservation equations of mass, momentum, and energy (Section 3.2-3.4), the equations of state that describe the thermodynamic behavior of matter (Section 3.5-3.7), and the constitutive model describing the mechanical response of rocks to elasto-plastic deformation (Section 3.8).

3.2 Equation of motion

The equations of motion for a continuous medium can be either Lagrangian or Eulerian. The differential equations for both approaches are given as follows:

	Lagrange	*Eulerian*	
Mass:	$\frac{D\rho}{Dt} + \rho\frac{\partial v_i}{\partial x_i} = 0$	$\frac{\partial \rho}{\partial t} + \frac{\partial}{\partial x_i}(\rho v_i) = 0$	(3.1)
Momentum:	$\frac{Dv_i}{Dt} = f_i + \frac{1}{\rho}\frac{\partial \sigma_{ji}}{\partial x_j}$	$\frac{\partial v_i}{\partial t} + v_j\frac{\partial v_i}{\partial x_j} = f_i + \frac{1}{\rho}\frac{\partial \sigma_{ji}}{\partial x_j}$	(3.2)
Energy:	$\frac{De}{Dt} = f_i v_i + \frac{1}{\rho}\frac{\partial}{\partial x_j}(\sigma_{ij} v_i)$	$\frac{\partial e}{\partial t} + v_i\frac{\partial e}{\partial x_i} = f_i v_i + \frac{1}{\rho}\frac{\partial}{\partial x_j}(\sigma_{ij} v_i)$	(3.3)

where v_i describes the velocity, ρ the density of the material, e the specific internal energy, σ_{ji} the stress tensor, and f_i the external body forces (per unit mass).
To solve the differential equations, iSALE makes use of a first-order finite difference scheme. The behavior of material is described by constitutive equations which are divided into equations of state (EOS) described in Section 3.5 and strength models described in Section 3.8 (Pierazzo *et al.*, 2008). However, the given set of equations is underdetermined (system with four variables and three equations). To solve the system of equations additional equations describing the matter and behavior are required. σ is a function of ρ and e

($\sigma = f(\rho, e)$) and can be subdivided into a scalar part P (pressure) and a deviatoric part s (deviatoric stress), $\sigma = P + s$, with $P = f(\rho, e)$ and $s = f(v_i, P, e)$. In separating these two terms, the forces that act on the material due to volume changes (compression or expansion expressed as changes in P) can be calculated independently of the forces that act on the material due to the change in shape (changes in deformation expressed by s).

iSALE includes both an Eulerian and Lagrangian numerical solver as well a mixture of the two (Arbitrary Lagrangian Eulerian). In the Lagrangian mode (Figure 3.1B), to represent the geometry of the simulated material the computational mesh is defined (Collins *et al.*, 2012). The volume of material is fixed to the points within the mesh (vertices), which move with the material. The material flow is defined through the distortions of the cells: the cells defined by adjacent vertices become deformed in shape and size due to the forces acting on them. The entire mesh in space is deformed, and mass, momentum, and energy are transported by moving. The change in volume of a cell is only caused by the change in density; the mass is invariant (Collins *et al.*, 2012).
The main advantage of the Lagrangian description is the smaller number of derivatives that are included in the Lagrangian description of the differential equations for conservation (Equations 3.1-3.3). Numerical inaccuracies are reduced as less finite differential approximations have to be used. In addition, material interfaces are always along cell boundaries which is not necessarily the case in the Eulerian description as described later on.
However, the Lagrangian method often faces the problem of extreme deformation of cells. This usually causes numerical problems as grid resolution (given by the number of cells per reference area) varies significantly and becomes infinitesimally small where empty pore space is erased. If very small distances occur, the calculation of one time step may become very small. This results from the Courant-Friedrichs-Lewy (CFL) criterion, which ensures that information may not propagate entirely across any cell in one time step. It limits the time step according to the equation $\Delta t \leq \frac{\Delta x}{c}$, where Δx is the minimum cell dimension and c is the sound speed in the case of the Lagrangian description. These high distortions may force the simulation to stop. A possible solution for the problem is to erase numerical cells if the deformation exceeds a certain threshold or some sort of re-gridding is required (e.g. Anderson, 1987).
In the Eulerian description (Figure 3.1A), deformations are described relative to a fixed position, the mesh remains fixed throughout the simulation, and material is advected through the numerical grid. The variables of the model are calculated at the fixed points of the grid. Mass, momentum, and energy flow across cell boundaries. In contrast to the Lagrangian description, changes of the mass of a cell are caused by changes in density; the volume of the cell is invariant (Collins *et al.*, 2012). In the Eulerian description, the

mesh must be defined for the entire area in which material moves. This requires a much greater number of cells to achieve the same resolution as the Lagrangian description. In this description cells may be completely filled with material, partially filled or empty and may contain a mixture of materials. A mixed cell is often not representative of a physical situation because the different materials are not uniformly mixed; the materials are separated by a sharp interface (Collins *et al.*, 2012). If that is the case, it is important that these sharp interfaces are maintained between different materials or between material and a void space in order to keep the width of zones of mixed cells as small as possible. But the advection of material through the fixed mesh will cause numerical diffusion, which will result in smearing of interfaces over a number of cells which leads to an increase of mixed cells (Collins *et al.*, 2012). In order to preserve sharp boundaries, a procedure called *interface reconstruction* (e.g. Benson, 1992, 2002) is needed.
All models shown in this thesis have been carried out in the Eulerian mode of iSALE which has been demonstrated to be more appropriate and efficient for impact simulations (Collins *et al.*, 2012).

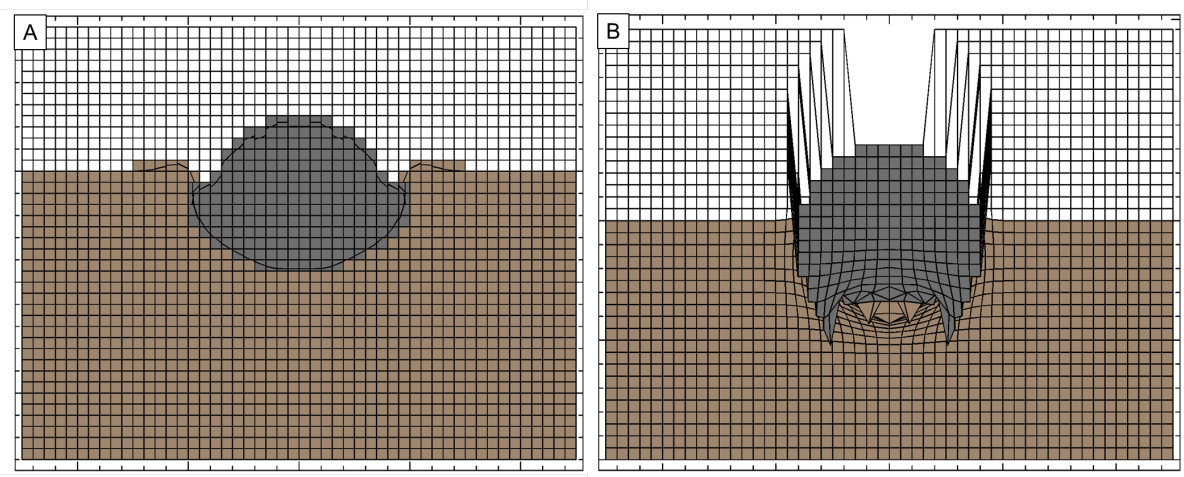

Figure 3.1: Eulerian and Lagrangian description of the deformation of continuous media. In (A) the Eulerian description, material flows through the computational mesh as it moves. In (B) the Lagrangian description, the computational mesh moves with the material.

3.3 The numerical grid

The material in iSALE is considered as a continuum. The computational domain in iSALE is divided into a grid of nodes which form a mesh of computational cells. The iSALE mesh geometry is shown in Figure 3.2. Quantities describing the state of matter are defined for each cell, such as pressure, density, mass, or energy. Vector parameters such as velocity and stress are quantified at the vertices of the cell. iSALE uses Cartesian cylindrical coordinates in two-dimensions where the left boundary is the symmetry axis. The mesh

rotates around that axis. This 2D geometry only allows for modeling vertical impacts. The mesh consists of a high-resolution zone and an extension zone in which the cell size increases gradually by a certain factor (usually 3–5 %). This method enables the model to cover a much larger space within the computational domain without increasing the number of cells in order to minimize the computational expense and to reduce disturbances due to reflections of the shock wave at the boundaries of the mesh. Due to the fact that it is impossible to define satisfactory boundary conditions for continuous outflow for shock waves, the grid has to be chosen to be as large as possible to avoid or minimize any reflections at the boundaries of the grid. Introducing extended cells provides a methods to enlarge the grid and keep the computational expenses reasonable at the same time.

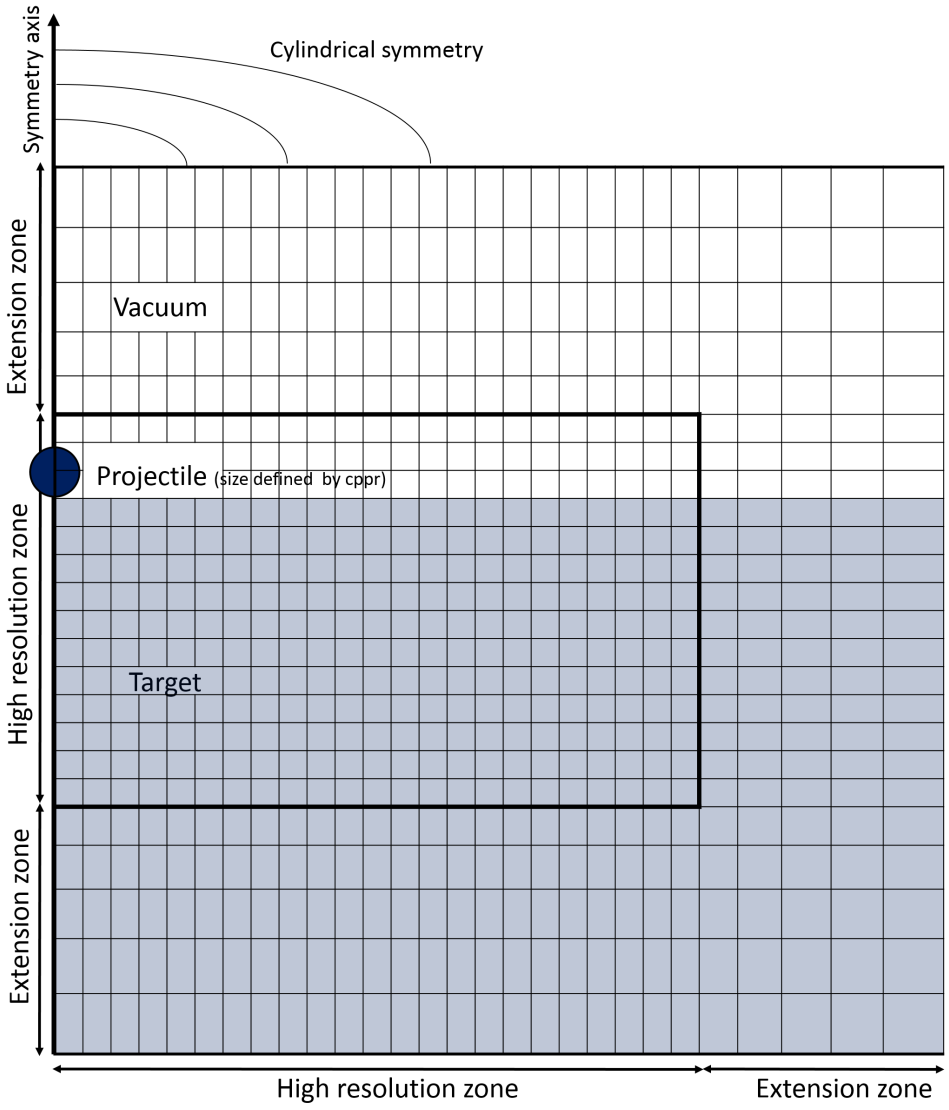

Figure 3.2: Schematic illustration of the iSALE mesh geometry. The target is shown as a bluish color, the space above is simulated as vacuum. The area inside the bold line represents the high-resolution zone. The entire mesh rotates about the symmetry axis.

It is important to choose a sufficient resolution of a model that not only allows for processes to be resolved by an adequate number of cells but also offers feasible computational time and space. In general, the more cells and the smaller the space increments, the more accurately the processes such as wave propagation or crater excavation can be calculated. A commonly used measure for the resolution is given by the number of cells by which the projectile radius is resolved, called cells per projectile radius (cppr).

3.4 Lagrangian tracer particles

iSALE uses Lagrangian tracer particles to record material parameters as a function of time and space, such as density, pressure, peak pressures, shock, and particle velocities. Tracers are massless and are initially placed in the center of each computational cell. They may be considered as representative for the volume of material initially located in the same cell. Tracers move along with material through the grid according to the velocity field. A detailed description of the concept of tracer particles is given in Pierazzo *et al.* (1997) or in Pierazzo and Melosh (2000). Tracer particles are, for instance, used to determine the highest pressures (peak shock pressures) a material has experienced during the passage of a shock wave. Isobars of peak shock pressures can then be defined that enclose all tracers that experienced a certain pressure level. By means of the number of tracers enclosed and their representative volume, the total volume that has undergone a certain shock pressure can be calculated. This concept has successfully been used in several modeling studies in different hydrocodes e.g. to quantify the amount of melt generated in an impact at arbitrary scale. Note that this method is much less diffusive than the temperature field that is also given in iSALE.

3.5 Equations of state

The thermodynamic state of a material is described by the equation of state relating pressure, density, internal energy and temperature, and entropy. In contrast to when using standard equations of state, the simulations of impact processes require a thermodynamic description of material behavior reacting to several 100s of GPa and temperatures of several 1000s of degrees Celsius. The equation of state (EOS) for a certain material is unique and is usually based on experiments at low velocities and then extrapolated to high velocities, as it is not possible to reproduce with experiments the response of material at the high velocities typical of planetary impacts. Within this thesis, only the Analytical Equation of State (ANEOS) was used to describe the projectile and target material thermodynamically. However, iSALE also includes a Tillotson equation of state that is commonly used but was

not employed in this thesis work. The Tillotson EOS was exclusively developed to describe the propagation of shock waves (Tillotson, 1962) and is quite simplistic. The EOS is based on the Mie-Grüneisen equation (Poirier, 1991) and the Thomas-Fermi equation. It is divided between a compressional and expanding phase, thus material is either compressed to higher densities or expanded to lower densities. The pressure in the compressed state is expressed as:

$$P = \left(a + \frac{b}{\frac{E}{E_0 \eta^2} + 1} \right) \rho E + A\mu + B\mu^2 \tag{3.4}$$

and in the expanded state as:

$$P = a\rho E + \left(\frac{b\rho E}{\frac{E}{E_o \cdot \eta^2} + 1} + A\mu e^{-\beta(\rho_0 \rho - 1)^2} \right) \cdot e^{-\alpha\left(\frac{\rho_0}{\rho - 1}\right)^2} \tag{3.5}$$

where $\eta = \frac{\rho}{\rho_0}$ and $\mu = \eta - 1$ and $A, B, a, b, \alpha, \beta$ and E_0 are the material-dependent Tillotson parameters (see Melosh, 1989, pg. 233). For the transition from one phase to the other, an extrapolation is used. The Tillotson EOS is not able to relate pressure and density in a two-phase region and cannot compute the temperature or entropy of the material. Therefore the equation cannot be used for the modeling of melt production or vaporization. A much more sophisticated equation of state is represented by the Analytical Equation of State (ANEOS) (Thompson and Lauson, 1972). ANEOS accounts for phase transitions (solid-solid or solid-liquid phase), however the ANEOS that is used in iSALE is currently only capable of calculating one phase transition. The ANEOS is a software package that enables calculation of the thermodynamic state if two state variables are given. In iSALE these are, typically, density and internal energy to determine pressure and temperature (and entropy), which can be derived from the Helmholtz free energy $f(\rho, T)$ (see Equations 3.6-3.8) and are thermodynamically consistent.

$$P = \rho^2 \frac{\delta f}{\delta \rho} \tag{3.6}$$

$$S = -\frac{\delta f}{\delta T} \tag{3.7}$$

$$E = f + TS \tag{3.8}$$

Here, ρ is density, P is pressure, S is entropy, E is internal energy, and T is temperature. To develop a relationship for the Helmholtz free energy f, it is assumed by ANEOS that the free energy can be subdivided into a cold component E_c, a nuclear component f_n, and an electronic component f_e which can be expressed as follows (Littlefield, 1997):

$$f(\rho, T) = E_c(\rho) + f_n(\rho, T) + f_e(\rho, T) \tag{3.9}$$

To describe each of these components, physics-based models are used. According to Littlefield (1997), the cold component describes the response of the material at $0\,K$ where atomic and molecular vibrations and rotations are ignored. The nuclear component accounts for modifications to f due to thermal effects, and the electronic component becomes important at very high temperatures and moderate to high pressures.
It is possible to directly couple ANEOS to the hydrocode. However, as density and specific internal energy are used as independent variables, an iteration of temperature is required in order to find the correct target value of internal energy, but this is computationally expensive. Because of that, it is more common to use ANEOS to build equation of state tables that can be used in the hydrocode (here in iSALE) than it is to couple ANEOS directly to the hydrocode. To derive such tables requires the packaged ANEOS code and many input parameters (Thompson and Lauson, 1972; Thompson, 1990).

3.6 The ε–α porosity compaction model

Porosity plays a major role in impact cratering, as most planetary surfaces are porous and/or water saturated. Therefore, in numerical modeling, the treatment of porous material poses an additional challenge for the material model used. Porosity may be considered as a state variable such as density. The bulk modulus describes the resistance of matter to being compressed (change in density as a function of ambient pressure). In the of porosity, the compaction (the closure of pore space) needs to be described by a so-called compaction function. In the P–α–model (Hermann, 1969; Carroll and Holt, 1972), the porosity is a function of pressure P. In iSALE, the ε–α model (Wünnemann *et al.*, 2006; Collins *et al.*, 2011a) was implemented, which describes the crushing of pore space as a function of compressive volumetric strain ε_V. Note, in iSALE tensile strain is positive and compressive strain is negative. In the compaction function $\alpha = f(\varepsilon_V)$ the distension α is defined by $\alpha = \frac{1}{1-\Phi}$, with Φ being the porosity. If compression increases (volumetric strain decreases), distension decreases until all pore space is crushed out and the material is fully compacted ($\alpha = 1$). The compaction function is defined by an elastic-plastic transition strain ε_e to separate the elastic regime, where the decrease in pore space is not permanent ($\varepsilon_V > \varepsilon_e$), and a compaction regime where changes in porosity remain in the material after unloading ($\varepsilon_V < \varepsilon_e$). The compaction model can be combined with any EOS that exists for the relevant hydrocode.
To account for the compression of the matrix as well as the elastic compaction of pore

space, α as a function of volumetric strain can be expressed as follows:

$$\alpha = f(\varepsilon_V) = \begin{cases} \alpha_0 | \varepsilon_V > \varepsilon_e \\ \alpha_0 e^{\kappa(\varepsilon_V - \varepsilon_e)} | \varepsilon_V < \varepsilon_e \end{cases} \tag{3.10}$$

A schematic compaction function in the ε–α model is shown in Figure 3.3. In the compaction regime, pore space is crushed out approximately according to an exponential law where the rate of compaction is controlled by the exponent κ. In the idealized case, where all pore space is crushed out before compression starts, κ is equal to 1. If compression starts before pore space is completely closed, which is the more realistic assumption, $\kappa < 1$. Note that κ and ε_e are material parameters that need to be determined in compaction experiments. In this thesis, the parameter κ will remain constant using a value of $k = 0.98$ as suggested in Wünnemann *et al.* (2006).

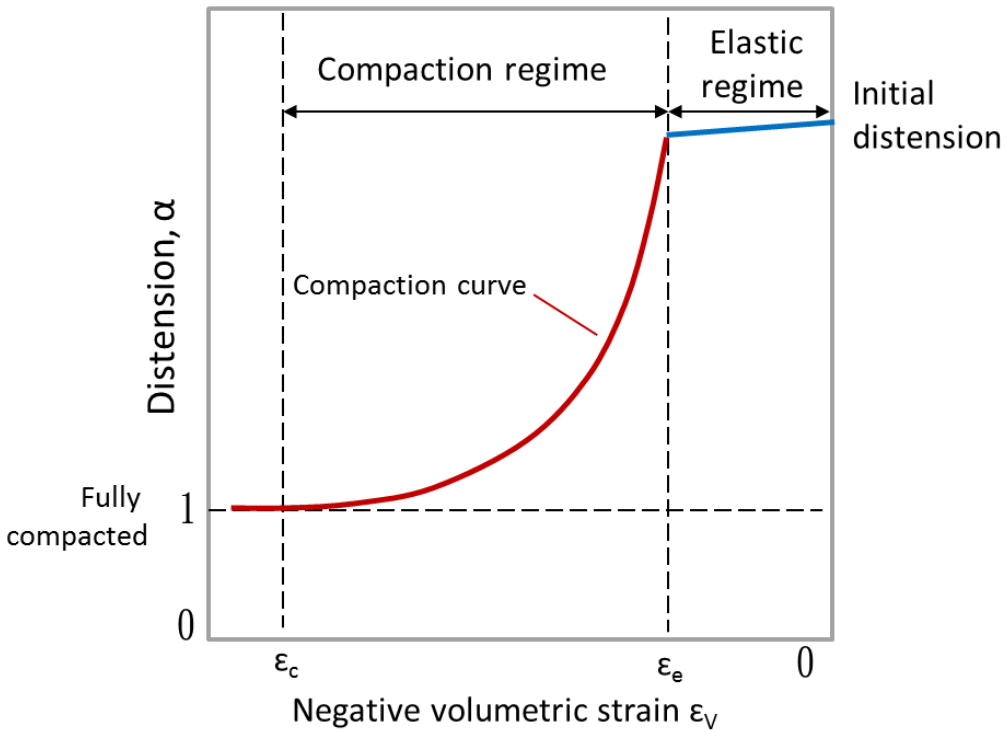

Figure 3.3: Illustration of the ε–α porous compaction model (modified after Wünnemann *et al.*, 2006). Negative volumetric strain is compressive. Pore space compaction starts if the volumetric strain is larger than the elastic threshold strain ε_e; if the volumetric strain is smaller, pore space collapse is not permanent.

Additionally, it has to be taken into account that the speed of sound c is smaller in porous material than in nonporous material. Consequently, c increases as pore space gradually decreases as a function of volumetric strain. The dependency of c as a function of α is taken into account by introducing the parameter χ, which is the ratio of the bulk wave

velocity of a porous material c_0 and a solid component c_{s0} ($\chi = \frac{c_0}{c_{s0}}$). It is assumed that the bulk sound speed of the porous material $c(\alpha)$ varies linearly with distension α in the elastic compaction regime:

$$c(\alpha) = c_{s0} + \frac{\alpha - 1}{\alpha_0 - 1}(c_0 - c_{s0}) \tag{3.11}$$

where α_0 represents the initial distension of the porous material. In this study porosities between 5 and 50 % have been considered. The most important parameters, ε_e and χ, affect shock and elastic wave propagation significantly. A parametrization of the ε_e value is carried out in Chapter 4 by the use of mesoscale models. The parameters are further calibrated in Chapter 6, which gives a detailed description of the influence of these parameters on pressure amplitudes and wave propagation.

3.7 Simulation of water-saturated material

Present porosity models assume that the pore space is filled with air or a void, in which case the effect when the pores are compacted is negligible (Collins *et al.*, 2011a). The ε–α-model also allows for modeling shock propagation in porous material. But, often rocks are saturated with water or ice. Consequently, another degree of complexity is added if the pores are not empty ("dry") but are completely or partially filled with water ("wet"). To describe material mixtures thermodynamically, an approach can be used where a separate EOS is developed for the mixture, which can then be treated as one material. A mixed-material EOS may be constructed by combining the EOSs of two (or more) pure materials prior to any simulation. In the case of fully water-saturated material, an approach originally proposed by Pierazzo *et al.* (2005) is used where an example for a basalt-water mixture is described. In this case, the material can be treated as a two-phase material mixture consisting of the matrix (quartzite) and water. The bulk behavior of the mixture represents some sort of average of the behavior of the two materials. This approach assumes total equilibrium (pressure and temperature) between the two (or more) materials and a constant mass ratio of the components, which may not always be appropriate.
With this boundary condition, a new table for a given porous material with a defined water content was generated by combining the ANEOS for each phase (water and quartzite). Note that this approach assumes that the water content in the material mixture is constant and does not change as a result of flowing or steaming of water through the material. As a consequence, the presence of water prevents complete closure of pores. Changes in pore volume result from the compression of the two components (water and quartzite) calculated by ANEOS. The behavior (compaction) of the mixture of dry porosity and

water-saturated matrix (partially water-saturated material) is modeled with the ε-α-model, where the compression of the "wet" matrix is calculated by the mixed ANEOS.

3.8 Constitutive model

The mechanics of rocks, namely how they respond to deformation, is a very complex parameter that depends on numerous parameters such as the confining pressure, temperature, strain rates and porosity, to name only the most important ones.
In iSALE a constitutive strength model describes stress (σ_{ij}) as a function of strain (ε_{ij}), strain rate ($\dot{\varepsilon}_{ij}$), pressure (P), temperature (T), and the deformation history that may be expressed as a scalar parameter D (Equation 3.12):

$$\sigma_{ij} = g(\varepsilon_{ij}, \dot{\varepsilon}_{ij}, P, T, D) \tag{3.12}$$

In a first step the strain rate is calculated from the change in the velocity field. The time-integrated $\dot{\varepsilon}$ yields the total strain ε. The elastic stress σ is calculated from the linear relationship of ε with the bulk modulus K and shear modulus μ. Both elastic parameters are pressure and temperature dependent and are given by the EOS. The elastic stress that rocks can sustain is limited. In iSALE, elastic-plastic failure is considered by comparing the calculated elastic stress with the maximum possible stress Y the matter can resist that is defined by the yield envelop. The elastic stress is expressed as the 2nd invariant of the stress tensor J_2 which is a function of the principal stresses ($J_2 = \frac{1}{6}((s_{xx} - s_{yy})^2 + (s_{yy} - s_0)^2) + (s_0 - s_{xx})^2 + s_{xy}^2$). If $\sqrt{J_2}$ exceeds the yield stress Y, then shear failure has occurred. iSALE provides different strength models that define the yield envelope Y as a function of pressure, temperature, and deformation history D (further down also called damage).
Different strength models are available that describe different rheologies of matter: liquids are described by a viscous rheology where the stress tensor depends on the strain rate $\dot{\varepsilon}$ ($s_{ij} = 2\eta\dot{\varepsilon}_{ij}$, where η is the kinematic viscosity).
The Drucker-Prager strength model (Drucker and Prager, 1952) is used for granular materials. In this model $Y = Y_0 + \beta P$, where Y_0 is the yield strength at zero pressure and β the coefficient of friction for the material. More complex strength models are required to describe the behavior of competent rocks (Ivanov *et al.*, 1997; Collins *et al.*, 2004). The Johnson-Cook model (Johnson and Cook, 1983; Davison *et al.*, 2011) is mostly used to describe failure of metals, which are not subject of this work. In this thesis a strength model proposed by Collins *et al.* (2004) was used in most simulations. In this model, the yield strength is a non-linear function of the pressure P. Additionally, it is taken into account that the pristine (intact) material is much stronger than material that has

already undergone one or several failure cycles; such material is considered damaged. This approach allows for taking into account the deformation history. In this so-called ROCK model (Collins *et al.*, 2004; Ivanov *et al.*, 1997), the yield strength Y_i of the intact rock is given by the following (Lundborg, 1968):

$$Y_i = Y_{i0} + \frac{\beta_i P}{1 + \frac{\beta_i P}{Y_{im} - Y_{i0}}} \tag{3.13}$$

The parameter Y_{im} is the limiting strength at high pressure and can be estimated from the Hugoniot elastic limit (Melosh, 1989, p.35). Pressure is defined by P, β_i is the coefficient of internal friction, and Y_{i0} is the cohesion of the intact material (strength at zero pressure). As stated already, it is important in material modeling to distinguish between the intact state and the state where material has already undergone failure (damaged state). Damage is described by a scalar parameter D, where $D = 0$ represents the fully intact state, and $D = 1$ corresponds to entirely damaged material. The shear component of D is a function of plastic strain ($D = min(\frac{\varepsilon_p}{\varepsilon_f}, 1)$). If the material has reached its maximum state of damage ($D = 1$), the yield strength is given by a simple Drucker-Prager yield surface:

$$Y_d = \min\left(Y_{d0} + \beta_d P, Y_{dm}\right) \tag{3.14}$$

Here, Y_{dm} is the limiting strength for the damaged material, Y_{d0} is the cohesion of the damaged material, which is usually assumed to be zero, and β_d is the coefficient of friction for damaged material. For a partially damaged state, the yield strength is given by

$$Y = Y_d D + Y_i(1 - D) \tag{3.15}$$

using the damage quantity D; Y_d and Y_i are the yield strengths for the damaged and intact material, respectively. Figure 3.4 shows the yield strength as it depends on pressure for the intact and damaged material, where the yield envelope for sandstone is used as an example. The points are based on experimental data. Note that the vast majority of available experimental data to characterize the strength behavior of rocks are based on quasi-static experiments. Further, model parameters often have to be adjusted to fit observations because of the poor knowledge of dynamic hardening and scale effects. The rate dependency is often not available, in particular for the extreme high strain rates in impacts.

An overview of strength models used in hydrocodes is given in Holsapple (2009). For further details on how strength has been treated in this work, see the description of the used strength model presented in Section 7.2.3 of Chapter 7.

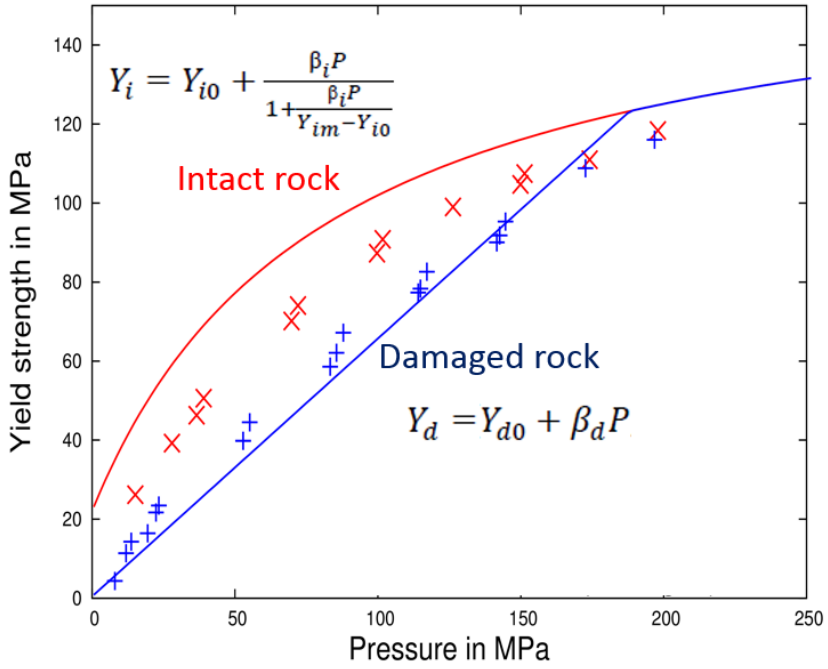

Figure 3.4: Illustration of yield strength as a function of pressure for intact and damaged material. The points represent experimental data for Berea sandstone (Lomov *et al.*, 2001).

3.9 Modifications to iSALE

In the framework of this thesis, iSALE has been modified in several respects. The most important development was to implement routines that enable us to simulate the propagation of shock waves through a heterogeneous material on a mesoscale in 2D and 3D. Previously, iSALE was only capable of simulating impact scenarios where a projectile strikes a half space (compare Figure 3.2) or a sphere.

For mesoscale modeling of the propagation of a shock wave through a material in which single pores are resolved, new setup routines have been implemented. With the new routines it is now possible to define a certain number of pores or a large sample size that is filled up with either regularly or randomly distributed pores (mesh of pores). For the latter case, a porosity value can be set. For all cases, the pores can have different shapes (squares, circles, rhombi) and pore space contents (empty, water, or any other material). The offset of single pores as well as their size and number can be defined. Size, shape and overlapping are optional input parameters.

Additionally, to simulate water-saturated material, it was necessary to create a new ANEOS table by making use of the ANEOS package (Thompson, 1990) for a mixture of quartzite and water.

In order to record an elastic wave signal and determine seismic parameters, which is one of the main objectives of this thesis (compare Chapter 6), gauge points have been introduced into the grid to record thermodynamic and mechanical parameters of the elastic wave at a defined distance from the point of impact as a function of time. This was done for every time step within the code in the subroutine *timestep.F90*. To process and visualize the data, the isaleplot tool and more recently the pysaleplot tool have been used. The pysaleplot tool was developed by Thomas Davison.

4 Propagation of impact-induced shock waves in porous sandstone using mesoscale modeling

This chapter has been published as the following peer-reviewed article:

Güldemeister N., Wünnemann K., Durr N., Hiermaier S., 2013. *Propagation of impact-induced shock waves in porous sandstone using mesoscale modeling.* Meteoritics and Planetary Science 48, 115-133, http://dx.doi.org/10.1111/j.1945-5100.2012.01430.x.

Abstract

Generation and propagation of shock waves by meteorite impact is significantly affected by material properties such as porosity, water content, and strength. The objective of this work was to quantify processes related to the shock-induced compaction of pore space by numerical modeling, and compare the results with data obtained in the framework of the Multidisciplinary Experimental and Modeling Impact Research Network (MEMIN) impact experiments. We use mesoscale models resolving the collapse of individual pores to validate macroscopic (homogenized) approaches describing the bulk behavior of porous and water saturated materials in large-scale models of crater formation, and to quantify localized shock amplification as a result of pore space crushing. We carried out a suite of numerical models of planar shock wave propagation through a well-defined area (the "sample") of porous and/or water-saturated material. The porous sample is either represented by a homogeneous unit where porosity is treated as a state variable (macroscale model) and water content by an equation of state for mixed material (ANEOS) or by a defined number of individually resolved pores (mesoscale model). We varied porosity and water content and measured thermodynamic parameters such as shock wave velocity and particle velocity on meso- and macroscales in separate simulations. The mesoscale models provide additional data on the heterogeneous distribution of peak shock pressures as a consequence of the complex superposition of reflecting rarefaction waves and shock waves originating from

the crushing of pores. We quantify the bulk effect of porosity, the reduction in shock pressure, in terms of Hugoniot data as a function of porosity, water content, and strength of a quartzite matrix. We find a good agreement between meso-, macroscale models and Hugoniot data from shock experiments. We also propose a combination of a porosity compaction model (ε-α model) that was previously only used for porous materials and the ANEOS for water-saturated quartzite (all pore space is filled with water) to describe the behavior of partially water saturated material during shock compression. Localized amplification of shock pressures results from pore collapse and can reach as much as four times the average shock pressure in the porous sample. This may explain the often observed localized high shock pressure phases next to more or less unshocked grains in impactites and meteorites.

4.1 Introduction

Porosity and water content are typical properties for rocks of the upper crust of Earth such as sandstone. Regolith breccias on the Moon are characterized by a significant amount of porosity, and the presence of subsurface water on Mars is widely accepted. Bulk density of a number of asteroids is $\rho < 1.3\,g\,cm^{-3}$ which corresponds to a very high amount of empty pore space and porosities of up to 75 % (Britt *et al.*, 2002), and comets are known to have very low densities (e.g. Richardson *et al.*, 2007). These are only a few examples of the importance of porosity and water on planetary bodies and other cosmic objects. Impact cratering plays an important role in all of these bodies, and it can be assumed that in particular the formation of small to midsize craters is affected by the presence of porous and water-saturated material. In the case of water-saturated material, it is important to distinguish between fully saturated materials, where all pore space is filled with water, and partially water-saturated materials, where 50 % of the pore space is filled with water. Hypervelocity impact crater formation is characterized by the generation of shock waves. It is well known that porosity affects shock wave propagation, attenuation, and shock heating. The crushing of pore space is an effective mechanism to absorb shock waves (Zel'dovich and Raizer, 2002, Chapter 11), and the additional plastic work involved in the compaction of pore space causes higher shock temperatures in porous material than in competent materials at the same shock pressures. This may cause an increase in shock-induced melting in porous materials; however, on the other hand, the shock wave attenuates faster in porous material, and low impedance pore contents, i.e., air and/or water, result in lower shock wave velocities and pressures in porous materials so that a smaller volume of material experiences sufficiently high shock pressures for melting. Both processes are competing factors and quantifying their net effect on the production of impact melt can be

determined only by numerical modeling (Wünnemann *et al.*, 2008). Another consequence of lower shock pressures and faster attenuation of the shock waves in porous material is a decrease in crater efficiency (Wünnemann *et al.*, 2006, 2011) and a decrease in ejection velocities (Housen and Holsapple, 2003). The effect of porosity and water content on crater formation has been addressed in studies of terrestrial and extraterrestrial craters, in impact experiments, and numerical modeling (e.g. Kieffer *et al.*, 1976; Love *et al.*, 1993; O'Keefe *et al.*, 2001; Holsapple *et al.*, 2002; Goldin *et al.*, 2006; Britt *et al.*, 2002). Apparently, the presence of pore space and water affects impact processes on different scales. The overall bulk behavior of porous material can be observed on the scale of natural craters in terms of crater size and the generated melt volume. By means of microscopic observations of shock-induced modifications such as planar deformation features (PDF), high-pressure mineral phases, and melt in rock samples that have undergone shock compression, the amplitude of the shock load, and thus the decay with distance from the point of impact, can be estimated (Stöffler and Langenhorst, 1994; Langenhorst and Deutsch, 2012). However, initially porous material often shows a somewhat ambiguous picture. Localized high shock pressure phases occur next to more or less unshocked grains in impactites and meteorites (Kieffer *et al.*, 1976; Grieve *et al.*, 1996). Studies on shock metamorphism in porous Coconino sandstone at the Meteor crater (Kieffer, 1971) revealed two distinct phenomena that occur during shock-induced pore collapse: Depending on the initial shock pressure, the closure mechanism of a pore can either be described as "shrinking" or "jetting". In both cases, an amplification of the shock pressure occurs, while "jetting" causes stronger localized pressure amplifications than "shrinking". Kieffer (1971) described the process of "jetting" as extrusion of material. The open pore space collapses and the material surrounding the pore is then injected into pore space. Although Kieffer (1971) described the process more phenomenologically, a quantitative description of the process is still lacking. Numerical modeling of shock propagation in heterogeneous porous material has been carried out on meso- and macroscales. On the mesoscale, the heterogeneous structure including open or water-filled pores is resolved explicitly (Crawford *et al.*, 2003; Ivanov, 2005b; Riedel *et al.*, 2008; Borg and Chhabildas, 2011). On the macroscale, processes are studied that are affected by the presence of pore space but that occur on a scale several orders of magnitude larger than the actual size of an individual pore, such as the formation of impact craters. In the latter case, porosity is usually treated as a state variable and the change in porosity due to shock compression is taken into account by a so-called compaction model such as the P–α model (Kerley, 1992; Carroll and Holt, 1972) and the ε–α model (Wünnemann *et al.*, 2006). Laboratory impact experiments using a sandstone, Seeberger Sandstein, as a target (Poelchau *et al.*, 2013), carried out in the framework of the Multidisciplinary Experimental and Modeling Impact Research Network (MEMIN), provide new data on the meso- and macroscales to further our understanding of

the thermodynamic and mechanical response of heterogeneous, porous, dry, or (partially) water-saturated material to shock loading (Kenkmann *et al.*, 2011; Schäfer *et al.*, 2006). Detailed observations on pore space collapse as a function of crater depth (Buhl *et al.*, 2013), the ejecta dynamics (Sommer *et al.*, 2013), the effect on crater morphometry and morphology (Dufresne *et al.*, 2013), and shock-recovery experiments with samples of Seeberger sandstone (Kowitz *et al.*, 2013b) are reported in this issue. The reproduction of any of these observations by numerical modeling implies appropriate material models to describe the thermodynamic behavior of porous material for different degrees of water saturation. Previous approaches used meso-scale models (Crawford *et al.*, 2003; Ivanov, 2005b; Riedel *et al.*, 2008; Borg and Chhabildas, 2011) to develop appropriate material models that describe the bulk behavior of dry porous material and material mixtures in case of fully water-saturated rocks (Pierazzo *et al.*, 2005). The goal of this work is to bring meso- and macroscale observations into accordance and to quantify processes on different scale. On the macroscale this includes the reduction of shock pressure and increase of temperature whereas mesoscale modeling aims at the quantification of localized amplification of peak shock pressures in the vicinity of single pores. Mesoscale modeling will also be used to test a new macroscale model describing the bulk behavior of partially water-saturated material. The goal is to find a universal description of material mixtures of silicates and water that also contain open pore space.

Finally we will compare modeling results with literature data of sandstones with similar properties as the Seeberger sandstone used in the framework of the MEMIN project. We also include new Hugoniot data for the Seeberger sandstone that were obtained by flyer plate experiments. In the first section we provide information on the shock physics code iSALE, the setup and range of the numerical experiments (parameter studies) and the material models used. In the next section we present the results of shock amplification due to pore space collapse considering the collapse of a single pore and a set of pores followed by the investigations of bulk effects of pore space collapse on shock wave propagation. In this section, detailed resolution and dimensionality tests are carried out first. Additionally, the section comprises investigations of shock wave propagation through porous material and water-saturated material as well as the effect of strength in porous material. Finally, a comparison of the meso- and macroscale model is carried out. In the last section we discuss implications of our results.

4.2 Methods

4.2.1 Numerical hydrocode

We used the shock physics code iSALE 2-D/3-D (Wünnemann *et al.*, 2006; Elbeshausen *et al.*, 2009, and references therein) for both meso- and macroscale studies. iSALE is based on the original SALE (Simplified Arbitrary Lagrangian Eulerian) code by Amsden *et al.* (1980). To simulate hypervelocity impact processes in solid materials, SALE was modified to include an elasto-plastic constitutive model and fragmentation model (Collins *et al.*, 2004), various equations of state (EOS), and multiple material handling (e.g. Ivanov *et al.*, 1997; Elbeshausen and Wünnemann, 2011a). The code includes a porosity compaction model, the so-called ε–α model (Wünnemann *et al.*, 2006; Collins *et al.*, 2011a), that enables modeling of shock wave propagation in porous materials. Basically, the code consists of three components: the numerical solver of the equations describing the motion of matter (that are based on the conservation equations of mass, momentum, and energy), the equation of state dealing with the thermodynamic behavior of matter (see the next section), and the constitutive model describing the mechanical response of rocks to elasto-plastic deformation. The equations of motion for a continuous medium can be either Lagrangian or Eulerian. iSALE includes both a Eulerian and Lagrangian numerical solver. In the Eulerian description, the cells of the computational domain are fixed in space and material is advected through the numerical grid. In Lagrangian models, material initially located in a computational cell is fixed and the transport of material is calculated by the movement and deformation of the whole grid in space. The latter numerical approach often faces the problem of extreme deformation of cells, for instance, if in a mesoscale model an open pore is completely closed as a result of shock compression. This usually causes numerical problems as grid resolution (given by the number of cells per reference area) varies significantly and becomes infinitesimally small where empty pore space is erased. To fix the problem, numerical cells have to be eroded if deformation exceeds a certain threshold or some sort of re-gridding is required (e.g. Anderson, 1987). In Eulerian models, the grid resolution is constant in space and the closure of a pore is naturally described by the flow of matter through the computational mesh. All models shown in this chapter were carried out in the Eulerian mode of iSALE. Although iSALE contains sophisticated constitutive models describing the mechanical response of a material to large stresses, we employed a simple von Mises yield criterion to account for plastic material failure. The von Mises model defines a constant stress where plastic yielding occurs and matter experiences permanent deformation. We neglected any dependency of yield strength on the deformation history (damage), pressure, temperature, and strain rate (e.g. Collins

et al., 2004). This simplification makes our models less realistic, but enables us to relate macroscopic and mesoscopic strength parameters in a simple way to ensure the consistency of models on different scales. This study aimed at developing a methodological approach that would be applied in follow-up studies for more complex material behavior.

4.2.2 Equation of state for porous materials

The equation of state (EOS) describes the thermodynamic behavior of the material and is therefore key for modeling shock wave propagation. In the form used in iSALE, it relates the state parameters internal energy and density with pressure and temperature. Prior to the actual model run, iSALE generates tables of the state parameters by utilizing the Analytic EOS (ANEOS) (Thompson and Lauson, 1972). During the simulation, the pressure and temperature for a given density and internal energy are looked up in the table; intermediate states are interpolated among the closest neighbors in the discrete state table. We used the modified version of ANEOS for quartzite (Melosh, 2007) taking molecular clusters in the vapor phase into account to calculate the thermodynamic state of the solid component and incorporating the phase transition from quartz to stishovite; however, due to the low-to-moderate shock pressures considered in this study, we did not expect any differences in comparison with the original ANEOS version. Usually, quartz undergoes various phase changes which, however, are too complex to be all considered in the EOS of the numerical code (Melosh, 2007). The solid component of the material under consideration is quartzite in all models. In a geological context, quartzite rarely contains any porosity. To avoid confusion, we approximated the material behavior of any quartz-rich, porous water-saturated or partial water saturated rock, such as the Seeberger sandstone, by the thermodynamic properties of quartzite and water (described by ANEOS) plus an additional procedure to account for the presence of pore space. In the following, we also use the term "dry porosity" if pore space is empty; if water is present, we indicate this by the term "wet porosity". To calculate the thermodynamic state of a porous material, three different cases have to be distinguished:

1. In the case of porous material (pores are empty), the thermodynamic state of matter is significantly affected by the crushing of pores. The presence of porosity causes changes in density due to the closure of pore space that has to be taken into account by so-called compaction models (Wünnemann *et al.*, 2006; Hermann, 1969; Carroll and Holt, 1972), The iSALE code combines the ε–α porosity compaction model (Wünnemann *et al.*, 2006) and the ANEOS to determine the thermodynamic

state in porous material. The ε–α model describes the crushing of pore space as a function of compressive volumetric strain ε_V (which is defined negative in our model). In the compaction function $a = f(\varepsilon_V)$ the distension α is defined by $\alpha = 1/(1-\phi)$, with ϕ being the porosity. If compression increases (volumetric strain decreases), distension decreases until all pore space is crushed out and the material is fully compacted ($\alpha = 1$). The compaction function is defined by an elastic-plastic transition strain ε_e to separate the elastic regime, where the decrease in pore space is not permanent ($\varepsilon_V > \varepsilon_e$)), and α compaction regime where changes in porosity remain in the material ($\varepsilon_V < \varepsilon_e$). In the compaction regime, pore space is crushed out approximately according to an exponential law where the rate of compaction is controlled by the exponent κ. Note, κ and ε_e are material parameters that need to be determined in compaction experiments. The parameter values for the porosity model that have been considered for the macroscale simulations of a dry porous material are listed in Table 4.1. More details are given in Wünnemann *et al.* (2006).

2. In case of water-saturated material (pores are filled with water), we used an approach proposed by Pierazzo *et al.* (2005). If all pore space is filled with water (100 % saturation), the material can be treated as a two-phase material mixture consisting of the matrix (quartzite) and water. The thermodynamic state of such a material mixture can be calculated by assuming that both phases have to be in a thermodynamic equilibrium (same temperature and pressure). With this boundary condition, a new table for a given porous material with a defined water content can be generated by combining the ANEOS for each phase (water and quartzite). The procedure is described in Pierazzo *et al.* (2005). Note that the water content in the material mixture is fixed and any change in the distribution by flowing or steaming of water through the material is not taken into account. As a consequence, we assumed that the presence of water prevents complete closure of pores, although the used ANEOS for water-quartzite mixtures allows for compression of the water phase in equilibrium with the quartzite matrix.
3. In the case of a partially water-saturated material, with some pores completely filled with water, and others completely dry, we combined the porosity compaction model and the tabulated ANEOS for mixed material according to the relative proportion of dry and wet pore space.

In summary, homogenized or macroscopic models used for this study are based on the ANEOS for quartzite and water and the ε–α porosity compaction model. This enables the modeling of dry, partially water saturated, and fully water-saturated porous materials under shock loading on a macroscale. The described procedure is applicable to any other porous material and is not limited to quartzite as matrix and water-filled or empty pores; however, the large contrast in terms of compressibility between the two different phases,

such as water and quartzite, may lead to disequilibrium states that cannot be treated by the procedure for mixed materials as described above.

Table 4.1: Parameters used in the $\varepsilon - \alpha$ porosity model

Parameter	**Value**
α	1.25, 1.43, 1.54, 1.67, 2.0
ϕ in %	20, 30, 35, 40, 50
ε_e	$-1.0 \cdot 10^{-5}$, $-7.5 \cdot 10^{-2}$, $-3.0 \cdot 10^{-2}$
κ	0.98, 1.0

4.2.3 Model setup

We chose a model setup very similar to typical laboratory shock wave-recovery experiments (Langenhorst and Hornemann, 2005) to carry out meso- and macroscopic numerical simulations of shock wave propagation in porous wet and dry sandstone. The principal model setup is shown in Figure 4.1. We generated a planar shock wave by impacting a so-called "flyer plate" on a "buffer plate" at velocities ranging from 500 to 4000 $m\,s^{-1}$ corresponding to initial shock pressures generated at the interface between the flyer and the buffer plate of 2.6–28 GPa. The flyer plate is resolved in vertical direction by 600 cells and the buffer plate by 100 cells. The radius of the cylindrical setup is resolved by 1400 and 1700 cells, respectively. The resolution of the "sample" varies according to the number of pores (Section 4.3.1). A well-defined shock plateau propagates through the buffer plate into the sample. The impulse length of the shock wave is given by the thickness of the flyer plate. In all simulations, it is longer than the extent of the sample; we did not model the unloading. The impacting flyer plate and the buffer plate as well as the solid matrix material consisted of quartzite in all models in this study. The models can be looked at as "numerical experiments" where the "sample" either represents a mesoscopically resolved sample containing a single or several pores embedded in a quartzite matrix or a macroscopic sandstone sample where the number of pores is infinite and porosity is described by the state variable distension α. While in the former case pores are resolved directly by the model, the bulk effect of porosity on the thermodynamic state is considered in the latter case by combining the ANEOS for mixed material and the ε–α porosity compaction model as described in the previous section. In the mesoscale models, the resolved pores can be either empty or filled with water and the size, geometry, and distribution can be varied according to the chosen porosity; however, for this study, we used only pores with a

quadratic cross section.

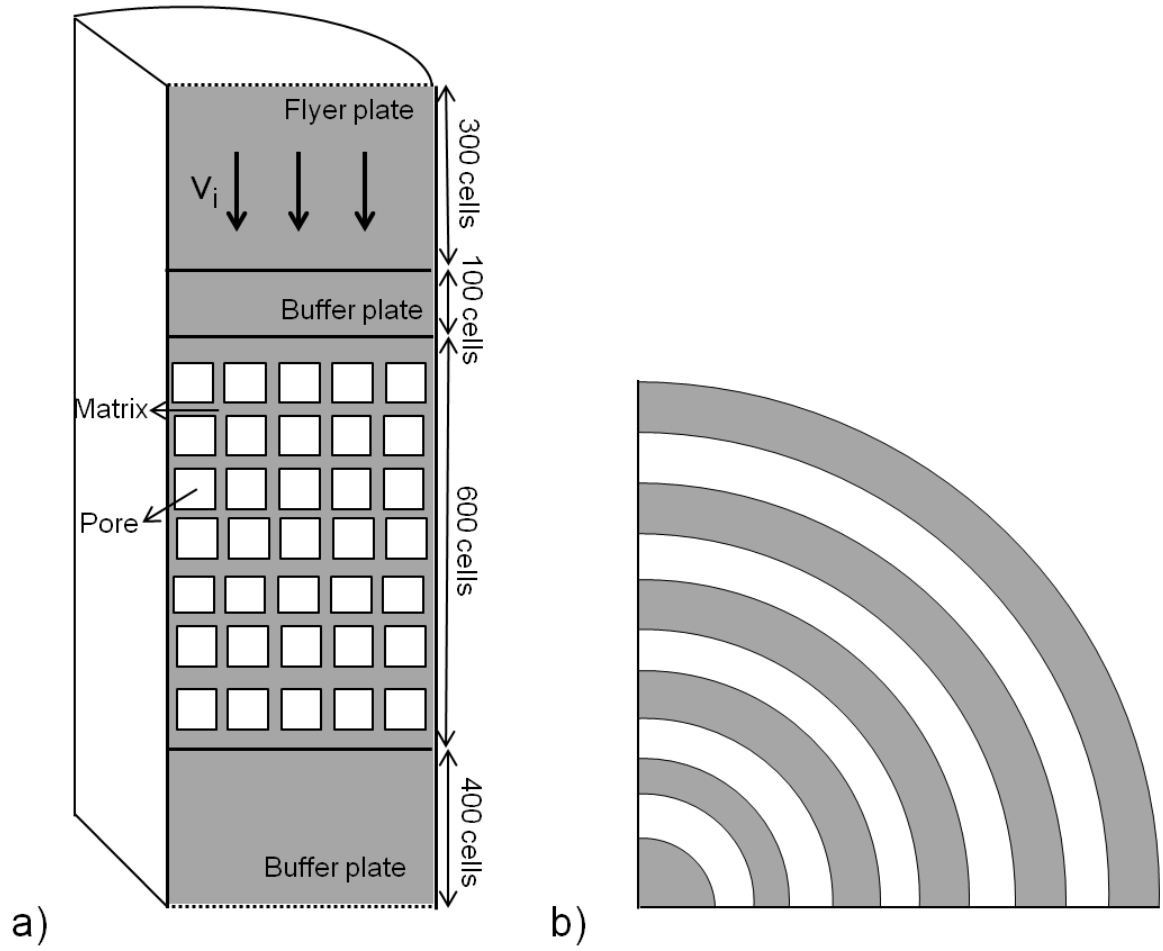

Figure 4.1: a) Illustration of the mesoscale model setup including the flyer (or impact) plate, the buffer plate, and the sample with resolved pores (the shown number of pores is only representative for the actual number of pores that varies in different simulations). The shown pores can be empty or filled with water. The matrix consists of quartzite. b) Plane view of the 2-D cylindrically symmetric computational grid inside the sample with resolved pores represented by rings with rectangular cross-section. In macroscale models, the number of pores is infinite and porosity is considered by the ε–α porosity compaction model.

Schade and Wünnemann (2007) studied the effect of geometry and found that pore geometry has an effect on peak pressure distribution and localized pressure increase due to pore collapse. The highest pressures have been observed for a cubic geometry in contrast to a rhombic (lowest pressure increase) or cubic-rhombic geometry. However, the effect of pore geometry has been neglected in the present study of pore collapse. We presume that the effect of pore geometry on shock wave propagation is negligible if the number of pores located close to one another is high. The variety of possible geometries is infinite and a systematic analysis is beyond the scope of this study. An overview of all mesoscale models that have been carried out is given in Table 4.2. We first looked at the collapse of a single pore under different pressure conditions. Then, we systematically

increased the number of pores to investigate the propagation of a shock wave through a heterogeneous target. The most desirable setup for this study would have been a random distribution of pores in space over a 3-D sample very much like how pore space distribution looks in a thin section of sandstone. Although such a study is in principle feasible, the requirements on computer power are high and the computation time would be very long. Therefore, we used a simplified approach where pores are represented by rings with a rectangular cross-section on a 2-D cylindrically symmetric grid (Figure 4.1). The pores are regularly distributed in the computational grid ("checkered pattern"). We always ensured a symmetric arrangement of pores with respect to the symmetry axis. In the case of a single pore, the pore is located on the symmetry axis. To test whether this simplified setup is sufficient to study the mesoscopic effects of porosity on shock propagation, we compared the 2-D simulations with uniform pore distribution with 2-D and 3-D simulations where pores are represented by cubes that were randomly distributed in the sample (Table 4.2). The distribution of pores does not seem to influence the modeling results significantly and the 3-D simulations agree well with the obtained 2-D modeling results (Section 4.4.2). Besides the geometry and dimensionality of the setup, resolution is key to generate quantitatively meaningful results. Although resolution should be as high as possible, we also have to consider computation time and hardware resources available for this study. We measured resolution in terms of the number of cells per pore length (CPL). We carried out resolution tests yielding an acceptable resolution of 8 CPL for 2-D and 3-D (Section 4.4.1) if a large number of pores had to be resolved. For single pore models, where peak shock distribution in the vicinity of the pore was studied in much detail, a resolution of 60 CPL was required (Section 4.3.1). In summary, we carried out systematic numerical experiments varying the number of pores (1–12), the bulk porosity (20–50 %), and the initial shock pressure (2.6–28 GPa). We also studied the effect of water saturation and the yield strength of the matrix (quartzite) ranging between 0 and 1 GPa. Finally, we compared the results of the mesoscale numerical experiments with macroscopic models where the sample contained an infinite number of pores with the same bulk porosity (20–50 %).

Table 4.2: Overview of numerical mesoscale simulations (including resolution tests)

Flyer/buffer plate material:		**Quartzite**						
Matrix material:		**Quartzite**						
Cross profile of pore geometry:		**Squares**						
No. of pores	**Pore filling**	**Dimension**	**Pressures in buffer plate** (GPa)[a]	**Flyer plate velocity** ($km\,s^{-1}$)[b]	**CPL** (cells per pore length)	**Number of cells** in computational domain	**Porosity**	**Distribution**
1	Empty	2-D	6,14,22,28	1,2,3,4	120	1000 x 1400	-	-
		2-D	6,14,22	1,2,3,4	60	1000 x 1400	-	-
		2-D	6,14,22	1,2,3	30	1000 x 1400	-	-
		2-D	6,14,22	1,2,3	10	1000 x 1400	-	-
1	Water	2-D	14,28	2,4	120	1000 x 1400	-	-
3/6/8	Empty	2-D	6	1	60	1000 x 1400	-	-
		2-D	14	2	60	1000 x 1400	-	-
		2-D	22	3	60	1000 x 1400	-	-
		2-D	28	4	60	1000 x 1400	-	-
12	Empty	2-D	6	1	60	1500 x 1400	-	-
		2-D	14	2	60	1500 x 1400	-	-
∼500	Empty	2-D	2.6,6,14,22,28	0.5,1,2,3,4	8	325 x 17000	0	Uniform
		2-D	2.6,6,14,22,28	0.5,1,2,3,4	8	325 x 1700	20	Uniform
		2-D	2.6,6,14,22,28	0.5,1,2,3,4	8	325 x 1700	30	Uniform
		2-D	2.6,6,14,22,28	0.5,1,2,3,4	8	325 x 1700	35	Uniform
		2-D	2.6,6,14,22,28	0.5,1,2,3,4	8	325 x 1700	40	Uniform
		2-D	2.6,6,14,22,28	0.5,1,2,3,4	8	325 x 1700	50	Uniform
		2-D	6,14,22	1,2,3	8	325 x 1700	20	Random
		2-D	6,14,22	1,2,3	4	162 x 850	20	Uniform
		2-D	6,14,22	1,2,3	4	162 x 850	20	Uniform
		2-D	6,14,22	1,2,3	2	81 x 425	20	Uniform
		3-D	6,14	1,2	8	168 x 765 x 162	20	Uniform
		3-D	14	2	8	168 x 765 x 162	20	Random
∼500	Water 100 %	2-D	6	1	8	325 x 1700	20	Uniform
		2-D	14	2	8	325 x 1700	20	Uniform
		2-D	22	3	8	325 x 1700	20	Uniform
∼500	Water 50 %	2-D	6	1	8	325 x 1700	20	Uniform
		2-D	14	2	8	325 x 1700	20	Uniform
		2-D	22	3	8	325 x 1700	20	Uniform

[a]The pressure in the buffer plate is the mean pressure at the interface between flyer and upper buffer plate
[b]Each pressure value represents one experiment with a given flyer plate velocity

4.2.4 Processing of model results

We recorded several thermodynamic parameters as density, pressure, peak pressures, shock, and particle velocities in space, and time during shock wave propagation through the sample. To study the localized mesoscopic effects of pore collapse in the vicinity of a single pore or an array of pores, we used Lagrangian tracer particles to record peak shock pressures. Tracers are massless and are initially placed in the center of each computational cell. They may be considered as representative for the volume of material initially located in the same cell. Tracers move along with material through the grid and record the thermodynamic path during the passage of the shock wave. We determined the highest pressures each tracer had experienced and obtained the peak pressure distribution. The final pressure distribution is a result of shock loading and superposition of reflecting shock fronts originating from the collapse of pores. Finally, we plotted isobars of peak shock pressures enclosing all tracers that experienced a certain pressure level and calculated the volume by means of the number of tracers enclosed and their representative volume. By doing so, we need to consider that a small number of tracers experience very high pressures, sometimes up to 100 times the initial shock pressure, which is most likely a numerical artifact. Such high pressures are certainly not representative to define the range of shock pressure amplification due to pore collapse. Therefore, we define some critical volume that we consider to be significant to estimate the range of pressure increase due to the closure of pores. We define the critical volume as 20 % of the initial pore volume. In other words, we consider only peak pressures that have been experienced by a volume that is at least 20 % of the initial pore volume. This is a bit of an arbitrary definition; however, we noticed that only an insignificantly small volume (or a small number of tracers) undergoes higher pressures and we consider this material fraction as negligible. To work out the thermodynamic bulk behavior of the porous sample in mesoscopic models, we determined the particle velocity u_p and the velocity of the shock front U_S. A series of numerical experiments for different flyer plate velocities, and thus different initial shock pressures, enable us to plot Hugoniot curves in the $U_S - u_p$ space. Hugoniot curves can be compared for different porosities and water contents. In the case of the mesoscale models, the particle velocities vary across the shock front significantly due to the heterogeneities (pores) causing localized pressure amplifications and reflections at pore boundaries. To address this fact, we averaged the shock wave parameters over a row of computational cells (radial direction) at a certain distance the shock front has traveled through the sample (sample depth). Vertical profiles of particle velocity (along columns of cells) at different points in time are used to determine the shock wave velocity U_S in the models. Due to the heterogeneities (pores), the shock front was somewhat uneven and we determined the

shock wave velocity U_S in several parallel profiles and calculated mean values. We used particle velocity variations to estimate the increase and decrease in shock pressure as a result of pore space crushing or we averaged out the variations to determine the bulk behavior of the heterogeneous material. By means of the Rankine-Hugoniot equations (e.g. Chapter 11 in Zel'dovich and Raizer, 2002, Section 2.1 of this thesis), particle and shock wave velocity, u_p and U_S, can be used to calculate density ρ_s, specific volume V_s, and pressure P during shock compression in the sample. The initial bulk density for the porous "dry" and "wet" material varied from 1955 to 2297 $kg\,m^{-3}$ according to the chosen porosity and degree of water saturation. The density of the matrix material is 2650 $kg\,m^{-3}$ given by the ANEOS for quartzite.

4.3 Results: Shock amplification due to pore space collapse

4.3.1 Resolution test - pore collapse

To study the complex interaction of the shock wave with empty pores on a mesoscale, sufficient resolution (sufficiently large computational domain or number of cells covering the area under consideration) is required. Therefore, we first carried out a suite of simulations varying the resolution. We determined the volume of material in the sample which had experienced a maximum peak pressure that was four times the initial shock pressure considering different resolutions. Resolution is measured in terms of the number of cells per pore length (CPL). We used 10, 30, 60, and 120 CPL and varied the initial shock pressure between 6, 14, and 22 GPa. Figure 4.2 shows how the volume of material that has experienced a pressure four times the initial pressure changes with increasing resolution from 10 to 120 CPL. Independent of the shock wave pressure, all models approach approximately the same volume at 60 CPL, which is considered as the "true" volume. Further increasing the resolution (120 CPL) does not show any significant difference in volume. Therefore, we concluded that 60 CPL poses a reasonable compromise to keep the error in our simulations as small as possible and the computation time reasonable. Similar results regarding the required resolution in iSALE to determine shock volumes have been obtained by Wünnemann *et al.* (2008).

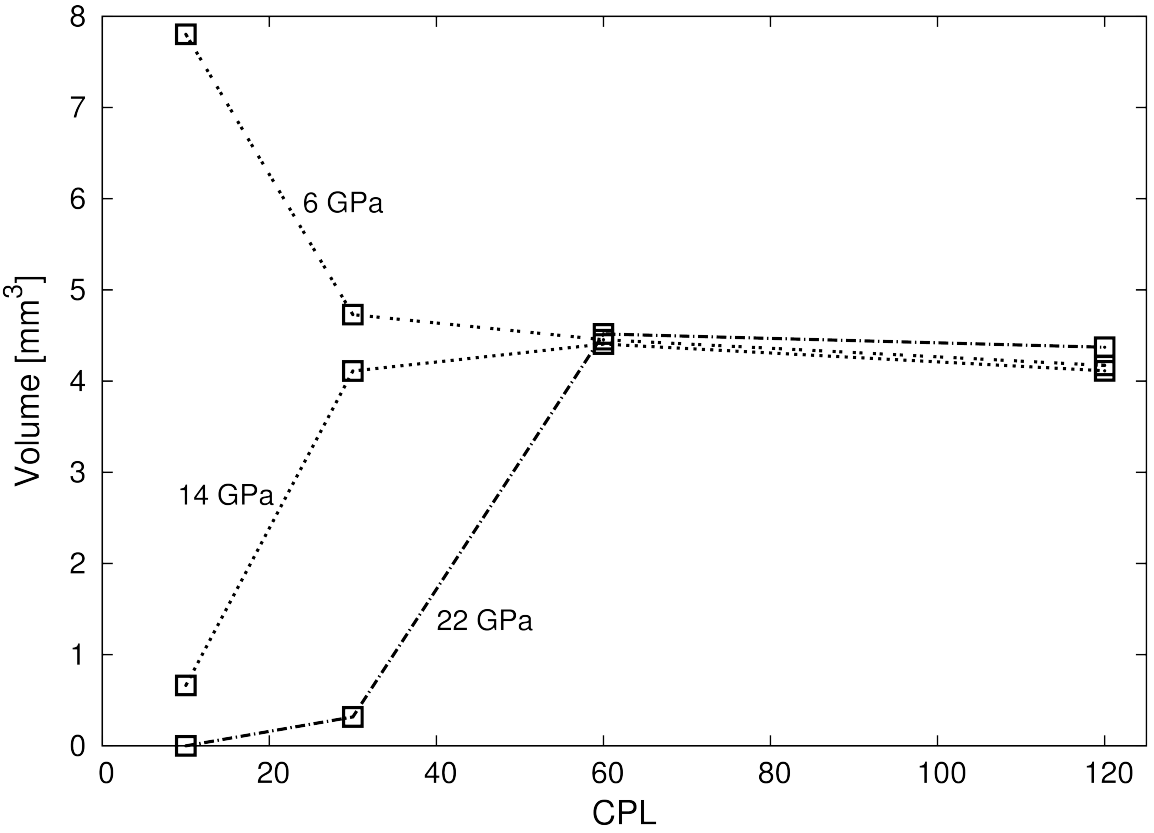

Figure 4.2: Volume of material in the sample that experiences a maximum peak shock pressure four times the initial shock pressure of 6, 14, and 22 GPa versus resolution in CPL (cells per pore length). At a resolution of 60 CPL, the volume is not dependent on resolution anymore.

4.3.2 Collapse of single pores

First, we studied the collapse of an isolated pore. The pore has a quadratic cross-section and is located on the symmetry axis of the 2-D cylindrically symmetric grid. The geometry corresponds to a cylinder. At the point in time when the shock front first hits the boundary of the pore, it is turned into a rarefaction wave traveling in the reverse direction unloading the material from shock pressure (Figure 4.3a). The volume of the pore decreases gradually as material at the boundary to the pore is set into motion after shock release (Figure 4.3b and 4.3c). When the pore is completely closed, a secondary shock wave is generated that propagates approximately spherically outward from the original center of the pore (Figure 4.3d). Note that the whole sample undergoes a relative motion downward in the direction of the shock front. The secondary shock wave superimposes with the release wave and the initial shock wave causing pressure amplifications in the material that was originally surrounding the pore. Figure 4.4a illustrates the maximum pressure distribution relative to the initial shock pressure after the collapse of a single pore for an initial pressure of 6,

14, and 22 GPa. Maximum shock pressures were recorded in the proximity of the pore to quantify the maximum amplification that could be expected due to pore collapse. As a maximum, the pressure increased up to four times of the initial pressure. The highest pressures could be observed in the zone where the pore was initially located. Note that the material, and thus tracers, experienced a relative motion downward as can be seen by the location of the initial pore in Figure 4.4a (dashed square). The absolute pressure amplification slightly depends on the amplitude of the initial shock wave: For a shock pressure of 6 GPa (flyer plate impact velocity $v_i = 1000\,m\,s^{-1}$), the maximum observed pressure reached 17.5 GPa (approximately three times the initial pressure); for 14 GPa (flyer plate impact velocity $v_i = 2000\,m\,s^{-1}$), the shock pressure was locally amplified to 61 GPa (approximately 4.4 times the initial pressure), and for 22 GPa (flyer plate impact velocity $v_i = 3000\,m\,s^{-1}$), the maximum pressure went to 65 GPa (approximately three times the initial pressure) always considering that 20 % of the initial pore volume experienced the determined pressure. It is possible that smaller fractions of material experienced even higher shock pressures, but according to the given resolution limit (too small number of tracers), the volume was probably not significant to be considered in our analysis. Other pore-collapse mechanisms despite the here observed "shrinking" mechanism may influence the pressure amplification. Kieffer *et al.* (1976) distinguished two different mechanisms resulting in the closure of an open pore. "Shrinking" is considered the gradual closure of the pore from all sides and occurs at low-to-moderate shock pressures. If the shock pressure exceeds a certain threshold, Kieffer *et al.* (1976) described that material is "jetting" into the pore space from the point where the shock front first interacts with the pore boundary that may be considered as a "free surface". Kieffers description of pore closure is based on observations at shocked Coconino sandstone. Schade and Wünnemann (2007) reproduced the process in mesoscale modeling of pore crushing. In all models of the present study, pores were crushed by the shrinking mechanism. Apparently, the maximum shock pressure of 22 GPa in the present study was not sufficient to induce the jetting. However, the formation of jets entering the pore is very sensitive to the pore geometry and how the shock front is aligned to the sides of the pore. Thus, the lack of jetting at 22 GPa in our models may have been rather caused by the simplified geometry and planar alignment of the shock front to the upper side of the pore than by too low shock pressure. Similar numerical experiments with water-filled pores have been carried out. As we do not include any opening of cracks in our model, where the pressurized water can escape, the pore cannot be closed and, therefore, we observe only a very minor shock pressure amplification in the vicinity of the pore (at 22 GPa initial shock pressure, 24 GPa were observed as a maximum).

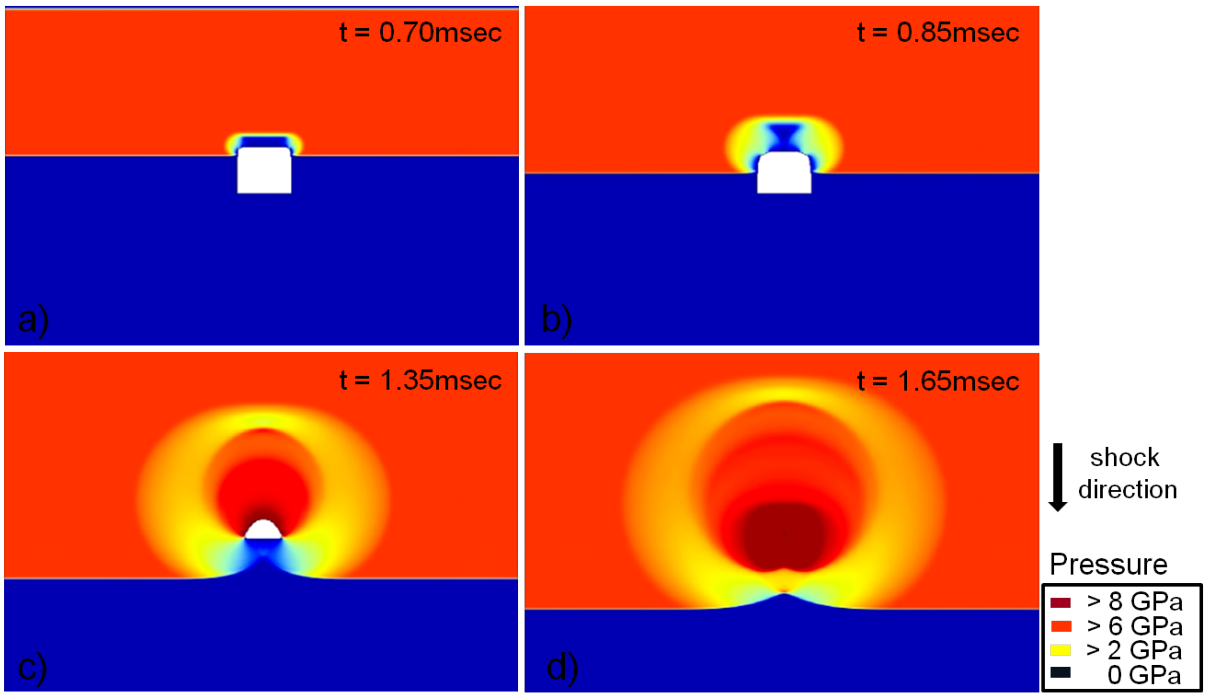

Figure 4.3: Snapshot series of the collapse of a single pore (white square) due to shock compression with an initial pressure of 6 GPa. The series shows the different states of pore collapse and the evolving pressure with time. Zero pressure represents unshocked material.

4.3.3 Collapse of a set of pores

An isolated pore may occur in a generally dense material. In porous material, such as sandstone, pores are located relatively close to one another, separated only by individual grains, and shock waves originating from pore closure may interact with one another. Therefore, we set up an array of pores separated by one pore length from one another and analyzed the shock wave propagation through the sample. The same 20 % volume criterion as described above was applied to determine significant peak shock pressure amplifications. For a sample with three pores each resolved by 60 cells, the maximum pressure ranges from about 10 to 23 GPa for corresponding initial shock pressure amplitudes of 6–22 GPa, respectively. By increasing the number of pores to 12, the observed maximum peak pressures changed only insignificantly (9, 17, 23 for initial shock pressure amplitudes of 6, 14, 22 GPa). Considering the 20 % volume criterion, on average, the amplification of shock pressure is less than two times the initial pressure due to interaction of shock and release waves originating from adjacent pores. Figures 4.4b and 4.4c, however, depict the distribution of peak shock pressures in the proximity of 3 and 12 pores neglecting that only a certain volume of initial pore space is considered. The amplification varies similar to the single pore case between 1.5 and 4 times of the initial pressure. For the array of 12 pores, the highest pressures are located in the first row of pores, which explains why the

same maximum peak pressures occur in the 3 and 12 pore case. Those maximum pressures occur when the first row of pores is closed. The pressure amplification decreases with the collapse of additional pore space due to energy consumption. Reflections and interferences of the shock and release wave from neighboring pores reduce the pressure amplification. By considering 20 % of the initial pore volume that has experienced a certain pressure, we observed only a maximum amplification of less than two times the initial shock pressure. We considered a threshold of 20 % of the initial pore volume experiencing a certain pressure to be more representative for shock amplification in porous material.

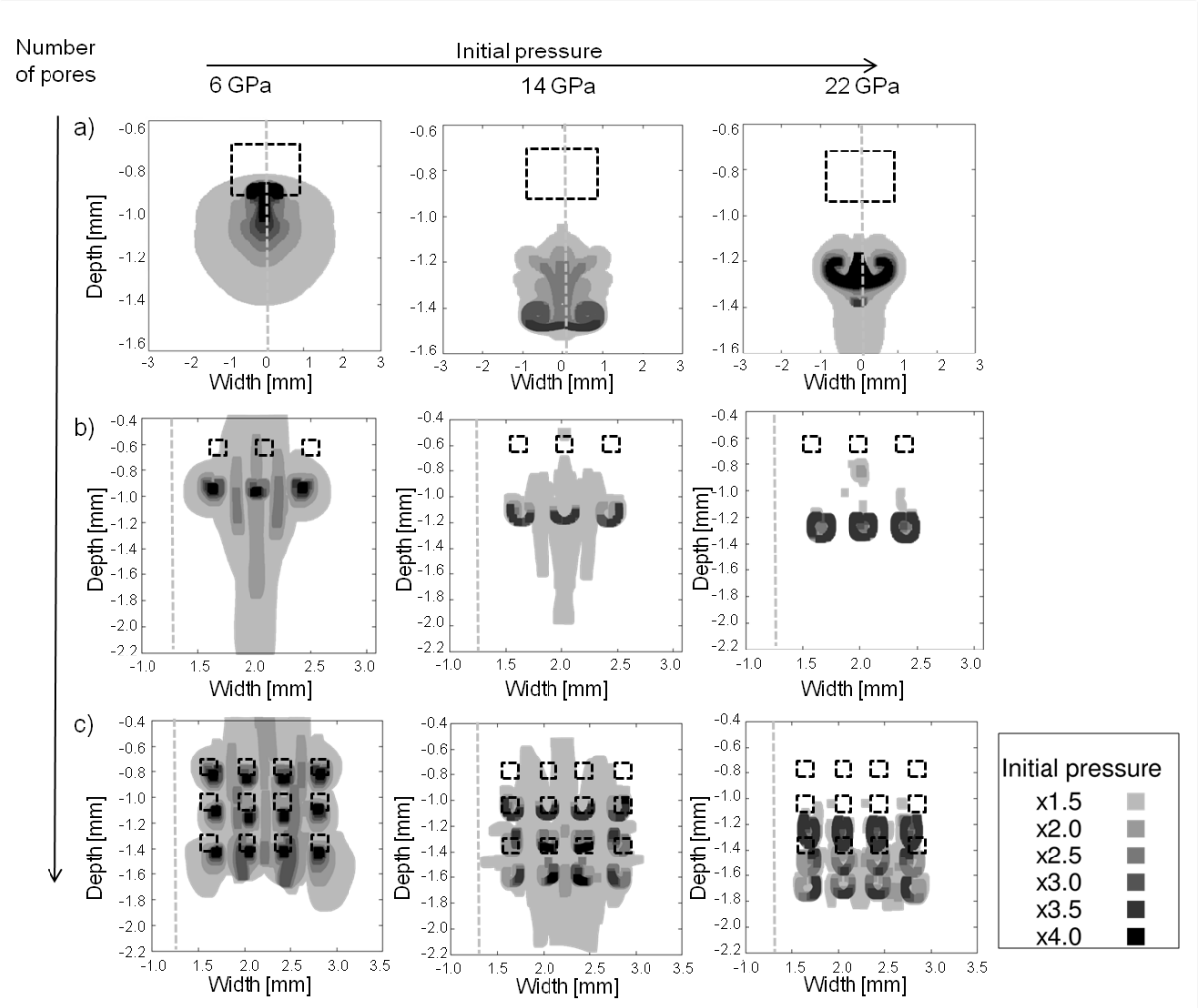

Figure 4.4: Peak pressure distribution for (a) a single pore, (b) 3 pores, and (c) 12 pores; each pore is resolved by 60 CPL with an initial pressure of 6, 14, and 22 GPa from left to right. The contour lines show pressure distinctions of 1.5 to 4 times the initial pressure. The light gray dashed lines indicate the position of the symmetry axis. The dashed squares indicate the original positions of the pore(s) in the unshocked material. Each frame represents the final stage (after complete closure of the pore) that we define to be reached when the shock wave has propagated through the entire sample. The peak pressures are the final peak pressures the material has experienced.

4.4 Results: Bulk effects of pore space collapse on shock wave propagation

4.4.1 Resolution test - shock propagation

To study the bulk effects of pore space crushing on the propagation of shock waves by mesoscale modeling the number of pores needs to be increased significantly; however, the number of pores resolved in mesoscale modeling can only be representative for very small sample sizes (i.e., few mm). In crater formation models in sandstone, the number of pores is infinite and other methods to describe the bulk behavior of porous material have to be applied as will be discussed further below. To resolve an as large as possible number of pores, the resolution of each pore has to be reduced significantly in comparison with the investigations above on pore space collapse. We assume that localized pressure amplification due to single pore collapse where a high resolution was necessary does not contribute to the bulk behavior of shock wave propagation. Nevertheless, we have to ensure that resolution is sufficient for the study on shock propagation in this section. We carried out resolution tests for shock wave experiments as described above where the sample was perforated with about 500 pores that were resolved by 2, 4, and 8 CPL. Vertical pressure profiles where lateral variations are averaged out (see Section 4.2.4 in Methods) are shown in Figure 4.5a for all three different resolutions. In all three cases, the pressure oscillates due to the pores in the sample; however, maximum and minimum pressure fluctuations vary depending on the CPL value. The average level of the shock plateau (mean value of the oscillations) was approximately constant for 4 and 8 CPL ($3.6\,GPa$), but significantly shifted to lower pressures for 2 CPL ($3.0\,GPa$; Figure 4.5b). Apparently, a resolution of 2 CPL is insufficient for the given study. For all models (2-D and 3-D) in the study on shock propagation, we used 8 CPL.

4.4.2 Dimensionality and distribution of pores

A vast majority of models in this study were carried out on a 2-D cylindrically symmetric grid. Pores have a quadratic cross-section and are arranged in a checkerboard pattern (Figure 4.1). This simplified setup certainly does not reflect a typical natural distribution of pores in porous material such as sandstone. We have already stated that pore geometry does not affect the bulk behavior. We now demonstrate that distribution and dimensionality

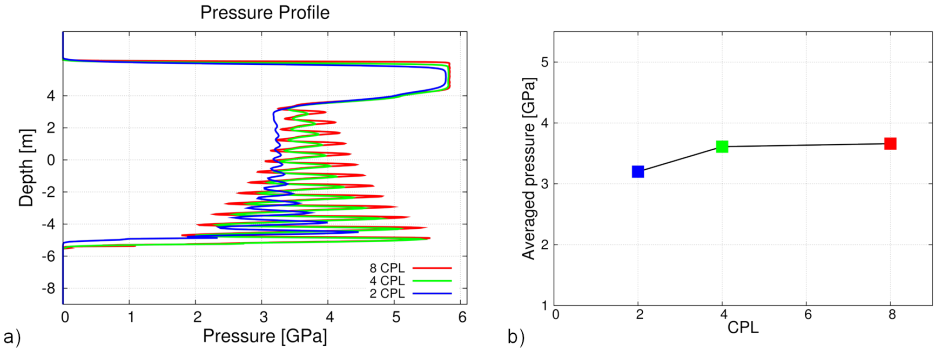

Figure 4.5: Resolution tests with a grid containing a large number of pores, each pore is resolved by 2, 4, and 8 CPL representing comparable pressure profiles through the sample (a) where zero depth represents the interface of the flyer and the buffer plate and (b) the corresponding averaged level of shock plateau pressure in dependency on CPL. In Figure 4.5b, the three different symbols (resolutions) are all plotted for the same time corresponding to a point in time when the shock wave has traveled through most of the sample material.

(3-D cubes instead of 2-D rings) of pores play only a minor role in the quantification of shock propagation in heterogeneous material. Regarding the dimension of the model, we compared pressure profiles of 3-D simulations and 2-D simulations, both resolving pores by 8 CPL (Figure 4.6). The 3-D simulations were conducted on a smaller grid to save computation time. So the number of cells of the sample was in total 50,400 in 3-D and 195,000 in 2-D. Additionally, we compared the effect of a random distribution of pores in 3-D with the regular checkerboard pore distribution in 2-D. The size of pores was not varied. The bulk porosity of the sample was kept constant in all three cases shown in Figure 4.6. Although the observed oscillations in the vertical pressure profiles differ among the three cases, the mean shock plateau is approximately the same. In Figure 4.7, we compare the pressure profiles for regular and random pore distribution in 2-D for three different initial shock pressures. For $6\,GPa$, the averaged shock pressure profiles agree well. With increasing initial pressure, the models show slight differences in the average pressure level of the shock plateau, indicating that with an increase in shock pressure, the pore distribution has an increasing effect on pressure distribution and the overall shock propagation in our mesoscale models. We also have to keep in mind that the model with randomly distributed pores represents only one possible assembly of pores in a sample. Other distributions of pores would cause small differences in the pressure profile. Nevertheless, the influence of the distribution of pores is small and we assume that the uniform checkerboard distribution on a 2-D cylindrically symmetric grid, where pores are represented by rings with a quadratic cross-section, is a sufficient approximation for this study where the implementation of a large number of simulations is crucial.

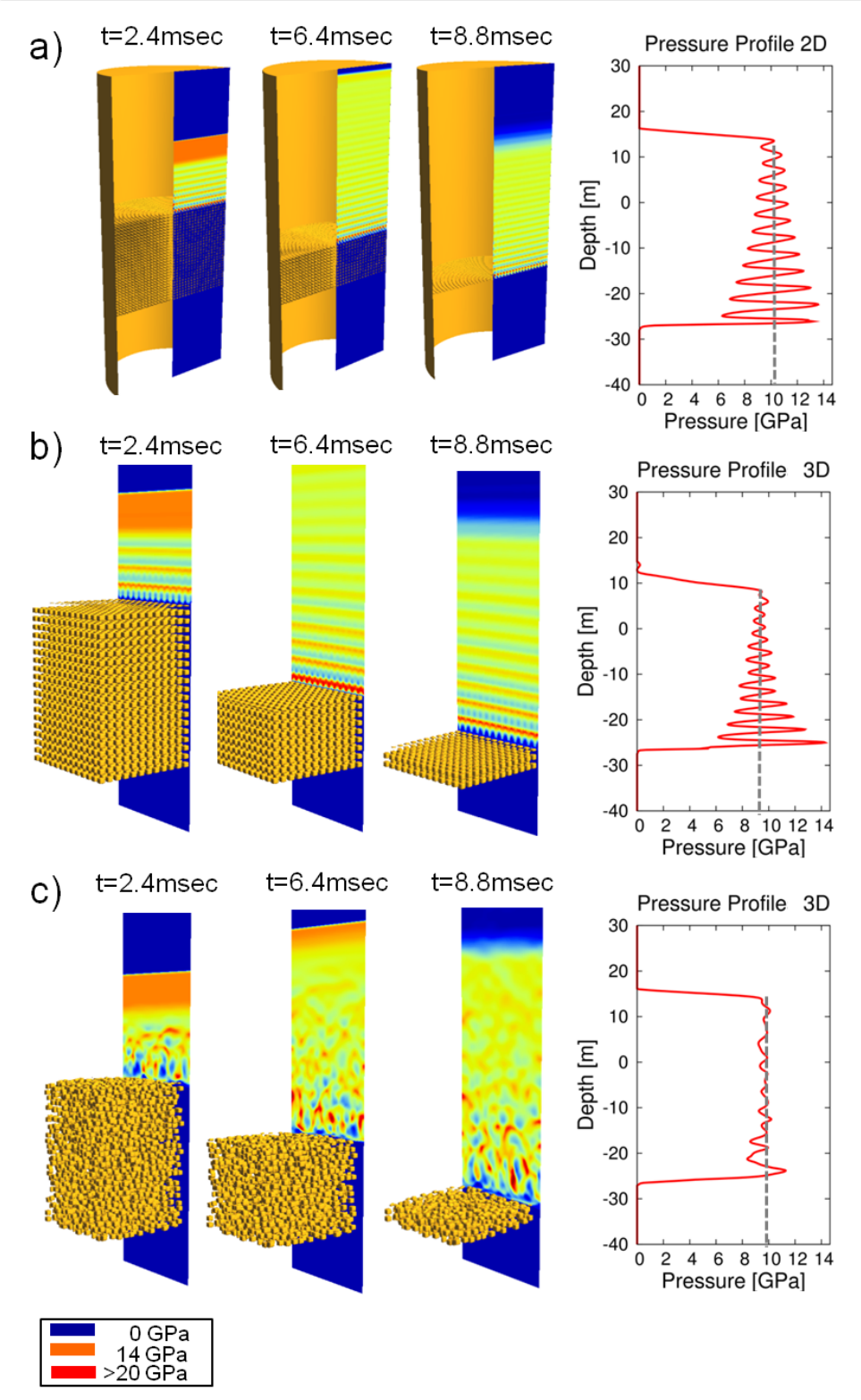

Figure 4.6: Comparison of a 2-D simulation (regular distribution (a)) with a 3-D simulation (regular (b) and random distribution (c)). Pores are resolved by 8 CPL. The contour plots (left) show snapshots of the pressure distribution in the sample after 2.4, 6.4, and 8.8 ms. The vertical profiles (right) depict the corresponding shock pressures, which are averaged over a row of computational cells at a certain distance the shock front has traveled through the sample at t = 6.4 ms (for all profiles). The profiles include the mean pressure value in the sample indicated by the dashed lines, which is about the same for all three cases.

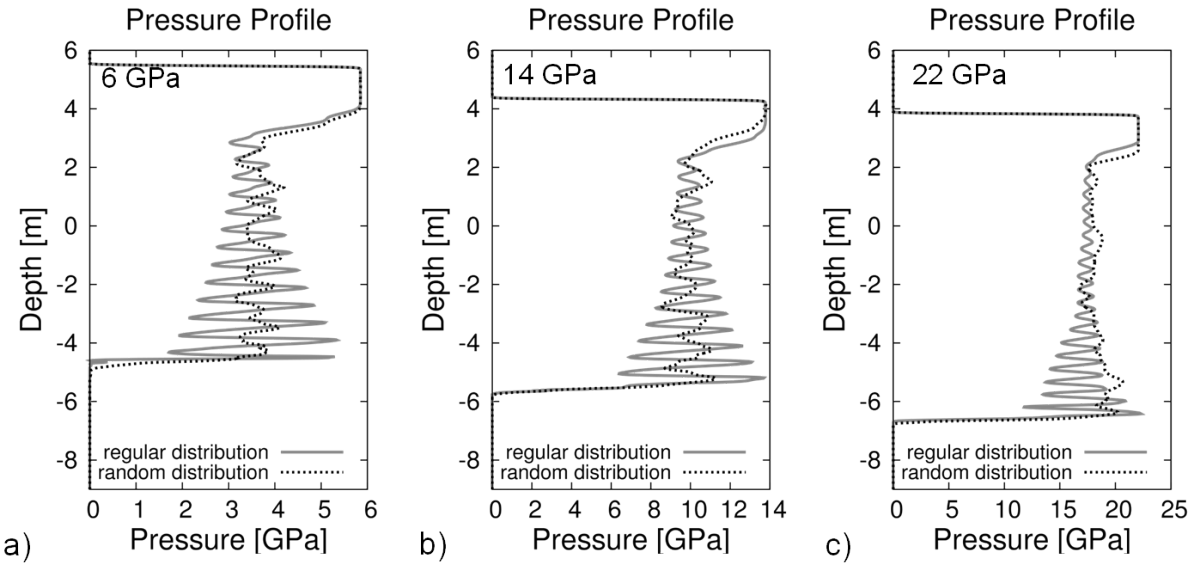

Figure 4.7: Comparison of pressure profiles for a random and regular distribution of pores in 2-D. The initial pressures are 6, 14, and 22 GPa from left to right. The profiles represent snapshots of shock wave propagation at the same point in time after impact of the flyer plate on the buffer plate. Zero depth represents the interface of the flyer and the buffer plate. The thickness of the flyer plate is identical in all cases. The dashed lines represent the random distribution, the solid lines the regular distribution.

4.4.3 Shock propagation in dry porous materials

If a shock wave propagates from solid material without pores (buffer plate) into porous material (sample), the shock pressure amplitude decreases at the interface due to the impedance contrast as a consequence of the reduced bulk density in the sample. The average shock amplitude is expected to decrease for the same reason, although we observe localized shock pressure amplification as a result of pore crushing. The crushing of pore space consumes shock wave energy; rarefaction waves originate from the pore interface (the pressure in an empty pore is zero) and interact with the primary shock wave. Overall, these processes lead to a decrease in the shock pressure amplitude in the sample. We quantified this process by modeling shock propagation at different amplitudes through a sample containing approximately 500 pores. The bulk porosity was varied between 0 % and 50 % by changing the size and number of pores. For a sample of 20 % porosity and a shock pressure amplitude in the buffer plate of 6, 14, and 22 GPa, the averaged pressures decreased to 3.4, 9.5, and 17 GPa. An example of a pressure profile for an initial shock pressure of 6 GPa is shown in Figure 4.8. The oscillations in the graph of the porous sample are caused by (1) local pressure amplifications and (2) rarefaction waves from the

pore interface. The locally observed shock amplifications are smaller compared with an isolated pore or an array of 3 or 12 pores as stated above due to interferences of reflections from adjacent pores and lower resolution. The local pressure amplifications reach values of over $20\,GPa$; however, this is in particular the case for the "first" pores in the grid that are crushed. The local pressure amplification decreases with the propagation of the shock wave. Different bulk porosities significantly affect shock wave propagation through the sample. The higher the porosity, the faster is the reduction in the shock wave amplitude in the sample. The presence of more pore space requires additional plastic work to crush out open pore space. The shock pressures and shock wave velocities are smaller for higher porosities. Figure 4.9 illustrates the effect of porosity on shock wave propagation in the $U_S - u_p$ space. Each symbol represents the result of a single mesoscale model for a given porosity and initial shock pressure. With an increase in porosity, the shock wave velocities decrease with respect to particle velocities. The discontinuity in the Hugoniot curve in the $U_S - u_p$ diagram represents a solid-state phase transition of quartz. To summarize, the propagation of a shock wave through a sample with a large number of resolved pores results in an overall decrease in shock pressure. In all experiments, the pore space is completely crushed out.

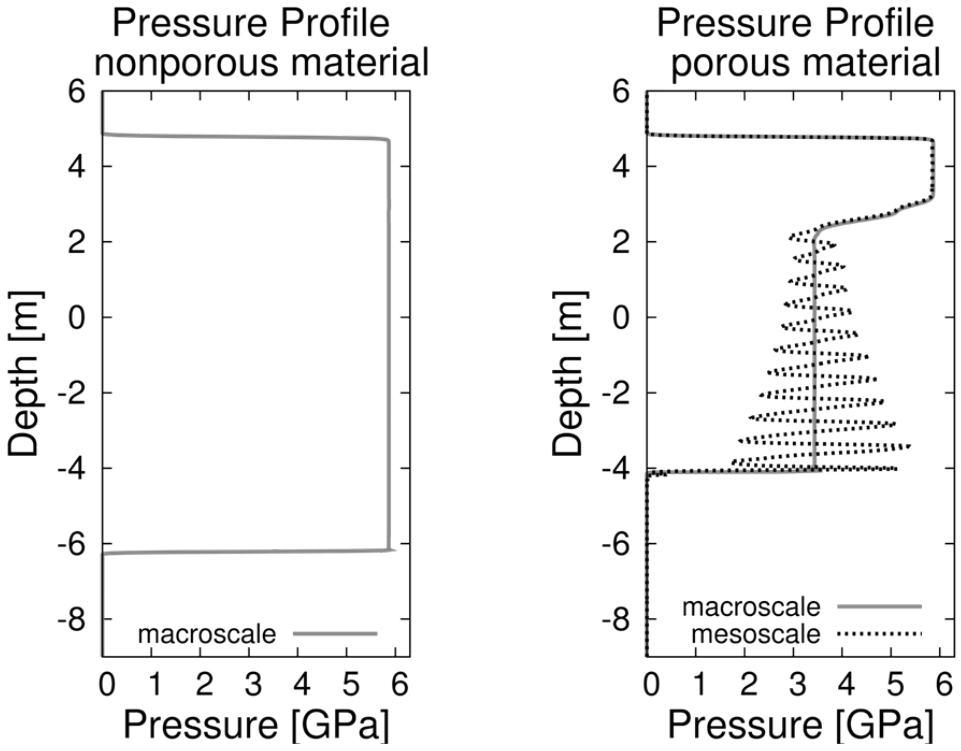

Figure 4.8: Comparison of pressure profiles through a nonporous (left) sample and porous (right) sample. Both profiles represent snapshots of shock wave propagation at the same point in time after impact of the flyer plate on the buffer plate. In the porous case (right), shock pressure is significantly decreased in the sample and the shock front propagates slower than in the nonporous case. In the porous case (right), the dashed line represents the mesoscale model; the solid line, the macroscopic model. Zero depth represents the interface of the flyer and the buffer plate.

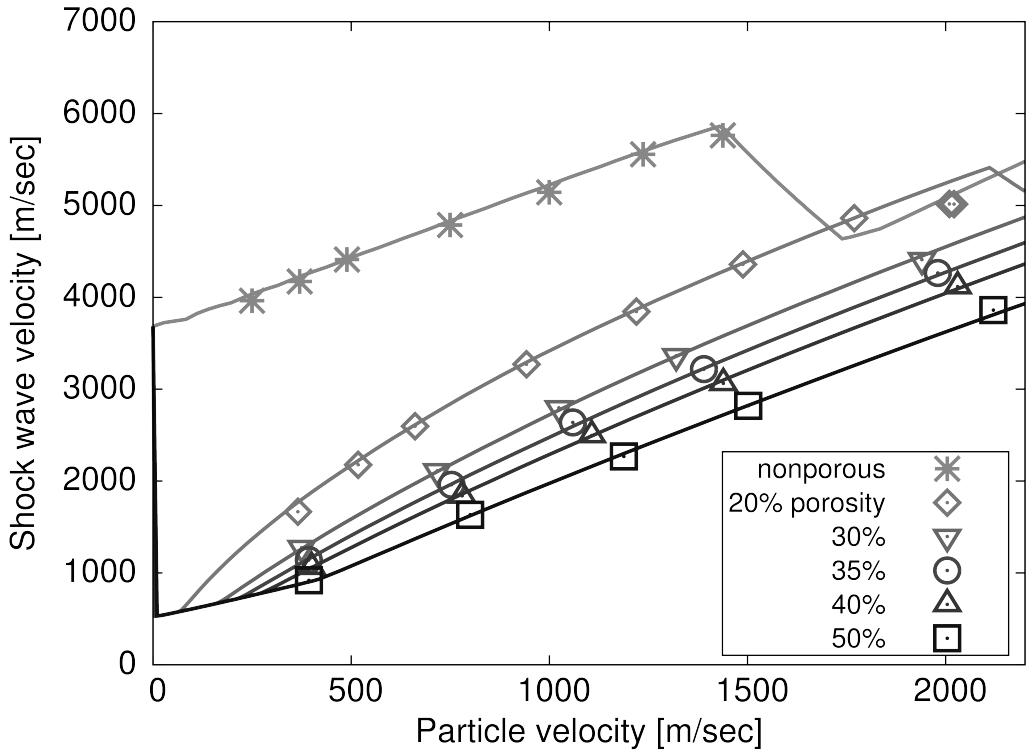

Figure 4.9: Hugoniot curves in the $U_S - u_p$ space for a nonporous quartzite and quartzite with different porosities. The points indicate data derived from mesoscale modeling. The lines indicate the Hugoniot data obtained by the macroscale model. The line for the nonporous material also includes a phase transition of quartz in the quartzite to the high-pressure phase stishovite. All data were obtained for a yield strength of $Y = 0$.

4.4.4 Effect of strength on shock propagation in porous material

For the results in the previous sections, we assumed that the strength of the matrix surrounding the pores is small in comparison with shock pressure and therefore negligible. However, to generate Hugoniot data for lower shock pressures, the resistance of the material against plastic deformation becomes important for the crushing of pores and, thus, for the propagation of shock waves. We carried out a suite of numerical experiments where we assumed a yield strength Y for the matrix of 1 and $0.5\,GPa$, respectively. The strength of the matrix can be considered as crushing strength of the pores. If strength is zero ($Y = 0$), the material behaves similar to a fluid allowing pores to close at small amplitudes of a compression wave. For $Y > 0$, crushing occurs if compression exceeds the yield strength of the matrix, or more precisely if $J_2 > Y^2$, where J_2 is the second invariant of the deviatoric stress tensor. The $U_S - u_p$ plot in Figure 4.10 (dashed lines, symbols) shows that the occurrence of an elastic regime depends on the yield strength of the matrix.

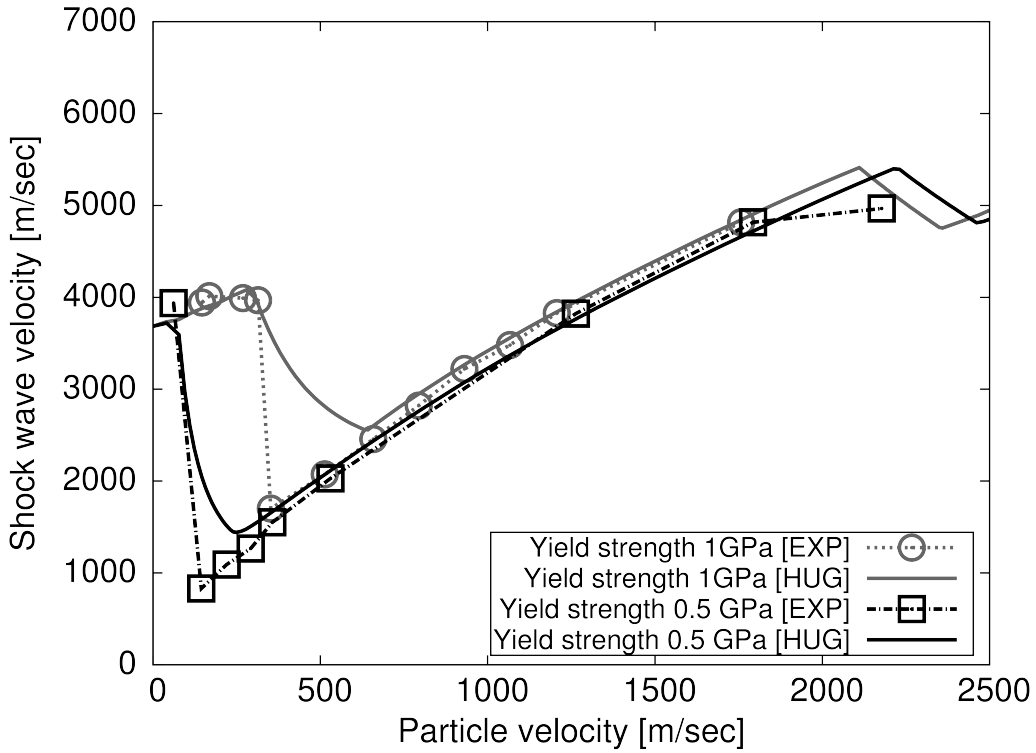

Figure 4.10: Hugoniot curves in the $U_S - u_p$ space for different yield strengths Y. The points indicate data derived from mesoscale modeling [EXP]. The lines indicate the Hugoniot data provided by the macroscale model [HUG] where values for $\varepsilon_e = -7.5 \cdot 10^{-2}$ corresponding to $Y = 1\,GPa$ and $\varepsilon_e = -3.0 \cdot 10^{-2}$ corresponding to $Y = 0.5\,GPa$ have been used (Section 4.4.6)

The onset of crushing pore space and plastic deformation is shifted toward higher particle velocities (higher shock pressures) with increasing strength of the surrounding matrix. The compaction of pores occurs very abruptly once the shock pressure is in excess of the yield strength. There is hardly any transitional regime recognizable where pores are closed only partially. This is due to a very short rise time of the shock front. In the mesoscale models with Y of $1\,GPa$, plastic deformation and crushing of pore space occur at a particle velocity u_p of $300\,m\,s^{-1}$ corresponding to a pressure P of $3\,GPa$, and for Y of $0.5\,GPa$, crushing of pores already starts at u_p of $80\,m\,s^{-1}$ corresponding to a pressure P of $0.8\,GPa$. The hydrodynamic material shows no resistance to pore crushing; plastic deformation starts immediately. In the plastic and shock wave regime, the curves for different strengths lie very close to one another confirming that strength is almost negligible for high shock pressures. Regarding the previously described pressure amplifications, yield strength has, therefore, no significant effect on the maximum pressure distribution.

4.4.5 Shock propagation in water-saturated material

The presence of water hampers the crushing of pores. Our mesoscale models of the propagation of a shock wave traveling through a sample, where the individually resolved pores are partially or completely filled with water, show that shock waves travel faster and with higher shock amplitudes through water-saturated material compared with a material with "empty" pore space (Figure 4.11). Figure 4.11 depicts a comparison of pressure profiles for the same instance in time for all three cases (100 % water saturation, 50 % water saturation, 0 % water saturation) as well as for the nonporous case. The initial shock pressure at the flyer-buffer plate interface was $6\,GPa$. In the 100 % and 50 % water-saturated case, the oscillations are not as prominent as in the dry case. The observed localized pressure amplification is smaller for the water-saturated sample as already stated above. Hugoniot data for the different cases of water-saturation are plotted in the $U_S - u_p$ space in Figure 4.12 (symbols represent the results from mesoscale modeling). The particle and shock wave velocities decrease by adding empty pore space. The fastest attenuation of the shock wave is observed in the case of a dry porous material. In all three porous cases shown in Figure 4.11, the porosity is 20 %. In the case of 100 % water saturation (all pores are filled with water), the volume of pore space changes only little and the absorbed energy due to plastic work carried out to close pores is much smaller compared with a dry target (all pores are empty). For an initial pressure of $6\,GPa$, about 80 % and for $22\,GPa$, only 45 % of the initial volume of water remains in the sample. A decrease in water volume

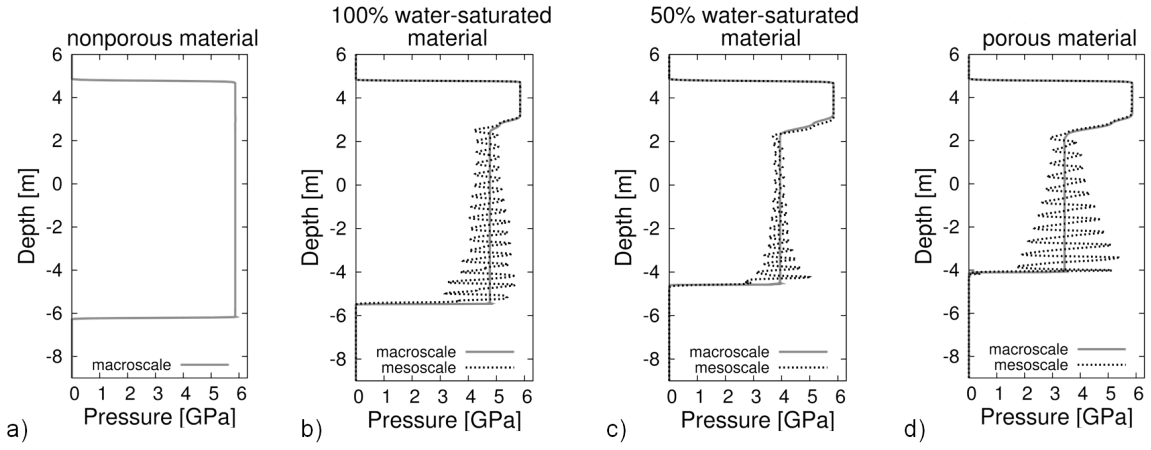

Figure 4.11: Snapshots of pressure profiles at the same point in time after impact of the flyer plate on the buffer plate through a) a nonporous, b) 100% water-saturated (all pore space is filled with water), c) 50% water-saturated (50% of pore space are filled with water, 50% are empty), and d) porous sample (all pore space is empty). The porosity in the sample is 25%. The initial shock pressure is 6 GPa. The dashed lines indicate data derived from mesoscale modeling; the gray solid line represents data from the macroscopic model. Zero depth represents the interface of the flyer and the buffer plate.

as response to shock loading is due to the compressibility of water. Thus, there is no mass-loss of water. An increase in initial pressure results in a larger reduction in pore space leading to an increase in pressure in water-filled pores. The partially water-saturated case (50 % of the pores are filled with water and the other 50 % are empty) represents a transition between the completely dry and wet cases. For an initial shock pressure of 6, 14, and 22 GPa, the pressure amplitude decreases to 4.8, 11.8, and 22 GPa in the fully water-saturated material. For shock pressure $> 22\,GPa$, the reduction in pressures is not observable anymore which might be caused by the fact that a significant amount of energy is converted into thermal energy.

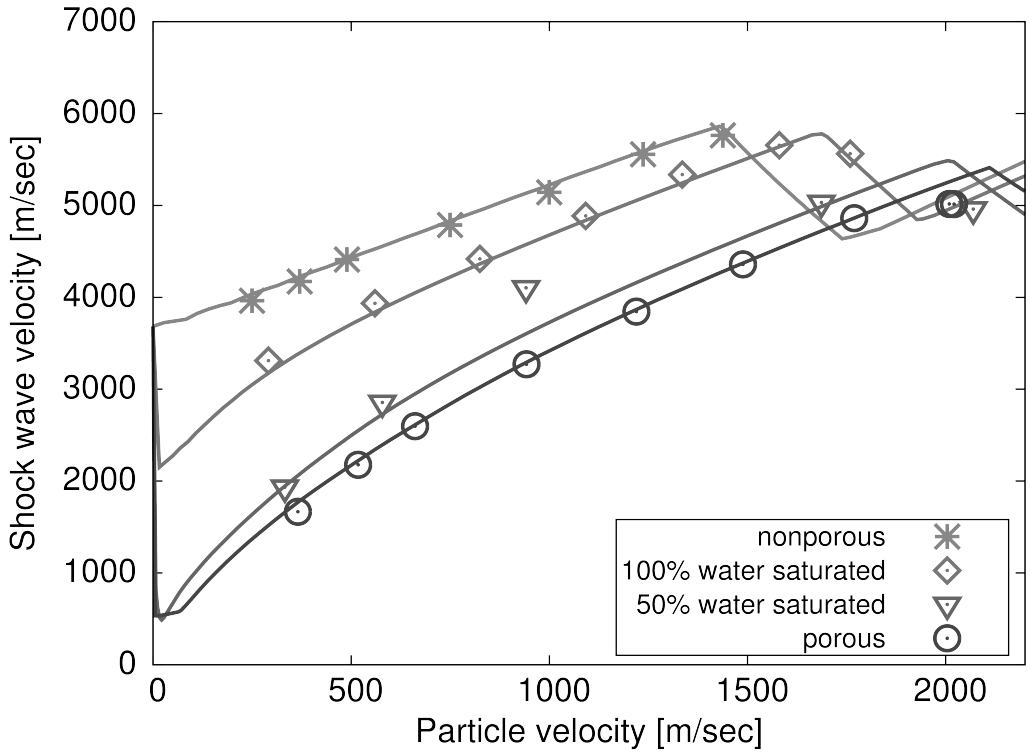

Figure 4.12: Hugoniot curves in the $U_S - u_p$ space for nonporous quartzite and quartzite of different degrees of water saturation. The symbols represent the data obtained with the mesoscale model the lines indicate Hugoniot data of the macroscopic model. The changes in slopes in the $U_S - u_p$ diagram are associated with a solid state phase transition of quartz, where the high pressure phase represents stishovite.

4.4.6 Comparison of meso- and macroscopic models

We compare the results from mesoscale modeling for different porosities, water saturation, and strength of the matrix with macroscopic (or homogenized) material models describing the bulk behavior of porous and mixed (water + quartzite) material that have been

proposed before (Pierazzo *et al.*, 2005; Wünnemann *et al.*, 2006). Figure 4.11 illustrates that both model approaches provide similar results for shock wave pressure and propagation velocity through the porous sample by averaging the pressures in the mesoscale simulation. Generally, we find a very good agreement in terms of Hugoniot data in $U_S - u_p$ space between the macroscopically determined data and data obtained from the mesoscale models as shown in Figures 4.9, 4.10, and 4.12. A similar good match was achieved when comparing other thermodynamic state parameters such as pressure, density, and internal energy. In the case of 100 % water-saturated pores, the models confirm that ANEOS for a quartzite-water mixture assuming thermodynamic equilibrium between the water and the quartzite phase is a reasonably good approximation to describe material behavior. This implies that the crushing of pore space is insignificant, although the water content changes due to the compressibility. However, we do not allow the water to flow or steam into the matrix material. To compare meso- and macroscale models for low shock pressures where material strength plays an important role, the crushing strength Y of the matrix in the mesoscale models has to be related to the elastic threshold strain ε_e (material parameter for ε–α model). Crushing first occurs if the stress exceeds the yield strength Y of the matrix. According to the constitutive model as described in Section 4.2.1, this is given if the square root of the second invariant of the deviatoric stress tensor is equal to or larger than Y ($J_2 > Y^2$). For simplicity, we made use of a von Mises yield criterion (Y is constant and does not depend on deformation history (damage), pressure, or temperature to derive a relationship between the macroscopic and mesoscopic parameters. We are aware of the fact that the von Mises criterion is not typical for rock materials. However, a constant yield strength allows for direct analytic comparison between the elastic threshold parameter in the macroscale model (ε–α model) and the yield strength of the matrix in the mesoscale model. A more complex material model requires at least three or more parameters that are difficult to compare with the single parameter ε_e, in the ε–α model. The next step would be to use a more realistic material model to analyze the relationship between ε_e and other macroscopic strength parameters such as the coefficient of friction and cohesion in intact and damaged state (Collins *et al.*, 2004). This would require additional extensive parameter studies which are beyond the scope of this paper. According to Hook's law, a constant strength of $1\,GPa$ yields an elastic threshold strain of 0.071 using an elastic modulus (Young's modulus) of $14\,GPa$ that was determined by laboratory experiments for Seeberger sandstone as used in the MEMIN cratering experiments (Kenkmann *et al.*, 2011; Moser *et al.*, 2013). At the onset of plastic yielding (crushing of pores), the strain is given by

$$\varepsilon_e = \frac{Y}{E} \tag{4.1}$$

where ε_e can be considered as the elastic threshold strain, Y is the yield strength of the matrix and corresponds to the crushing strength, and E is Young's modulus. From a series of numerical experiments fitting the macroscopic and mesoscopic modeling results, we obtained an elastic strain threshold of 0.075 assuming a constant yield strength of $1\,GPa$. We consider the deviation between the empirically determined value of 0.075 and the analytically derived 0.071 as small. Similar good results were obtained for a smaller yield strength of $0.5\,GPa$ where we obtained an elastic strain threshold of 0.030, which only slightly deviates from the empirically determined value of 0.036. The results suggest that the volumetric crushing strain ε_e as an important input parameter in the ε–α compaction model for porous material can be derived from the yield strength of the grains supporting the porosity. However, the yield strength of individual grains does not correspond to the strength of a larger unit of the same material. Yield strength is a scale-dependent parameter. On the scale of the formation of craters in the framework of the MEMIN experiments (Kenkmann *et al.*, 2011; Schäfer *et al.*, 2006), the resistance of the material against plastic deformation is usually much softer (smaller yield strength of about $50\,MPa$) than the stated crushing strength. A meaningful relationship for strength on different scales is still lacking.

4.5 Discussion

The MEMIN project focuses on impact cratering in porous, dry, partially or completely water-saturated sandstone. The Seeberger sandstone used in the impact cratering experiments serves as an analog material representative for crater formation, for instance, in sedimentary targets on Earth. The heterogeneous character on the scale of pores and grains is in particular a challenge for numerical modeling of crater formation and shock wave propagation in sedimentary material. Detailed investigation of porous materials with some water content and their response to shock wave loading are lacking so far. Models of different scales (meso- and macroscales) are complementary. The macroscale models enable the simulation of the entire cratering processes, whereas the mesoscale models enable a detailed analysis of localized processes during shock compression. We find a good agreement between macroscopic and mesoscopic data. The comparison between meso- and macroscopic models demonstrates that for a sufficiently long duration of the shock plateau (covering an area of several pores), the effect of pore size, distribution, and geometry on shock propagation is negligible. For low shock pressures, the yield strengths of the matrix in the mesoscale models can be related to the volumetric threshold strain at the onset of pore crushing in the ε–α macroscale porosity compaction model. We find good agreement for the elastic and plastic regime for the mesoscopic and macroscopic approach (Figure

4.10). However, in the mesoscale model, the transition from the elastic to crushing regime is very abrupt, while a much more gradual transition can be observed in the macroscopic model. Any "smoothing" of the transition in the mesoscale models by using a more sophisticated strength model to describe material failure of the matrix was not successful. Once the stress amplitude of the compression wave exceeds the yield strength, pores are crushed out instantaneously, which presumably is caused by a very short rise time of the shock front. Complementary to our numerical approaches to determine Hugoniot data for sandstone, we compared our modeled Hugoniot data results with experimental data determined from laboratory shock experiments with Seeberger sandstone carried out in the framework of this study and Hugoniot data from the literature for Coconino sandstone (compiled in Ahrens and Gregson, 1964; Shipman *et al.*, 1971; Stöffler, 1982). Despite the slight variations in porosity and composition, we find a good agreement as shown by the Hugoniot curve in the pressure-specific volume space in Figure 4.13. The good correlation among experimental, meso-, and macroscale model data justifies the applicability of our mesoscale approach to test the macroscopic models describing dry and wet porous material and, in particular, partially water-saturated porous sandstone where the ε–α model has been combined with ANEOS for a water-quartzite mixtures.

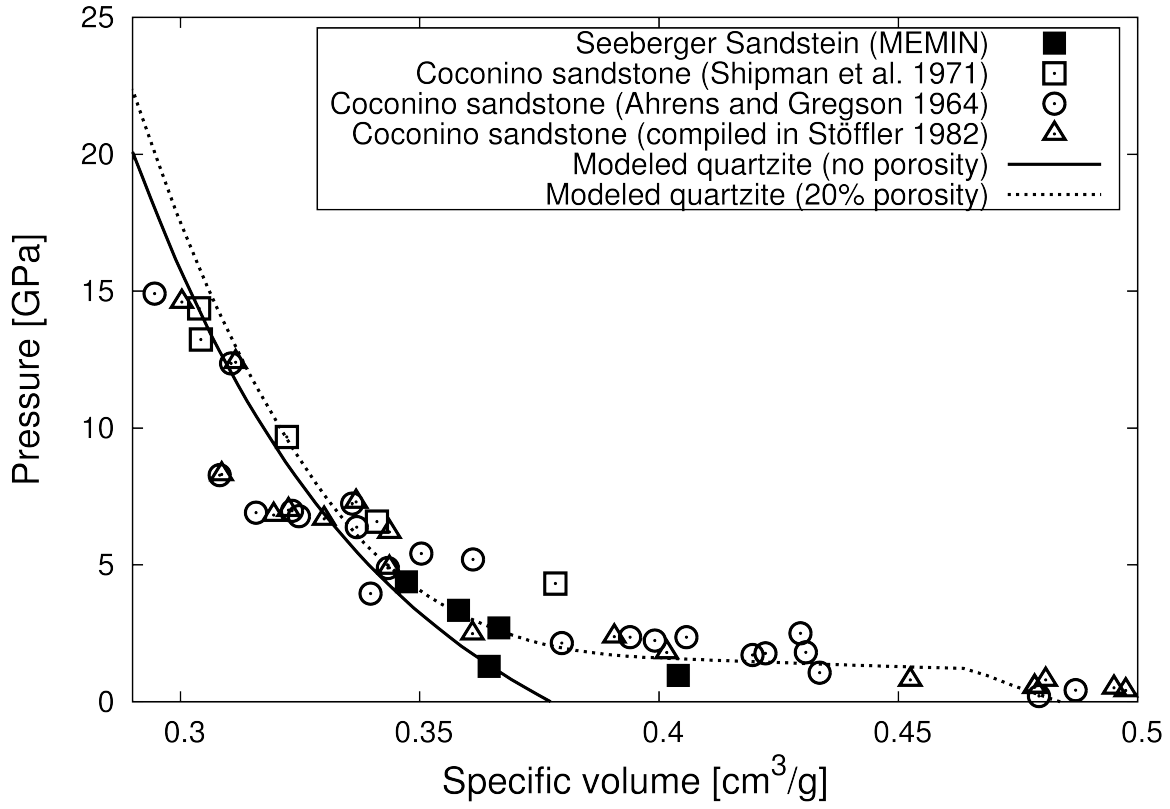

Figure 4.13: Comparison of numerical modeling results of quartzite material and laboratory shock experiment data showing Hugoniot curves in the $P - V$ space. The numerical modeling results are shown with lines; the shock experimental data are indicated by symbols.

In addition to the Hugoniot data, the MEMIN cratering experiments provide important standards the models can be tested against, and also serve for quantitative explanations for some unexpected observations. The quantification of shock amplification due to pore space collapse using mesoscale modeling is in good agreement with observations in shock experiments in dry sandstone at low shock pressures (5.0–12.5 GPa; Chapter 5 of this thesis). The experiments were carried out to identify and calibrate shock features in weakly shocked Seeberger sandstone (Kowitz *et al.*, 2013b). Despite low shock pressures (10 GPa), diaplectic glass was observed that forms in single crystal quartz at about 35 GPa (Stöffler and Langenhorst, 1994). The mesoscale models show that an amplification by a factor of 3–4 can occur in the vicinity of a pore, which is in excellent agreement with the observation of shock features representative for shock conditions 3.5 times the initial shock pressure. The amplification of shock pressure due to pore collapse as quantified in the mesoscale models also helps to understand the generation of small vapor and melt phases during the very first contact between the projectile and the target and provide important insights on the observation of planar deformation features in the ejecta of the MEMIN experiments (Ebert *et al.*, 2013). For the determination of peak pressure amplification using mesoscale models, we assumed that at least 20 % of the initial pore volume has experienced the amplified pressure conditions. The limitation of 20 % is chosen to satisfy the required resolution to obtain reliable results. However, very small volumes that undergo even higher pressures are conceivable, but cannot be resolved in our models. To model the crushing behavior of a given material accurately, direct measurements of either crushing curves (ε_e in macroscale ε–α model) or the strength of the matrix (yield strength Y in mesoscale models) are required. Detailed observations of pore space compaction underneath the MEMIN craters (Buhl *et al.*, 2013) enable an indirect measurement of the crushing behavior. By fitting the numerical models to porosity curves as a function of depth from the MEMIN experiments, crushing parameters for the modeled porous material can be obtained. However, the numerical simulations consider shock compression only. The release from shock pressure has not been considered in the macro- and mesoscale models in the present work. The change in porosity with depth underneath the crater in the MEMIN experiments shows that tensile bulking causes an increase in porosity at the near subsurface of the crater. To account for the gain in porosity as a result of shock unloading, further work is required. In fact, shear and tensile stresses may yield an increase in porosity. First preliminary results are shown in Collins *et al.* (2011b) and Güldemeister *et al.* (2013). Our work also showed that a combination of the ε–α model and an ANEOS for mixtures is applicable and enables the simulation of partially water-saturated materials. The mesoscale modeling approach is a direct way to describe shock wave propagation in porous sandstone with different degrees of water saturation (0, 50, and 100 % water filling). The results are thermodynamically consistent with the macroscopic models using the ε–α

model (0 % water filling), the ANEOS for material mixtures (100 % water filling), and a combination of both (e.g. 50 % water filling). We always assume that the water content remains constant in the computational cell. This does not account for the subsequent release in material mixtures and effect of flowing or steaming of water through the matrix material. In the framework of the MEMIN experiments, it was not possible to confirm whether this assumption holds true. In fact, the pore water disappeared in the direct proximity of the crater. Apparently, water can escape in case of very high shock pressures. It is unclear whether the process is dominated by thermal expansion of water vapor in the pore or by tensile fracturing and opening of pores. Further improvements for a more accurate treatment of material mixtures at high shock pressures and subsequent release are required.

4.6 Conclusion

To simulate laboratory cratering experiments in the framework of the MEMIN project, a detailed description of the thermodynamic behavior of porous sandstone with different water contents was required. We conducted a series of numerical simulations on the meso- and macroscales to study the effect of porosity and water-filling on shock wave propagation. The mesoscale models provide details on single pore collapse and the bulk response of a set of pores to shock propagation. The results from mesoscale models with previously proposed macroscopic models for the crushing of dry porosity (ε–α crushing model) and water-saturated porosity (ANEOS for material mixtures) are in good agreement. Thus, the propagation of shock waves through a porous material sample that is represented by a homogeneous unit where porosity is a state variable agrees very well with the one through a sample which explicitly resolves a finite number of pores. While the former approach allows for direct measurement of Hugoniot data (particle velocity, shock wave velocity), in the latter case, thermodynamic parameters vary due to the heterogeneous distribution of pores and Hugoniot data have to be determined by averaging over a representative area. The models show that the crushing of pore space is an effective mechanism for absorbing shock wave energy leading to a faster decay of the shock wave. In contrast, the closure of pores causes localized amplification of shock pressure in the vicinity of a single pore. The effect decreases slightly if several pores are located close to one another and reflections of shock and rarefaction waves originating from the pores superimpose. Furthermore, shock waves travel faster through water-saturated material than through porous material, and water-saturated pores are only slightly compacted compared with empty pores that are completely closed. Macroscopic models and laboratory experiment data showed a very good agreement in terms of Hugoniot data supporting applicability and accuracy

of our modeling approach. Mesoscale models of shock wave propagation in partially water-saturated material are also consistent with a novel approach of combining the ε–α crushing model for dry porosity and ANEOS for water-quartzite mixtures. Therefore, we conclude that this is a valid approach to describe the thermodynamic behavior of partially water-saturated material during shock wave compression.

Acknowledgments

This research is part of the MEMIN program supported by the German Science Foundation DFG (Research Unit FOR-887; WU 355/6-1). We are grateful to N. Artemieva for providing ANEOS data for water-quartzite mixtures and for her help with the ANEOS model. We thank J. Melosh and an anonymous reviewer for their constructive reviews. We also thank A. Deutsch for helpful comments on the manuscript.

Editorial Handling – Dr. Alexander Deutsch

5 Laboratory observations during shock experiments in porous sandstone and mesoscale modeling

This chapter represents parts of the following peer-reviewed article that has been published in:

Kowitz A., Güldemeister N., Reimold W.U., Schmitt R.T., Wünnemann K., 2013. *Diaplectic quartz glass and SiO_2 melt experimentally generated at only 5 GPa shock pressure in porous sandstone: Laboratory observations and meso-scale numerical modeling.* Earth and Planetary Science Letters 384, 17-26, https://doi.org/10.1016/j.epsl.2013.09.021.

The title of the chapter has been shortened and changed slightly in comparison to the originial publication in order to emphasize on the main content of this chapter.

Abstract

A combination of shock recovery experiments and numerical modeling of shock deformation in the low pressure range from 2.5 to 17.5 GPa in dry, porous Seeberger sandstone, a completely water-saturated sandstone, and a well-indurated quartzite provides new, significant insights with respect to the heterogeneous nature of shock distribution in such important, upper crustal material, for which too date no pressure-calibrated scheme for shock metamorphism exists. We found that pores are already completely closed at 2.5 GPa shock pressure. Whole quartz grains or parts of them are transformed to diaplectic quartz glass and/or SiO_2 melt starting already at 5 GPa, whereas these effects are not observed below shock pressures of 30–35 and $\sim$ 45 GPa, respectively, in shock experiments with quartz single crystals. The appearance of diaplectic glass or melt is not restricted to the zone directly below the impacted surface but is related to the occurrence of pores in a much broader zone. The combined amount of these phases increases distinctly with increasing shock pressure from 0.03 $vol.\,\%$ at 5 GPa to $\sim$ 80 $vol.\,\%$ at 17.5 GPa.

Numerical modeling at the meso-scale provides the explanation for the discrepancy of shock deformation in porous material and single-crystal quartz, in keeping with our experimental results. It confirms that pore space is completely collapsed at low nominal pressure and demonstrates that pore space collapse results in localized pressure amplification of up to 4 times the initial pressure. This provides an explanation for the formation of diaplectic quartz glass and lechatelierite as observed in the low-shock pressure experiments. The numerical models predict an amount of SiO_2 melt similar to that observed in the shock experiments. This also shows that numerical models are essential to provide information beyond the experimental capabilities.

5.1 Introduction

The progressive shock metamorphism of porous sandstone shows characteristic differences to that of quartz single crystals and quartzite, as summarized by Grieve *et al.* (1996). Besides the coexistence of various shock deformation effects that would be equivalent to very different shock pressures in non-porous rocks, a characteristic observation in shocked sandstone is the occurrence of diaplectic quartz glass and the high pressure phases stishovite and coesite already at comparatively low shock pressures (Kieffer, 1971; Kieffer *et al.*, 1976; Grieve *et al.*, 1996). Despite the apparent discrepancy an experimental investigation and calibration of the shock metamorphism of porous sandstone is still missing. The low shock pressure regime is particularly interesting as it is representative for the vast majority of rocks at, and in the vicinity of, impact structures. After a first report addressing this topic and highlighting the occurrence and development of shock features (Kowitz *et al.*, 2013b), we present here additional results of an extended study comprising a new set of seven shock recovery experiments with dry, porous sandstone in the low shock-pressure range from 2.5 to 17.5 GPa. In this context we have focused on two of the most important shock features: the development of diaplectic quartz glass and of SiO_2 melt, which both appear in porous sandstone (Kowitz *et al.*, 2013b) at much lower shock pressures compared to shock deformation of quartz single crystals where these effects are observed at $30 - 35$ and $45\,GPa$, respectively (e.g. Stöffler and Langenhorst, 1994). The aim of this work is to elucidate the causes for this discrepancy and to show that in porous material shock deformation deviates from that in dense, nonporous targets.

The laboratory impact experiments reported here were accompanied by meso-scale numerical modeling in order to gain insight into dynamic processes that can not be explained by static observations. The meso-scale models are able to resolve the response to shock of single pores and provide a description of pore collapse under shock loading, and a quantification of pressure amplification during shock propagation. Local effects may play

a significant role, which could be caused by the heterogeneity of the target material given by the presence of open pore space.

A strong collaborative work of laboratory shock experiments as part of Project 7 *"Low shock recovery experiments in sandstone"* within the MEMIN project and numerical modeling on the mesoscale is presented in this chapter.

5.2 Methods

5.2.1 Shock recovery experiments

Seven shock recovery experiments were conducted at the Fraunhofer Institut für Kurzzeitdynamik (Ernst-Mach-Institut), Efringen-Kirchen Division, Germany. Target specimens were cylinders ($\varnothing\, 1.5\, cm$, length $2\, cm$) of dry Seeberger sandstone (layer 3; grain size: $\sim 0.10\, mm$, porosity: $25 - 30\, vol.\%$, quartz content: $\sim 89\, vol.\%$; pore size: $20 - 100\, \mu m$). These experiments were carried out with a high-explosive driven flyer plate set-up (Figure 5.1) generating a single plane shock wave propagating into the sandstone cylinder (see also Kowitz *et al.*, 2013b; Stöffler and Langenhorst, 1994). Shock pressures of 2.5 to $17.5\, GPa$ at the top of the sample were achieved by different combinations of high explosives and thicknesses of the flyer and driver plates. The precision on shock pressure determination in the ARMCO iron driver plate is about $\pm 4\%$. Shock pressure in the sample is determined by graphic impedance matching (e.g. Langenhorst and Hornemann, 2005; Thoma *et al.*, 2005) using the Hugoniot data for Coconino sandstone (compiled in Stöffler (1982), and additional data of Shipman *et al.* (1971)). We had to revert to the Hugoniot data for Coconino sandstone because such data were not available for Seeberger sandstone yet. Therefore, the total error of pressure determination is estimated to be in the order of $\pm 1\, GPa$. High-quality polished thin sections were prepared for petrographic analysis. They were cut from the target cylinders parallel to the propagation direction of the shock front, parallel to the long axis and through the center of the shocked sandstone cylinders. Observations reported here were made only in the uppermost central part of the target slices, generally within areas of $\sim 5\, mm$ width and $\sim 300\, \mu m$ height. In deeper parts and near the outer edge of the sandstone cylinders interactions of different shock waves occur caused by reflections from the steel target chamber, which lead to localized pressure variations (see Kowitz *et al.*, 2013b); therefore, these areas were excluded from this study. All analytical work was carried out at the laboratories of the Museum für Naturkunde, Berlin. For quantification of diaplectic glass and melt amounts the image analyzing soft-

ware JMicroVision 1.2.7 was utilized in two different ways: 1. for marking individual small areas by hand (lower pressure experiments) and 2. for marking the areas automatically by utilizing gray-scale differences (higher pressure experiments). Micro-Raman spectroscopy was employed to identify diaplectic quartz glass and other SiO_2 phases (McMillan *et al.*, 1992; Fritz *et al.*, 2011).

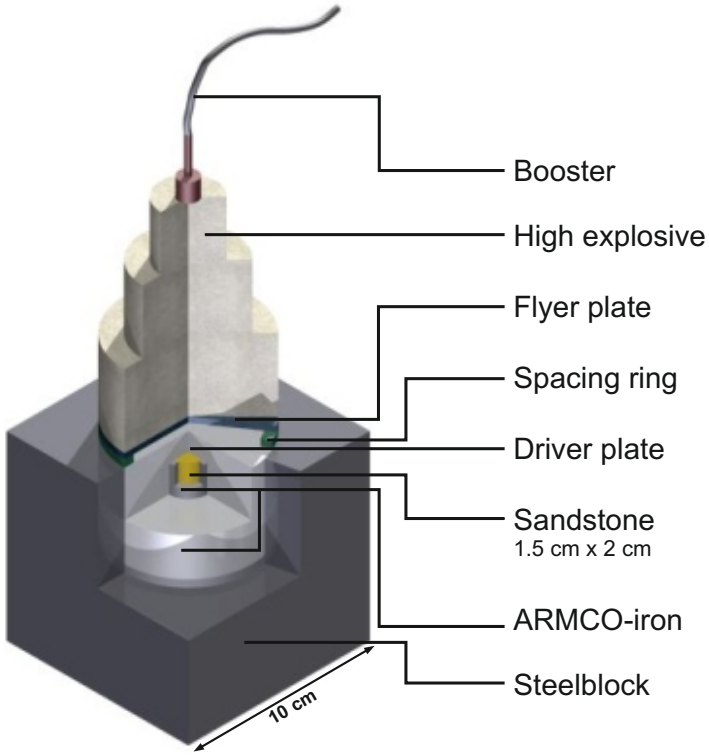

Figure 5.1: Experimental set-up for the shock recovery experiments with high explosives, outer steel block (momentum trap), ARMCO iron flyer plate, spacing ring of acrylic glass (diameter 64 mm, height 10 mm, wall thickness 4 mm), and inner ARMCO iron cylinder (diameter 48 mm, height 50 mm) containing the sandstone sample.

5.2.2 Numerical modeling of shock experiments

The setup of the numerical model is very similar to the model described in Chapter 4 and is already shown in Figure 4.1 of Section 4.2.3. Thus, we used again a planar model consisting of an accelerated flyer plate that impacts onto a buffer plate generating a planar shock wave, which then propagates through a sample containing resolved pores. Here we varied the impact velocities of the flyer plate between 700 and 2500 $m\,s^{-1}$ to generate shock pressures of 2.5 and 17.5 GPa in the sandstone sample according to the determined nominal pressures in the laboratory experiments. In these simulations the

flyer and iron plate consist of iron, the matrix surrounding the individual empty pores consists of quartzite. To account for plastic material failure of the quartzite matrix we made use of a simple von Mises yield criterion. The von Mises model defines a constant stress which has been set to $1\,GPa$ for the matrix in these simulations.
For the purpose of the analysis of the described experimental features we focused on two distinct setups. Firstly, the collapse of single pores, or an array of 12 pores, have been evaluated, whereby each pore was resolved by 60 $\times$ 60 computational cells, to quantify localized pressure amplifications during pore collapse. Secondly, the setup made use of a sample with a large number of pores, with each pore resolved by 8 $\times$ 8 up to 20 $\times$ 20 cells, representing the same porosity as used in the experiments to investigate the interaction of collapsing pores and the overall pressure distribution within the sample as response to shock loading. Here, we allowed an irregular distribution of pores where pore sizes may differ, always ensuring that the sample porosity is the same as in the experiments. This numerical approximation can be considered as a good representation of a natural porous sandstone sample as used in the shock experiments. The influence of pore distribution and resolution has already been discussed in detail in Güldemeister *et al.* (2013) (Chapter 4 of this thesis). Besides the visual investigation of processes occurring during pore collapse, the numerical models further enable the recording of several thermodynamic parameters during shock propagation through the sample as already described in Section 4.2.4. Thus, we can gain quantitative information about local pressure amplifications as well as qualitative information about the amount of material experiencing a certain pressure maximum to enable a comparison with the experimental results in terms of the production of melt due to pore space collapse.

5.3 Results and interpretation

5.3.1 Pore collapse

Backscattered electron (BSE) microscopic images demonstrate that in the shock recovery experiments the original pores (black areas in Figure 5.2a) are already entirely closed at a shock pressure of only $2.5\,GPa$ (Figure 5.2b). For comparison, numerical meso-scale models resolving 12 single pores were utilized (Figure 5.2c). In agreement with the observations made on the experiments, the models show that for an initial pressure of $2.5\,GPa$ all pore space (black areas) is immediately collapsed as response to shock loading. Thus, the process of complete collapsing of pore space is assumed to result in all shock phenomena

which are described in this chapter.

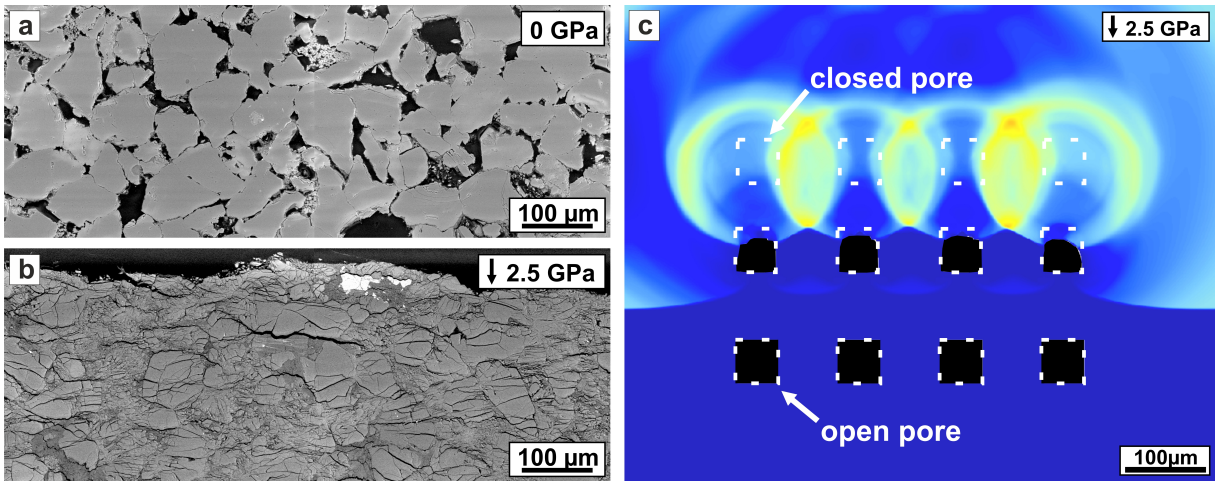

Figure 5.2: Comparison of quartz in BSE images of (a) unshocked and (b) shocked (2.5 GPa) Seeberger sandstone. Note the total closure of pore space (black areas in a) in the shocked sample (b). (c) Meso-scale model (pressure distribution) of collapse of an array of 12 pores at an initial shock pressure of 2.5 GPa. The figure represents an intermediate step when the shock wave has reached the second row of pores. The white squares show the initial position of the pores. The material surrounding the pores consists of quartzite. Open pore space (black areas) is completely collapsed after shock propagation.

5.3.2 Appearance of diaplectic quartz glass and SiO_2 melt formation in the shock experiments

In our experiments, the formation of diaplectic quartz glass and/or SiO_2 melt starts at grain boundaries, and the extent of diaplectic glass and/or molten areas increases with increasing shock pressure. At relatively low initial pressures (5–7.5 GPa) the occurrence of such areas is restricted to very small zones ($\sim$ 200–500 μm^2), which are clearly related to intergranular contacts (compare Figure 5.3a). At higher pressures (10–12.5 GPa) these zones are enlarged drastically. Boundary areas between quartz grains can be completely transformed to diaplectic glass or melt, and fractured cores of quartz grains are now filled with melt. At pressures of 15 to 17.5 GPa interconnected grains are affected by this widening of transformation zones until their complete transformation to diaplectic glass or melt has been achieved. In the samples shocked to 12.5–17.5 GPa, quartz grains also show development of more or less abundant sets of differently orientated planar deformation features (PDF). In the shock experiments the occurrence of diaplectic quartz glass and SiO_2 melt is not restricted to the material directly beneath the impacted surface but also develops in deeper parts of the studied area corresponding to a regime of slightly reduced

shock pressure. In the experiments starting at $5\,GPa$ high-resolution images show small areas filled with SiO_2 melt located at the origin of radiating fractures (Figure 5.3a). This

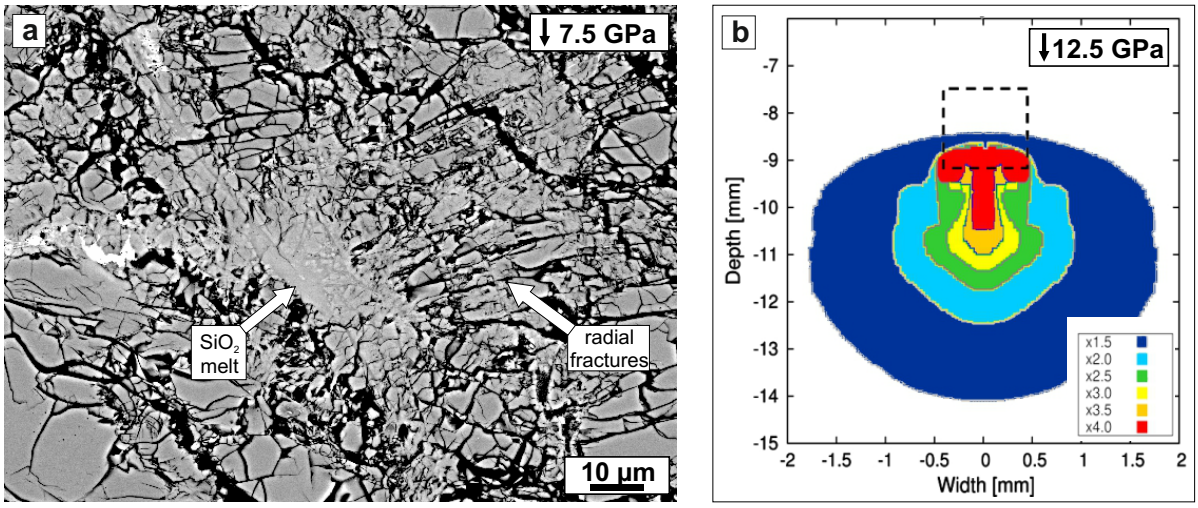

Figure 5.3: a) Center of a crush zone at the locus of a pre-existing pore, filled with SiO_2 melt. Radiating fractures have their origin in this center indicating collision of two or more quartz grains (BSE image). b) Peak pressure distribution after shock propagation for a single pore using meso-scale numerical modeling. The dashed line shows the original position of the pore. The initially applied shock pressure was $12.5\,GPa$. The colored contour lines show the different amplifications from 1.5 to 4 times the initial shock pressure. The highest amplification is 4 times the initial pressure.

clearly indicates locations of pre-existing pores that are now closed. The resulting collision of quartz grains and interference of shock waves obviously leads to enhanced pressures and temperatures, and therefore to the development of glass or melt.

To confirm these observations and to analyze the effect of open pore space on shock propagation in detail we have made use of numerical modeling. We investigated how the shock wave propagates around a single pore and how the collapse of pore space leads to local pressure amplification. The modeled pore (Figure 5.3b) has a quadratic cross section and is located on the symmetry axis of a 2D cylindrical grid. When a planar shock wave travels through a sample with a single resolved pore, at one point in time the shock front hits the boundary of the pore where it is converted to a rarefaction wave leading to instantaneous unloading of shock pressure. With further propagation the volume of the pore decreases gradually. At the time when the pore is completely closed, a secondary shock wave is generated that propagates roughly spherically outward from the original center of the pore. This secondary shock wave superimposes the release wave and the initial shock wave, resulting in pressure amplification in the material directly around the pore (compare Güldemeister *et al.*, 2013). Figure 5.3b shows the maximum pressure distribution relative to the initial pressure after the collapse of a single pore. Note that the material, and thus the respective tracer, experienced a relative downward motion. The recorded pressure amplification can exceed 4 times the initial pressure for the pressure

range used in the shock experiments (Figure 5.3b). Pore collapse during shock loading can lead to the formation of melt as the initial pressure of $12.5\,GPa$ that was used in the presented model is locally amplified to $60\,GPa$. The highest pressures can be observed in the zone where the pore was initially located.

5.3.3 Pressure clouding

In the shock recovery experiments the spatially resolved distribution of shock pressure was investigated by Raman spectroscopy. The variation of determined Raman spectra is illustrated in Figure 5.4a. The range of observed spectra (Figure 5.4a) clearly shows a progressive change with increasing shock pressure leading to the spectrum of diaplectic quartz glass, which is totally different from that of unshocked crystalline quartz. These characteristic changes of the spectra allow us to determine spatially resolved shock pressure distributions within the studied areas for each shock experiment. The observed areas were systematically mapped by Raman spectroscopy with special attention to homogeneous, unfractured areas. Note that the spatially resolved shock pressure values based on the appearance of the Raman spectra (Figure 5.4a) are for many measurement points higher than the nominal shock pressures of the different experiments.
For a systematic evaluation, the different Raman spectra were classified into five groups that represent the shock pressure ranges of 0, 1–23, 24–27, 28–35, and $\geqq 36\,GPa$, respectively. Figure 5.4b illustrates the distribution of these five ranges in the targets of our experiments with 5 to $17.5\,GPa$ nominal shock pressures. The number of spectra for undeformed quartz ($0\,GPa$, blue bars) decreases with increasing pressure, and disappears at 17.5 GPa. In contrast, the loci with spectra indicating pressures of 1–$23\,GPa$ (green bars) are first noted at $7.5\,GPa$. Their number increases to $12.5\,GPa$, and then decreases to $17.5\,GPa$. The spectra characteristic for pressures of 24–$27\,GPa$ (yellow bars) first appear at $10\,GPa$, their number increases to $15\,GPa$, and then decreases towards $17.5\,GPa$. The two other groups with spectra indicating 28–$35\,GPa$ (orange bars) and $\geqq 36\,GPa$ (red bars), respectively, first occur at $12.5\,GPa$, and then increase in number to $17.5\,GPa$. In general, the occurrence of these five groups of Raman spectra within the experiments displays a progressive sequence. In the experimentally shocked specimens Raman spectra typical for lower shock pressures start to occur, achieve their peak, and disappear at lower experimental shock pressures than Raman spectra characteristic for higher shock pressures. The most important conclusion from these observations is that, beginning at $10\,GPa$, a large number of quartz grains indicate by their Raman spectra shock pressures much higher than the nominal value for a given experiment. For example, at a nominal pressure of

$17.5\,GPa \sim 90\,\%$ of the Raman spectra indicate pressures $\geqq 24\,GPa$. The grains showing these spectra do not necessarily border directly on pre-existing pores, and should therefore not be directly affected by an increased pressure/temperature peak due to pore space collapse. The heterogeneous distribution of the spatially resolved Raman measurements is exemplified in Figure 5.4d. This figure displays an area of $\sim 2.2\,mm$ width at the center of the sample shocked to $12.5\,GPa$. It is obvious that areas of diaplectic quartz glass (red dots) are not restricted to the uppermost impacted surface but seem to be randomly distributed in deeper parts of this area as well. Furthermore, it is interesting that quartz grains with spectra indicating undeformed quartz are situated at the uppermost surface although this represents the impacted area. This image demonstrates that all groups of Raman spectra representing different shock pressure ranges exist in this area. However, most of them indicate shock pressures higher than $12.5\,GPa$, the initial shock pressure of this experiment. The numerical models support the implications from the shock experiments. They have shown that for porous material an overall decrease of shock pressure is observed for the onset of development of certain shock effects, but that also localized pressure amplifications due to single pore collapse occur. In the case of a heterogeneous porous material we can expect local effects associated with an increase in pressure not only in the zone of preexisting pores but also in their surroundings. We also computed a model where we induced $2.5\,GPa$ shock pressure into a sample with randomly distributed pores. Again we recorded the maximum pressures after shock wave propagation as shown in Figure 5.4c. Thus, widespread pressure amplification can be observed, which does not exclusively affect the regions of the tiny, preexisting pores alone but extends beyond. The obtained amplifications are not as high as observed for the case of an isolated pore (compare Figure 5.3b) due to reflections and interferences of shock and release waves from adjacent pores that can also cause local shock attenuation. However, the collapse of an isolated pore has already shown that a large zone ($\sim 15\,mm^2$) around the initial pore also experiences higher pressures than the initial pressure. Accordingly, the observed regions of material that experienced higher pressures provide an explanation for the occurrence of widespread shock deformed quartz in the experimental sample as confirmed by Raman spectroscopy.

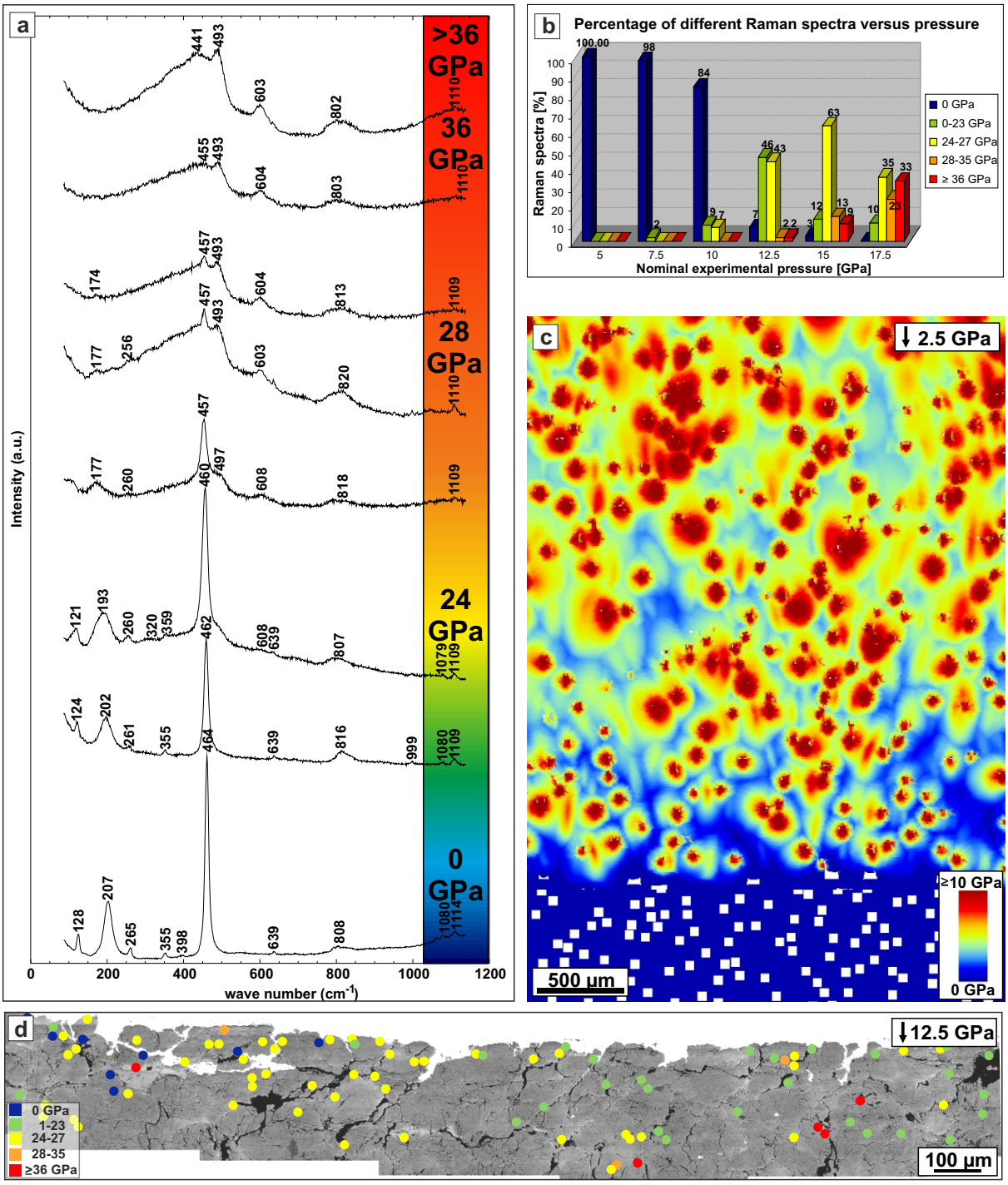

Figure 5.4: (a) Range of observed Raman spectra with increasing pressure. The pressure data given are based on experiments with quartz single crystals (McMillan *et al.*, 1992; Fritz *et al.*, 2011). Note the shift of the major quartz peak at 464 cm 1 to lower wave numbers with increasing pressure, and the change to a broad band with two broad peaks at shock pressures above 28 GPa. (b) Frequency distribution of five classes of Raman spectra representing shock pressures of 0, 1-23, 24-27, 28-35, and $\geqq 36\,GPa$, respectively, as measured for the experiments from 5 to 17.5 GPa. (c) Localized zones of pressure amplification after shock wave propagation through a representative sample with randomly distributed pores obtained by numerical modeling. The initial pressure is 2.5 GPa. Red colors indicate higher pressure, blue ones lower pressure. The zones of the highest pressure amplification are surrounded by zones (yellow) that experienced also higher pressures than the initial one. (d) Raman measurements within a selected part of the sample shocked to 12.5 GPa. Different colors illustrate different classes of Raman spectra for 0, 1-23, 24-27, 28-35, and $\geqq 36\,GPa$, respectively. Note the heterogeneous distribution of zones that experienced different shock pressures.

5.3.4 Spatial distribution of diaplectic glass and/or SiO_2 melt

In the shock experiments the diaplectic glass and melt areas are distributed heterogeneously, although - most obvious at higher experimental pressures - their amount generally decreases with increasing distance from the impacted surface. The unshocked samples and the sample shocked to $2.5\,GPa$ do not contain glassy or molten areas. Starting at $5\,GPa$, the amount of such areas increases with increasing shock pressure following a power law relationship (see below), and reaches $\sim 81\,vol.\%$ at $17.5\,GPa$ (Figure 5.5b, rhombs; Table 5.1). This means that in the lower shock pressure regime the increase of the diaplectic glass/silica melt amount is stronger developed (at $7.5\,GPa$: 13.3 times the amount at $5\,GPa$ and at $10\,GPa$ 5.5 times that amount) than in the higher pressure regime. Here the increase is about 3.3 fold (Table 5.1). This power law relationship would suggest a total transformation of crystalline quartz to diaplectic quartz glass and/or SiO_2 melt already at $\sim 18.8\,GPa$. Note that the experimentally determined values define a straight line in the double logarithmic plot and can be approximated by a power law: $y = 2 \cdot 10^{-6} x^{6.1}$ (inset Figure 5.5b).

Table 5.1: Comparison of experimental and modeled amounts of diaplectic quartz glass and SiO_2 melt [vol.%] in the 7 shock experiments

Experimental shock pressure (GPa)	**Experimental determined amount of diaplectic quartz glass and SiO_2 melt (vol.%)**	**Increase in amount (Experiments)**	**Modeled amount of diaplectic quartz glass and and SiO_2 melt (vol.%)**
2.5	0		0
5	0.03		0.02
7.5	0.4/1.6	13.33 times	0.2
10	2.2	5.5 times	1.6
12.5	7.4	3.36 times	8.2
15	24.5	3.31 times	18.6
17.5	80.6	3.29 times	27.5

We also computed numerical models for samples with randomly distributed pores where pressures were 2.5 to $17.5\,GPa$ corresponding to the experimental work. We determined the amount of material that experienced pressures over $30\,GPa$. This threshold was chosen in accordance with the assumption that the formation of diaplectic glass would start at about $30\,GPa$ in single crystal quartz (Stöffler and Langenhorst, 1994; Huffman and Reimold, 1996). The comparison of the model and the experimentally determined amounts of diaplectic quartz glass and/or SiO_2 melt (Figure 5.5b) shows a similar trend in the lower pressure regime (2.5–$12.5\,GPa$) but deviates at $15\,GPa$ and distinctly at $17.5\,GPa$ (Figure

5.5b, triangles), where the numerically determined amounts are much lower than the experimentally determined amounts. Figure 5.5c shows the numerical results representing the distribution of material that experienced more than 30 GPa (red regions) and that can be associated with the formation of melt or diaplectic glass. Note that the maximum pressures experienced by the material may decrease with further propagation of the shock wave into the sample cylinder. As already stated for the laboratory experiments, the results are only valid for the uppermost part of the sample.

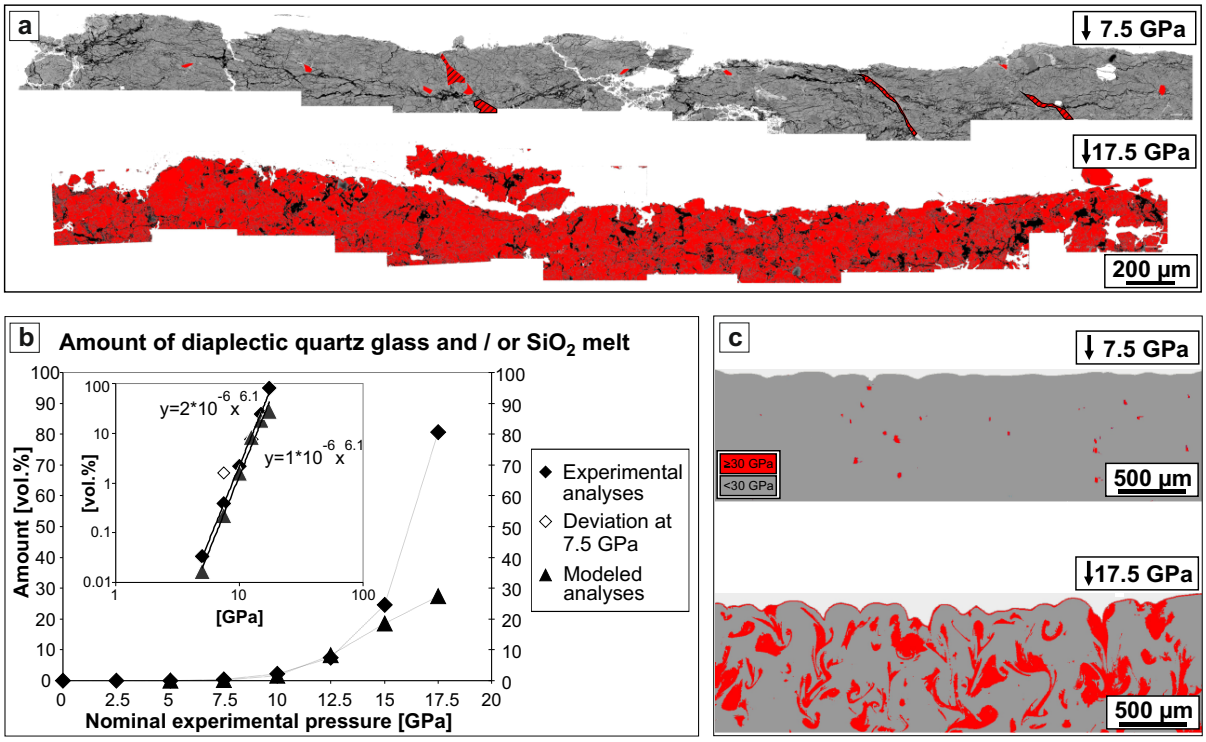

Figure 5.5: a) BSE images illustrating the amount of diaplectic quartz glass and/or SiO_2 melt (red areas) in the entire studied areas of the samples experimentally shocked to 7.5 and 17.5 GPa. Note the extraordinary increase with increasing pressure. b) Comparison of the experimentally determined (rhombs) and modeled (triangles) volume percentages of diaplectic quartz glass and/or SiO_2 melt in the samples of the experiments at 2.5 to 17.5 GPa. Note the two different illustrations: linear scales and double logarithmic scales (inserted graph). Fitting a power-law function to both the experimental and modeled data yields the same exponent of 6.1. c) Distribution of material that experienced pressures above 30 GPa (red) for an initial shock pressure of 7.5 GPa (top) and 17.5 GPa (bottom), respectively, obtained by numerical modeling. Gray regions have experienced pressures below 30 GPa.

5.4 Discussion

The results of this dual - experimental and modeling - study show that shock compression effects porous sandstone distinctly different from non-porous quartzite or quartz single crystals, especially at low shock pressures. In general, the shock pressures required to

produce a specific shock metamorphic effect in porous material are lower for porous than for non-porous targets - as a result of energy absorption due to pore collapse. The collapse mechanism is strongly dependent on individual porosity. In addition, the possible occurrence of localized shock amplification decreases with larger distance from the impacted surface.

In particular, the large contrast in shock impedance between quartz grains and pores leads to a distinctly heterogeneous distribution of shock pressures and temperatures in the target until pores are completely closed.

This causes a heterogeneous distribution of shock effects (e.g. local occurrence of diaplectic quartz glass and SiO_2 melt) at the microscopic scale, as observed in shock experiments and in nature, e.g. at Meteor Crater (Kieffer, 1971; Kieffer *et al.*, 1976) or at BP and Oasis craters in Libya (French *et al.*, 1974, and observations by W. U. Reimold). In contrast to our experiments at low shock pressures, the formation of diaplectic quartz glass and SiO_2 melt was observed normally at about 30–35 GPa and $> 45\,GPa$, respectively, in experimentally shocked quartz single crystals (e.g. Stöffler and Langenhorst, 1994) and therefore depends only on pore volume percentage and pore size. The drastic increase in the amount of diaplectic quartz glass and/or SiO_2 melt in the shock experiments with sandstone can be quantitatively approximated by a power law with an exponent of 6.1 (inset Figure 5.5b).

In addition to the laboratory shock experiments, meso-scale numerical modeling has been proven to be a useful tool to investigate the propagation of shock waves in heterogeneous materials, to determine pressure distribution within the material, and to quantify localized shock amplifications due to pore collapse. Note that the Hugoniot data used in the experiment and the numerical model are not the same. The experimental Hugoniot data are based on Coconino sandstone and the modeled Hugoniot data for sandstone are based on the ANEOS for quartzite coupled with the ε–α compaction model. However, the modeled data have been compared with Hugoniot data for Coconino sandstone showing a good agreement between the data (Güldemeister *et al.*, 2013, Chapter 4 of this thesis). Meso-scale modeling has confirmed the complete closure of pore space at very low pressures (2.5 GPa). Furthermore, the models provide an explanation for experimentally observed shock features in porous sandstone, in particular for shock features diagnostic for much higher pressures in non-porous quartz such as SiO_2 melt, diaplectic quartz glass, and quartz with PDF. They predict an amplification of up to 4 times the initial pressure considering that a significant volume of material, corresponding to at least 20 % of the initial pore volume, has experienced these strongly amplified pressure conditions. Please note that it is still possible that smaller volumes of material are experiencing even higher pressures than produced by the stated amplifications, which could facilitate the formation of melt at, e.g. 5 GPa, but the numerical models can not resolve such small volumes. This

explains some possible discrepancies between experiment and model. The determined volumes of melt within the shocked sample are in good agreement between numerical model and laboratory experiment for low shock pressures, because fitting a power-law function to both data yields the same exponent of 6.1. However, the determined volume of melt is much higher in the experiment than in the model for higher nominal pressures, especially at 17.5 GPa, which may be caused by the limited resolution of the numerical model. The resolution of the numerical "sample" varies according to the number of pores and is reduced by representing more than one single pore. We further have to keep in mind that our numerical model is still a simplified representation of the behavior of a natural rock sample under shock conditions. The discrepancies are further caused by the fact that the critical pressure for melting in porous material is reduced. The peak shock pressures required to melt porous material is lower than that for non-porous material, as shown in Wünnemann *et al.* (2008), which presents the qualitative effect of porosity on the critical pressure for melting. A further possible solution is presented in Kraus *et al.* (2012), who showed that the ANEOS equation for SiO_2 that has been used in the iSALE simulations underpredicts melt production in dense silica glass. Due to the collapse of pore space additional heat is generated during shock wave compression. The presence of porosity can be considered as quasi pre-heating a sample. In the present work we have always considered critical pressures for melting for a quartz single crystal. Considering a porous material, the chosen threshold of 30 GPa used in the numerical models has to be reduced accordingly.

5.5 Conclusions

A combination of shock experimentation and numerical modeling provides significant insight into the shock processes in dry, porous sandstone in the low shock pressure regime between 2.5 and 17.5 GPa:

1. Pore space is completely closed already at 2.5 GPa shock overprint.
2. Despite very low shock pressures, diaplectic glass/SiO_2 melt appear in porous material (starting at 5 GPa).
3. This effect is explained by effective pore collapse that can locally generate shock pressure amplification up to > 4 times (localized much higher) the average (nominal) shock pressure experienced by the specimen.
4. The effect of this shock pressure amplification is not exclusively restricted to the locus of preexisting pores but affects larger areas in their environs, as confirmed by Raman mapping.
5. The amount of diaplectic quartz glass and SiO_2 melt increases drastically with

increasing pressure (5–17.5 GPa), up to $\sim 80\,\%$ by volume at 17.5 GPa. Diaplectic glass/melt formation is not restricted to the zone directly below the impacted surface but is related to the occurrence of collapsed pores in a broader zone.

Acknowledgments

This work was funded through a grant to DFG research unit FOR-887, projects RE 528/8-2 (to W.U. Reimold and R.T. Schmitt) and WU 355/6-1 (to K. Wünnemann). The shock recovery experiments were carried out by Dr. A. Holzwarth, Ernst-Mach-Institut, Efringen-Kirchen Division. High-quality polished thin sections of the shocked samples were prepared by U. Heitmann, Westfälische Wilhelms-Universität Münster. The Raman investigations were carried out with the expert assistance of J. Fritz. We appreciate technical assistance for sample and container preparation and the subsequent investigations of the shocked samples by K. Born, P. Czaja, H.-R. Knöfler, H. Schneider, and A. Yener. A constructive review by Jay Melosh and critical comments by E. Buchner are appreciated.

Editorial Handling – Prof. Lars Stixrude

6 Quantitative analysis of impact-induced seismic signals by numerical modeling

This chapter has been published in the journal ICARUS as the following article:

Güldemeister N. and Wünnemann K. 2017. Quantitative analysis of impact-induced seismic signals by numerical modeling. *ICARUS* 296, 15-27, https://doi.org/10.1016/j.icarus.2017.05.010.

Abstract

We quantify the seismicity of impact events using a combined numerical and experimental approach. The objectives of this work are (1) the calibration of the numerical model by utilizing real-time measurements of the elastic wave velocity and pressure amplitudes in laboratory impact experiments; (2) the determination of seismic parameters, such as quality factor Q and seismic efficiency k, for materials of different porosity and water saturation by a systematic parameter study employing the calibrated numerical model. By means of "numerical experiments" we found that the seismic efficiency k decreases slightly with porosity from $k = 3.4 \cdot 10^{-3}$ for nonporous quartzite to $k = 2.6 \cdot 10^{-3}$ for 25 % porous sandstone. If pores are completely or partly filled with water, we determined a seismic efficiency of $k = 8.2 \cdot 10^{-5}$, which is approximately two orders of magnitude lower than in the nonporous case. By measuring the attenuation of the seismic wave with distance in our numerical experiments we determined the seismic quality factor Q to range between ~ 35 for the solid quartzite and 80 for the porous dry targets. For water saturated target materials, Q is much lower, < 10. The obtained values are in the range of literature values. Translating the seismic efficiency into seismic magnitudes we show that the seismic magnitude of an impact event is about one order of magnitude smaller considering a water saturated target in comparison to a solid or porous target. Obtained seismic magnitudes decrease linearly with distance to the point of impact and are consistent with empirical

data for distances closer to the point of impact. The seismic magnitude decreases more rapidly with distance for a water saturated material compared to a dry material.

6.1 Introduction

The vast majority of the kinetic energy of a cosmic body that strikes a planetary surface, asteroid, or comet is transferred to the target by compressing matter to high shock pressures. The internal energy of the shock wave causes a series of processes such as crater excavation, target deformation and fracturing, the ejection, heating, melting, and vaporization of matter, and the emission of light. Only a small poorly constrained amount of energy is converted into seismic energy.

As the initial shock wave propagates away from the point of impact it attenuates with distance until eventually its amplitude drops below some threshold, the Hugoniot Elastic Limit (HEL). The remaining plastic wave travels at a speed below the elastic wave speed so that an elastic precursor wave starts to run ahead the main pressure pulse. Elastic waves have a much larger range than plastic waves and shock waves in particular, although, in case of an impact, they carry only a small fraction of the initial impact energy. How much of the energy of the impactor is turned into seismic energy and how fast seismic waves attenuate in particular in materials of various properties is only poorly known and previous estimates range over four orders of magnitude (Schultz and Gault, 1975; Melosh, 1989).

On most planetary bodies (e.g. Mars; Teanby and Wookey, 2011) impact events pose the main source (beside volcanic events on volcanically active bodies) for seismicity due to the absence of tectonic activities, which is the main triggering mechanism for terrestrial earthquakes. As a consequence, a quantitative understanding of impact-induced seismic events is crucial for detailed seismic exploration of the interior and structure of planetary bodies.

So far the Moon is the only planetary body besides Earth, where seismic signals from natural and man-made rocket impacts have been recorded by seismometers during the Apollo program (Nakamura *et al.*, 1982; Nakamura, 2005; Godkova *et al.*, 2015). The seismic data was intensively used to constrain models of the internal structure of the Moon (e.g. Matsumoto *et al.*, 2015; Lognonne *et al.*, 2012). The newly available images from the Lunar Reconnaissance Orbiter Camera (LROC) that enable a more accurate determination of the coordinates of the Apollo rocket impacts (Robinson *et al.*, 2010) allow for further improvements of the analysis of the Apollo seismic data. Based on the assumption that seismic waves decay faster in hot and wet material, the observed relatively low attenuation of seismic waves suggests a rather cold and dry interior (Knapmeyer and Weber, 2015);

however, a better understanding of the relationship between properties such as porosity and water content and seismic properties would significantly contribute to improve data analysis and to further constrain compositional and structure models of the Moon.
New seismic data will become available from the InSight mission by NASA to probe into the Martian crust and interior by recording of the seismic activity, and meteoroid strikes are expected to be a major seismic source.
In addition to the seismic exploration of planetary objects, impact-induced seismicity has been considered as an important mechanism to alter the crater record on asteroids by erasing craters through global seismic shaking (e.g. Richardson *et al.*, 2005). The efficiency of this mechanism significantly depends on the amount of impact energy that is turned into seismic energy upon impact. Impact-induced seismic waves may result in a resurfacing process on asteroids and thus modify the crater record on them. The importance of this process may vary significantly due to the wide range of porosity in cosmic bodies. To better assess quantitatively the erasure of small craters by seismic shaking an in-depth knowledge of the impact-induced seismicity is crucial.
To quantify the amount of impact energy that is turned into seismic energy the seismic efficiency parameter k has been introduced as a ratio of seismic energy of an impact event and the kinetic energy of the impactor. Compared to earth- or moonquakes, the seismic efficiency of impact events is rather small. Only in two natural impact events the seismic efficiency has been measured directly, that are the Tunguska and the Chelyabinsk events. However, it has to be noted that in both cases the seismic signal was triggered by an airburst and the resulting blast wave in the atmosphere and not by an impact on the ground. Despite this large difference in triggering mechanism, Ben-Menahem (1975) suggests a seismic efficiency of $5–7 \cdot 10^{-5}$ that caused an earthquake magnitude of 5 in case of the Tunguska event. The Chelyabinsk event was estimated to have caused an earthquake magnitude of about 3.6 being the second largest ever seismically recorded meteor explosion (Heimann *et al.*, 2013; Tauzin *et al.*, 2013).
The fact that seismic efficiency varies over a large range may not only depend on the target properties, but also on the seismic source and the scale. Large explosions, which can be treated similar to an impact event, revealed seismic efficiency ranging from $3 \cdot 10^{-2}$ to $3 \cdot 10^{-3}$ (Titley, 1996). Gault and Heitoweit (1963) report values of 10^{-2} for small laboratory experiments. Slightly smaller values of 10^{-4} to 10^{-6} have been determined by McGarr *et al.* (1969). Schultz and Gault (1975) narrow the range of seismic efficiencies to 10^{-2}–10^{-5}, which may be considered as typical values for most impacts (Melosh, 1989).
More recently, Yasui *et al.* (2015) carried out impact experiments using glass beads targets to represent a regolith layer investigating the influence of projectile properties. They found values on the order of 10^{-5} and 10^{-4} for the seismic efficiency. Further, Richardson and Kedar (2013) recorded seismic signals in hypervelocity impact experiments into sand and

pumice targets. They determined seismic efficiencies on the order of 10^{-5} and 10^{-6}. In addition they also derived the seismic quality factor Q from the attenuation of the seismic wave with distance from the point of impact. The seismic quality factor quantifies the attenuation of the seismic wave and can be considered as a material property (e.g. Tonn, 1991). They determined Q-values of up to 8 for a sand target and below 3 for a pumice target. Other estimations for the seismic quality factor range from 26 for dry and 16 for wet sandstone (Hoerth *et al.*, 2014) to 70 for lunar regolith samples (Tittmann *et al.*, 1972) and up to values above 100 for dry sandstone (Winkler and Nur, 1979).

These estimates deviate by about four orders of magnitude for the seismic efficiency and up to two orders of magnitude for the quality factor, which clearly shows that the seismic parameters are not very well constrained and that they significantly depend on material properties. Numerical models, the only study addressing seismic signal originating from impact was published by Ivanov (2005a), do not provide any further constraints as the modeling results strongly depend on the employed material models that require rigorous calibration against experimental data to provide reliable results on seismic efficiency and attenuation in impact events.

Previously carried out impact experiments and numerical models have shown that porosity and water saturation have an important effect on shock wave propagation and the crater formation process (Kieffer *et al.*, 1976; Love *et al.*, 1993; Goldin *et al.*, 2006; Güldemeister *et al.*, 2013). Most planetary surfaces are porous and/or water saturated. Porosity and water content are typical properties for rocks of the upper crust such as sandstone. On the Moon, the regolith breccia contains a significant amount of porosity and the subsurface of Mars is characterized by the presence of water. Comets are known to have very low densities, which affects the propagation of seismic waves, as well. Shock waves decay much faster in porous materials than in nonporous materials (Güldemeister *et al.*, 2013) and wave velocities and amplitudes depend on target materials. In addition, porosity and water saturation also affect the decay of both, the shock wave and the elastic wave.

For a better assessment of the impact-induced seismicity and the determination of seismic parameters (seismic efficiency and quality factor) as a function of material properties we conducted a systematic parameter study using numerical experiments and making use of laboratory experiments that have been carried out in the framework of the same research project (Multidisciplinary Experimental and Modeling Impact Research Network MEMIN, Kenkmann *et al.* (2011)) and have been published previously (Moser *et al.*, 2013; Hoerth *et al.*, 2014). Both, numerical and laboratory experiments, allow for a variation of impact parameters and in particular material properties in terms of porosity or water saturation. However, in numerical models the parameter space can be expanded way beyond laboratory limitations and numerical experiments can be conducted on an arbitrary scale. The laboratory experiments carried out within another study (Kenkmann *et al.*,

2011) serve as benchmark to test and calibrate models.
Rigorous testing and calibration of models is crucial to provide reliable results. In the first step, our models are compared with the above mentioned previous works (e.g. Schultz and Gault, 1975) and experimental seismic data (Moser *et al.*, 2013; Hoerth *et al.*, 2014) from the available laboratory impact experiments carried out within MEMIN. In most experiments, only the first arrival time of the seismic wave was measured and only in a few cases amplitudes were determined. It requires high technical efforts to record the signal of an impact-induced compressive wave (e.g. Hoerth *et al.*, 2014). Therefore, the number of gauge points in the experimental setup was very limited. In turn, numerical models allow for a continuous recording of the propagation of the shock wave, the plastic waves, and its elastic precursor wave as a function of space and time.
The main of objectives of this work are: (1) The calibration of the numerical model against real-time measurements that were carried out in previous works: acoustic emission and pressure sensors, to determine wave velocities and pressure amplitudes in different target materials; a nonporous quartzite, a porous sandstone target, a tuff and a water saturated sandstone target. (2) The quantification of seismic parameters, the quality factor k and seismic efficiency Q, by using the calibrated numerical model, as a function of porosity and water saturation. We start with an overview of the experimental constraints and numerical approach to record seismic waves during the numerical impact experiments. Then, we describe the determination of the wave velocities, the calibration of numerical models using the seismic signals recorded during the previous experiments, and further numerical analysis to quantify the seismic quality factor and the seismic efficiency. We discuss implications of our results, their limitations, and a comparison with data from the literature. Finally, we provide some simple estimates of the magnitude of impact-induced earthquakes for some examples of impact events in Earth history based on our newly determined values for seismic efficiency and quality factor and compare the results with simple scaling laws to predict the seismic effects of impact events (Collins *et al.*, 2005; Melosh, 1989, and references therein).

6.2 Experimental constraints

Previously laboratory impact experiments have been carried out within the MEMIN project (Kenkmann *et al.*, 2011). Quartzite, sandstone, water saturated sandstone and tuff target blocks have been impacted with spherical steel, iron meteorite and aluminum projectiles at impact velocities between > 4.5 and $8\,km\,s^{-1}$. In this work we only refer to impact experiments using a target block size of $80 \times 80 \times 50\,cm$ edge length and iron or steel projectiles of $12\,mm$ impacting into a quartzite (0 % porosity), sandstone (~ 23 % porosity),

tuff ($\sim 43\,\%$ porosity), and water saturated sandstone ($50\,\%$ and $90\,\%$ saturation) target with a velocity of $4.6\,km\,s^{-1}$, which corresponds to impact energies of $74,600$ to $82,700\,J$, respectively, depending on the used projectile material. The experimental configuration and additional details on target properties are described in Poelchau *et al.* (2013) and Kenkmann *et al.* (2011). Seismic signal have been recorded in these experiments. Therefore, the impact experiments were equipped with a range of different diagnostics one of which was acoustic emission. The method and the resulting signal data using acoustic emission are presented in detail in Moser *et al.* (2013). In this work we always refer to the data by Moser *et al.* (2013) when we use acoustic emission data. In addition to the dynamic measurements, static measurements using ultrasound tomography have been carried out to image the interior structure of the target blocks before and after the impact experiments (Moser *et al.*, 2013). Both, the static and dynamic measurements, enable the determination of the wave velocity of the different target materials. Additional to the acoustic sensors, the target blocks have been equipped with pressure sensors developed and manufactured at EMI Freiburg (Hoerth *et al.*, 2014). Rigorous calibration of the sensors enabled to relate the measured voltage signal with mechanical stress amplitudes. The pressure sensors were positioned into boreholes in a sandstone and a partially water saturated target at distances of 25, 35 and $45\,cm$ from the point of impact to record the attenuation of the wave amplitude and to determine the wave velocity. The number of boreholes was limited in order to avoid any influence on the seismic wave propagation. It is not predictable if and to what extent the drilling of the holes caused any fracturing of the target material influencing shock and elastic wave propagation. Contrary to granular materials, where sensors can simply be embedded, it is difficult to position sensors inside component rocks. In contrast to the acoustic sensors, the usage of pressure sensors involved much more effort and the measurement technique was only employed in two "dry" sandstone and two water saturated experiments. The measured attenuation of the wave amplitude is essential for the calibration of material models employed in the numerical models as we discuss below. For the calibration we use the obtained signal data that has been published in Hoerth *et al.* (2014) and Moser *et al.* (2013). Further, numerical models are essential to expand the range (more gauge points, more numerical experiments applying different target properties) that is limited in laboratory experiments.

6.3 Numerical simulations

For the simulation of the laboratory impact experiments and the recording of seismic signals we used the iSALE-2D shock physics code (Wünnemann *et al.*, 2006). iSALE is based on the SALE hydrocode solution algorithm (Amsden *et al.*, 1980). To simulate hypervelocity impact processes in solid materials SALE was modified to include an elasto-plastic constitutive model, fragmentation models, various equations of state (EOS), and multiple materials (Melosh *et al.*, 1992; Ivanov *et al.*, 1997). To describe the mechanical response of the target material to deformation, an elasto-plastic constitutive model (Collins *et al.*, 2004) was included as well as a porosity compaction model (Wünnemann *et al.*, 2006; Collins *et al.*, 2011a) to account for the effect of porosity. In the numerical simulation we approximate the rectangular target blocks by a cylindrical geometry, which enables to run the simulations on a two-dimensional cylindrically symmetric grid at much less computational demands in comparison to a full three- dimensional simulation. The diameter of the cylindrical target in the numerical model corresponds to the edge length of the blocks in the experiments. All other impact parameters (impact velocity, projectile mass, diameter, and material) are the same in model and experiments. In the simulations the iron projectile is resolved by 24 cells per projectile radius (CPPR). The thermodynamic material behavior of the projectile and target during shock compression is modeled by the Analytical Equation of State (ANEOS, Melosh, 2007) for iron and quartzite, respectively. The resulting impact energy of $75,048\,J$ is kept constant in all numerical models.
According to the experiments, we put gauge points (specific cells in the numerical grid) at distances between 10 and $60\,cm$ to the point of impact. At these gauges different thermodynamic and mechanical parameters are recorded such as pressure, velocity, acceleration, and stress components as a function of time during the passage of the wave. Figure 6.1 shows the setup of the numerical experiment and the arrangement of gauge points. To calibrate the numerical models using experimentally determined pressure amplitudes and wave velocities we focus on the gauge points at distances of 25, 35 and $45\,cm$ to the impact point. For further analysis of the numerical data, additional gauge points have been considered.
In order to determine the seismic attenuation factor and the seismic efficiency, we focus on the recording of the elastic wave, in particular its first-arrival-time, velocity and pressure amplitude. We neglect any signals that arrive at the gauges at later times, we only record the first wave that arrives. The investigation of the cratering process itself, how crater size varies in different target materials, and how it is affected by target properties is beyond the scope of this work and we refer to Güldemeister *et al.* (2015) and Poelchau *et al.* (2013).

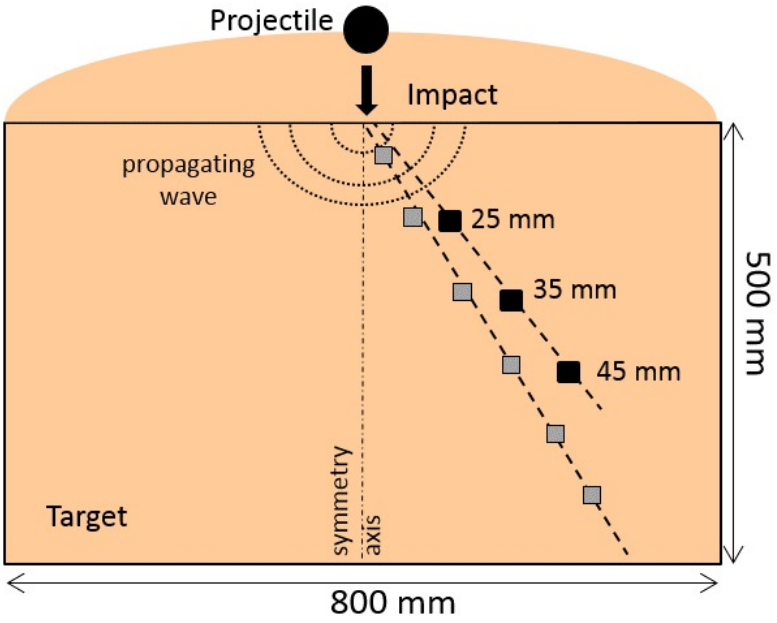

Figure 6.1: Setup of the numerical experiments including the arrangement of gauge points. The black symbols mark the location of the pressure gauges in the experiments. The grey symbols represent additional gauge points in the models at distances between 10 and 60 *cm* from the point of impact.

6.3.1 Material model

To account for different degrees of porosity and water saturation we use as target materials quartzite with $\sim 25\,\%$ porosity to mimic the sandstone targets in the experiments. For fully or partially water saturated sandstone targets, we add water to $50\,\%$ or $100\,\%$ of the pores. To approximate the tuff targets we assume a $\sim 43\,\%$ porous quartzite. The quartzite matrix in all target types was described by the ANEOS (analytical equation of state) for quartzite (Melosh, 2007). We use ANEOS for quartzite as the sandstone that was used in the experiments is composed of about $97\,\%$ of quartz (Kenkmann *et al.*, 2011). To simulate the "dry" porous sandstone and the experimental tuff (which corresponds to a highly porous sandstone in our models), the quartzite ANEOS was combined with the ε–α compaction model (Wünnemann *et al.*, 2006; Collins *et al.*, 2011a). Thus, for the description of the tuff material in the models we simply increase the porosity in comparison to the sandstone target, but do not change the composition of the matrix. This simplification was successfully employed in previous modeling studies. We also note, that for this study we are most interested in the elastic regime, where the equation of state

that describes the compaction of the matrix plays only a minor role. The water saturated material, in which case open pore space is assumed to be completely filled with water, was simulated as a two-phase material mixture. The mixture consists of 75 % quartzite content and 25 % water content and was achieved by combining the ANEOS of the two components (Güldemeister *et al.*, 2013; Pierazzo *et al.*, 2005). This ratios of the two components, water and quartz, corresponds to 100 % water saturation in the models in contrast to 90 % water saturation in the experiments we use for comparison. We consider this small difference in water saturation to be negligible. From the modeling perspective it is easier and more consistent to treat 100 % water saturated material as described. To simulate the partially water saturated target the mixed ANEOS for quartzite and water was combined with the ε–α compaction model so that only 50 % of the pore space is filled with water (12.5 % water content, 12.5 % open pore space). We additionally carried out simulations with material porosities of 12 %, 35 %, and 50 % and a material that contained 12.5 % water content without any additional porosity.

6.3.2 Simulation of porous material

The propagation velocity and attenuation of the amplitude of the generated waves including the elastic part are very sensitive to parameters of the porosity compaction model (ε–α porosity model) and it is essential to determine the parameters through detailed calibration of the models against experimental observations. The ε–α porosity model defines porosity as a function of compressive volumetric strain which is explained in detail in Wünnemann *et al.* (2006). Note, compressive volumetric strain is negative.
Its applicability has been validated by mesoscale modeling described in Güldemeister *et al.* (2013). The porosity model is described by 5 parameters, which are all explained in detail in Wünnemann *et al.* (2006). The relevant parameters for the given study are distension, defined by $\alpha = \frac{1}{1-\phi}$, where ϕ is porosity, the elastic threshold parameter ε_e and the sound speed ratio parameter χ both of which are described briefly in the following; for further details we refer to Wünnemann *et al.* (2006) and Collins *et al.* (2011a). All other parameters of the porosity compaction model are listed in Table 6.1 and correspond to values derived in Güldemeister *et al.* (2013).
The compaction function described by the porosity model can be subdivided into 4 regimes: elastic compaction, exponential compaction, power law compaction, and compression of the matrix (Collins *et al.*, 2011a). The elastic regime, where the decrease in pore space is not permanent ($\varepsilon_V < \varepsilon_e$, volumetric strain is smaller than the elastic threshold) is separated from the compaction regime (exponential and power-low compaction) where

changes in porosity remain in the material ($\varepsilon_V > \varepsilon_e$, volumetric strain is larger than the elastic threshold) by the elastic-plastic transition strain ε_e (elastic threshold). In other words, the elastic threshold parameter ε_e corresponds to a critical volumetric strain of the elastic regime where permanent closure of pores begins and pore space starts to collapse. It has a significant influence on the pressure and stress amplitude of the propagating wave (see Section 6.4 below). Another crucial parameter is the dependency of the speed of sound (bulk elastic wave speed) on porosity. The elastic wave velocity in porous material can be significantly lower than in the nonporous material (Collins *et al.*, 2011a), which has to be taken into account in the porosity model. The wave speed changes as shock-induced crushing of open pore space occurs. The ratio χ of the wave velocity of a porous material and a solid material is defined by the ratio of the bulk sound speed of the solid component (c_s) and the material with porosity (c_p) as stated in Equation 6.1. For intermediate porosities resulting from shock-induced pore space compaction, it is assumed that the speed of sound varies linearly with distension (α) in the elastic compaction regime as expressed in Equation 6.2 (after Collins *et al.*, 2011a).

$$\chi = \frac{c_p}{c_s} \tag{6.1}$$

$$c(\alpha) = c_s + \frac{\alpha - 1}{\alpha_0 - 1}(c_p - c_s) \tag{6.2}$$

Consequently, for the purpose of this work, we will carry out a calibration of the porosity model with regard to the determination of the elastic threshold parameter ε_e defining the onset of pore crushing during wave propagation and the parameter χ accounting for the dependency of wave velocities on target porosity. The calibration is essential for a quantitative analysis of the seismic signals at some distance from the point of impact, although no further pore crushing occurs at this distance.

6.4 Model calibration

For a systematic study on the impact-induced seismicity as a function of material properties by numerical experiments the required minimum resolution of the models has to be determined and material models need to be calibrated. First we carried out a resolution test. In a second step we used the available experimental data to calibrate the important parameters in the porosity compaction model ε_e and χ. All other parameters in the material models, such as strength, are listed in Table 6.1 and correspond to values stated in Güldemeister *et al.* (2013, 2015). The porosity parameters, in particular distension and the ratio of material sound speed as introduced in the previous section, have been

adjusted according to the target material.

Table 6.1: Material parameters used for the strength model in iSALE for the iron impactor and the sandstone target

Material parameter	**Values for iron impactor**	**Values for sandstone target**
Strength model	Johnson Cook (Johnson and Cook, 1983)	Pressure- and damage strength model for rock-like materials (Collins *et al.*, 2004)
Poisson' ratio	0.25	0.3
Cohesion of intact material Y_{i0} [MPa]	-	0.2
Cohesion of damaged material Y_{d0} [MPa]	-	0
Limiting strength at high pressure for intact material Y_{im} [MPa]	-	170
Limiting strength at high pressure for damaged material Y_{dm} [MPa]	-	170
Coefficient of internal friction for intact material β_i	-	1.8
Coefficient of internal friction for damaged material β_d	-	0.67
Shear strength of material at reference state JC_A [MPa]	175	-
Shear strength coefficient controlling strain dependence JC_B [MPa]	280	-
Shear strength coefficient controlling strain rate dependence JC_C	0.32	-
Shear strength exponent controlling strain dependence JC_N	0.001	-
Exponent in thermal softening term JC_M	0.55	-
Reference temperature [$^\circ K$]	293	-
Quartz melting point at zero pressure [°C]	1500	1873
Specific heat capacity [$J/(kgK)$]	200	800
Porosity parameters		
Initial distension of porous material α_0[a]	-	1.3333
Elastic threshold ε_e[a]	-	-0.75
Distension at transition from exponential to power-law compaction α_x[a]	-	1.1
Compaction rate parameter κ[a]	-	0.98
Ratio of porous to solid material sound speed χ[a]	-	0.6

[a] A detailed description of the porosity parameters are given in Wünnemann *et al.* (2006) and Güldemeister *et al.* (2013)

6.4.1 Resolution test

The modeling of wave propagation and the analyses of wave signals, pressure amplitudes, wave structure, and pressure decay tend to be very sensitive to the resolution of the computational grid. In previous studies on the propagation of shock waves a minimum resolution of 80 CPPR has been proposed (e.g. Wünnemann *et al.*, 2008). To test whether amplitudes and wavelength in our models converge with increasing resolution we carried out a suite of models with a resolution of 6-48 CPPR (cells per projectile radius) and determined pressure amplitudes and pressure pulse duration. Figure 6.2 shows how the maximum pressure in quartzite targets (nonporous) at three gauge points (different colors) having different distances to the point of impact change with resolution. We consider a resolution of 24 CPPR as sufficiently accurate for the present study as pressure amplitudes converge for a certain distance. Doubling the resolution leads to pressure differences below 10 % whereas a resolution of only 12 CPPR leads to pressure amplitudes

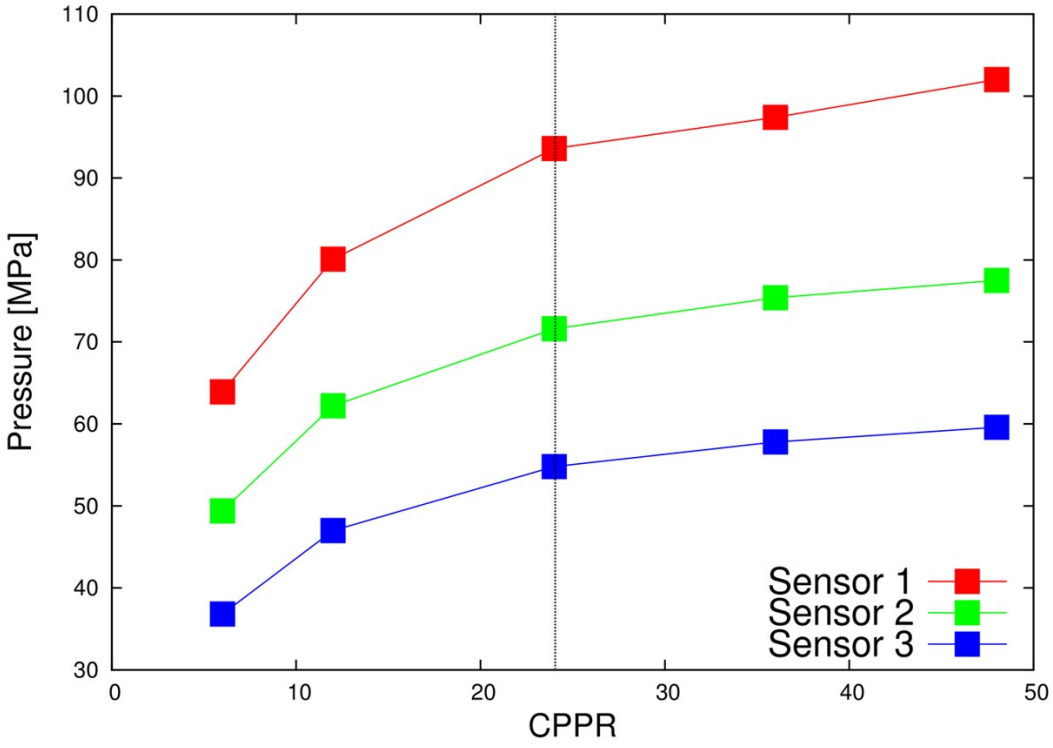

Figure 6.2: Resolution study for the impact of an iron projectile at velocity $5\,km \cdot s^{-1}$ onto a nonporous quartzite target. The pressure amplitude of the wave at three different gauge points with distances of 25 *cm*, 35 *cm* and 45 *cm* is plotted as a function of resolution in terms of cells per projectile radius (CPPR). The dashed line marks the resolution of 24 CPPR.

6.4.2 Calibration of parameter χ using wave velocities

To determine the χ-parameter, the ratio for the bulk speed of sound and the nonporous matrix, we use the experimentally determined elastic wave velocity for nonporous quartzite ($c_p = 5000\,m\,s^{-1}$), 25 % porous sandstone ($c_p = 3200\,m\,s^{-1}$), and 45 % porous tuff ($c_p = 2300\,m\,s^{-1}$) obtained by Moser *et al.* (2013) to estimate a linear dependency of c_p on initial porosity. χ is then calculated using Equation 6.1 and assuming c_s to be equal to c_p of quartzite ($c_p = 5000\,m\,s^{-1}$). Based on this simple assumption we can estimate χ for any given initial porosity. For sandstone and tuff we determined χ to be 0.46 and 0.6, respectively (see Table 6.2). Quartzite was used as a reference as it represents the matrix of the investigated materials.

To test the accuracy of this simple approach we recorded the arrival times of the elastic waves as a function of distance in our numerical models using different target porosities (see Figure 6.3). By linear regression through the data points the elastic wave velocity for the different materials with different porosities and water content can be determined and compared with the experimental measurements (Table 6.2). The deviation between model and experimental data is about 10 %, which is inside the tolerable range. The P wave velocities for a sandstone target have also been obtained by Hoerth *et al.* (2014) with $3200\,m\,s^{-1}$ which is in accordance with data of Moser *et al.* (2013) and comparable with the numerical data. The wave velocities are slightly smaller in the numerical experiments except for the water-saturated targets.

The difference between model and experiment may be due to different reasons: in the experiment, the velocity has been determined using the first arrival time at the sensor, which sometimes is difficult to determine accurately. This is described in the previous work by Moser *et al.* (2013) who carried out the measurements of the wave velocities in the experiments. Further, in the near-field the waves travel as shock waves at a significantly higher velocity than the speed of sound causing reduced travel times, which is in particular significant at gauge points close to the impact point. Note, in the entire work, we always refer to the arrival of the P wave and do not consider any S waves when recording the seismic wave and its first arrival.

The wave velocity for a quartzitic material is also supported by literature data ranging from 4500 to $5700\,m\,s^{-1}$ (Pavloskii, 1976; Ahrens and Gregson, 1964). Ahrens and Gregson (1964) also state values for different sandstones with wave velocities in the range of $3000\,m\,s^{-1}$.

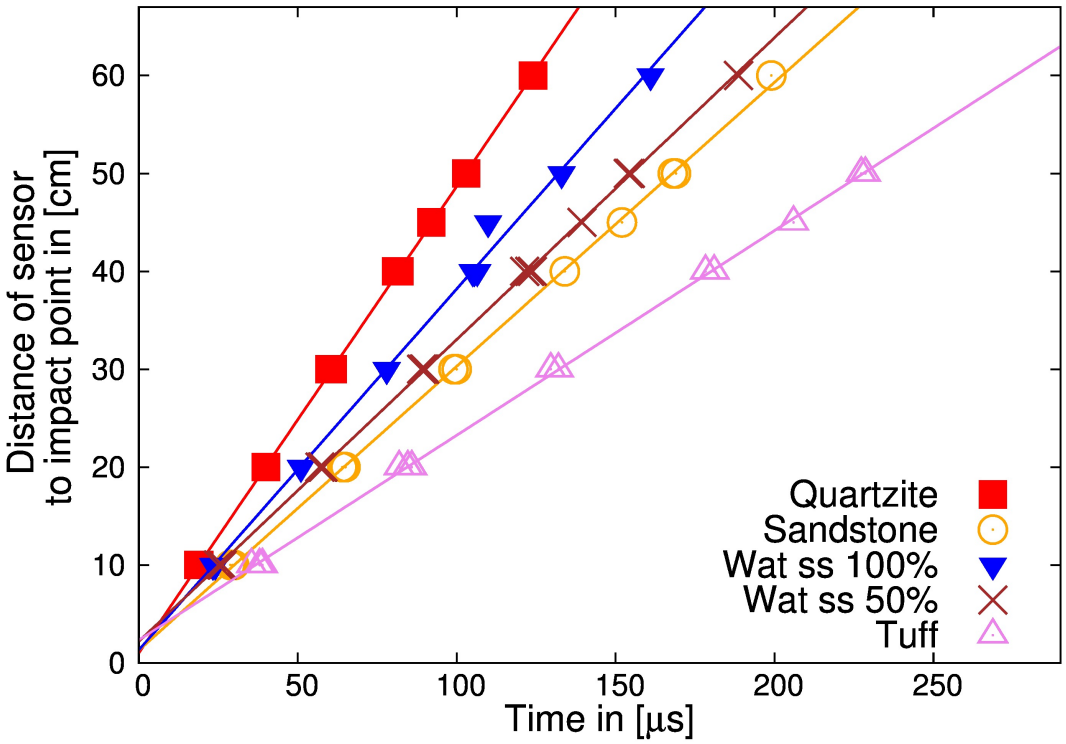

Figure 6.3: Travel times of elastic wave signals in numerical experiments for five different target materials of different porosity and water saturation. The velocities have been determined from the slope of a line fitted to the data. The numerical experiments used targets with a block size of $80\,x\,80\,cm$ and an iron impactor of $12\,mm$ in diameter. The arrival times have been measured at gauge points located at distances between 10 and $60\,cm$ from the point of impact

6.4.3 Calibration of critical elastic threshold ε_e using pressure amplitudes

Since no so-called crushing curves (porosity as a function of pressure or volumetric strain; Wünnemann *et al.*, 2006) were available for the different materials we used constraints from experiments to calibrate important parameter such as the elastic threshold ε_e which defines the resistance of porous material to pore space crushing. The elastic threshold has a significant effect on the pressure amplitudes of the propagating wave. We varied the elastic threshold in our models, which corresponds to an earlier or later onset of pore crushing and, thus, a decrease or increase of the zone where the elastic precursor occurs. An elastic threshold value of $\varepsilon_e = 0.0$ results in an immediate onset of pore space collapse if any compressive wave propagates through the material. As a maximum value for ε_e we assume -0.3; note that negative strain is compressive. To define the correct threshold where pore

space starts to collapse, we varied the ε_e-value in our models until the pressure amplitude at three gauge points match the recorded values in a sandstone target experiment measured by the calibrated EMI sensors (see Hoerth *et al.*, 2014). Figure 6.4a shows the maximum pressure amplitudes (black squares) measured at three gauge points for a dry sandstone target. The maximum pressures at the sensors are 53, 47 and 33 MPa at distances to the point of impact of 25, 35 and 45 cm, respectively. The colored lines represent the recorded signals in the numerical models at the same gauge points, for different ε_e-values ranging from -0.05 to -0.15. As expected, the sensor closest to the impact point shows the highest pressure amplitude that decreases with distance. Comparing different elastic threshold values, larger absolute values or later onset of crushing lead to larger pressure amplitudes, which in turn means that the process of a later onset of crushing during the impact event consumes less energy. In contrast an immediate crushing of pore space would consume much more energy resulting in a weaker shock wave resulting in smaller pressure amplitudes of the elastic wave. The best agreement with the observed wave amplitudes was achieved for $\varepsilon_e = -7.5 \cdot 10^{-2}$, where the maximum pressure at numerical gauge points at distances of 25 cm, 35 cm, 45 cm have amplitudes of about 51, 42, and 32 MPa, respectively. ε_e of $-7.5 \cdot 10^{-2}$ allows for a small resistance against crushing which is in good agreement to previously determined ε_e-values (Güldemeister *et al.*, 2013), where ε_e has been determined in mesoscale simulations.
The elastic threshold value of $-7.5 \cdot 10^{-2}$ is used for all porous target materials. The elastic threshold value has no influence on the elastic wave velocities.
The elastic wave is measured in a regime where no pore crushing is present anymore (farther away from the point of impact). Thus, the elastic wave velocity is not influenced by the effect of pore crushing at the subsurface of the crater.

Table 6.2: Experimentally and numerically determined wave velocities for different target materials and the numerically derived porosity parameters.

	Model parameters			**Wave velocities**	
Target material	Porosity Φ	Elastic threshold ε_e	Speed of sound ratio χ (rounded values)	Experiment c_p in $m\,s^{-1}$ (Moser et al. 2013)	Model c_p in $m\,s^{-1}$
Quartzite	0 %	No porosity model	No porosity model	5000	4800
Sandstone	25 %	$-7.5 \cdot 10^{-2}$	0.6	3200	2900
Tuff	43 %	$-7.5 \cdot 10^{-2}$	0.46	2300	2090
Water saturated sandstone (50 %)	25 %	$-7.5 \cdot 10^{-2}$	0.6	2890	3080
Water saturated sandstone (100 %)	0 %	No porosity model	No porosity model	Not determined	3680

Comparing the numerical wave forms (Figure 6.4a) and the experimental wave forms (Figure 6.4b, Hoerth *et al.* (2014)), they show similar features. They both show a distinct first onset of the signal. However, the unloading process is slower in the laboratory experiment at each sensor than in the numerical experiment. The time shift between the model and experiment is due to different triggering methods when the recording of the signal starts.

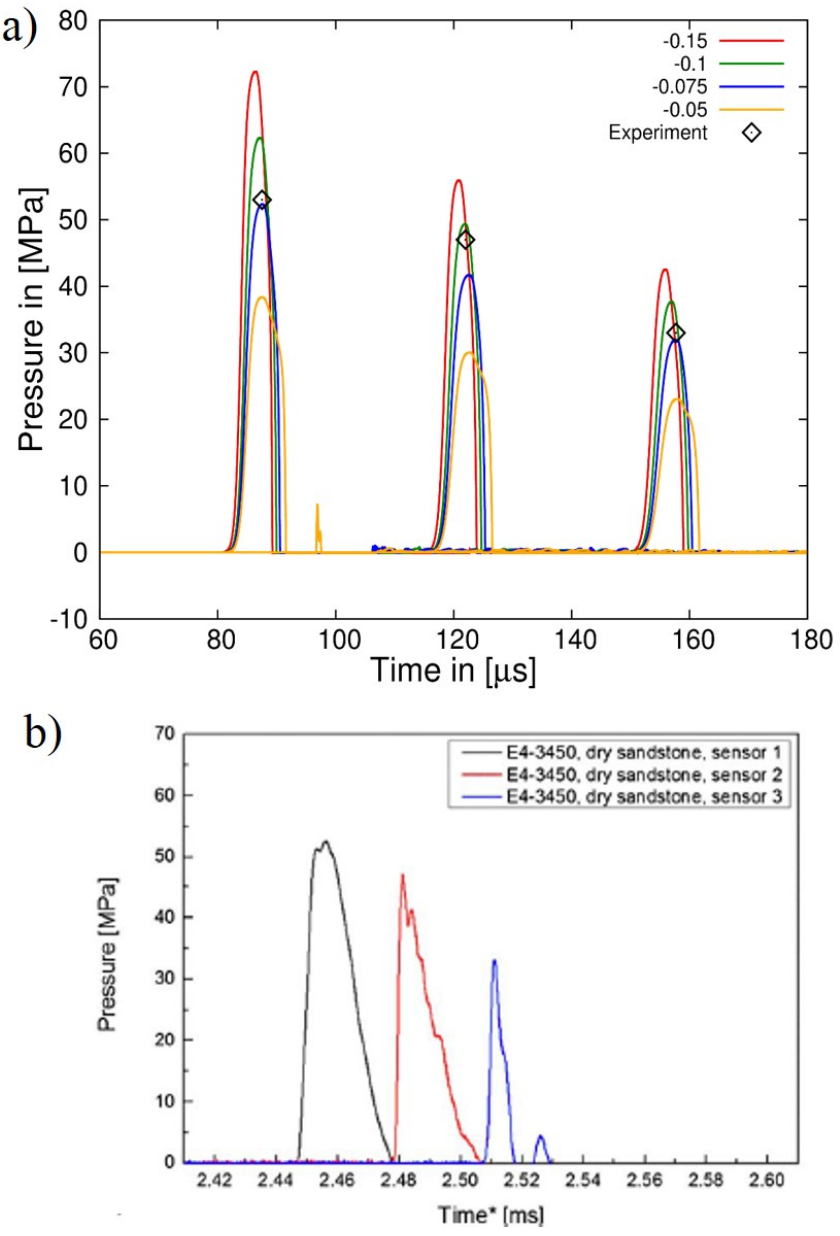

Figure 6.4: a)Pressure signals recorded by numerical sensors at 25, 35 and 45 cm distance from the impact point considering an impact of an iron projectile with a velocity of 5 $km \cdot s^{-1}$ impacting into a dry sandstone target material. The signals are shown for four different values of the elastic threshold parameter ($-5.0 \cdot 10^{-2}$, $-7.5 \cdot 10^{-2}$, $-1.0 \cdot 10^{-1}$, $-1.5 \cdot 10^{-1}$). The pressures obtained in the laboratory experiments are indicated by squared symbol. b) Seismic signals recorded in a dry sandstone target during an impact experiment at three sensors with distances of 25, 35 and 45 cm from the impact point (after Hoerth *et al.*, 2014).

6.5 Results

6.5.1 Analysis of seismic wave signal

With the first contact of the impactor and the target a shock wave is generated. The initial peak shock pressure is about 60 GPa inside the isobaric core in the vicinity of the point of impact. Poelchau *et al.* (2013) calculated these maximum shock pressure for dry sandstone experiments and steel projectiles using the planar impact approximation and material parameters for Coconino sandstone and steel compiled in Melosh (1989). However, the peak shock pressure depends on target and projectile properties. The shock wave travels into the target as well as into the impactor. At the back side of the impactor it is reflected and travels back into the target as a rarefaction wave. The generated rarefaction wave, which travels faster than the initial shock wave, eventually, overtakes the shock wave causing a rapid reduction of the high pressure amplitude. While the hemispherically expanding shock wave initially attenuates only due to geometric spreading, it decays much faster as a consequence of the superimposing rarefaction wave. Eventually, it weakens into a plastic stress wave preceded by an elastic precursor that, finally, converges into an entirely elastic wave (Chapter 5 in Melosh, 1989).
To quantify the decay behavior of the shock wave and the elastic wave for different target materials we recorded the peak pressure at an arbitrary number of gauge points (with distances between 10 and 60 cm from the impact point) in our numerical experiments. Figure 6.5 shows the peak pressure amplitudes as a function of distance in a double logarithmic plot. Two different attenuation regimes can be identified: the plastic (shock) and the elastic regime. In the shock regime, attenuation is much faster than in the elastic regime. This change in attenuation occurs at a distance of about 12 cm for all materials. The boundary does not exist for the fully water saturated sandstone as there exists no shock regime. For both regimes the largest pressure amplitudes occur in the nonporous material, decrease with porosity, and are the lowest if the pores are completely or partially filled with water. The pressure decay with distance can be described by a power-law function for both regimes with a much more rapid decrease in the plastic wave regime and a shallower decay in the elastic regime. The power law fits are represented as straight lines in Figure 6.5 and the corresponding decay exponents are listed in Table 6.3.
In the shock regime the decay exponent varies between -1.9 and -3.4, with lower absolute values corresponding to sandstone and quartzite and the higher absolute values for the highly porous tuff and fully or partially water-saturated material, the exponent increases with porosity (see Table 6.3). These exponents agree with the range of decay exponents for plastic waves in the literature based on theoretical considerations (Holsapple (1993)

proposed exponents of −3.6 for the shock wave regime and −1.8 for a plastic wave regime) and numerical modeling (Pierazzo *et al.*, 2008). Pierazzo *et al.* (2008) state exponent values between −1.2 and −2.3 depending on impact velocity using aluminum projectiles and targets.

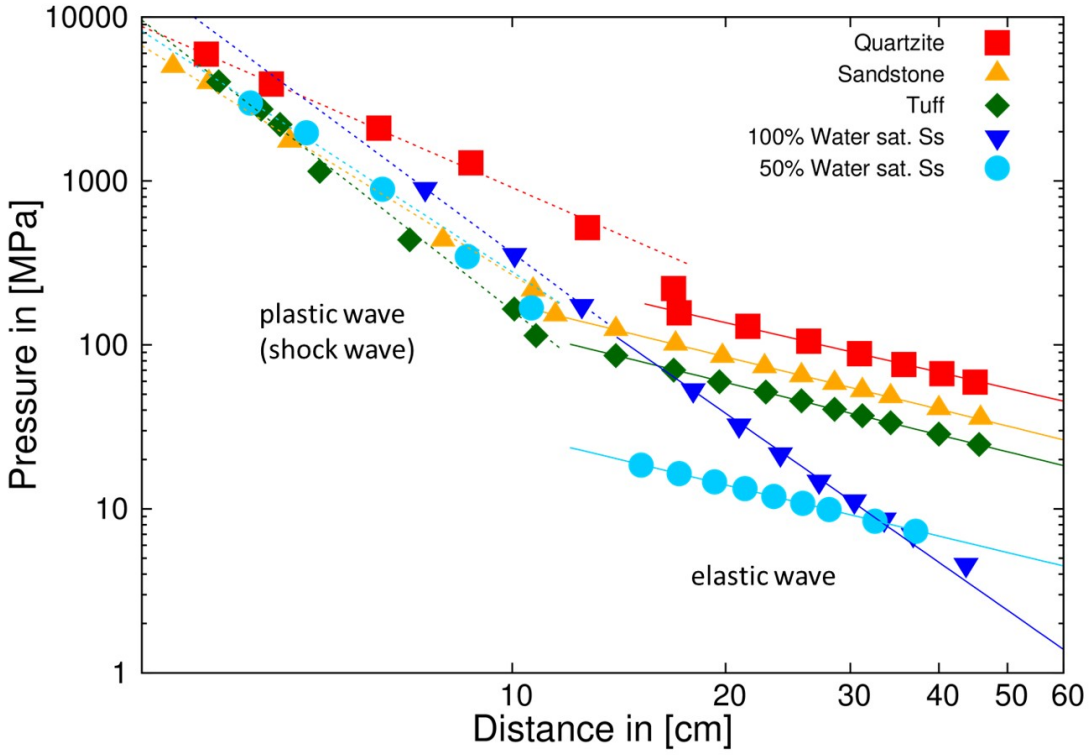

Figure 6.5: Pressure amplitudes of the elastic wave as a function of distance for different target materials in a double logarithmic plot. Lines correspond to power law fits in both regimes. The figure shows pressure amplitudes and the decay according to a power law of the shock and elastic wave, presenting a clear distinction between the shock and elastic regime. The decay is much stronger in the shock regime

In the elastic regime the wave amplitude decays very similar in all "dry" materials and the partially water saturated material with a decay exponent of −1.0 for the nonporous quartzite, −1.03 to −1.06 for "dry" porous materials, and −1.06 for partially water saturated sandstone. A decay exponent of −1 corresponds to pure spherical geometric spreading and no dissipative processes are at work. In case of the fully water-saturated sandstone the elastic wave decays as fast as the plastic wave with an exponent of −3.01 (see Table 6.3). The fully water saturated sandstone functions as a reference material here. It shows about the same decay behavior in the plastic regime as the partially water saturated sandstone in which case the elastic wave decays slower due to the presence of pore space than in the fully saturated material.
Except for the fully water saturated target, the exponents are consistent with a decay behavior of an elastic wave of −1.18 as suggested by Holsapple (1993).

Table 6.3: Decay exponents for different materials in the shock and elastic wave regime

Material	Shock decay exponent	Elastic decay exponent
Quartzite	-1.88	-1.0
Sandstone	-2.67	-1.06
Tuff	-3.4	-1.06
50% water saturated sandstone	-2.8	-1.03
100% water saturated sandstone	-3.2	-3.01

Figure 6.6 shows typical wave signals as recorded in the numerical models at three locations for different target material. The wave amplitudes are plotted as a function of time for three successive gauge points with distances of 25, 35, and 45 cm from the point of impact.

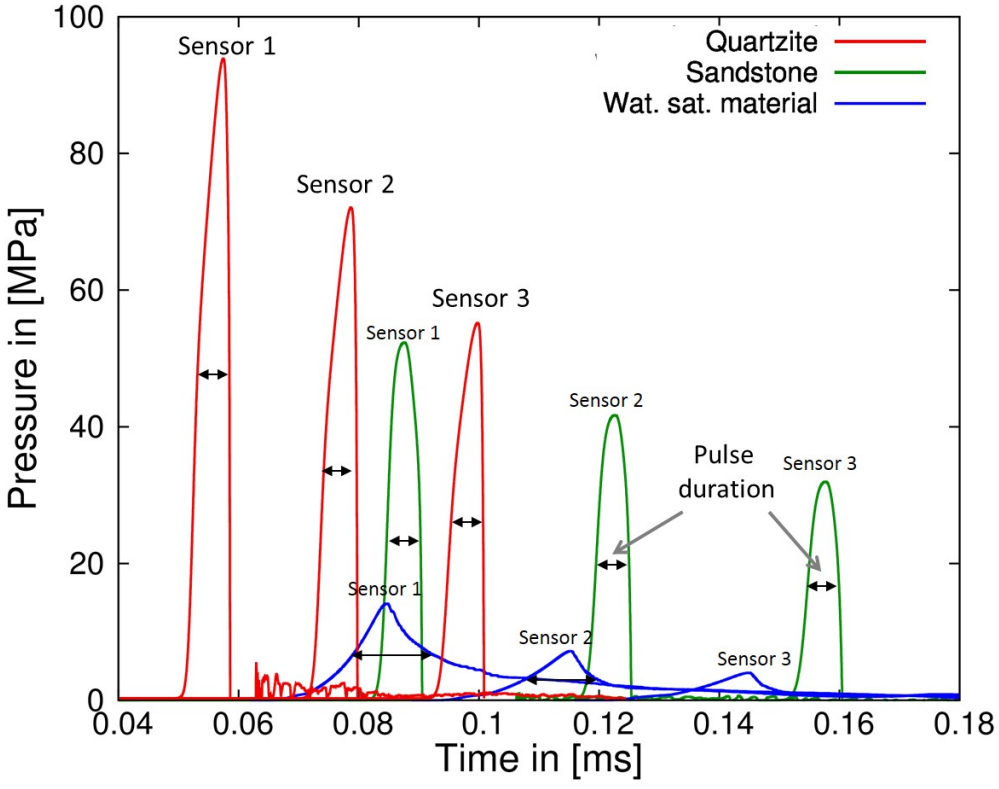

Figure 6.6: Typical seismic signal recording the pressure amplitude at three sensors in 25, 35 and 45 cm distance from the point of impact for three different materials

Besides wave amplitudes the signals allow for the determination of the pulse duration. We define the length of the pressure pulse in time at the half-value-width as indicated in Figure

6.6. Apparently, the waves are not dispersive in case of quartzite and sandstone material and we determine a pulse duration of $\Delta t = 5\,\mu s$. The signals recorded in water-saturated material appear to be very different, which makes the determination of the pulse duration more difficult (see Figure 6.6). The differences of the signals for the quartzite/sandstone and water-saturated material may be explained by the fact that for the "'dry"' material the pressure drops to zero because the material fails whereas in water saturated material the water content can sustain some pressure as it does not undergo mechanical failure. The pulse duration is approximately twice as long as for the dry material with $\Delta t = 10.06\,\mu s$. The measured length at gauge points 2 and 3 are almost the same, which means that dispersive effects are negligible. The pulse duration can be translated into wavelength λ with elastic wave velocity c_p; $\lambda = c_p \cdot \Delta t$. The complete characterization of elastic waves in different materials from the numerical models is summarized in Table 6.4.

6.5.2 Seismic attenuation factor Q

As described above and illustrated in Figure 6.5, the seismic wave attenuates as the elastic energy associated with the wave is continually absorbed during wave propagation through the target material. This is considered as an inelastic damping, intrinsic attenuation or absorption and can be quantified by the seismic quality factor. In addition the wave attenuates due to geometric spreading, which, however, will not be considered here for the calculation of the quality factor.

Q is a material property characteristic for specific rock types. It strongly depends on porosity and water saturation (Winkler and Nur, 1979) but is not scale dependent. Non-attenuative materials (competent rocks with low porosity) have high Q-values ranging from 500 and 1000 (Gusmeroli *et al.*, 2010). Highly porous and fractured rocks (attenuative materials) have low Q-values between 10 and 100 (Gusmeroli *et al.*, 2010). A smaller quality factor corresponds to a faster attenuation of a seismic wave.

To determine the seismic quality factor from the numerical experiments we used the so-called spectral ratio method, which is based on the assumption that the amplitude of an elastic signal attenuates proportional to an exponential function (Aki and Richards, 2002):

$$A(x) = A_0 e^{-\beta \cdot x} \tag{6.3}$$

where $A(x)$ and A_0 are the amplitudes at two different distances, x is the distance between two gauge points and β is the attenuation coefficient. As an elastic wave signal with a long wavelength (length of the pressure pulse) attenuates slower than a short wave, β is a

function of length:

$$\beta = \frac{-\pi}{\lambda \cdot Q} \tag{6.4}$$

Thus, the quality factor can be determined by

$$Q = \frac{-\pi}{\beta \cdot \lambda} \tag{6.5}$$

if the wave length λ (represented by the length of the pressure pulse) and the attenuation coefficient β are known. Both parameters can be measured in our numerical experiments as described above.

Note, in the previous section we use power-laws to describe the decay behavior of the shock wave as it is commonly done and employ the same parametrization to quantify the attenuation of the elastic wave in order to compare the results with theoretical considerations of the impact-induced decay of a pressure wave for different regimes (shock, intermediate, elastic) in the literature (Holsapple, 1993). In seismology the attenuation of seismic waves is routinely described by an exponential law (Equation 6.3). Following this approach, we derive the attenuation coefficient β by fitting Equation 6.3 to the peak pressure values of the elastic wave in our numerical experiments for different target materials. The resulting attenuation coefficients (Table 6.4) show a small increase with increasing "dry" porosity and a strong increase if pore space is filled with water. Water content has a significant effect on attenuation causing a very fast attenuation of seismic wave amplitudes. With the elastic wave velocity c_p and the wavelength λ for different materials with varying porosity and water content (see Table 6.4) we obtain seismic quality factors ranging from $Q = 57$ for the highly porous tuff and $Q = 6.5$ for fully water saturated sandstone (25 % water content) (Table 6.4). Note, these results are strongly affected by the different wavelength we observe in nonporous quartzite ($\lambda = 24\,mm$), 25 % porous sandstone ($\lambda = 14.5\,mm$) and water-saturated sandstone ($\lambda = 37\,mm$).

For a more systematic approach we also determined the quality factor for materials with porosities of 12, 35 and 50 % and partially water saturated material (Table 6.4). Figure 6.7a shows how the quality factor depends on porosity and water saturation. The quality factor increases slightly with increasing porosity, which leads to a slower attenuation at higher porosity. This may not be consistent with what one would intuitively expect, namely that the wave amplitude attenuates faster in porous material. However, the increase of the quality factor may be explained by the fact that we observe an increase in wavelength and a decrease of wave velocity with porosity.

For the water-saturated target we obtain a very small quality factor which corresponds to the largest attenuation coefficient. As mentioned already above water acts as a very strong wave absorber.

Comparing the numerically obtained values with values from experiments, we find a higher quality factor ($Q = 43$) for sandstone targets (Table 6.4; Hoerth *et al.*, 2014; Winkler and Nur, 1979). For the water-saturated material the experimental value obtained by Hoerth *et al.* (2014) ($Q = 16$) is larger than the numerical value ($Q = 6.5$) but in better agreement than for the sandstone target. Measurements of the quality factor carried out by Winkler and Nur (1979) yielded that in partially water saturated sandstone ($Q < 15$) much smaller values occur than in dry sandstone (between 100 and 140 for Berea and Mallison sandstone), which is consistent with the results obtained in this work. However, for a water saturated sandstone the values are more in agreement with data ($Q < 15$) obtained by Winkler and Nur (1979) than with the experimental work by Hoerth *et al.* (2014). Note, Hoerth *et al.* (2014) used only three gauge points to derive Q in contrast to the 8 gauge points we used in our numerical experiments which may result in the described differences.

6.5.3 Seismic efficiency k

The seismic efficiency relates the seismic energy to the kinetic energy, which is defined by the impact energy $E_{imp} = m/(2v_i^2)$ where m represents the mass of the projectile and v_i the impact velocity. The seismic efficiency is then defined as $k = E_{seis}/E_{imp}$. We assume that k is a scale independent parameter. Following the approach of Schultz and Gault (1975) we determine the seismic efficiency in our numerical experiments. The approach is based on Rinehardt (1960), who used a simple model of a sawthoothed stress pulse to derive a relationship between kinetic energy E_{kin} and the pressure amplitude P of a pulse that propagates through the target material.

$$\frac{E_{kin}}{A} = \frac{1}{6} \cdot \frac{P^2}{\rho c_p}$$

where ρ is density, c_p is the wave velocity and A the surface area of the wave front, defined by $A = 1/2 \cdot 4\pi x^2$. Substituting this relationship into the definition of the seismic efficiency of Schultz and Gault (1975) yields

$$k = \frac{1}{3} \cdot \frac{\pi x^2 P^2 \Delta t}{\rho c_p E_{imp}} \tag{6.6}$$

All parameters in Equation 6.6 can be determined by the analysis of the wave signal in the numerical simulation, including the pulse duration Δt, the pressure amplitude P recorded at the gauge point at distance x to the point of impact. The impact energy is the same

for all simulations ($E_{imp} = 75,048\,J$). With the given parameters (Table 6.4) and by averaging over results at three distances (25, 35 and 45 cm) with a variation of about 3.5 % we determined a seismic efficiency k of about $2.6 \cdot 10^{-3}$ for a sandstone target. This variation may increase when considering a larger range of distances between the gauge points. However, as the pressure will decrease with increasing distance, the variations are still small enough to achieve reliable results.
The seismic efficiency for a quartzite is slightly larger ($k = 3.4 \cdot 10^{-3}$) and for a 100 % water-saturated sandstone target about two orders of magnitude smaller ($8.2 \cdot 10^{-5}$) than for the sandstone target. The seismic efficiency decreases slightly with increasing porosity following a linear trend and significantly by inserting water into the target material (Table 6.4, Figure 6.7b). More energy is lost during wave propagation in a porous and/or water saturated target due to the process of pore crushing compared to a solid target material and consequently less energy is available to be transformed into seismic energy leading to smaller k-values. The observed higher value for high porosities as seen in Figure 6.7b is most likely caused by uncertainties during the analysis of the recorded signal. Water operates again as a very efficient wave absorber as most of the energy is absorbed and almost no energy remains as seismic energy. Thus, larger seismic energies are expected for competent rock, whereas small efficiencies and very small remaining seismic energies may be the result of a fully water-saturated target. The values for different porous sandstones correlate quite well with literature values ranging from 10^{-3} to 10^{-5} (Melosh, 1989) as well as with the experimental data from the MEMIN experiments obtained by Hoerth *et al.* (2014) ($k = 5 \cdot 10^{-3}$ for sandstone).

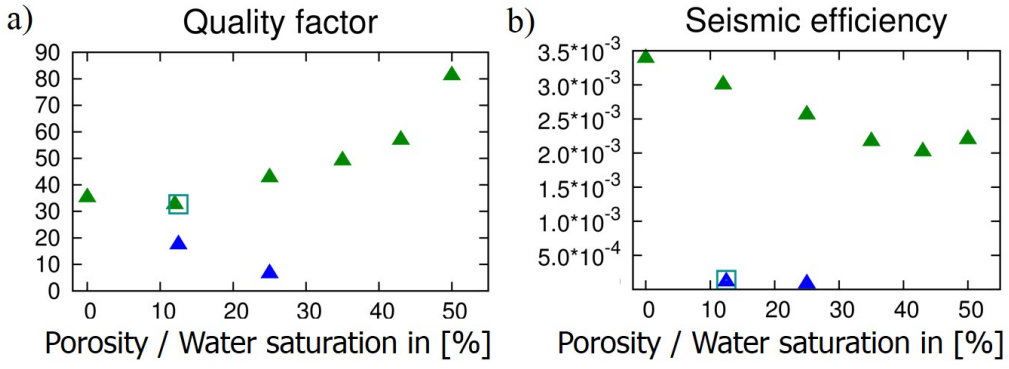

Figure 6.7: Dependencies of a) seismic quality factor and b) seismic efficiency on porosity. The green symbols represent the result for the "dry" porous material, blue symbols for the fully water saturated material (12 and 25 % water content) and the open symbol for the partially water saturated material (12.5 % open pore space, 12.5 % water content).

Table 6.4: Seismic parameters for different target materials

Material	**Power law exponents**	**Wave velocity c_p in $[m\,s^{-1}]$**	**Pulse duration in $[\mu s]$**	**Wave-length in $[mm]$**	**Attenuation coefficent β**	**Seismic quality factor**	**Seismic efficiency k**
Quartzite	1.00	4800	5	24	-3.72	35	$3.39 \cdot 10^{-3}$
Sandstone (25% porous)	1.06	2900	5	14.5	-5.07	43	$2.56 \cdot 10^{-3}$
Tuff	1.06	2100	5	10.5	-5.26	57	$2.02 \cdot 10^{-3}$
Fully water saturated sandstone (25% water content)	3.01	3680	10	37	-13.00	6.5	$8.2 \cdot 10^{-5}$
Sandstone (12% porous)	1.03	4000	5	20	-4.82	32	$3.00 \cdot 10^{-3}$
Sandstone (35% porous)	1.06	2500	5	12.5	-5.12	49	$2.18 \cdot 10^{-3}$
Sandstone (50% porous)	1.09	1460	5	7.3	-5.30	81	$2.20 \cdot 10^{-3}$
Partially water saturated sandstone (12.5% water content, 12.5% empty pore space)	not determined	3080	7	21.1	-4.55	17	$1.12 \cdot 10^{-3}$
Fully water saturated sandstone (12.5% water content)	1.03	4200	8	33.6	-5.25	32	$1.37 \cdot 10^{-4}$
Literature data							
Fully water saturated sandstone (Hoerth *et al.*, 2014)				52		16	
Sandstone (25% porous) (Hoerth *et al.*, 2014)				52		26	
Berea and Malisson Ss (Winkler and Nur, 1979)				52		100-40	
Partially water saturated sandstone (Winkler and Nur, 1979)						< 15	

6.6 Discussion

We have shown that laboratory and numerical experiments are complimentary. Laboratory experiments provide ground truth data, but due to the complicated setup, the small number of the acoustic sensors and pressure gauges, and the limited number of different target materials a systematic study of the dependency of seismicity on material properties such as porosity and the degree of water-saturation is difficult. In turn, numerical models

allow for detailed analysis of seismic signals for materials with a range of different porosities and water-saturations, but thorough calibration of material model parameters, in the present study we focused on those affecting compaction of porosity, is essential to obtain reliable results. We identified the elastic threshold parameter ε_e and the speed of sound ratio χ as most important parameters having a significant effect on the characteristics of impact-induced elastic waves.

In our numerical experiments we observe a small increase of seismic efficiency with increasing pressures, which is caused by the fact that the pressure amplitudes in the far-field are affected by the crushing processes in the near-field, which is controlled by the elastic threshold parameter. Thus, a correct calibrated elastic threshold value and the correct determination of pressure amplitudes in the far-field is essential for a correct parameter calculation. Changing the absolute value of the elastic threshold parameter by ± 0.025 leads to pressure amplitudes that deviate by about $\pm 8\,MPa$ at the respective gauge point ($\sim 15\,\%$). The deviations are about the same at each sensor. Larger absolute threshold values (later onset of crushing) would lead to larger pressure amplitudes, lower threshold values (earlier onset of crushing) to smaller pressure amplitudes. These differences in pressure amplitude in turn would lead to a change of the seismic efficiency of about $40\,\%$ ($\Delta k = 0.001$). The mentioned error estimations are carried out for sandstone as a representative material.

The experiments provided data of pressure amplitudes recorded at only three points in the target block with errors of about $10\,\%$ ($\pm 3\,MPa$ for sensor 3, furthermost sensor, and $\pm 5\,MPa$ for the closest sensor to the impact point) which were due to uncertainties in the calibration method. The calibration method and measurement of the data are explained in Hoerth *et al.* (2014). The errors are in the same range as the numerical errors. This leads to the assumption that the correct determination of the threshold value underlies these errors. Since the pressure deviations are the same at different distances, the decay rate is constant with distance. Consequently, as the quality factor only depends on the attenuation coefficient, the quality factor is independent of pressure amplitude and distance. Thus, the determination of the seismic quality factor is not affected by the elastic threshold parameter.

Deviations of our results from those stated by Hoerth *et al.* (2014) using only three gauge points and literature data may be explained as follows: Hoerth *et al.* (2014) make the assumption of identical wave lengths for different materials (e.g. dry and wet). However, in our models show, the wave length may be significantly different with respect to the material, in particular if water is involved. In the numerical simulation of impacts into wet targets it was difficult to determine the pulse duration (and further the wave length) correctly due to a very broad recorded signal. Additionally, the wavelength depends on the size scale, for larger impacts we expect longer wavelengths. Larger projectiles cause longer

shock pulses as the shock wave has to travel through the projectile before it is turned into a release waves, which defines the length of the shock pulse (see e.g. Melosh, 1989, p. 54). Although it is not very well known, it appears to be natural that, while the shock wave attenuates, the resulting seismic wave has also a longer wavelength. However, whereas the quality factor is not dependent on the size-scale of the impact event, the attenuation coefficient is dependent on the wavelength and therefore on the scale of the event.
The numerical approach has the advantage that materials of different porosities and/or water saturation can easily be taken into consideration and a large number of gauge points to record elastic wave signals and thermodynamic and mechanical parameters on an arbitrary size-scale is possible.
Further improvements of the material models, in particular for water-saturated materials, will allow for a more accurate determination of the signals. So far we used a mixed-material approach described in detail in Güldemeister *et al.* (2013), which may not reproduce the actual process of the compaction of water-filled pores very well.

6.7 Implications of impact seismicity

In order to assess how different seismic efficiencies resulting from different target properties may change the seismic magnitude, we calculated the magnitude for different impact events of different size (impact energy). To calculate the seismic magnitude, we used Equation 6.7 where k represents the seismic efficiency and E_{imp} the impact energy (Melosh, 1989).

$$M = (log_{10}(k \cdot E_{imp}) - 4.8)/1.5 \tag{6.7}$$

Considering the commonly used value of $k = 10^{-4}$, the equation becomes:

$$M = 0.67 log_{10} E_{imp} - 5.87 \tag{6.8}$$

So far only the commonly established value of $k = 10^{-4}$ has been used to calculate the seismic efficiency. Here we consider a range of k values taking different target properties (porosity/water saturation) into account. Figure 6.8 shows the seismic magnitudes for impact events of different size considering a range of seismic efficiencies with respect to different target properties. We used seismic efficiencies obtained in a solid, a "dry" porous, and a "wet" target in comparison to the established value of $k = 10^{-4}$. The seismic magnitude is reduced by about one magnitude in water-saturated material compared to a solid and "dry" porous target, where the seismic magnitudes are similar. According to our study, previous estimates of the impact-induced seismic magnitude assuming $k = 10^{-4}$ best approximate impacts into "wet" target. A comparable impact event in a dry target

(solid or porous material) results in a significantly larger seismic magnitude than previously suggested.

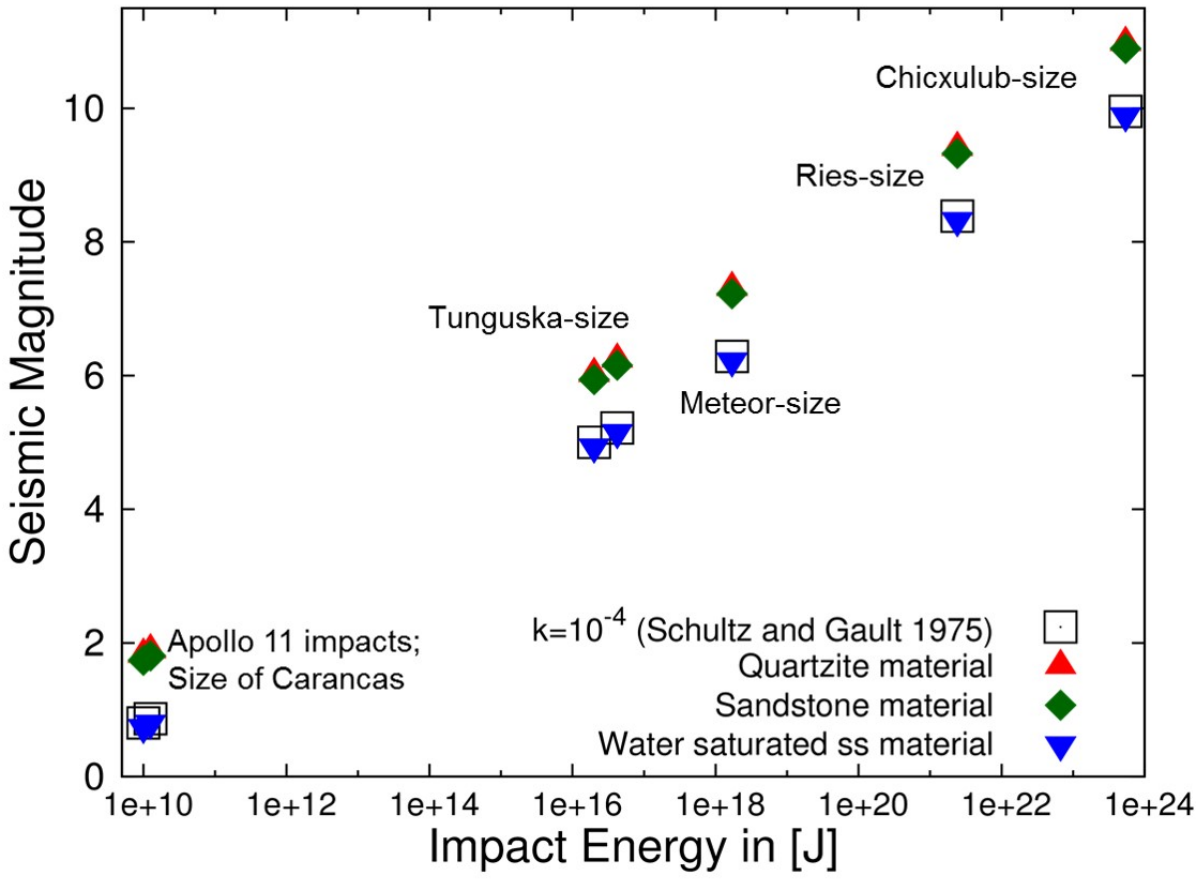

Figure 6.8: Influence of target dependent seismic efficiencies on resulting seismic magnitudes for a range of impact energies (size of impact event). The names of the impact events are only for reference to the approximate size/energy of the impact event

To further assess the consequences of an impact-induced earthquake or any quake on a planetary body it is important to estimate the strength of the seismic wave as a function of distance that can be expressed by an "effective" seismic magnitude following Collins *et al.* (2005). Collins *et al.* (2005) suggest a parametrization that is based on empirical data from earthquakes to relate the effective seismic magnitude to the actual seismic magnitude and the distance from the point of impact. In these equations the attenuation of the effective seismic magnitude is subdivided into three regimes. Figure 6.9 shows the effective seismic magnitudes as shaded areas as a function of distance for three different impact scenarios (Chicxulub-, Ries- and Meteor-sized impact events) considering two different seismic efficiencies; for quartzite (upper limit of shaded area) and water saturated sandstone (lower limit of shaded area), which covers the range of obtained seismic efficiencies in this work. These estimates may be improved by the use of the seismic quality factor Q that was determined for different materials in this work. Due to the much larger

scale of the chosen impact scenarios we recalculated β by adjusting the much larger wavelength in Equation 6.4 for the given examples. Therefore we used the respective impact energies (Chicxulub-size: $E_{imp} = 5.43 \cdot 10^{23}\,J$; Ries-size: $E_{imp} = 2.4 \cdot 10^{21}\,J$; Meteor-size: $E_{imp} = 1.7 \cdot 10^{18}\,J$) and numerically determined pulse durations (Chicxculub-size: $\Delta t = 2.2\,sec$; Ries-size: $\Delta t = 0.7\,sec$; Meteor-size: $\Delta t = 0.04\,sec$) for the mentioned impact events. The wavelengths have been determined using the different wave velocities for the three used materials (quartzite, sandstone, water saturated sandstone; Table 6.4). The used quality factors for those materials are also listed in Table 6.4.

We calculated the amplitudes in a certain distance from the point of impact for different material properties (quality factor, wavelength of the seismic signal) using Equation 6.3 and converted the amplitudes into a magnitudes ($M = log(A)$). The results are shown as symbols in Figure 6.9. For a water saturated material, even for large scale impact event, the seismic magnitude decreases more rapidly with distance compared to a "dry" material. For distances closer to the impact point our data agree well with the estimates based on the empirical relationships. At larger distances the estimates based on this work predict a much faster attenuation of the effective seismic magnitude.

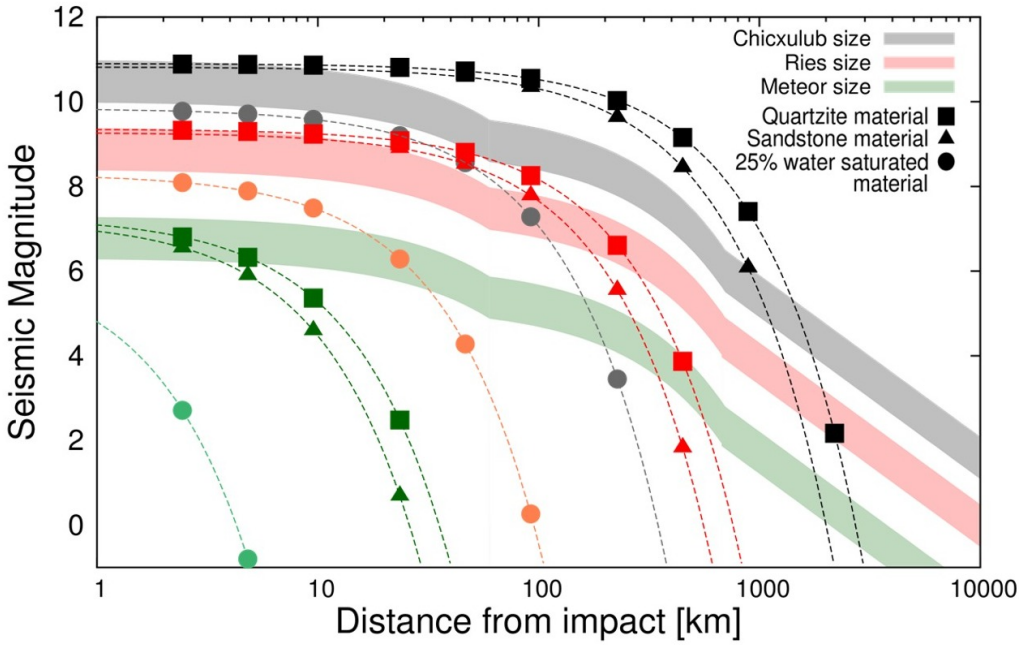

Figure 6.9: Effective seismic magnitudes as a function of distance (logarithmic scale) considering different impact scenarios (black data points - Chicxulub-size: $E_{imp} = 5.43 \cdot 10^{23}\,J$, $\Delta t = 2.2\,sec$; red data points - Ries-size: $E_{imp} = 2.4 \cdot 10^{21}\,J$, $\Delta t = 0.7\,sec$; green data points - Meteor-size: $E_{imp} = 1.7 \cdot 10^{18}\,J$, $\Delta t = 0.04\,sec$) and numerically determined pulse durations into different target materials. The shaded areas indicate the range of the effective seismic magnitude for the three cases using an upper limit and lower limit of the seismic efficiency of $3.39 \cdot 10^{-3}$ and $8.2 \cdot 10^{-5}$, respectively. The attenuation was calculated according to the parametrization of Collins *et al.* (2005). The dashed lines and data points represent estimates of the attenuation of the seismic wave using Equation 6.3 (amplitudes are converted into magnitudes using $M = log(A)$) and the range of attenuation factors for the different material as stated in Table 6.4

6.8 Conclusion

Determination of seismic parameters in numerical simulations calibrated by laboratory impact experiments in competent rocks represents a novel approach that allows for a quantitative assessment of the impact-induced seismicity on an arbitrary scale and for different target materials. Most previous studies where seismic signals were recorded and analyzed to determine the seismic efficiency of impact events used granular target material, mostly sand (Richardson and Kedar, 2013), and are much smaller in size in comparison to natural impacts (e.g. Tunguska airburst event; Ben-Menahem, 1975). Thorough validation and calibration of crucial material models in our numerical experiments we have carried out in this study and previous work (Güldemeister *et al.*, 2013, 2015) is essential to give confidence in the accuracy of our results. Based on rigorous testing of our models we identified porosity and water content as key parameters for the seismic efficiency of impact events. Model parameters defining the material response to compressive wave such as the crushing strength (in our model expressed by an elastic-plastic transition strain ε_e). We would expect the same small effect considering different strength of the material. However, the influence of the yield strength of the material on seismic efficiency is not covered by this study.

According to our study the biggest difference occurs between dry and wet targets with a seismic efficiency on the order of 10^{-3} and 10^{-5}, respectively. These values fall in the range of previous estimates (Hoerth *et al.*, 2014; Melosh, 1989; Schultz and Gault, 1975; Gault and Heitoweit, 1963), but for the likely case of an impact into a relatively dry target our value for the seismic efficiency ($k \sim 10^{-3}$) is about one order of magnitude larger than commonly used estimates ($k \sim 10^{-4}$). While the smaller k-values suggest an underestimation of the seismic consequences of an impact effect, we also show that the seismic waves tend to decay much faster than in previously suggested parametrization to predict the seismic attenuation (Collins *et al.*, 2005). Water serves again as a strong absorption agent as waves decay faster in wet than in dry targets. The determined quality factors are generally in good agreement with literature data from seismology.

In conclusion, numerical models give new insights on seismic parameters of impact events into different lithologies. Besides better estimates of the seismic hazard of impact events on Earth, they deliver important constrains for the interpretation of seismic data that have been recorded during the Apollo missions on the Moon and will be obtained by the InSight mission on Mars. In both cases impacts are considered as an important seismic source for lunar and martian quakes. The seismic signals and the associated energies from which we can estimate the impact energy by using the constrained seismic efficiencies may give some indications of the impactor's energy and target properties than can be correlated with observations of impact flashes. For example the lunar impact flash that

was detected on March 17th, 2013 associated with an impact in Mare Imbrium (Moser *et al.*, 2015) may help to validate impact models by comparing the size of the crater with the brightness of the flash.
With respect to seismic parameters the new data provide important constraints in order to gain further knowledge from natural observation during and after an impact event on Earth or on any other planetary surface.

Acknowledgments

This research is part of the MEMIN program supported by the German Science Foundation DFG (Research Unit FOR-887; WU 355/6-2). We gratefully acknowledge the developers of iSALE-2D; including Gareth Collins, Kai Wünnemann, Dirk Elbeshausen, Boris Ivanov, and Jay Melosh. We thank two anonymous reviewers for their constructive comments that significantly contributed to improve the manuscript.

7 Scaling impact crater dimensions in competent rock by numerical modeling and laboratory experiments

This chapter has been published as the following peer-reviewed article:

Güldemeister N., Wünnemann K., Poelchau M.H., 2015. *Scaling impact crater dimensions in cohesive rock by numerical modeling and laboratory experiments.* In Osinski, G.R., and Kring, D.A., eds., Large Meteorite Impacts and Planetary Evolution V: Geological Society of America Special Paper 518, p. 17-29, https://doi.org/10.1130/2015.2518(02).

Abstract

Laboratory and numerical cratering experiments into sandstone and quartzite targets were carried out under conditions ranging from pure strength- to pure gravity-dominated crater formation. Numerical models were used to expand the process of crater formation beyond the strength-dominated laboratory impact experiments up to the gravity regime. We focused on the effect of strength and porosity on crater size and determined scaling parameters for two cohesive materials, sandstone and quartzite, over a range of crater sizes from the laboratory scale to large terrestrial craters. Crater volumes and diameters of experimental and modeling data were measured, and scaling laws were then used to determine μ-values for these data in the strength and gravity regimes. These μ-values range between 0.48 and 0.55 for sandstone and between 0.49 and 0.64 for quartzite. The scaled crater dimensions in numerical models agree quite well with experimental observations. An accurate definition of the strength parameter in pi-group scaling is crucial for predicting the crater size, in particular, in the transitional regime from strength to gravity scaling. We determined an effective strength value that accounts for the weakening of target material due to the accumulation of damage. Using the numerical models, we

found an effective strength of $4.6\,kPa$ for quartzite and $3.2\,kPa$ for sandstone, which are almost five orders smaller than the quasi-static experimental strength values that only account for the intact state of the target material.

7.1 Introduction

The study of impact craters has the potential to provide important insights into the mechanical properties of the crust and can also improve the precision of dating planetary surfaces with crater size-frequency distributions. Both require a comprehensive understanding of the relationship between crater size and the impactor's velocity and mass and the way in which this relationship is affected by the properties of the projectile and the target, such as density, strength, porosity, as well as the gravitational field. Experimental crater data from laboratory and field experiments have been used to derive scaling laws (e.g. Holsapple, 1993; Schmidt and Housen, 1987), which are based on dimensionless ratios of the main physical parameters that influence crater formation. Within certain limits, these ratios, or "pi-groups", can be used to extrapolate experimental data to impact processes on planetary surfaces. Scaling laws differentiate between two regimes, the strength and the gravity regime. In the strength regime, the strength of the target material is the dominant factor that halts the excavation process and constrains the size of the crater, while gravity has a negligible effect on cratering. This typically occurs when the size scale of the impact is small, i.e., for small projectiles. As projectile sizes increase, the influence of gravity on crater excavation becomes increasingly important and can replace target strength as the dominant factor constraining crater size, as long as all other conditions remain constant. Target material properties can have a major influence when the transition between these two regimes takes place on a planetary body. For example, target porosity, water saturation, and the compressive and tensile limits of the target rock are factors that constrain crater sizes and must be taken under consideration. Furthermore, the resistance of rocks to plastic deformation is difficult to parametrize, in particular, if the number of parameters used to describe the material behavior is intended to be small. For instance, the yield envelope of a simple Mohr-Coulomb model of the shear failure of matter requires only two parameters, the cohesion and dry friction coefficient. However, for complex behavior of rocks under a dynamic load, such a model may be too simplistic. On the other hand, much of the data that have been used to calibrate scaling laws are based on laboratory cratering experiments in granular target material such as sand that can be well described by a Mohr-Coulomb strength model. While scaling laws do incorporate the transition of impact crater dimensions from the strength- to the gravity-dominated regime, empirical data are relatively limited (Schmidt, 1980).

As an alternative to laboratory and field cratering experiments, computer simulations can be used to conduct numerical experiments over a much broader parameter space (e.g. Wünnemann *et al.*, 2011). While hypervelocity impact experiments in solid rocks are limited to the strength regime, numerical models can expand the impact processes in the same solid rocks up to gravity-dominated crater formation. Validating the numerical models against laboratory-scale experiments increases the level of confidence for model results of realistic dimensions for natural craters. In addition to the scale invariance, numerical models can be used to investigate the effect of independent material properties by varying only one parameter at a time. However, all these advantages of numerical modeling over experiments come at a price; adequate and thoroughly tested material models are required to simulate the behavior of rock under extremely dynamic strain rates, stresses, and pressure conditions.

In a number of previous experimental and modeling studies, the effect of porosity and water saturation was recognized as an important parameter affecting the size of a crater resulting from an impact of given mass and velocity (Love *et al.*, 1993; Wünnemann *et al.*, 2006; Baldwin *et al.*, 2007). Recent improvements of material models in hydrocode simulations (Wünnemann *et al.*, 2006; Collins *et al.*, 2011a) that have been validated against micro- and macroscale observations (Güldemeister *et al.*, 2013; Kowitz *et al.*, 2013a) have enabled a more thorough investigation of the effects of porosity (e.g. Wünnemann *et al.*, 2011). Sophisticated strength models account for the complex behavior of rock during crater formation and take fracturing and brittle deformation as well as granular flow into consideration (Collins *et al.*, 2004).

In this study, we present a combined approach of laboratory cratering experiments carried out within the MEMIN *(Multidisciplinary Experimental and Modeling Impact research Network)* program, and numerical modeling. Our goal is, on the one hand, to calibrate our material models against the data from experiments. This aims at determining material parameters such as cohesion and crushing strength of pore space, etc., under dynamic conditions. On the other hand, we present a suite of numerical experiments ranging from pure strength- to pure gravity-dominated crater formation in order to upscale previously published crater size-scaling results from experiments (Poelchau *et al.*, 2013, 2014) to natural crater dimensions, and to confirm previously suggested scaling relationships (Holsapple and Housen, 2007). In particular, we investigate the effect of strength and porosity on crater size and how specific scaling parameters can be obtained for impact scenarios where crater size is controlled by both gravity and strength.

7.2 Methods

7.2.1 Pi-group-scaling

Scaling laws describe the relationship among the characteristics of the impactor (diameter L, density δ, impact velocity U, mass m), the target (density ρ, strength Y) and the morphometry of the transient crater (diameter D, depth d, volume V). The main goal of scaling laws is to extrapolate results obtained by small-scale laboratory impact experiments to the dimension of natural craters on planetary surfaces. By using dimensionless ratios, they make laboratory craters directly comparable to kilometer-sized craters and can predict crater sizes for an impactor of a given size, mass, and velocity. In the most commonly used so-called Pi-group scaling (e.g. Holsapple, 1993), the dimensionless ratios that describe the properties of projectile and target are given by:

$$\pi_2 = \frac{g \cdot L}{U^2}, \qquad \pi_3 = \frac{Y}{\rho \cdot U^2}, \qquad \pi_4 = \frac{\rho}{\delta} \tag{7.1}$$

Note, that for π_2 we neglect here the geometry factor of 1.61 for spherical projectiles. Accordingly, the crater diameter D and volume V are expressed relative to the projectile mass m:

$$\pi_V = \frac{V \cdot \rho}{m}, \qquad \pi_D = D \cdot \left(\frac{\rho}{m}\right)^{\frac{1}{3}} \tag{7.2}$$

We do not consider the dimensionless ratio for the crater depth π_d in this work. We also neglect the effect of the impact angle, which has been investigated numerically in detail by Elbeshausen *et al.* (2009) and by Davison *et al.* (2011) and experimentally by several workers, e.g. Gault and Wedekind (1978); Burchell and Whitehorn (2003). Scaling laws are expressions that relate the scaled crater dimensions π_D and π_V to the gravity-scaled impact size π_2, the strength-scaled impact size π_3, and the ratio of target and projectile density π_4:

$$\left.\begin{matrix}\pi_V \\ \pi_D\end{matrix}\right\} = f\left(\pi_2, \pi_3, \pi_4\right)$$

$$\left.\begin{matrix}\pi_V \\ \pi_D\end{matrix}\right\} = \left.\begin{matrix}\frac{V \cdot \rho}{m} \\ D \cdot \left(\frac{\rho}{m}\right)^{\frac{1}{3}}\end{matrix}\right\} = f\left(\frac{g \cdot L}{U^2}, \frac{Y}{\rho \cdot U^2}, \frac{\rho}{\delta}\right)$$

The functional relationships f are given by power laws with scaling parameters μ, ν, K_1, K_2, K_3 and K_4 (e.g. Housen and Holsapple, 2003):

$$\pi_D = K_1 \cdot \left[\pi_2 \cdot \pi_4^{\frac{2+\mu-6\nu}{-3\mu}} + \left(K_2 \pi_3 \cdot \pi_4^{\frac{2-6\nu}{-3\mu}} \right)^{\frac{2+\mu}{2}} \right]^{\frac{-\mu}{2+\mu}} \tag{7.3}$$

$$\pi_V = K_3 \cdot \left[\pi_2 \cdot \pi_4^{\frac{6\nu-2-\mu}{3\mu}} + \left(K_4 \cdot \pi_3 \cdot \pi_4^{\frac{6\nu-2}{3\mu}} \right)^{\frac{2+\mu}{2}} \right]^{\frac{3\mu}{2+\mu}} \tag{7.4}$$

The theoretical limits for the scaling exponent μ in Equations 7.3 and 7.4 are given by $\mu = 1/3$ if pure momentum scaling applies and by $\mu = 2/3$ if crater size is proportional to impact energy (Holsapple, 1993). According to Holsapple and Housen (2007) the parameter ν is $\sim$ 0.4 for most materials.

Depending on the impact scenario, the π_2-term (gravity-scaled size) or the π_3-term (strength-scaled size) may dominate. For example, for a large natural crater on Earth, the effect of strength is negligible, and gravity dominates, whereas for small (laboratory) craters in cohesive material, gravity is not significant, and strength dominates the formation of the crater. Theoretically, the transition between the two regimes occurs when the terms inside the brackets in Equations 7.3 and 7.4 are equal (Holsapple, 1993). Thus, in Equation 7.4, the term for the gravity-scaled size

$$\left(\pi_2 \cdot \pi_4^{\frac{6\nu-2-\mu}{3\mu}} \right)$$

has to be equal to the term for the strength-scaled size

$$\left(K_4 \cdot \pi_3 \cdot \pi_4^{\frac{6\nu-2}{3\mu}} \right).$$

However, laboratory-scale craters have to be considered as gravity-dominated if the strength of the target material is negligible, such as in granular materials. Equations 7.3 and 7.4 are simplified as follows for pure gravity- and strength-dominated regimes, respectively (Housen and Holsapple, 2003):

$$\pi_V = K_3 \cdot K_4^{\frac{-3\mu}{2}} \cdot \pi_3^{-\frac{3\mu}{2}} \cdot \pi_4^{1-3\nu} \qquad \text{(strength dominated)} \tag{7.5}$$

$$\pi_D = K_1 \cdot K_2^{-\frac{\mu}{2}} \cdot \pi_3^{-\frac{\mu}{2}} \cdot \pi_4^{\frac{1}{3}-\nu} \qquad \text{(strength dominated)} \tag{7.6}$$

$$\pi_V = K_3 \cdot \pi_2^{-\frac{3\mu}{2+\mu}} \cdot \pi_4^{\frac{2+\mu-6\nu}{2+\mu}} \qquad \text{(gravity dominated)} \tag{7.7}$$

$$\pi_D = K_1 \cdot \pi_2^{-\frac{\mu}{2+\mu}} \cdot \pi_4^{\frac{2+\mu-6\nu}{3(2+\mu)}} \qquad \text{(gravity dominated)} \tag{7.8}$$

For the comparison of strength- and gravity-dominated craters, it has to be taken into

account that gravity causes late-stage modifications such as slumping of oversteepened crater walls, and in the case of large structures over a few km in diameter, the crater floor collapses and rises upward, forming the typical morphology of complex craters. To exclude these effects, the size of the transient crater in the case of gravity-dominated crater formation is considered as the appropriate measure of the impact energy. The determination of the diameter and the volume of the transient crater is relatively straightforward if the effect of gravity is small, which is usually the case on the laboratory scale. Then, the final crater corresponds approximately to the size of the transient crater. For strength-dominated craters like those generated in the MEMIN project and used as experimental constraints in the present study, spallation can cause significant enlargement of the crater; in these experiments, the transient crater has to be reconstructed (see Dufresne *et al.*, 2013; Poelchau *et al.*, 2013, 2014, for a discussion on this issue). Note that we always refer to the diameter D and volume V of the transient crater throughout this work. In the case of large gravity-dominated craters, the definition of the transient crater is more difficult because crater growth overlaps with gravity-driven modifications in space and time (e.g. O'Keefe and Ahrens, 1993). Here, we follow the method suggested by Elbeshausen *et al.* (2009), who showed that the point in time when the maximum crater volume is reached can be used to define the dimensions of the transient crater. To predict crater sizes for any given π_2, π_3, and π_4 values, the scaling parameters μ, ν, and K must be known. These parameters, and in particular the scaling exponent μ, can be determined through power-law fits using Equations 7.5 - 7.8 to the results from a series of laboratory and/or numerical experiments. Power-law fitting provides the values for μ and K. The scaling parameters depend on material properties that are not considered in the dimensionless ratios so far. Holsapple and Housen (2007) gave μ values for sand or cohesive soil of $\mu = 0.41$, for water, wet soils, and rock of $\mu = 0.55$, and for highly porous material of $\mu = 0.40$. Elbeshausen *et al.* (2009) and Wünnemann *et al.* (2011) suggested expressing μ as a function of the coefficient of friction, and K as a function of porosity in the gravity regime. Note, that according to the principles of pi-group scaling, the scaling exponent μ can be determined by cratering experiments in either the strength or gravity regime. Ideally, the scaling parameters are material properties and can be determined independently, regardless of whether an experimental or modeling approach is used.

However, the scaling parameters may be significantly affected by the material model used to describe strength, i.e., the dynamic resistance of material against shear deformation. As stated already, strength is a very complex material property that depends on the strain rate, confining pressure, temperature, and the deformation history (damage) (see also Section 7.2.3). In the definition of the dimensionless parameter π_3, it is expressed only by a scalar value, which may oversimplify the conditions, and it is unclear which measurable strength parameter should be used for Y in Equation 7.3 and 7.4.

7.2.2 Laboratory experiments

The laboratory impact cratering experiments were carried out at the Fraunhofer Ernst-Mach-Institute (EMI) in Freiburg, Germany, using quartzite and sandstone as targets. We used 2.5, 10 and 12 mm spherical projectiles composed either of steel or iron meteorite with densities of 8.1 and 7.8 $g\,cm^{-3}$, respectively, which were accelerated to velocities between 2500 to 5500 $m\,s^{-1}$. The sandstone has a porosity of 23 %. The density of the quartzite is 2.65 $g\,cm^{-3}$, and the density of the porous sandstone is 2.05 $g\,cm^{-3}$. The uniaxial compressive strength (UCS) of the target material was measured to be 292 MPa for the quartzite target and 67 MPa for the sandstone. These UCS values were determined under quasi-static conditions (Poelchau *et al.*, 2013, 2014), and it is expected that the strength behavior during the impact, as a very dynamic process, may be very different. For example, brittle fracturing and the accumulation of damage in the target lead to a weaker bulk behavior of the target material and thus to lower strength than for intact target material. Material failure results in a lower strength than the intact material. Using the measured UCS values for Y in the strength scaling Equations (7.5 and 7.6) may overestimate the actual resistance of the target material against shear failure, and the strength-scaled size π_3 may be assumed to be too large for a given crater size π_D and π_V. The experimental configuration and further properties of the target materials have been described in detail in Kenkmann *et al.* (2011) and Poelchau *et al.* (2013, 2014).
The dimensions of the generated craters were obtained by three-dimensional (3-D) scanning techniques (Dufresne *et al.*, 2013). As mentioned already, the size of the final craters is significantly enlarged due to spallation. The size of the transient crater, which we consider throughout this work, was estimated using methods presented in Poelchau *et al.* (2014). This method assumes a parabolic shape of the transient crater. To constrain the parabola, 3-D scans of the crater and high-speed videos of the impact process were used. The 3-D scans of the crater morphology give an estimation of the maximum depth of the parabola, which should lie above the crater floor. High-speed videos give an estimation of the furthest extent of the ejecta flow field, which defines the maximum width of the parabola. Based on these constraints, the rotational volume of the parabola can be calculated, giving an estimation of the transient crater volume. Poelchau *et al.* (2014) assumed a volumetric error of < 10 % for this method. Note that in order to determine the scaling parameters as described in the previous section "Pi-Group Scaling", π_2 and π_3 must be varied over as large a range as possible. In this regard, the MEMIN experiments are limited, and different values for π_2 and π_3 only result from small differences in impact velocity (π_2 and π_3) and projectile size (π_2). In previous studies of cratering experiments in granular targets in the gravity regime, it was possible to vary π_2 over several orders of magnitude

by using a centrifuge to simulate increased gravity conditions (e.g. Schmidt and Housen, 1987; Housen and Holsapple, 2003).

7.2.3 Numerical modeling

We carried out numerical impact experiments over three orders of magnitude for π_3 and eight orders of magnitude for π_2 in order to determine the scaling parameters for strength- and gravity-dominated crater formation. We used the iSALE-2D shock physics code (Wünnemann *et al.*, 2006) to perform a suite of numerical simulations. iSALE is based on the SALE hydrocode solution algorithm (Amsden *et al.*, 1980). To simulate hypervelocity impact processes in solid materials, SALE was modified to include an elasto-plastic constitutive model, fragmentation models, various equations of state (EOS), and multiple materials (Melosh *et al.*, 1992; Ivanov *et al.*, 1997). More recent improvements include a modified strength model (Collins *et al.*, 2004) and a porosity compaction model (Wünnemann *et al.*, 2006; Collins *et al.*, 2011a). To describe the thermodynamic state of the projectile and target material, we used an analytical equation of state (Thompson and Lauson, 1972) for iron and for quartzite (Melosh, 2007), respectively. The analytical equation of state for quartzite was combined with the ε–α compaction model (Wünnemann *et al.*, 2006) to simulate the porous sandstone target with a porosity of 23 %. The iron projectile was resolved by 12 cells per projectile radius (CPPR). The dimension of the computational domain was of the same size as the target blocks in the laboratory experiments, with a grid size of 800×1000 cells. The target density was $2.65\,g\,cm^{-3}$ for the quartzite target and $2.0\,g\,cm^{-3}$ for the sandstone target. The density of the projectile was $7.84\,g\,cm^{-3}$. To carry out numerical impact experiments in the strength regime for different π_3 values, we varied the impact velocities from 2000 to $20,000\,m\,s^{-1}$ to cover a range of π_3 values over three orders of magnitude ($\sim 10^{-3}$ to $\sim 10^{-5}$). For the gravity scaling, we varied only the impactor size L from $0.012\,m$ to $300,000\,m$, corresponding to π_2 values over a range of eight orders of magnitude ($\sim 10^{-9}$ to $\sim 10^{-1}$). However, by increasing the impactor size to such large dimensions, the scaling laws may not strictly be applicable because density and gravity are not constant anymore, and for the very extreme cases where projectiles are more than $100\,km$ in diameter, the target surface cannot be considered to be flat anymore. Nevertheless, such a theoretical study allows for a better interpolation and determination of the scaling parameters. The gravity was set to $9.81\,m\,s^{-2}$ (Earth gravity), and the impact velocity was kept constant at $5000\,m\,s^{-1}$. The choice of a relatively low impact velocity of $5000\,m\,s^{-1}$, which is below the escape velocity on Earth, is justified to allow for a direct comparison with the experiments, which

were conducted at the same velocity range. We assume a constant temperature in the target, even in case of very large impactors, to avoid effects of thermal softening or partial melting of the target. The crater diameter and volume were recorded during the numerical simulation. The transient crater was determined at the point in time during the simulation when the maximum crater volume was reached (see Elbeshausen *et al.*, 2009). A list of all models that were carried out for strength and gravity scaling and the resulting scaled crater dimensions are given in Table 7.1.

Strength in iSALE

In order to model crater formation in the strength regime, it is essential to use a sophisticated constitutive model describing the mechanical material behavior during crater formation. We used a strength model proposed by Collins *et al.* (2004) to account for rock failure if stresses exceeded a certain threshold, the yield surface. In this model, the yield strength is a function of the pressure P. Additionally, it is also important to take into account that the pristine (intact) material is much stronger than material that has already undergone failure (damaged). Therefore, the yield strength is also a function of the deformation history. In order to introduce the material parameters to describe the resistance to plastic deformation in our model, we state here the parametrization of the yield envelope and refer for further details to Collins *et al.* (2004) and Ivanov *et al.* (1997). Accordingly, the yield strength Y_i of the intact rock is given by Lundborg (1968):

$$Y_i = Y_{i0} + \frac{\beta_i P}{1 + \frac{\beta_i P}{Y_{im} - Y_{i0}}} \tag{7.9}$$

The parameter Y_{im} is the limiting strength at high pressure and can be estimated from the Hugoniot elastic limit (Melosh, 1989, p.35). Here, β_i is the coefficient of friction, and Y_{i0} is the cohesion of the intact material at zero pressure. It is common in most strength models to use the second invariant of the stress tensor J_2 to describe the stress state at a given location:

$$J_2 = \frac{(s_1 - s_2)^2 + (s_2 - s_3)^2 + (s_3 - s_1)^2}{6} \tag{7.10}$$

where s_1, s_2, s_3, are the principle deviatoric stresses. Equation 7.10 can be simplified to the following expression in a uniaxial compressive strength test:

$$J_2 = \frac{(s_1 - s_2)^2}{3} = \frac{Y_{UCS}^2}{3} \tag{7.11}$$

Table 7.1: Parameters and calculated pi-group values for strength and gravity scaling

Strength scaling						
Strength Y_{i0} [MPa]	Projectile diameter [m]	Impact velocity$[m\,s^{-1}]$	π_3	π_4	π_V	π_D
290	0.012	4000	0.006839623	2.95886792	34.63523423	6.12157177
290	0.012	4500	0.005404146	2.95886792	39.63736221	6.06395698
290[a]	**0.012**	**5000**	**0.004377358**	**2.95886792**	**56.10131962**	**6.84679798**
290	0.012	7500	0.001945493	2.95886792	119.0353534	8.71423746
290	0.012	10000	0.00109434	2.95886792	230.1693071	11.9550696
290	0.012	15000	0.000486373	2.95886792	378.8772122	13.6835134
290	0.012	20000	0.000273585	2.95886792	400.2247747	13.2514024
96.9	0.012	2000	0.009141509	2.95886792	12.73756574	4.39312798
96.9	0.012	3000	0.004062893	2.95886792	25.58719218	5.32936836
96.9[a]	**0.012**	**5000**	**0.001462642**	**2.95886792**	**60.88631133**	**7.48992311**
96.9	0.012	7500	0.000650063	2.95886792	130.7374783	10.5146997
96.9	0.012	10000	0.00036566	2.95886792	211.4211792	12.171125
96.9	0.012	12500	0.000234023	2.95886792	295.0931653	13.4674579
60	0.012	2000	0.007549069	3.94614997	2.91E+001	6.08477186
60	0.012	2500	0.004831404	3.94614997	3.95E+001	6.54276544
60	0.012	3000	0.003355142	3.94614997	5.04E+001	7.4587526
60	0.012	3500	0.002465002	3.94614997	5.88E+001	8.1784568
60	0.012	4000	0.001887267	3.94614997	8.35E+001	8.30931211
60	0.012	4500	0.001491174	3.94614997	1.01E+002	8.96358865
60[a]	**0.012**	**5000**	**0.001207851**	**3.94614997**	**1.16E+002**	**9.68329285**
60	0.012	7500	0.000536823	3.94614997	2.14E+002	11.8424054
60	0.012	10000	0.000301963	3.94614997	3.00E+002	13.7398074
22.7	0.012	2000	0.002856064	3.94614997	4.30E+001	6.67362075
22.7	0.012	3000	0.001269362	3.94614997	7.23E+001	8.1784568
22.7[a]	**0.012**	**5000**	**0.00045697**	**3.94614997**	**1.32E+002**	**9.87957581**
22.7	0.012	7500	0.000203098	3.94614997	2.68E+002	12.692965
22.7	0.012	10000	0.000114243	3.94614997	3.64E+002	13.7398074
22.7	0.012	12500	7.31E-005	3.94614997	3.64E+002	13.3472415
Gravity scaling						
Strength Y_{i0} [MPa]	Projectile diameter [m]	Impact velocity$[m\,s^{-1}]$	π_2	π_4	π_V	π_D
290	0.012	5000	4.71E-009	2.95886792	52.1160677	6.913775176
290	0.12	5000	4.71E-008	2.95886792	54.8305513	7.12983065
290	12	5000	4.71E-006	2.95886792	49.3257564	6.841756684
290	120	5000	0.000047088	2.95886792	33.3618512	5.833497805
290	400	5000	0.00015696	2.95886792	20.6062138	4.969275908
290	600	5000	0.00023544	2.95886792	17.620125	4.825238925
290	800	5000	0.00031392	2.95886792	15.4664351	4.393488069
290	1000	5000	0.0003924	2.95886792	13.8325428	4.470619873
290	2000	5000	0.0007848	2.95886792	10.0562551	3.893319646
290	3000	5000	0.0011772	2.95886792	8.14955582	3.672943062
290	4000	5000	0.0015696	2.95886792	7.11334738	3.168885641
290	6000	5000	0.0023544	2.95886792	6.31305135	3.024776639
290	8000	5000	0.0031392	2.95886792	5.79514464	2.873537807
290	15000	5000	0.005886	2.95886792	4.92413941	2.448628708
290	30000	5000	0.011772	2.95886792	4.22689358	2.232573234
290	60000	5000	0.023544	2.95886792	3.72597331	1.872480777
290	120000	5000	0.047088	2.95886792	1.98089318	1.663922427
290	300000	5000	0.11772	2.95886792	1.44884021	1.382755035
290	400000	5000	0.15696	2.95886792	1.66100509	1.440312213
290	500000	5000	0.1962	2.95886792	1.44744752	1.234148623
60	0.012	5000	4.71E-009	3.94614997	90.858361	8.571022725
60	0.12	5000	4.71E-008	3.94614997	93.4911249	8.898160997
60	1.2	5000	4.71E-007	3.94614997	89.3179141	8.571022725
60	12	5000	4.71E-006	3.94614997	80.2152731	8.251081495
60	120	5000	0.000047088	3.94614997	52.3751958	6.608193093
60	400	5000	0.00015696	3.94614997	27.3751424	5.103357042
60	600	5000	0.00023544	3.94614997	27.7840611	4.910999739
60	800	5000	0.00031392	3.94614997	21.552253	4.526285131
60	1000	5000	0.0003924	3.94614997	18.3303712	4.239712005
60	1200	5000	0.00047088	3.94614997	19.8017451	4.057168849
60	2000	5000	0.0007848	3.94614997	13.8212708	3.611606522
60	3000	5000	0.0011772	3.94614997	12.0386186	3.402238028
60	4000	5000	0.0015696	3.94614997	11.0408033	3.081642522
60	6000	5000	0.0023544	3.94614997	9.65720187	2.878816793
60	8000	5000	0.0031392	3.94614997	8.70597589	2.69398367
60	12000	5000	0.0047088	3.94614997	7.56219404	2.420823212
60	15000	5000	0.005886	3.94614997	7.07821721	2.289967904
60	30000	5000	0.011772	3.94614997	5.52608842	1.962829632
60	60000	5000	0.023544	3.94614997	3.51782064	1.701119014
60	120000	5000	0.047088	3.94614997	2.81481667	1.506798881
60	300000	5000	0.11772	3.94614997	1.68855391	1.223497137
60	400000	5000	0.15696	3.94614997	1.4266684	1.188041891
60	500000	5000	0.1962	3.94614997	1.257234	1.177678936

[a]The highlighted data are the results that have been used for the crater profiles in Figure 7.1.

In uniaxial compression, the hydrodynamic pressure P in Equation 7.9 is given by $P = \frac{Y_{UCS}}{3}$, and the second invariant J_2 equals $(Y_i)^2$. Thus, strength can be expressed as:

$$Y_i \left(P = \frac{Y_{UCS}}{3} \right) = \frac{Y_{UCS}}{\sqrt{3}} \tag{7.12}$$

By rearranging Equation 7.9 and substituting the expression for Y_i and P, we can calculate the strength value Y_{i0} at $P = 0$ (cohesion of the intact material) in the uniaxial compressive strength test, which, in the following, is denoted as Y_{P0} . Note that the value depends on the coefficient of friction, which was not measured for the given material. Here, we use the value $\beta = 0.8$, which has been estimated in previous studies (Kenkmann *et al.*, 2011). Models of the cratering experiments with $\beta = 0.8$ are in good agreement in terms of crater dimensions and correspond to typical values found in the literature (Scott and Nielsen, 1991). Accordingly, the estimated cohesion of the material in the uniaxial compressive strength tests is $Y_{P0} = 96.9\,MPa$ for quartzite and $Y_{P0} = 22.7\,MPa$ for sandstone. As stated already, it is important to distinguish in material modeling between the intact state and the state where material has already undergone failure (damage state). If J_2 is in excess of $(Y_i)^2$, the material fails and begins to accumulate damage. Damage is described by a scalar parameter D, where $D = 0$ represents the fully intact state and $D = 1$ corresponds to entirely damaged material. D is a function of plastic strain. If material has reached its maximum state of damage ($D = 1$), the yield strength is given by a simple Drucker-Prager yield surface:

$$Y_d = \min\left(Y_{d0} + \beta_d P, Y_{dm}\right)$$

where Y_{dm} is the limiting strength for the damaged material, Y_{d0} is the cohesion of the damaged material which is usually assumed to be zero, and β_d is the coefficient of friction for damaged material. For a partially damaged state, the yield strength is given by $Y = Y_d D + Y_i(1-D)$ using the damage quantity D. All material parameters used in iSALE to model crater formation in sandstone and quartzite are listed in Table 7.2. We chose a very similar set of strength parameters for sandstone and quartzite, as both rocks are compositionally very similar (almost pure SiO_2), and porosity is the only major variable. Therefore we assume the same coefficient of friction for both the intact and damaged state. According to the UCS measurements, the sandstone is much weaker than the quartzite at zero pressure and we also estimated that the limiting strength at high pressure Y_{im} is lower for sandstone than for quartzite. This is more or less an arbitrary choice; however these parameters do not affect the model results significantly as the strength limit is only achieved for an ambient pressure of $\sim 20\,GPa$, which is only reached during the very early stage of crater formation, where only a small fraction of the crater volume is evolved. Note that we do not consider the effect of strain rate on the yield strength in our model. Indeed,

Y_{UCS} and the corresponding Y_{i0} probably underestimate the actual resistance against shear failure. However, as we demonstrate in Section 7.3, our models are in reasonably good agreement with the observed crater sizes, and we therefore assume that the effect of rate dependence is negligible. We also account for thermal softening in our model as described in Collins *et al.* (2004). As the temperatures are relatively small due to the relatively low impact velocities, we consider this effect to be negligible and do not further discuss it here. It should be noted that the strength parameters used in the numerical models are not suited for the Y parameter used for crater scaling in π_3. The right choice of this parameter requires further discussion, which is subject of the following "Results" section.

Table 7.2: Material parameters used for the strength model in iSALE for quartzite and sandstone

Parameter for rock model	**Values for quartzite**	**Values for sandstone**
Uniaxial compressive strength Y_{UCS} [MPa]	292	67
Cohesion of intact material Y_{i0} [MPa] (see Eq. 7.12)	96.9	22.75
Cohesion of damaged material Y_{i0D} [MPa]	0	0
Limiting strength at high pressure for intact material Y_{im} [MPa]	1000	170
Limiting strength at high pressure for damaged material Y_{imD} [MPa]	1000	170
Coefficient of internal friction for intact material β_i	1.8	1.8
Coefficient of internal friction for damaged material β_d	0.67	0.67
Poisson's ratio	0.3	0.3
Quartz melting point at zero pressure [$°C$]	1600	1600
Specific heat capacity [$J/(kgK)$]	800	800
Initial distension of porous material α_0[a]	-	1.3333
Elastic volumetric strain threshold ε_{e0}[a]	-	0.1
Distension at transition from exponential to power-law compaction α_x[a]	-	1.1
Compaction rate parameter κ[a]	-	0.98
Ratio of porous to solid material sound speed χ[a]	-	0.6

[a] A detailed description of the porosity parameters are given in Wünnemann *et al.* (2006) and Güldemeister *et al.* (2013). The porosity model parameters α_x and χ were introduced, defined, and described in Collins *et al.* (2011a).

7.3 Results

7.3.1 Modeling of experimental craters

First, we compared cross sections of crater profiles for experimental craters with results from numerical modeling as shown in Figure 7.1 for both the quartzite target (Figure 7.1A) and the sandstone target (Figure 7.1B). The simulations were carried out with a strength model as described in the previous section, "Strength in iSALE", using the set of parameters listed in Table 7.2. The experimental crater profiles along three cross sections in different directions (dotted lines in Figure 7.1) were obtained from 3-D scans (Dufresne *et al.*, 2013) and differ slightly. In particular, the enlargement due to spallation varies in different directions, indicating that existing heterogeneities in the target significantly affect spallation. Anisotropy and/or heterogeneous effects were not considered in the models. The approximate transient crater (solid black line in Figure 7.1) was estimated by fitting a parabola to the inner part of the crater, using constraints from the crater morphology for the depth and from high-speed videos of the impact process for the width of the parabola (see also Kenkmann *et al.*, 2011; Hoerth *et al.*, 2013; Dufresne *et al.*, 2013). Generally, there was a reasonably good agreement between the approximate reconstruction of the experimental transient crater (solid black line in Figure 7.1) and the transient crater profile of the numerical model (dashed gray line in Figure 7.1) at the time when the maximum crater volume was reached. All simulations were stopped at the transient crater, and we did not simulate how material was ejected from the surface by spallation, enlarging the craters significantly. The computation time would have been significantly longer, and our goal was to conduct a sufficient number of models for a proper parameter study. The agreement, in particular with respect to crater depth, was somewhat better for the sandstone target (Figure 7.1B) than for the quartzite target (Figure 7.1A). The depth of the modeled crater in quartzite was slightly smaller than the depth of the approximate experimental transient crater, but the diameter was in very good agreement. Thus, a good fit can be achieved ("Model Y_{P0}" in Figure 7.1) by using the material strength Y_{P0} (as derived in the Section 7.2.3 - "Strength in iSALE") for the Y_{i0} parameter in the strength model (Equation 7.9). We also used the only available directly measured material property (compressive strength, Y_{UCS}) for the yield strength at zero pressure, Y_{i0}, in our models ("Model Y_{UCS}" in Figure 7.1) to avoid the bias from the estimated value from the coefficient of friction. As noted already, this parameter was measured under static conditions. To assess whether strain-rate hardening had an effect on our modeling results, we tested the effect of different strength values on crater volume and diameter. We used the following two values for the parameter Y_{i0} in the strength model (Equation 7.9) in order to test the

sensitivity of our models: (1) Y_{P0} , which corresponds to the estimated value of cohesion at zero pressure in an UCS experiment, and (2) the experimentally measured Y_{UCS}, which is significantly larger. We could have also chosen any arbitrarily larger value, as there are no empirical data available for the strain-rate hardening for the given material. We did not observe significant differences with respect to the size of the transient crater (Figure 7.1, dashed lines) when either the Y_{UCS} value or the Y_{P0} value, which is smaller by a factor of ~ 3, was used. Furthermore, the model profiles using Y_{P0} and $Y_{UCS} = Y_{i0}$ are very similar for quartzite and sandstone, showing only minor differences. The experimental crater shows a larger depth than the modeled crater into quartzite and a slightly smaller diameter than the modeled crater into sandstone. The deviation of the experimental crater from the modeled crater is less than 10 % and 20 % for crater diameter and crater volume, respectively, for the quartzite target. For the sandstone target, the data deviate by ~ 20 % for crater volume and crater diameter. Although the experimental and modeling profiles do not match perfectly, we could show that the models agree with the experiments in general and that the choice of the strength value in the range between Y_{P0} and Y_{UCS} (which corresponds to a factor of three, approximately) does not make much of a difference. The influence of strength is more apparent if the value for Y_{i0} varies by an order of magnitude. The two examples comparing experimental crater sizes with numerical models for two different lithologies demonstrate that our strength model describes the behavior of rocks reasonably well, and we can now proceed to vary the projectile diameter to cover a large range of the parameter space with regard to pi-group-scaling.

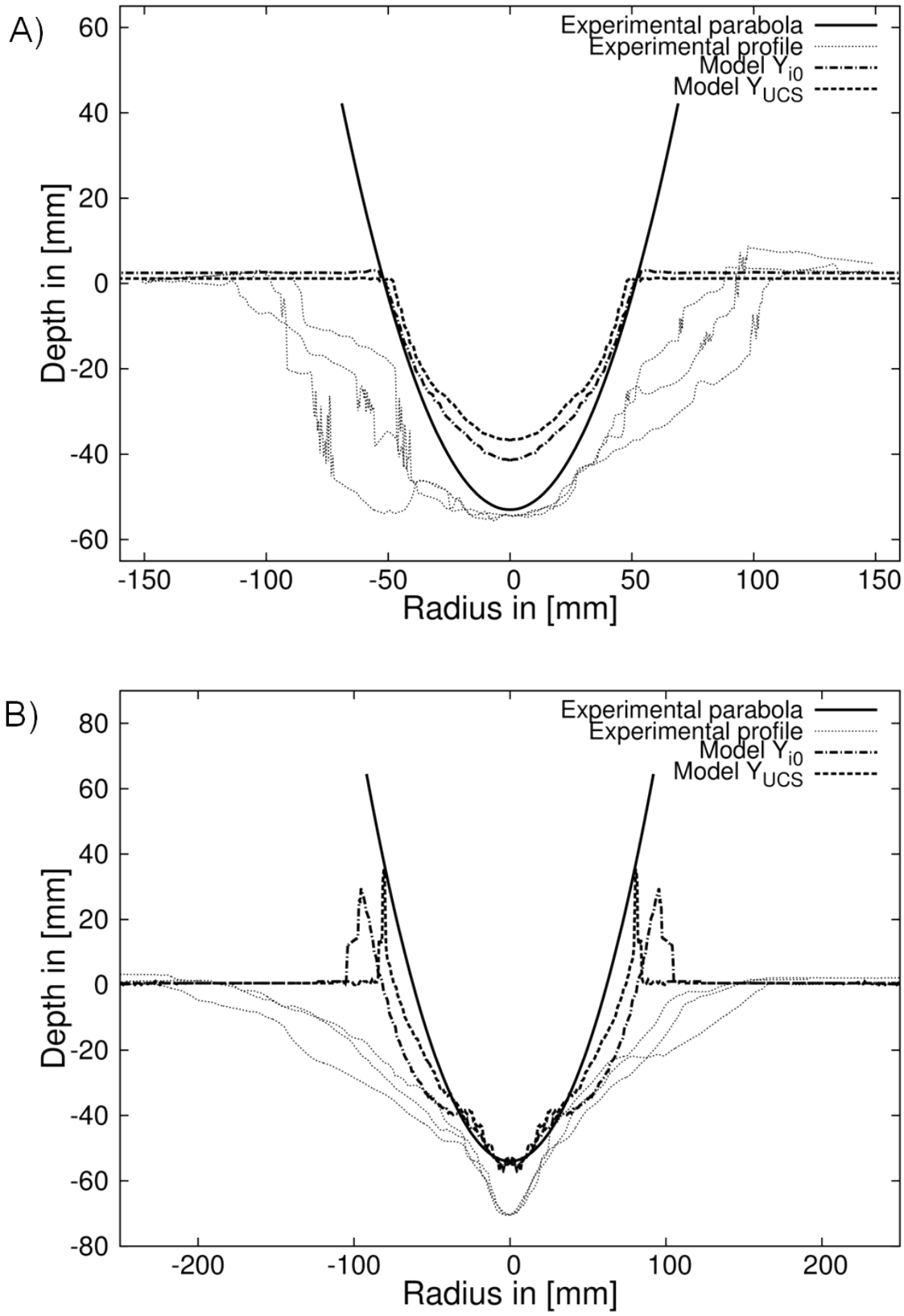

Figure 7.1: Comparison of crater profiles from numerical models with experimental profiles for (A) quartzite target and (B) sandstone target. The solid black line represents the parabolic estimate of the experimental transient crater. The dotted thin black lines show experimental crater profiles, and the dashed lines show modeled crater profiles accounting for different target strengths, where the value used for cohesion is either Y_{P0}, using Equation 7.9 ("Model Y_{i0}"), or simply Y_{UCS} ("Model Y_{UCS}"; see also Table 7.2). Higher cohesion values lead to slightly smaller craters.

7.3.2 Strength scaling

On the scale of laboratory cratering experiments in competent rock with yield strengths of several tens to hundreds of megapascals, the effect of gravity is negligible, and crater size is controlled by strength. Therefore, we used Equations 7.5 and 7.6 to plot the experimental and numerical data for the strength regime (strength-scaled size π_3) in Figure 7.2 for the scaled crater diameter $\pi_2 \cdot (1/\pi_4)^{1/3-\nu}$ (Figure 7.2B) and scaled crater volume $\pi_V \cdot (1/\pi_4)^{1-3\nu}$ (Figure 7.2A) for quartzite and sandstone targets. The factors $(1/\pi_4)^{1/3-\nu}$ and $(1/\pi_4)^{1-3\nu}$ were used to normalize the effects of the density ratio of projectile and target, with $\nu = 0.4$ (Holsapple and Housen, 2007). The variation in π_3 results from different impact velocities in the cratering experiments and numerical models ($U_{exp} = 2500 - 5400\,m\,s^{-1}$; $U_{model} = 2000 - 20,000\,m\,s^{-1}$). The projectile diameter L was $2.5\,mm$, $10\,mm$, and $12\,mm$ in the experiments and was kept constant at $L = 12\,mm$ in the numerical models. For further details on the experimental results, see also Poelchau *et al.* (2013, 2014). To determine π_3 by Equation 7.9, we used the Y_{P0} values for sandstone and quartzite listed in Table 7.2 (see Section 7.2.3 - "Strength in iSALE"). The larger Y_{P0} of the quartzite target led to higher π_3 values of the quartzite data than for craters in sandstone for otherwise equal impact conditions. In the diagram showing scaled crater volume (cratering efficiency; Figure 7.2A), the π_V values from models (blue) and experiments (red) agree well for sandstone. This holds true for the quartzite target as well, although there are only very few experimental data available, which all plot almost on the same spot. The π_V values for quartzite are generally larger than for the sandstone targets for small π_3 values. The difference almost disappears for large values. Assuming that the deviation of the two trend lines results from the presence of pore space in sandstone in contrast to the nonporous quartzite, we conclude that porosity generally causes a decrease in cratering efficiency, shifting the scaling curve toward lower π_V values. Impacts with higher impact velocities or weaker target strengths (smaller π_3 values) result in larger craters corresponding to a negative slope of the trend line. The slope is slightly steeper for nonporous quartzite. The scaled crater diameters do not show exactly the same trend (Figure 7.2B). In fact, the data for porous and nonporous targets almost plot along the same line for higher π_3 values, and the difference between the two lithologies is only very small here. This implies that the determined Y_{P0} is a good measure of target strength and that porosity has a more significant effect on volume through the crater depth.

For comprehensive purposes, we also included the scaling results using the UCS strength values in Figure 7.2. The data are shifted to larger π_3 values caused by higher strength values but show the same trends as using Y_{P0}.

Power-law fits of the data were used to determine the scaling parameter μ for π_V and

π_D for porous sandstone and nonporous quartzite modeling data separately by using Equations 7.5 and 7.6. In order to fit the data and to determine the scaling exponent, the strength in π_3 is defined by the strength Y_{P0} ($96.9\,MPa$ for quartzite, $22.75\,MPa$ for sandstone). Using the UCS values here would lead to the same scaling exponents. It is actually not important what strength value is actually used in the definition of π_3 when plotting the data just for the strength regime. For the models, the results as described here are insensitive to variations in strength by a factor of 2 or 3. When later plotting the gravity regime, the choice of Y becomes important as the gradual transition from gravity- to strength-dominated cratering is more sensitive to the strength parameter (see Section 7.3.3 - "Gravity Scaling"). All fitting results are listed in Table 7.3. The μ values for π_V and π_D fits are 0.48 ± 0.01 and 0.52 ± 0.01 for sandstone and 0.55 ± 0.05 and 0.64 ± 0.05 for quartzite, respectively. The value of μ is thus slightly smaller for porous sandstone than for nonporous quartzite. Poelchau *et al.* (2014) obtained a μ value for π_V from the experiments of 0.55 ± 0.05 for sandstone, which is slightly above the value obtained from numerical experiments (0.48). Holsapple and Housen (2007) reported values of $\mu = 0.55$ for "hard" rocks in the strength regime and $\mu = 0.41$ for porous sand in the gravity regime. Generally, these data are more or less consistent considering the given accuracy, in particular, with respect to the reconstruction of the transient crater size from the experimental data. Apparently, μ also varies slightly depending on whether scaled crater volumes or scaled crater diameters are used. The exponents are slightly increased when using π_D. Thus, the crater diameter increases at a faster rate with increasing impact velocity (decreasing π_3) than crater volume for a constant yield strength of the material.

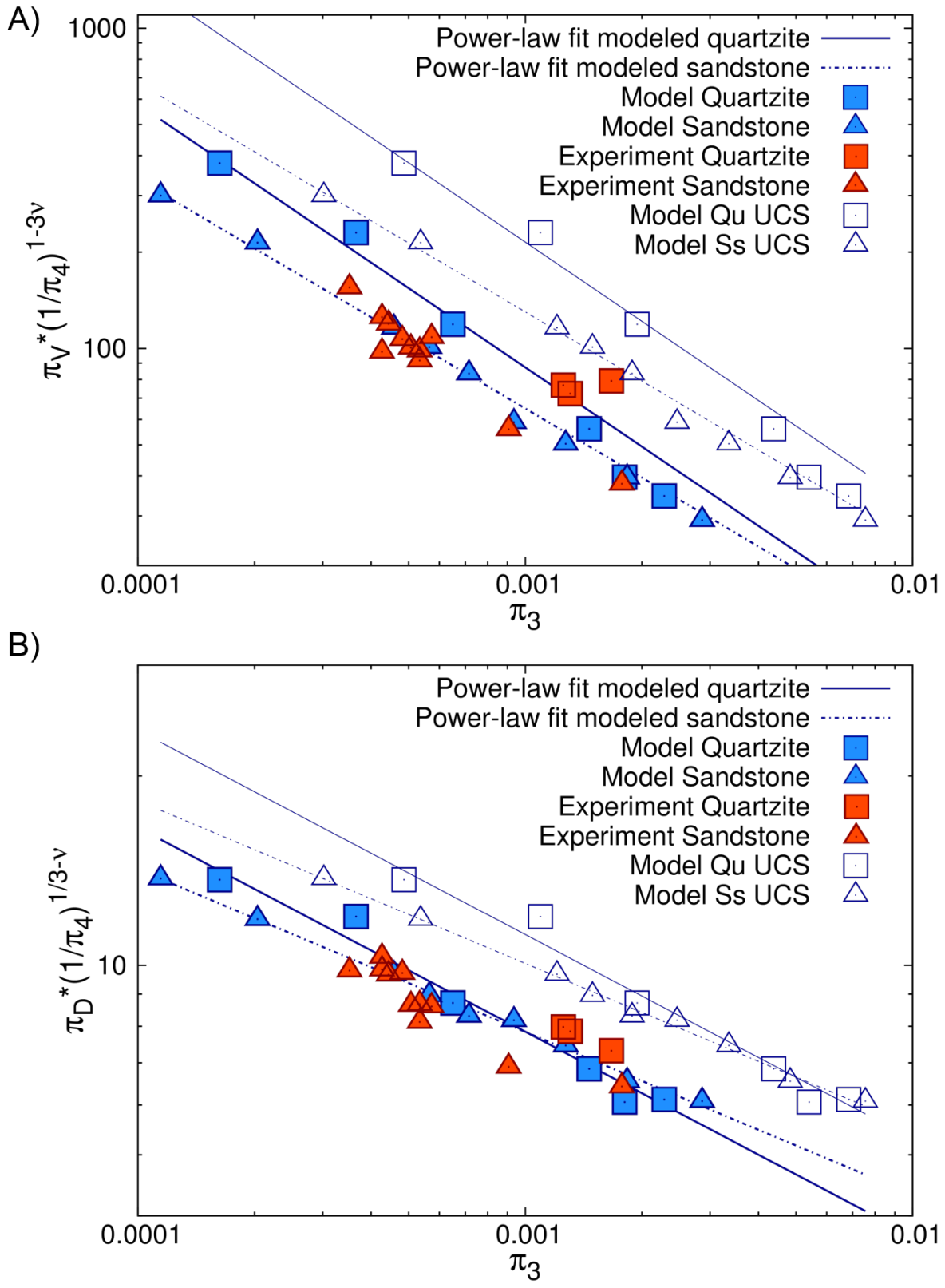

Figure 7.2: Strength scaling of transient crater volumes and diameters from numerical (blue) and laboratory experiments (red). (A) Strength-scaled crater size π_3 vs. the cratering efficiency $\pi_V \cdot (1/\pi_4)^{1-3\nu}$. (B) π_3 vs. $\pi_D \cdot (1/\pi_4)^{1/3-\nu}$. The solid lines are fits to the numerical data for quartzite (squares) and porous sandstone (triangles). In addition to the data using Y_{P0} for strength, both plots also include data using uniaxial compressive strength (UCS) strength values (open symbols). Qu-quartzite; Ss-sandstone.

7.3.3 Gravity scaling

We have demonstrated so far that our numerical models of crater formation in competent rock (sandstone and quartzite) are generally in good agreement with the results from laboratory experiments. The models now enable us to extrapolate our results to the scale of natural craters. With increasing projectile size, gravity gradually becomes more important and eventually controls crater size entirely. In particular, for the transition from the strength to gravity regime, both mechanisms, strength and gravity, affect the size scaling of craters as a function of the properties of the impactor. Figure 7.3 A shows the results of a suite of numerical models using the same parameters for the two different target lithologies given in the section "Strength in iSALE" and listed in Table 7.2. Note that for the results presented here, we used the measured value for Y_{UCS} for the strength parameter Y_{i0} in our strength model (Equation 7.9). As demonstrated in the previous section, varying the strength by a factor of 3 did not lead to significant effects on the resulting crater size and changes in the strength scaling. Figure 7.3 shows the gravity-scaled size π_2 versus the scaled crater diameter π_D. The density scaling term π_4 in Equation 7.8 is ~ 1 for $\mu = 0.55$, $\nu = 0.4$, and has therefore been omitted. The strength and gravity regimes can be clearly separated: If strength dominates, the crater size π_D is independent of π_2, and the data plot along a horizontal line (π_D = constant) for impacts at the same velocity. This is the case for the laboratory craters in quartzite and sandstone (red symbols in Figure 7.3A) and accordingly also for the modeled craters (blue symbols) of similar size. In this regime, the craters in porous material (sandstone) lie above the craters in nonporous quartzite. This is in contrast to strength scaling, where crater formation in nonporous materials is more efficient; however, in the π_2-π_D plot in Figure 7.3A, the larger Y_{UCS} values for quartzite ($292\,MPa$) in comparison to the sandstone ($67\,MPa$) cause less efficient crater formation in the strength regime, as the strength value is no longer factored in. For increasing π_2 (increasing L), no experimental data for competent rock are available, and we have to rely on modeling results. For very large π_2 values, the data plot as a straight line in a double logarithmic diagram. In the gravity regime, the scaled crater size is independent of π_3 (strength) and becomes only a function of π_2, so that the simplified π scaling given in Equation 7.8 applies (Figure 7.3B). Interestingly, the scaled crater size in porous material (sandstone) is smaller than in the nonporous target rocks (quartzite), which confirms the observations using strength scaling on a π_3-π_V-plot. At the transition from strength to gravity scaling, the curves for porous sandstone and nonporous quartzite intersect. The transition regime ranges over several orders of magnitude and is rather broad, making it very hard to define the threshold value for π_2 in a double logarithmic plot where pure gravity scaling begins and Equation 7.8 applies. The determination of the

scaling parameter μ by fitting Equation 7.8 to the data is very sensitive to the choice of the π_2 range, where crater size is no longer affected by strength. For this reason, we fitted the more generalized expression in Equation 7.3, where π_D is a function of π_2 and π_3, to the data. In order to obtain a reasonable fit to the experimental and modeling data in the strength regime in Figure 7.3, we had to choose a value for Y in Equation 7.3 that was significantly smaller than Y_{UCS} or Y_{P0} . Note that our strength model accounts for weakening of material due to the accumulation of damage. The strength for $P = 0$ of completely damaged material is $Y_{d0} = 0$. Therefore, we define the effective strength with $Y_{d0} < Y_{eff} < Y_{P0} < Y_{UCS}$. Note, the defined effective strength is not the same as that used by Holsapple and Housen (2007). We can only estimate the relationship between Y_{eff} and Y, but we believe that it becomes important for the transition from gravity to the strength regime. We find $Y_{eff} = 4.62\,kPa$ for quartzite and $Y_{eff} = 3.2\,kPa$ for sandstone. We found $\mu = 0.49$ for quartzite and $\mu = 0.55$ for sandstone. In comparison to the values obtained by strength scaling, μ is lower for quartzite and larger for sandstone. We interpret these inconsistencies as a measure of the accuracy of the method we suggested here to determine the scaling parameters for cohesive material. To visualize the difference, we also plotted lines for μ, which was determined by strength scaling from Figure 7.3B, to the model results in Figure 7.3B showing only the gravity regime. We further obtained the scaling parameter K_1 by fitting Equation 7.3 to the data. For quartzite, we obtained a value of 0.73 considering the gravity and strength regime. K values obtained by fitting Equations 7.5, 7.6, and 7.3 considering either gravity or strength regime are given in Table 7.3. Holsapple and Housen (2007, Table 1 herein) obtained values of 1.15 for nonporous and 0.90 for porous materials. Both are lower than the values obtained by numerical experiments in the gravity regime (K_1: 1.32 for quartzite, 1.19 for sandstone; Table 7.3).

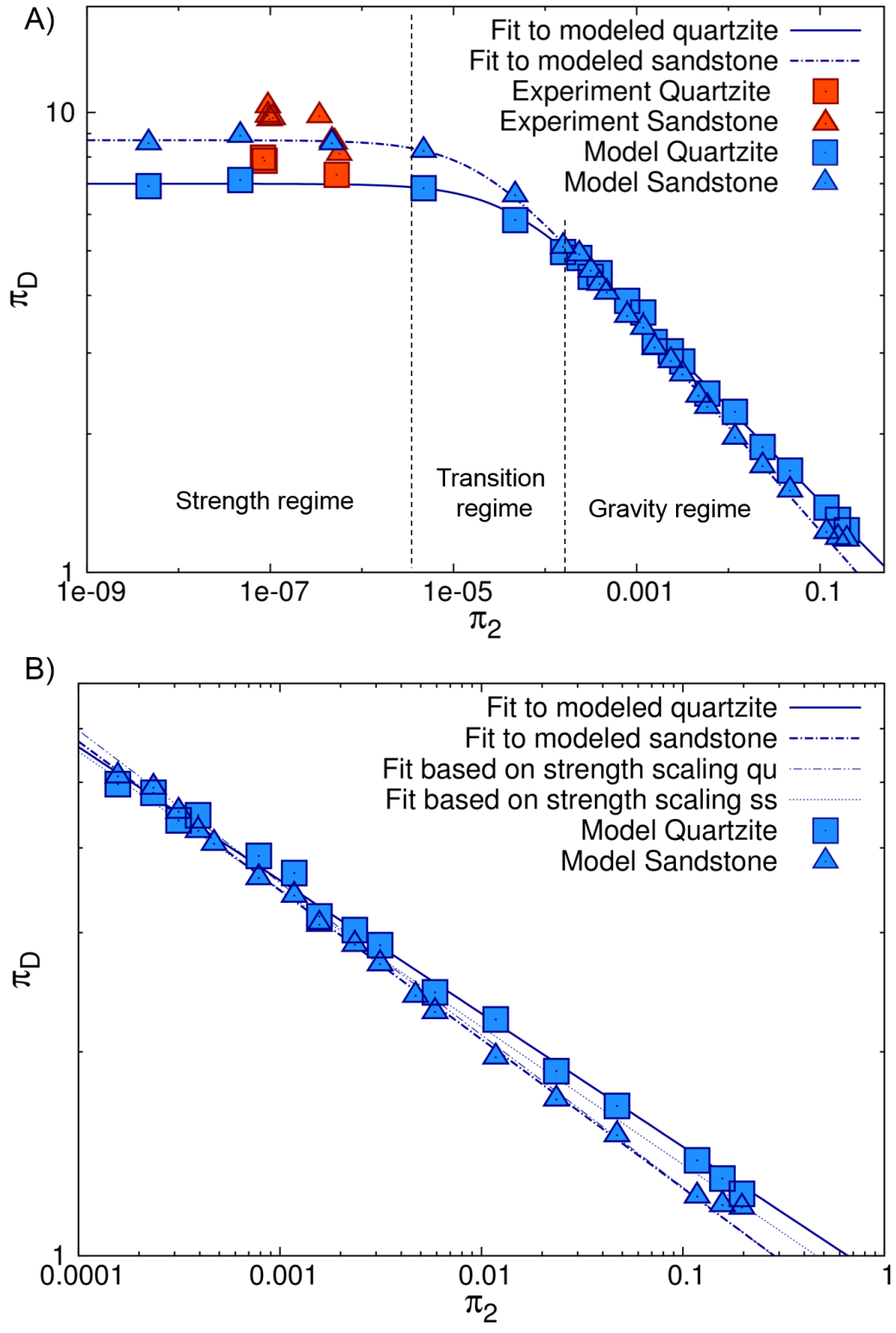

Figure 7.3: Gravity scaling for quartzite and sandstone target materials. The scaled size π_2 vs. scaled crater diameter π_D is plotted. (A) The curves are fits to the data based on Equation 7.3. Experimental data are also shown (red triangles and squares); variation of experimental π_D values is mainly due to variation of the impact velocity. (B) Curves are fits to the data based on Equation 7.8. Additional fitted curves using scaling parameters determined by strength scaling ($\mu = 0.64$ for quartzite and $\mu = 0.52$ for sandstone) are shown as dotted lines. Only the gravity regime is shown; qu-quartzite; ss-sandstone.

7.4 Discussion and conclusion

Our coupled approach of laboratory and numerical cratering experiments into sandstone and quartzite enables us to determine the important scaling exponent μ for cohesive material over a range of crater sizes from the laboratory scale to large terrestrial craters in both the strength and gravity regimes. In previous studies using laboratory experiments, size scaling in the gravity regime was only possible for granular materials or wet soils with no or very little cohesion (e.g. Schmidt, 1980; Housen and Holsapple, 2003). Additionally, we investigated the effect of porosity on cratering efficiency. Generally, the different μ values we found for the strength and gravity regimes, using experimental and modeling data, and measuring crater volume and diameter, fall in an interval of 0.48–0.55 for sandstone and 0.49–0.64 for quartzite, which roughly match the value suggested by Holsapple and Housen (2007) of 0.55 for the strength regime. The values we obtained for the scaling parameter K_1 are in excess of the literature data (Table 7.3). However, the values obtained for strength scaling deviate significantly from the data obtained by gravity scaling and values given by Holsapple and Housen (2007). All data are summarized in Table 7.3. As we noted earlier, the reconstruction of the size of the transient crater in the experiments is a rough estimation (see discussion in Poelchau *et al.*, 2013, 2014), and the available data do not cover a very large range of π values, which gives the power-law fit of the data a large error margin. On the other hand, the results of the numerical experiments largely depend on the material model, which was validated against observations, but it currently cannot be verified in detail if the actual behavior of rocks is described adequately. If we consider the variations in μ as the approximate error of the determination method, the difference in μ between porous sandstone and nonporous quartzite is negligible. Thus, porosity does not seem to affect the scaling exponent significantly considering errors of ± 0.05 (quartzite) and ± 0.01 (sandstone) for the obtained μ values. This is in agreement with modeling studies on crater size scaling in granular material with varying porosities by Wünnemann *et al.* (2011). They claimed that porosity causes only a shift of the scaling line toward lower crater efficiencies, but it does not affect the slope of the line that is related to μ by some function (see Equations 7.3 and 7.4). Wünnemann *et al.* (2011) and Elbeshausen *et al.* (2009) showed by numerical modeling that the scaling exponent may be a function of the coefficient of friction, which was kept constant in our models for quartzite and sandstone. Surprisingly, the μ we found in our study for "hard" rock does not agree with the μ of granular material with the same coefficient of friction (Wünnemann *et al.*, 2011; Elbeshausen *et al.*, 2009). This discrepancy might be a result of the different strength models used in these studies (Drucker Prager strength model) and the one used in the present work (ROCK model (Collins *et al.*, 2004), which accounts for intact and damaged material), which requires further investigation. In particular, the strain rate

dependency of the coefficient of friction may need to be considered in the strength model in the simulations of crater formation. The meaning of the strength parameter Y in pi-group scaling has been a long-lasting matter of debate. Often, the UCS value or the cohesion for a given material is used. For pure strength scaling (Equations 7.5 and 7.6), this works in principle as long as a consistent definition is used to convert a given set of laboratory or numerical data into π_3. For crater size scaling at large crater dimensions (π_2 scaling), an accurate definition of Y is crucial to predict crater size, in particular, in the transitional regime from strength to gravity scaling (Equations 7.7 and 7.8). A single parameter may be too simplistic to express the complex behavior of material with respect to strength during crater formation. The main issue is that Y_{UCS} or Y_{P0} only account for the intact state. Weakening of matter due to the accumulation of damage is not considered. Therefore, it is of no surprise that significantly smaller values have to be chosen for Y than the measured Y_{UCS} or Y_{P0}. We introduced an effective strength value Y_{eff}, with $Y_{d0}(= 0) < Y_{eff} < Y_{P0}$, but we currently cannot provide any equations to calculate or estimate this effective strength Y_{eff}. In our modeling study, we found that Y_{eff} is ~ 5 orders of magnitude smaller than Y_{UCS} for quartzite and for sandstone. The ratio of Y_{eff} to Y_{UCS} may depend on the presence of porosity. A systematic parameter study is required to further investigate the problem. The scale dependency of the deformation processes may be also related to the strain rate, which is currently not taken into account in our strength model. However, we assume that this effect is small; only when strength changes by an order of magnitude or more does it have a significant effect on crater size. In conclusion, the results presented here confirm the applicability of previously suggested scaling laws to predict crater size in hard rock and provide new constraints on the important scaling parameters and first estimates of the effective strength.

Table 7.3: Scaling exponents and strength for two different target materials using different scaling techniques

	Scaling exponent μ			**Scaling parameter K**				**Strength**		
	Strength scaling	Strength scaling	Gravity scaling	Gravity scaling K_1 Eq. 7.8	Strength scaling K_1/K_2, Eq. 7.6	Strength scaling K_3/K_4, Eq. 7.5	Strength scaling KHH[a] converted	UCS strength Y_{UCS} (MPa)	Cohesion Y_{P0} (MPa)	Effective strength Y_{eff} (kPa)
Fitted parameter	π_D	π_V	π_D	π_D	π_D	π_V	π_D			
Quartzite	0.64	0.55	0.49	1.32	1.30/1.06	0.87/1.15	1.15[b]	292	96.9	4.621
Sandstone	0.52	0.48	0.55	1.19	1.28/0.93	0.97/1.03	0.90[c]	67	22.75	3.2333

[a] The value KHH is from Holsapple and Housen (2007) (Table 1) for the ratio of crater to projectile radius R/a. To convert to the constant K_1 for π_D, $K_1 = KHH(6/\pi)^{1/3}$

[b] "Wet soils and rock"; (Holsapple and Housen, 2007)

[c] "Highly porous scaling"; (Holsapple and Housen, 2007)

Acknowledgments

This work was supported by the German Science Foundation DFG (Research Unit FOR-887; WU 355/6-1; KE 732/17-1). We gratefully acknowledge the developers of iSALE-2D, including Gareth Collins, Kai Wünnemann, Dirk Elbeshausen, Boris Ivanov, and Jay Melosh. We thank G. Collins and K. Holsapple for their constructive reviews.

8 Conclusions

To learn more about the consequences of impact cratering on Earth and on planetary surfaces and how material properties influence the propagation of shock and elastic waves and how that may, in turn, affect the consequences for the environment, this thesis aimed to investigate the influence of target properties, in particular porosity, on impact cratering and the corresponding processes in detail.
Laboratory impact experiments and natural observations have allowed for a profound understanding of how target properties affect the crater formation process. However, these approaches are limited because of (1) the small scale of laboratory experiments, (2) the parameter space (limited target and projectile dimensions and impact velocities), and (3) the static observations in natural craters that do not allow for complete reconstruction of dynamic processes. Supplementary to the classic approaches, numerical modeling is an important tool that allows for the study of the effect of porosity, water saturation and strength on different scales.
The usage of numerical models always requires calibration and validation of the material models, a parametrized description of the behavior of matter under shock compression and mechanical deformations. The well-calibrated and validated models then have been used to quantify processes on the small scale using mesoscale simulations, to quantify seismic properties looking at impact-induced seismicity, and to improve our understanding of how strength and porosity affect scaling laws that enable the upscaling of small-scale experiments to the dimensions of natural crater sizes.

In the following, the main results are summarized, and a short discussion related to each chapter is provided. Finally, limitations of the numerical approach, general conclusions, and an outlook are given.

8.1 Summary of results

Chapter 4 focuses on the development of a mesoscale model using the iSALE shock physics code to simulate shock wave propagation in porous material. The mesoscale

models resolve individual pores and grains and enable a detailed and direct comparison with analyses of shocked sample material. The models were used to investigate the shock wave-induced collapse of single pores distributed in a sample area and how the crushing of pores affects shock wave propagation. The results from mesoscale modeling were then used to refine and validate previously suggested macroscopic models to describe the effect of porosity on large-scale processes such as the propagation of the shock wave in a target and the formation of a crater. The study was motivated by the fact that porosity significantly affects shock wave propagation and the crater formation (lower crater efficiency) and that often shock effects are present in grains directly next to grains that do not show any shock effects. A detailed analysis on the mesoscale was lacking so far. The main results of the study are:

- Shock pressures are locally amplified by a factor of 3-4 as a consequence of the collapse of pore space, which explains the occurrence of shock effects at low nominal pressures and therefore the observation of shock features in an environment of small craters where the initial pressures are expected to be too small to result in any observed shocked material.
- The effect of pressure amplification decreases slightly if several pores are located close to one another and the reflections of shock and rarefaction waves originating from the pores superimpose.
- In general, the crushing of pore space is an effective mechanism for absorbing shock wave energy, resulting in faster decay of the shock wave in porous material than in nonporous material. Shock waves travel faster through water-saturated material than through porous material, and water-saturated pores are only slightly compacted compared with empty pores that are completely closed.

The good correlation among experimental, meso-, and macroscale model data presented in this study justifies the applicability of our mesoscale approach to test the macroscopic models describing dry and wet porous material and, in particular, partially water-saturated porous sandstone. The laboratory cratering experiments provide important standards the models can be tested against, and also offer quantitative explanations for some unexpected observations. For example, the amplification of shock pressure due to pore collapse as quantified in the mesoscale models also helps us understand the generation of small vapor and melt phases during the very first contact between the projectile and the target and provide important insights on the observation of planar deformation features in the ejecta of the laboratory experiments (Ebert *et al.*, 2013). The pressure amplification further explains the occurrence of highly shocked material next to unshocked material.
Given the mentioned accomplishments, this work presents a pioneer study in mesoscale modeling of shock wave processes in planetary sciences. It represents the first systematic

study which was followed by e.g. the work from Davison *et al.* (2014). Thus, the new models developed here pave the way for subsequent studies and help to address some of the main questions related to shock features occurring at impact events, such as the formation of melt at low initial pressures. Thus, this novel study opens the door for future investigations of possibly shocked material that is found in natural impact craters, formed during impact or shock experiments, or even returned from planetary missions.

In **Chapter 5** the mesoscale approach was used to investigate the melting of quartz at relatively low shock pressures in porous sandstone. Laboratory shock experiments show that shock features in quartz such as diaplectic glass occur at significantly lower shock pressures than in nonporous rocks. However, microanalytic observations on samples from experiments are limited to relating the state of matter after the shock experiments with its initial state; models can provide insight into the dynamic processes that lead to shock-induced modifications.
The main outcomes of this study are:

- The mechanism by which pores collapse and the localized shock amplifications are strongly dependent on porosity. In addition, the possible occurrence of localized shock amplification (as described in Chapter 4) decreases as the distance from the impacted surface increases.
- The experiments show that pore space is completely closed at very low nominal shock pressures ($2.5\,GPa$).
- The localized pressure amplifications determined by numerical models provide an explanation for experimentally observed shock features in porous sandstone, in particular for shock features diagnostic of much higher pressures in nonporous quartz such as SiO_2 melt, diaplectic quartz glass, and quartz with PDF.
- Consequently, the formation of diaplectic glass/SiO_2 melt in porous material is possible despite very low shock pressures (starting at $5\,GPa$).

The combination of shock experiments and numerical modeling provides significant insight into the shock processes in dry, porous sandstone in the low shock pressure regime between 2.5 and $17.5\,GPa$. The combined study shows that shock compression in porous sandstone is distinctly different from that in nonporous quartzite or single quartz crystals, especially at low shock pressures. Despite small discrepancies between the model and the experiment, this study showed again that models can be used exceptionally well to support and interpret observations from shock experiments. Further, these models provide explanations for observed shock features by investigating the propagation of shock waves in heterogeneous materials, determining the pressure distribution within the material, and quantifying localized shock amplifications due to pore collapse.

Further, I investigated how shock waves attenuate into elastic waves. Thus, **Chapter 6**, focuses on the propagation of seismic waves in porous material in numerical and laboratory experiments and the numerical determination of seismic parameters for different material properties. Specifically, I investigated two seismic parameters: (1) the seismic quality factor to quantify how fast the seismic wave attenuates and (2) the seismic efficiency defining how much of the kinetic energy is transferred into seismic energy. Previous estimates for these seismic parameters deviate by a few orders of magnitude, which shows that the parameters are not very well constrained and significantly material dependent. The outcomes of this work were:

- The seismic parameters are significantly affected by different target properties. The seismic efficiency decreases slightly with porosity and significantly with water saturation. The seismic quality factor is also much lower for wet than for dry material.
- The seismic efficiency ranges between values of $2 \cdot 10^{-3}$ to $3.4 \cdot 10^{-3}$ for sandstone and quartzite material and was $8 \cdot 10^{-5}$ for water-saturated material. In contrast, the seismic efficiency during an earthquake is, with values of 10^{-1} to 10^{-2}, much larger.
- The obtained quality factor ranges between values of 35 and 80 for a quartzite and sandstone material and decreases down to 6.5 for water-saturated materials.
- The predicted seismic magnitudes are reduced by about one order of magnitude in water-saturated material compared to "dry" materials, showing that seismic magnitudes are also significantly affected by target properties.

The numerical approach used in this work to investigate seismic or elastic waves has the advantage that materials of different porosities and/or water saturation can easily be taken into consideration. Further, a large number of gauge points which are needed to record the elastic wave signals in order determine thermodynamic and mechanical parameters can be used in numerical simulations. Thus, determining seismic parameters in numerical simulations represents a novel approach that allows for a quantitative assessment of the impact-induced seismicity on an arbitrary size scale and for different target materials. In conclusion, numerical models give new insights into the seismic parameters of impact events for different lithologies. Besides better estimates of the seismic hazard of impact events on Earth, numerical models also deliver important constraints for the interpretation of seismic data that have been recorded during planetary missions, as impacts are considered an important seismic source for e.g. lunar and martian quakes. The seismic signals and the associated energies from which we can estimate the impact energy by using the constrained seismic efficiencies may give better indications of the impactor's energy and target properties than can be correlated with observations of impact flashes as they also

provide information about the impact conditions.

After the successful calibration and validation of material models of porous (dry and water-saturated) materials describing the response of matter to shock and elastic compression, macro-scale effects were investigated, in particular the crater size. In **Chapter 7** the previous results were upscaled to natural crater dimensions. Important parameters in scaling laws to predict the resulting crater size for a given impact energy were constrained. This work was motivated by the fact that strength of the target material is especially complicated to consider when upscaling from experimental to the natural crater sizes; in particular, the transition from the strength to gravity regime is highly complicated. Therefore, a so-called effective strength value was introduced and determined to account for the weakening of target material due to the accumulation of damage. The main findings here were:

- Numerical modeling allowed us to determine material-dependent scaling parameters K and μ and the strength Y. Here, the scaling exponent μ is not significantly affected by the presence of porosity.
- The prediction of an effective strength parameter was successful.
- The presence of porosity reduces cratering efficiency, and a greater crater strength leads to reduced scaled crater sizes.
- The effective strength Y_{eff} is ~ 5 orders of magnitude smaller than the static strength Y_{UCS} for quartzite and for sandstone. The ratio of Y_{eff} to Y_{UCS} may depend on the presence of porosity.

In conclusion, the results presented here confirm the applicability of previously suggested scaling laws to predict crater size in hard rock and provide new constraints on the important scaling parameters and first estimates of the effective strength. Although it was not possible to provide any equations to calculate the effective strength Y_{eff}, estimates of such a strength value are essential in impact cratering, as they provide an important approach to treat, in particular, the transition from the strength to the gravity regime.
Previous experiments have only been carried out in sand and thus in the gravity regime. The experiments presented here use, for the first time, cohesive materials; thus, they are novel because they were carried out in the strength regime. The new experimental data also provide an important set of data to use in numerical models. This enabled us to finally upscale the numerical results from the laboratory scale to natural dimensions. In conclusion, the models connect all different regimes and scales.

8.2 Limitations

This work has focused on numerical simulations, while observations from laboratory experiments enabled us to validate and calibrate the required material models. Most of previous laboratory cratering experiments have been carried out into granular materials. Those experiments, however, only allowed to define a small number of parameters to be defined, and those parameters can only vary one at a time and are limited to a small parameter range (size and velocity of impactor, target characteristics). In numerical models, these parameters can be varied independently, and a larger range of scale can be covered. There are, however, limitations regarding numerical simulations.

A model-inherent general problem in all numerical models is resolution. The required or most sufficient resolution is often limited by computer power or the very long, inefficient run times of the simulations. The main issue I faced was, that resolution limits do not allow for addressing processes on very different scales in a single model. Particularly, mesoscale models require very high resolution to represent single pores and grains. The structure of natural rocks have to be represented as detailed as possible to investigate the heterogeneous processes during shock wave propagation. Macro-scale models of crater formation, in contrast, provide important information about bulk processes such as crater excavation, ejection of matter and the propagation of the shock wave. As processes on the meso- or microscale have significant effects on macro-scale processes, these processes have to be investigated in two different models. This works enables the combination of both approaches.

The porous compaction model, which is incorporated in iSALE and was introduced in Section 3.6 and applied in Chapter 4, is limited in a way as it treats the material as a homogeneous unit, assuming that pore space is uniformly distributed within the medium. It does not account for possible local effects that may occur due to any heterogeneities in the material. However, the new implementation of a mesoscale model has overcome this shortcoming, as it resolves heterogeneities as they occur in natural materials where pore sizes are not uniformly distributed and may have a large range in size. The mesoscale models, however, still represent only a simplification of the natural rock structure, as they do not resolve any grain boundaries.

Further, as the numerical code is based in continuum mechanics, it does not account for any effects of fracturing or breaking up of material. However, one of the most important collateral effects of impact cratering on planetary surfaces is fracturing and fragmentation of the target rocks surrounding the crater (Collins, 2014). Impact-induced fracturing increases porosity, which may have an influence on cratering and wave propagation that is in addition to the processes described within this work. The effect of dilatant material, where porosity increases as a result of unloading, was neglected in this work. The concept

of dilatancy during impact processes is introduced and explained in detail in Collins (2014). In the presented studies, often there was an issue with the availability of a correct and reliable numerical material model for the different materials. Thus, sometimes a proper characterization of the material was not available, and many parameters had to be determined by indirect observations from experiments. However, the reproducibility of the laboratory experiments gave us confidence to use the experiments for the calibration of the models.

Further issues arose with the material models that were used for the water-saturated material, where a material mixture of quartzite and water was used. This mixed-material approach is described in detail in Section 4.2.2. Using this approach may not reproduce the actual process of compacting water-filled pores very well because it was always assumed that the water content remained constant in the computational cell. The re-distribution of water content during shock compression and the subsequent release in material mixtures was not taken into account. In the framework of the MEMIN experiments, it was not possible to confirm whether this assumption holds true. Nevertheless, the approach of the mixed-material was well tested against experimental data and numerical mesoscale models, which gave us confidence that the approach is applicable.

In Chapters 4 and 5, during the post-processing of mesoscale simulations, peak pressures and melt volumes were determined. For the determination of peak pressure amplifications, it was assumed that at least 20 % of the initial pore volume experienced the amplified pressure conditions. The limitation of 20 % was chosen to satisfy the required resolution to obtain reliable results. However, very small volumes that undergo even higher pressures are conceivable, but cannot be resolved in our models. This may explain some discrepancies between the model and the experiments, but as the volumes that possibly experience much larger pressures are very small, they do not affect the results significantly.

To determine the amount of melt numerically, either peak pressures can be calculated considering a certain threshold or the final release-state temperature can be used. In Chapter 5, maximum shock pressures were used instead of post-shock temperatures as an indicator for final material temperature and its physical state (e.g. melt). Using post-shock temperatures requires very long calculations on very fine meshes, and it is numerically diffusive. Thus, to keep the numerical model efficient, we did not calculate the complete release of the material and thus were not able to obtain post-shock temperatures. The peak shock pressure is considered to be more accurate to determine shock-induced heating, although it does not account for additional heating due to plastic work.

Despite all these limitations, numerical models are still better than any of its alternatives. Numerical simulations remain the only tool that is able to investigate all processes that occur during and after an impact event and can cover the entire range of scale, from the scale of laboratory experiments to the scale of natural craters, varying a large number of

parameters independently.

8.3 Conclusions and outlook

To quantify the consequences of an impact event, profound knowledge about shock and elastic wave behavior is required. This mainly depends on projectile and target properties. Within this work, focus was given on the influence of target properties on impact cratering considering porous, dry, and partially or completely water-saturated sandstone. The project in which this thesis has been carried out provides, for the first , a detailed analysis of the behavior of those materials under shock loading using laboratory impact experiments in combination with numerical models.

In order to achieve the main goal of this thesis - the quantification and qualification how shock and elastic wave propagations and crater formation and size depend on material properties - the necessary steps have been successfully fulfilled. The validation and calibration of numerical material models by using experimental observations was successful. New material models have been developed to treat complex geologic materials such as sandstone or water-saturated sandstone. Carrying out a validation of the new material models with regard to shock and elastic wave propagation and crater sizes was achieved. Finally, a better understanding of the crater formation process on different scales was gained.
Before this work, a detailed investigation of porous materials with some water content and their response to shock wave loading was lacking. Thus, models of different complementary scales (meso- and macroscales) were applied in this thesis. Macroscale models enable the simulation of the entire cratering process, whereas the mesoscale models enable a detailed analysis of localized processes during shock compression.

Major conclusions derived from the presented research, according to the main goals, are:

- Petrophysical properties of rocks significantly affect hypervelocity impact processes with respect to wave amplitudes, velocities, crater dimensions, pressure distributions in the impacting material and impact-induced seismicity. The resulting environmental consequences are therefore also dependent on target properties, as shock and elastic wave propagation change their behavior with target porosity and water saturation.
- Shock waves attenuate faster in porous material. The volume of material that exhibits high pressures is smaller, although localized pressure amplifications are present during shock wave propagation.

- Less seismicity is induced by an impact if the impacted target material is porous in comparison to a nonporous target. The attenuation of elastic waves is similar in porous and nonporous material but much faster in water-saturated material. The smallest seismic shaking after an impact is observed if the target contains water.
- Porosity and strength result, in general, in smaller craters. Thus, taking into account target properties may change crater statistics when new craters are added to the existing crater record. This will play a role in age determination of planetary surfaces. Thus, target properties, such as porosity and water saturation, have to be taken into account by applying crater size-frequency distribution.

The obtained parameters and new findings of this research project help us interpret observations from newly formed crater structures on Earth and planetary surfaces taking into account material properties of the impacted body.
The findings may allow better predictions of the size and shape of an impact structures in the future by considering the effect of target properties, assuming that they are known. Vice versa, conclusions can be drawn about the characteristic of the impacted body and its interior in the case of impact events that are observed on Earth or on planetary bodies in the future by taking into account the findings of this work, such as the seismic efficiency or possibly formed shock features due to localized shock amplification.
In the case of a porous target, shock features can be observed even in very small impact structures due to localized shock amplification caused by pore collapse. If shock features are observed in the environment of a small crater structure, where usually low shock pressures are expected during the impact event, the conclusion of a possibly porous impacted body can be drawn. This fact may also lead to the identification of a new impact structure as evidence for an impact event by observed shock features is given. Thus, some impact craters may be added to the present crater records.
Water prohibits the propagation of shock waves and significantly decreases the shock pressures. Despite the fact, that in water-saturated bodies fewer impact craters are usually present, this may not reflect the actual impact flux on the planetary body. Due to the large impedance contrast to the surrounding material, localized shock pressure amplifications occur, which also leads to the observation of shock features in impact craters in a wet target environment. This also has to be considered in crater counting.
To estimate the age of a planetary body, crater size-frequency distribution is the common technique. The work presented here provides essential information for future age determination. If a body exhibits fewer craters due to erosion as a result of seismic shaking, the age of the body would be underestimated. Seismic shaking may have additionally contributed to the modification of an impact structure or to the modification of an entire

planetary body in the case of small asteroids or comets and erosion of existing impact craters. The newly obtained parameters may allow one to predict to what extent the body has changed as a consequence of seismic shaking, assuming that the impact conditions are known. With the finding that the seismic efficiency is reduced for impacts in porous and in water-saturated targets, we can conclude that the impact-induced seismic shaking is stronger in nonporous bodies, which leads to a stronger modification and possibly a reduced number of observed craters on the surface. In contrast, weaker seismic shaking in porous and water-saturated targets results in the observation of more craters, as less modification has taken place. This may lead to a wrong interpretation when considering crater statistics, where less and smaller craters correspond to a younger age of the body whereas more craters correspond to older ages. Therefore, target properties and their effect on seismic shaking have to be taken into account when looking at the present crater record.

Generally, crater sizes are smaller in strength and porous targets, which would result in a younger age of the body, although the impact flux may be the same on a comparable nonporous target where more craters are observed, leading to the determination of an older age.

In conclusion, the findings of this work make possible a prediction of the target properties, which gives important information for crater statistics. By knowing the target properties, it can be estimated if more or fewer craters or smaller or larger craters are expected. As such, target properties have a significant effect on crater counting, and they cannot be neglected when crater statistics are used to determine the age of a planetary body.

References

Ahrens, T. J. and Gregson, V. G., J. (1964). Shock compression of crustal rocks: Data for quartz, calcite, and plagioclase rocks. *Journal of Geophysical Research*, **69**(22), 4839–4874.

Aki, K. and Richards, P. (2002). *Quantitative Seismology*. University Science Books, Sausalito, CA.

Alvarez, L. W., Alvarez, W., Asaro, F., and Michel, H. V. (1980). Extraterrestrial cause for the cretaceous-tertiary extinction. *Science*, **208**(4448), 1095–1108.

Amsden, A. A., Ruppel, H. M., and Hirt, C. W. (1980). SALE: A Simplified ALE Computer Program for Fluid Flow at all Speeds. Technical Report LA-8095, Los Alamos National Laboratory, Los Alamos, New Mexico, USA. 105 pages.

Anderson, Jr., C. E. (1987). An overview of theory of hydrocodes. *International Journal of Impact Engineering*, **5**, 33–59.

Baldwin, E., Milner, D., Burchell, M., and Crawford, I. (2007). Laboratory impacts into dry and wet sandstone with and without an overlying water layer: Implications for scaling laws and projectile survivability. *Meteoritics & Planetary Science*, **42**, 1905–1914.

Baldwin, R. B. (1971). On the history of Lunar impact cratering: The absolute time scale and the origin of planetesimals. *Icarus*, **14**(1), 36–52.

Ben-Menahem, A. (1975). Source parameters of the Siberia explosion of June 30, 1908, from analysis and synthesis of seismic signals at four stations. *Physics of the Earth and Planetary Interiors*, **11**, 1–35.

Benson, D. J. (1992). Computational methods in Lagrangian and Eulerian hydrocodes. *Computer Methods in Applied Mechanics and Engineering*, **99**, 235–394.

Benson, D. J. (2002). Volume of fluid interface reconstruction methods for multi-material problems. *Applied Mechanics Reviews*, **55**(2), 151–165.

Borg, D. and Chhabildas, L. C. (2011). Three-dimensional dynamic loading simulations of sand. *International Journal of Impact Engineering*, **20**, 111–123.

Britt, D., Yeomans, D., Housen, K., and Consolmagno, G. (2002). Asteroid Density, Porosity, and Structure. In W. Bottke, A. Cellino, P. Paolicchi, and R. Binzel, Publisher, *Asteroids III*, Pages 485–500. Univ. of Arizona Press, Tucson.

Buhl, E., Poelchau, M. H., Dresen, G., and Kenkmann, T. (2013). Deformation of dry and wet sandstone targets during hyper-velocity impact experiments, as revealed from the MEMIN program. *Meteoritics & Planetary Science*, **48**, 71–86.

Burchell, M. J. and Whitehorn, L. (2003). Oblique incidence hypervelocity impacts on rock. *Monthly Notes of the Royal Astronomical Society*, **341**, 192–198.

Carroll, M. M. and Holt, A. C. (1972). Static and dynamic pore-collapse relations for ductile porous materials. *Journal of Applied Geophysical Research*, **43**, 1626–1636.

Collins, G. S. (2014). Numerical simulations of impact crater formation with dilatancy. *Journal of Geophysical Research: Planets*, **119**, 2600–2619.

Collins, G. S. and Wünnemann, K. (2005). How big was the Chesapeake Bay impact? Insight from numerical modeling. *Geology*, **33**(12), 925–928.

Collins, G. S., Melosh, H. J., Morgan, J. V., and Warner, M. R. (2002). Hydrocode Simulations of Chicxulub Crater Collapse and Peak-ring Formation. *Icarus*, **157**, 24–33.

Collins, G. S., Melosh, H. J., and Ivanov, B. A. (2004). Modeling damage and deformation in impact simulations. *Meteoritics & Planetary Science*, **39**, 217–231.

Collins, G. S., Melosh, H. J., and Marcus, R. A. (2005). Earth Impact Effects Program: A Web-based computer program for calculating the regional environmental consequences of a meteoroid impact on Earth. *Meteoritics & Planetary Science*, **40**(6), 817–840.

Collins, G. S., Melosh, H. J., and Wünnemann, K. (2011a). Improvements to the $\varepsilon - \alpha$ porous compaction model for simulating impacts into high-porosity solar system objects. *International Journal of Impact Engineering*, **38**, 434–439.

Collins, G. S., Melosh, H. J., Wilson, C. R., and Wünnemann, K. (2011b). Numerical simulations of crater formation with dilatancy. *AGU Fall Meeting*, (Abstract P34A-07).

Collins, G. S., Wünnemann, K., Artemieva, N., and Pierazzo, E. (2012). *Numerical modelling of impact processes*. Blackwell Publishing Ltd.

Crawford, D. A., Barnouin-Jha, O. S., and Cintala, M. J. (2003). Mesoscale computational investigation of shocked heterogeneous materials with application to large impact craters. In *Large Meteorite Impacts Conference*, Page 4119, Nördlingen, Germany.

Davison, T. M., Collins, G. S., and Ciesla, F. J. (2010). Numerical modelling of heating in porous planetesimal collisions. *Icarus*, **208**(1), 468 – 481.

Davison, T. M., Collins, G. S., Elbeshausen, D., Wünnemann, K., and Kearsley, A. (2011). Numerical modeling of oblique hypervelocity impacts on high strength ductile targets. *Meteoritics & Planetary Science*, **46**(10), 1510–1524.

Davison, T. M., Cielsa, F. J., Collins, G. S., and D., E. (2014). The effect of impact obliquity on shock heating in planetesimal collisions. *Meteoritics & Planetary Science*, **49**, 2252–2265.

Drucker, D. C. and Prager, W. (1952). Soil mechanics and plastic analysis for limit design. *Quarterly of Applied Mathematics*, **10**(2), 157–165.

Dufresne, A., Poelchau, M. H., Kenkmann, T., Deutsch, A., Hoerth, T., Schäfer, F., and Thoma, K. (2013). Crater morphology in sandstone targets: the MEMIN impact parameter study. *Meteoritics & Planetary Science*, **48**, 50–70.

Durr, N., Sauer, M., Güldemeister, N., Wünnemann, K., and Hiermaier, S. (2013). Mesoscale investigation of shock wave effects in dry and water-saturated sandstone. Volume 58 von *Proceedings of the 12th Hypervelocity Impact Symposium*, Pages 289–298.

Ebert, M., Hecht, L., Deutsch, A., and Kenkmann, T. (2013). Chemical modification of projectile residues and target material in a MEMIN cratering experiment. *Meteoritics & Planetary Science*, **48**, 134–149.

Elbeshausen, D. (2012). *Dreidimensionale numerische Modellierung schräger Meteoriteneinschläge - Strategien und Anwendungen* -. Dissertation, Freie Universität Berlin, Fachbereich Geowissenschaften. 283 pages.

Elbeshausen, D. and Wünnemann, K. (2011a). iSALE-3D: A three-dimensional, multi-material, multi-rheology hydrocode and its applications to large-scale geodynamic processes. In *Proceedings of 11th Hypervelocity Impact Symposium (HVIS)*, Volume 2 von *Schriftenreihe Forschungsergebnisse aus der Kurzzeitdynamik*, Pages 287–301. Fraunhofer Verlag.

Elbeshausen, D. and Wünnemann, K. (2011b). The Effect of Target Topography and Impact Angle on Crater Formation â Insight from 3D Numerical Modelling. *Lunar and Planetary Science Conference*, **XLII**(Abstract 1778).

Elbeshausen, D., Wünnemann, K., and Collins, G. S. (2009). Scaling of oblique impacts in frictional targets: Implications for crater size and formation mechanisms. *Icarus*, **204**(2), 716–731.

French, B., Underwood Jr, J., and Fisk, E. (1974). Shock-metamorphic features in two meteorite impact structures, Southeastern Libya. *Geol. Soc. Am. Bull.*, **85**, 1425–1428.

French, B. M. (1998). *Traces of Catastrophe: A Handbook of Shock-Metamorphic Effects in Terrestrial Meteorite Impact Structures*. LPI Contribution No. 954. Lunar and Planetary Institute, Houston. 130 pages.

Fritz, J., Wünnemann, K., Reimold, W., Meyer, C., and Hornemann, U. (2011). Shock experiments on quartz targets pre-cooled to 77 K. *Int. J. Impact Eng.*, **38**, 440–445.

Gault, D. E. and Heitoweit, E. D. (1963). The partition of energy for hypervelocity impact craters formed in rock. Volume 2 von *Proceedings of the sixth symposium on hypervelocity impact*, Pages 419–456.

Gault, D. E. and Wedekind, J. A. (1978). Experimental studies of oblique impact. In *Lunar and Planetary Science Conference*, Volume IX, Pages 3843–3875.

Gault, D. E., Quaide, W. L., and Oberbeck, V. R. (1968). Impact cratering mechanics and structures. In B. M. French and N. M. Short, Publisher, *Shock metamorphism of natural materials*, Pages 87–99. Mono Book Corps, Baltimore.

Godkova, T., Lognonne, P., Miljkovic, K., and Gagnepain-Beyneix, J. (2015). Impact cutofffrequency - momentum scaling law inverted from apollo seismic data. *Earth and Planetary Science Letters*, **427**, 57–65.

Goldin, T. J., Wünnemann, K., Melosh, H. J., and Collins, G. S. (2006). Hydrocode modeling of the Sierra Madera impact structure. *Meteoritics & Planetary Science*, **41**, 1947–1958.

Grieve, R. A. F. and Dence, M. R. (1979). The terrestrial cratering record: II. The crater production rate. *Icarus*, **38**(2), 230–242.

Grieve, R. A. F., Langenhorst, F., and Stöffler, D. (1996). Shock metamorphism of quartz in nature and experiment: Ii.significance in geoscience. *Meteoritics & Planetary Science*, **31**, 6–35.

Gusmeroli, A., Clark, R. A., Murray, T., Booth, A. D., Kulessa, B., and Barrett, B. E. (2010). Seismic wave attenuation in the uppermost glacier ice of storglaciaren, sweden. *Journal of Glaciology*, **56**, 249–256.

Güldemeister, N. and Wünnemann, K. (2017). Quantitative analysis of impact-induced seismic signals by numerical modeling. *Icarus*, **296**, 15–27.

Güldemeister, N., Durr, N., Wünnemann, K., and Hiermaier, S. (2013). Propagation of impact-induced shock waves in porous sandstone using mesoscale modeling. *Meteoritics & Planetary Science*, **48**, 115–133.

Güldemeister, N., Wünnemann, K., and Poelchau, M. H. (2015). Scaling impact crater dimensions in cohesive rock by numerical modeling and laboratory experiments. *Geological Society of America Special Papers*, **518**, SPE518–02.

Hartmann, W. K. (1965). Terrestrial and Lunar flux of large meteorites in the last two billion years. *Icarus*, **4**(2), 157 – 165.

Hartmann, W. K. (1977). Relative crater production rates on planets. *Icarus*, **31**(2), 260 – 276.

Heider, N. and Kenkmann, T. (2003). Numerical simulation of temperature effects at fissures due to shock loading. *Meteoritics & Planetary Science*, **38**, 1451–1460.

Heimann, S., Gonzalez, A., Wang, R., Cesca, S., and Dahm, T. (2013). Seismic characterization of the chelyabinsk meteor's terminal explosion. *Seismological Research Letters*, **84**(6), 1021–1025.

Hermann, W. (1969). Constitutive equation of state for the dynamic compaction of ductile porous materials. *Journal of Applied Geophysics*, **40**, 2490–2499.

Hertzsch, J. M., Ivanov, B. A., and Kenkmann, T. (2005). Numerical simulation of shock propagation in heterogeneous solids. In C. Koeberl and H. Henkel, Publisher, *Impact tectonics*, Pages 423–445. Springer.

Hiermaier, S., Könke, D., Stilp, A. J., and Thoma, K. (1997). Computational Simulation of the Hypervelocity Impact of Al-Spheres on Thin Plates of Different Materials. *International Journal of Impact Engineering*, **20**, 363–374.

Hoerth, T., Schäfer, F., Thoma, K., Kenkmann, T., Poelchau, M., Lexow, B., and Deutsch, A. (2013). Hypervelocity impacts on dry and wet sandstone: Observations of ejecta dynamics and crater growth. *Meteoritics & Planetary Science*, **48**, 23–32.

Hoerth, T., Schäfer, F., Nau, S., Kuder, J., Poelchau, M., Thoma, K., and Kenkmann, T. (2014). In situ measurements of impact-induced pressure waves in sandstone targets. *Journal of Geophysical Research: Planets*, **119**, 2177–2187.

Holsapple, K. A. (1987). The scaling of impact phenomena. *International Journal of Impact Engineering*, **5**(1-4), 343–355.

Holsapple, K. A. (1993). The scaling of impact processes in planetary sciences. *Annual Review of Earth and Planetary Sciences*, **21**(1), 333–373.

Holsapple, K. A. (2009). On the strength of the small bodies of the solar system: A review of strength theories and their implementation for analyses of impact disruptions. *Planetary and Space Science*, **57**(2), 127–141.

Holsapple, K. A. and Housen, K. R. (2007). A crater and its ejecta: An interpretation of Deep Impact. *Icarus*, **191**(2, Supplement 1), 586–597.

Holsapple, K. A. and Schmidt, R. M. (1987). Point source solutions and coupling parameters in cratering mechanics. *Journal of Geophysical Research*, **92**(B7), 6350–6376.

Holsapple, K. A., Giblin, I., Housen, K. R., Nakamura, A. M., and Ryan, E. (2002). Asteroids Impacts: Laboratory Experiments and Scaling Laws. In W. F. Bottke, P. Paolicchi, R. P. Binzel, and A. Celino, Publisher, *Asteroids III*, 3, Pages 443–462. University of Arizona Press.

Housen, K. R. and Holsapple, K. A. (2003). Impact cratering on porous asteroids. *Icarus*, **163**(1), 102–119.

Huffman, A. R. and Reimold, W. U. (1996). Experimental constraints on shock-induced microstructures in naturally deformed silicates. *Tectonophysics*, **256**(1-4), 165–217. Neville L. Carter.

Ivanov, B. A. (2003). Large impact crater modeling: Chicxulub. *Large Meteorite Impact Conference*, **III**(Abstract 4067).

Ivanov, B. A. (2005a). Numerical Modeling of the Largest Terrestrial Meteorite Craters. *Solar System Research*, **39**(5), 381–409.

Ivanov, B. A. (2005b). Shock melting of permafrost on mars: Water ice multiphase equation of state for numerical modeling and its testing. Volume XXXVI.

Ivanov, B. A. and Artemieva, N. A. (2002). Numerical modeling of the formation of large impact craters. *Geological Society of America Special Paper*, **356**, 619–630.

Ivanov, B. A. and Deutsch, A. (1999). Sudbury impact event: Cratering mechanics and thermal history. *Geological Society of America Special Paper*, (339), 1–9.

Ivanov, B. A. and Deutsch, A. (2002). The phase diagram of caco3 in relation to shock compression and decomposition. *Physics of the Earth and Planetary Interiors*, **123**(1-2), 131–143.

Ivanov, B. A., de Niem, D., and Neukum, G. (1997). Implementation of dynamic strength models into 2D hydrocodes: Applications for atmospheric breakup and impact cratering. *International Journal of Impact Engineering*, **20**(1-5), 411–430. Hypervelocity Impact Proceedings of the 1996 Symposium.

Johnson, G. R. and Cook, W. H. (1983). A constitutive model and data for metals subjected to large strains, high strain rates and high temperatures. In *Proceedings of the 7th International Symposium on Ballistics*, Pages 541–547.

Kenkmann, T., Artemieva, N. A., Wünnemann, K., Poelchau, M. H., Elbeshausen, D., and Nunez del Prado, H. (2009). The Carancas meteorite impact crater, Peru: Geologic surveying and modeling of crater formation and atmospheric passage. *Meteoritics & Planetary Science*, **44**(7), 985–1000.

Kenkmann, T., Wünnemann, K., Deutsch, A., Poelchau, M. H., Schäfer, F., and Thoma, K. (2011). Impact cratering in sandstone: The MEMIN pilot study on the effect of pore water. *Meteoritics & Planetary Science*, **46**(6), 890–902.

Kerley, G. I. (1992). CTH equation of state package: Porosity and reactive burn models. Technical Report SAND92-0553, Sandia National Laboratories.

Kieffer, S. W. (1971). Shock metamorphism of the coconino sandstone at meteor crater, arizona. *Journal of Geophysical Research*, **76**(23).

Kieffer, S. W., Phakey, P. P., and Christie, J. M. (1976). Shock processes in porous quartzite: Transmission electron microscope observations and theory. *Contributions to Mineralogy and Petrology*, **59**, 41–93.

Knapmeyer, M. and Weber, R. (2015). *Seismicity and Interior Structure of the Moon*. Cambridge University Press.

Kowitz, A., Güldemeister, N., Reimold, W. U., Schmitt, R. T., and Wünnemann, K. (2013a). Diaplectic quartz glass and SiO2 melt experimentally generated at only 5 GPa shock pressure in porous sandstone: Laboratory observations and meso-scale numerical modeling. *Earth and Planetary Science Letters*, **384**, 17–26.

Kowitz, A., Schmitt, R. T., Reimold, W. U., and Hornemann, U. (2013b). First MEMIN shock recovery experiments in dry, porous sandstone at low shock pressure (5-12.5 GPa). *Meteoritics & Planetary Science*, **48**, 99–114.

Kowitz, A., Güldemeister, N., Schmitt, R. T., Reimold, W. U., Wünnemann, K., and Holzwarth, A. (2016). Revision and recalibration of existing shock classifications for quartzose rocks using low-shock pressure (2.5-20 GPa) recovery experiments and meso-scale numerical modeling. *Meteoritics & Planetary Science*, **10**, 1741–1761.

Kraus, R., Stewart, S., Swift, D., Bolme, C., Smith, R., Hamel, S., Hammel, B., Spaulding, D., Hicks, D., Eggert, J., and Collins, G. (2012). Shock vaporization of silica and the thermodynamics of planetary impact events. *Journal of Geophysical Research*, **117**, E09009.

Langenhorst, F. and Deutsch, A. (2012). Shock metamorphism on minerals. *Elements*, **8**(1), 31–36.

Langenhorst, F. and Hornemann, U. (2005). Shock experiments on minerals: Basic physics and techniques. *EMU Notes in Mineralogy*, **7**, 1–31.

Latham, G., Ewing, M., Dorman, J., Press, F., Toksoz, N., Sutton, G., Meissner, R., Duennebier, F., Nakamura, Y., Kovach, R., and Yates, M. (1970). Seismic data from man-made impacts on the moon. *Science*, **170**(3958), 620–626.

Littlefield, D. L. (1997). Aneos extensions for modeling hypervelocity impact. *IJIE*, **20**, 533–544.

Lognonne, P., Kobayashi, N., Garcia, R., Weber, R., Johnson, C., and Gagnepain-Beyneix, J. (2012). Lunar interior as seen by seismology: from apollo to future missions. Volume 39 von *39th COSPAR Scientific Assembly, COSPAR Meeting*, Page p.1102.

Lomov, I. N., Hiltl, M., Vorobiev, O. Y., and Glenn, L. A. (2001). Dynamic behavior of berea sandstone for dry and water-saturated conditions. *International Journal of Impact Engineering*, **26**, 465–474.

Love, S. G., Hörz, F., and Brownlee, D. E. (1993). Target porosity effects in impact cratering and collisional disruption. *Icarus*, **105**(1), 216–224.

Lundborg, N. (1968). Strength of rock-like materials. *International Journal of Rock Mechanics and Mining Sciences*, **5**(5), 427–454.

Matsumoto, K., Yamada, R., Kikuchi, F., Kamata, S., Ishihara, Y., Iwata, T., Hanada, H., and Sasaki, S. (2015). Internal structure of the moon inferred from apollo seismic data and selenodetic data from grail and llr. *Geophysical Research Letters*, **42**, 7351–7358.

McGarr, A., Latham, G. V., and Gault, D. E. (1969). Meteoroid impacts as sources of seismicity on the Moon. *Journal of Geophysical Research*, **74**, 5981–5994.

McGill, G. E. (1977). Craters as "fossils": The remote dating of planetary surface materials. *Geological Society of America Bulletin*, **88**(8), 1102–1110.

McMillan, P., Wolf, G., and Lambert, P. (1992). A Raman spectroscopic study of shocked single crystalline quartz. *Phys. Chem. Miner.*, **19**, 71–79.

Melosh, H. J. (1989). *Impact cratering: A geologic process*, Volume 11. Oxford Monographs on Geology and Geophysics, Oxford University Press. 253 pages.

Melosh, H. J. (2007). Hydrocode equation of state for SiO2. *Meteoritics & Planetary Science*, **42**(12), 2035–2182.

Melosh, H. J. and Ivanov, B. A. (1999). Impact crater collapse. *Annual Review of Earth and Planetary Sciences*, **27**, 385–415.

Melosh, H. J., Ryan, E., and Asphaug, E. (1992). Dynamic fragmentation in impacts - hydrocode simulation of laboratory impacts. *Journal of Geophysical Research*, **97**(E9), 14735–14759.

Michael, G. G. and Neukum, G. (2010). Planetary surface dating from crater size-frequency distribution measurements: Partial resurfacing events and statistical age uncertainty. *Earth and Planetary Science Letters*, **294**(3-4), 223 – 229.

Monaghan, J. J. (1992). Smoothed particle hydrodynamics. *ARAA*, **30**, 543–574.

Moser, D., Poelchau, M. H., Stark, F., and Grosse, C. (2013). Application of non-destructive testing methods to study the damage zone underneath impact craters of MEMIN laboratory experiments. *Meteoritics & Planetary Science*, **48**, 87–98.

Moser, D. E., Suggs, R. M., Kupferschmidt, L., and Feldman, J. (2015). Lunar impact flash locations from nasa's lunar impact monitoring program. Nasa technical report.

Nakamura, Y. (2005). Farside deep moonquake and deep interior of the Moon. *Journal of Geophysical Research*, **110**, 1–12.

Nakamura, Y., Latham, G., and Dorman, H. (1982). Apollo lunar seismic experiment - final summary. *Journal of Geophysical Research*, **87**, A117–A123.

O'Keefe, J. D. and Ahrens, T. J. (1993). Planetary cratering mechanics. *Journal of Geophysical Research*, **98**(E9), 17011–17028.

O'Keefe, J. D., Stewart, S. T., Lainhart, M. E., and Ahrens, T. J. (2001). Damage and rock-volatile mixture effects on impact crater formation. *International Journal of Impact Engineering*, **26**(1-10), 543–553.

Pavloskii, M. N. (1976). Measurements of the velocity of sound in shock compressed quartzite, dolomite, anhydrite, sodium chloride, paraffin, plexglass, polyethylene and fluoroplast-4. *J. Appl. Mech. and Tech. Phys., Polyethylene*, **5**, 136.

Pierazzo, E. and Collins, G. S. (2003). A brief introduction to hydrocode modelling of impact cratering. In P. Claeys and D. Henning, Publisher, *Submarine Craters and Ejecta-Crater Correlation*, Pages 323–340. Springer, New York.

Pierazzo, E. and Melosh, H. J. (1999). Hydrocode modeling of Chicxulub as an oblique impact event. *Earth and Planetary Science Letters*, **165**(2), 163–176.

Pierazzo, E. and Melosh, H. J. (2000). Hydrocode modeling of oblique impacts: The fate of the projectile. *Meteoritics & Planetary Science*, **35**(1), 117–130.

Pierazzo, E., Vickery, A. M., and Melosh, H. J. (1997). A reevaluation of impact melt production. *Icarus*, **127**(2), 408–423.

Pierazzo, E., Artemieva, N. A., and Ivanov, B. A. (2005). Starting conditions for hydrothermal systems underneath martian craters: Hydrocode modeling. *GSA Special Paper*, **384**, 443–457.

Pierazzo, E., Artemieva, N. A., Asphaug, E., Baldwin, E. C., Cazamias, J., Coker, R., Collins, G. S., Crawford, D. A., Davison, T. M., Elbeshausen, D., Holsapple, K. A., Housen, K. R., Korycansky, D. G., and Wünnemann, K. (2008). Validation of numerical codes for impact and explosion cratering: Impacts on strengthless and metal targets. *Meteoritics & Planetary Science*, **43**(12), 1917–1938.

Poelchau, M., Kenkmann, T., Hoerth, T., Schäfer, F., Rudolf, M., and Thoma, K. (2014). Impact cratering experiments into quartzite, sandstone and tuff: The effects of projectile size and target properties on spallation. *Icarus*, **242**, 211–224.

Poelchau, M. H., Kenkmann, T., Thoma, K., Hoerth, T., Dufresne, A., and Schäfer, F. (2013). The MEMIN research unit: Scaling impact cratering experiments in porous sandstones. *Meteoritics & Planetary Science*, **48**, 8–22.

Poirier, J. P. (1991). *Introduction to the Physics of the Earth's Interior*. Cambridge University Press, New York, 2 edition. 312 pages.

Richardson, J. and Kedar, S. (2013). An experimental investigation of the seismic signal produced by hypervelocity impacts. *44rd Lunar and Planetary Science Conference, LPI Contribution*, **1719**, 2863.

Richardson, J. E., Melosh, H. J., Greenberg, R. J., and P., O. D. (2005). The global effects of impact-induced seismic activity on fractured asteroid surface morphology. *Icarus*, **179**, 325–349.

Richardson, J. E., Melosh, H. J., Lisse, C. M., and Carcich, B. (2007). A ballistics analysis of the Deep Impact ejecta plume: Determining Comet Tempel 1's gravity, mass, and density. *Icarus*, **190**(2), 357–390.

Riedel, W. (2000). Beton unter dynamischen lasten. meso- und makromechanische modelle und ihre parameter. In K. Thoma and S. Hiermaier, Publisher, *Forschungsergebnisse aus der Kurzzeitdynamik*, Nummer 5. Fraunhofer Institute for High Speed Dynamics, Ernst-Mach-Institute.

Riedel, W., Wicklein, M., and Thoma, K. (2008). Shock Properties of Conventional and High Strength Concrete, Experimental and Mesomechanical Analysis. *International Journal of Impact Engineering*, **35**, 155–171.

Rinehardt, J. S. (1960). *On fractures caused by explosions and impacts*, Volume 55. Quarterly of the Colorado School of Mines, Golden, Colorado.

Robinson, M., Brylow, S., Tschimmel, M., Humm, D., Lawrence, S., Thomas, P., Denevi, B., Bowman-Cisneros, E., Zerr, J., Ravine, M. A., Caplinger, M. A., Ghaemi, F. T., Schaffner, J. A., Malin, M. C., Mahanti, P., Bartels, A., Anderson, J., Tran, T. N., Eliason, E. M., McEwen, A. S., Turtle, E., Jolliff, B. L., and H., H. (2010). Lunar reconnaissance orbiter camera (lroc) instrument overview. *Space Science Reviews 150*, **150**(1-4), 81–124.

Schade, S. and Wünnemann, K. (2007). Numerical Modeling of Pore Space Collapse Due to Shock Wave Compression. *Lunar and Planetary Science Conference*, **XXXVIII**(Abstract 1338).

Schäfer, F., Thoma, K., Behner, T., Nau, S., Kenkmann, T., Wünnemann, K., and Deutsch, A. (2006). Impact experiments on dry and wet sandstone. In *Proceedings: First International Conference on Impact Cratering in the Solar System*, Volume 612 von *ESA Special Publication*, Pages 1–6. European Space Research and Technology Centre (ESTEC), Noordwijk, NL.

Schmidt, R. M. (1980). Meteor crater: Energy of formation - implications of centrifuge scaling. Proc. Lunar Planet. Sc. Conf. 11th, Pages 2099–2128.

Schmidt, R. M. and Housen, K. R. (1987). Some recent advances in the scaling of impact and explosion cratering. *International Journal of Impact Engineering*, **5**, 543–560.

Schultz, P. H. and Gault, D. E. (1975). Seismic effects from major basin formations on the moon and mercury. *The Moon*, **12**, 159–177.

Scott, T. E. and Nielsen, K. C. (1991). The effects of porosity on the brittle-ductile transition in sandstones. *Journal of Geophysical Research*, **96**(B1), 405–414.

Shipman, F. H., Gregson, V. G., and Jones, A. H. (1971). A shockwave study of coconino sandstone. Technical report, General Motors Corporation and National Aeronautics and Space Administration.

Shoemaker, E. M. (1977). Why study impact craters? In D. J. Roddy, R. O. Pepin, and R. B. Merrill, Publisher, *Impact and Explosion Cratering: Planetary and Terrestrial Implications*, Pages 1–10. Pergamon Press., New York.

Shuvalov, V. and Dypvik, H. (2004). Ejecta formation and crater development of the Mjølnir impact. *Meteoritics & Planetary Science*, **39**(3), 467–479.

Sommer, F., Reiser, F., Dufresne, A., Poelchau, M. H., Hoerth, T., Deutsch, A., Kenkmann, T., and Thoma, K. (2013). Ejection behavior characteristics of experimental impacts into dry and wet sandstone. *Meteoritics & Planetary Science*, **48**, 33–49.

Stöffler, D. (1982). Density of minerals and rocks under shock compression. In K. H. Hellwege, Publisher, *Landolt-Börnstein - Numerical Data and Functional Relationships in Science and Technology. New Series, group 5.*, Volume 1, Pages 120–183. Springer, Berlin.

Stöffler, D. and Langenhorst, F. (1994). Shock metamorphism of quartz in nature and experiment: I. basic observation and theory. *Meteoritics & Planetary Science*, **29**, 155–181.

Tauzin, B., Debayle, E., Quantin, C., and N., C. (2013). Seismoacoustic coupling induced by the breakup of the 15 february 2013 chelyabinsk meteor. *Geophysical Research Letters*, **40**, 3522–3526.

Teanby, N. A. and Wookey, J. (2011). Seismic detection of meteorite impacts on Mars. *Physics of The Earth and Planetary Interiors*, **186**, 70–80.

Thoma, K., Hornemann, U., Sauer, M., and Schneider, E. (2005). Shock waves - phenomenology, experimental, and numerical simulation. *Meteoritics & Planetary Science*, **40**(9/10), 1283–1298.

Thompson, S. L. (1990). ANEOS Analytical Equation of State for Shock Physics Codes Input Manual. Technical Report SAND89-2951 UC-404, Sandia National Laboratories. 76 pages.

Thompson, S. L. and Lauson, H. S. (1972). Improvements in the Chart D radiation-hydrodynamic CODE III: Revised analytic equations of state. Technical Report SC-RR-71 0714, Sandia National Laboratory, Albuquerque, New Mexico. 118 pages.

Tillotson, J. H. (1962). Metallic equations of state for hypervelocity impact. Technical Report GA-3216, General Atomic, San Diego, CA. 73 pages.

Titley, S. (1996). Seismic energy as an agent of morphologic modification on the moon. Technical report, United States Geological Survey open-file report, Flagstaff, AZ.

Tittmann, B. R., Abdel-Gawad, M., and Housley, R. M. (1972). Elastic velocity and q factor measurements on apollo 12, 14, and 15 rocks. In *Lunar Science Conference, 3rd, Houston, Tex., Proceedings 3. Houston, Texas.*, Pages 2565–2575, Cambridge, Mass., USA. MIT Press.

Tonn, R. (1991). The determination of the seismic quality factor q from vsp data: a comparison of different computational methods. *Geophysical Prospecting*, **39**, 1–27.

Weaver, H. A., A'Hearn, M. F., Arpigny, C., Boice, D. C., Feldman, P. D., Larson, S. M., Lamy, P., Levy, D. H., Marsden, B. G., Meech, K. J., and et al. (1995). The Hubble Space Telescope (HST) observing campaign on comet Shoemaker-Levy 9. *Science*, **267**, 1282–1288.

Wicklein, M. (2006). Zellulares aluminium: Entwicklung eines makromechanischen materialmodells mittels mesomechanischer simulation. In K. Thoma and S. Hiermaier, Publisher, *Forschungsergebnisse aus der Kurzzeitdynamik*, Nummer 9. Fraunhofer Institute for High Speed Dynamics, Ernst-Mach-Institute.

Winkler, K. and Nur, A. (1979). Pore fluids and seismic attenuation in rocks. *Geophysical Research Letters*, **6**, 1–4.

Wünnemann, K. and Ivanov, B. A. (2003). Numerical modelling of the impact crater depth-diameter dependence in an acoustically fluidized target. *Planetary and Space Science*, **51**, 831–845.

Wünnemann, K. and Lange, M. A. (2002). Numerical modeling of impact-induced modifications of the deep-sea floor. *Deep Sea Research Part II: Topical Studies in Oceanography*, **49**(6), 969–981.

Wünnemann, K., Morgan, J. V., and Jödicke, H. (2005). Is Ries crater typical for its size? An analysis based upon old and new geophysical data and numerical modeling. *GSA Special Paper: Large Meteorite Impacts III*, **384**, 67–83.

Wünnemann, K., Collins, G. S., and Melosh, H. J. (2006). A strain-based porosity model for use in hydrocode simulations of impacts and implications for transient crater growth in porous targets. *Icarus*, **180**, 514–527.

Wünnemann, K., Collins, G. S., and Osinski, G. R. (2008). Numerical modelling of impact melt production in porous rocks. *Earth and Planetary Science Letters*, **269**(3-4), 530–539.

Wünnemann, K., Nowka, D., Collins, G. S., Elbeshausen, D., and Bierhaus, M. (2011). Scaling of impact crater formation on planetary surfaces - insights from numerical modeling. In *Proceedings of 11th Hypervelocity Impact Symposium (HVIS)*, Pages 1–16.

Yasui, M., Matsumoto, E., and Arakawa, M. (2015). Experimental study on impact-induced seismic wave propagation through granular materials. *Icarus*, **260**, 320–331.

Zahnle, K. and MacLow, M. M. (1994). The collision of Jupiter and comet Shoemaker-Levy 9. *Icarus*, **108**, 1–17.

Zel'dovich, Y. B. and Raizer, Y. P. (2002). *Physics of Shock Waves and High-Temperature Hydrodynamic Phenomena*. Courier Dover Publications. 916 pages.

Eidesstattliche Erklärung

Ich erkläre hiermit, dass ich diese Dissertation mit dem Thema

Numerical modeling of meteorite impact-induced shock and elastic wave propagation and crater formation in heterogeneous material

selbstständig angefertigt habe und keine anderen als die angegebenen Quellen und Hilfsmittel verwendet wurden. Geistiges Eigentum anderer Autoren wurde als solches gekennzeichnet.
Des Weiteren erkläre ich hiermit, dass ich an keiner anderen Stelle ein Prüfungsverfahren beantragt bzw. die Dissertation in dieser oder anderer Form bereits einer anderen Fakultät als Dissertation vorgelegt habe.

Berlin, September 19, 2017

(Nicole Güldemeister)

Lebenslauf

Der Lebenslauf ist in der Online-Version aus Gründen des Datenschutzes nicht enthalten.

Danksagung

Mein Dank gilt Dr. Kai Wünnemann für die Betreuung und Begutachtung dieser Arbeit. Vielen Dank für das Heranführen an das spannende Gebiet der Impaktforschung und der numerischen Modellierung. Ich danke ihm für die zahlreichen Diskussionen, die Möglichkeit an zahlreichen Konferenzen teilzunehmen und die tolle Unterstützung!
Des Weiteren möchte ich Prof. Dr. Georg Kaufmann für die Begutachtung dieser Arbeit danken. Ein besonderen Dank möchte ich an Prof. W. Uwe Reimold richten, für die Leitung unserer Gruppe am Museum und die Vermittlung spannender Themen der Impaktforschung fernab numerischer Modellierung. Dem MEMIN Sprecher Prof. Thomas Kenkmann sowie Michael Poelchau als Koordinator der Forschergruppe möchte ich für die gute Zusammenarbeit und dem Austausch innerhalb des Projektes danken. Zudem wäre ohne die finanzielle Unterstützung der Deutschen Forschungsgemeinschaft im Rahmen des MEMIN Programms diese Arbeit nicht möglich gewesen. Astrid Kowitz, Dorothee Moser und Nathanael Durr haben maßgeblich zum Gelingen dieser Arbeit beigetragen, in dem gemeinsame Publikationen entstanden sind und so der Anwendungsbereich der numerischen Modellierung erweitert werden konnte. Vielen Dank dafür! Die Ausführung vieler Anwendungen von iSALE wäre ohne die Arbeit von Gareth Collins nicht möglich gewesen. Ich danke ihm dafür und für die zahlreichen Diskussionen über iSALE, vor allem technischer Natur. Mein weiterer Dank gilt der gesamten iSALE Community, insbesondere den Entwicklern von iSALE und Thomas Davison für die Bereitstellung vom *pysaleplot* tool.
Meinen Kollegen am Museum für Naturkunde Berlin vor allem Astrid Kowitz, Robert Luther, Christopher Hamann, Dirk Elbeshausen, Friedrich Krien, Michael Bierhaus, Daniela Nowka, Tanja Mohr-Westheide, Marie Hofmann, Felix Kaufmann, Tomke Fröchtenicht, Sebastian Block, Mathias Ebert, Patrice Zaag, Elena Martellato, Menghua "Peter" Zhu, Ulli Raschke möchte ich für die gute fachliche Zusammenarbeit aber auch für die lockere Atmosphäre und fachfremde Gespräche danken.

Ein großes Danke geht an meinen Großen, Gregor, und an meine zwei Kleinen, Mika & Linus, denen ich einfach dafür danken möchte, dass es sie gibt! Auch wenn die Kleinen doch zu einer Verzögerung dieser Arbeit beigetragen haben, bin ich sehr dankbar für diese willkommene Ablenkung und Bereicherung. Meine kleine Familie hat mir in den letzten Jahren immer wieder gezeigt, was wirkich wichtig ist und mich im richtigen Moment

abgelenkt und dennoch immer wieder motiviert und angespornt!
Zuletzt möchte ich meinen Eltern großen Dank aussprechen, auf die ich immer zählen konnte und kann; Danke für Eure Unterstützung und Euer Vertrauen.
VIELEN DANK!